CONTENTS

Page

PREFACE . . . . iii 1/A5

INTRODUCTION 1 1/A8

SCIENTIFIC INVESTIGATIONS WITH SHUTTLE LIDAR 4 1/A11
  RATIONALE FOR LIDAR ON SPACE SHUTTLE 4 1/A11
  SCIENTIFIC OBJECTIVES 7 1/A14
    Introduction 7 1/A14
    Scientific Objective 1: Global Flow of Water Vapor and Pollutants 10 1/B3
    Scientific Objective 2: Stratospheric and Mesospheric Chemistry and Transport 24 1/C3
    Scientific Objective 3: Radiative Models 34 1/C13
    Scientific Objective 4: Meteorological Data 46 1/D12
    Scientific Objective 5: Upper Atmospheric Waves 58 1/E12
    Scientific Objective 6: Thermospheric Chemistry and Transport . . . 67 1/F7
    Scientific Objective 7: Magnetospheric Sun and Weather Relationships 74 1/F14
  CANDIDATE SHUTTLE LIDAR EXPERIMENTS 80 1/G6

SHUTTLE ATMOSPHERIC LIDAR PROGRAM EVOLUTION 89 2/A2

APPENDIX A - DESCRIPTIONS OF SHUTTLE BORNE LIDAR EXPERIMENTS 95 2/A8

APPENDIX B - LASERS OF POTENTIAL USE FOR SHUTTLE LIDAR 163 2/F7

APPENDIX C - TRANSMITTING AND RECEIVING OPTICS CONSIDERATIONS 175 2/G5

APPENDIX D - SPECTRAL DISCRIMINATORS AND DETECTORS FOR SHUTTLE LIDAR 193 3/A14

APPENDIX E - GLOSSARY 219 3/C13

Item 830-I

NAS1.21:433

APR 2 3 1980

NASA SP-433

COMPLETED

ORIGINAL

Shuttle Atmospheric Lidar Research Program

Final Report of Atmospheric Lidar Working Group

MICROFILMED FROM
BEST AVAILABLE COPY

NASA National Aeronautics and Space Administration

235
~~226~~

NASA SP-433

Shuttle Atmospheric Lidar Research Program

Final Report of Atmospheric Lidar Working Group

Scientific and Technical Information Branch 1979
National Aeronautics and Space Administration
Washington, DC

For sale by the National Technical Information Service, Springfield, Virginia 22161 Price $9.25

PREFACE

The work described in this report was conducted by the NASA Atmospheric Lidar Working Group, which was formed by the NASA Offices of Space Science and Applications. The working group was coordinated by the Atmospheric Lidar Study Office at the NASA Langley Research Center. The purpose of this working group was to

(1) Review and expand upon the scientific rationale for a spaceborne atmospheric lidar described in the 1973 report: "Science Objectives of the Atmospheric, Magnetospheric, and Plasmas in Space (AMPS) Payload for Spacelab/Shuttle" and consider additional applications objectives.

(2) Identify the equipment to conduct this research and, in the case of development items, assist NASA in defining a program of technological research and development that will eventually lead to the necessary flight systems.

(3) Identify areas of theoretical and laboratory research which must be undertaken to support the program.

The working group was initially convened in September 1977. The material presented in this report is a result of eight meetings of the working group, with each meeting lasting several days. The membership of this international working group is

Shelby G. Tilford (Chairman)	NASA Headquarters
Edward V. Browell (Project Scientist)	NASA Langley Research Center
Vincent Abreu	University of Michigan
Sidney A. Bowhill	University of Illinois
Allan I. Carswell	York University, Canada
Marie-Lise Chanin	Centre National de la Recherche Scientifique, France
Giorgio Fiocco	Laboratorio Plasma Spazio, Italy
Gerald W. Grams	Georgia Institute of Technology
Richard Hake, Jr.	SRI International
E. D. Hinkley	Jet Propulsion Laboratory
Robert D. Hudson	NASA Goddard Space Flight Center
Charles L. Korb	NASA Goddard Space Flight Center
M. P. McCormick	NASA Langley Research Center
S. H. Melfi	NASA Goddard Space Flight Center
A. Mooradian	MIT Lincoln Laboratory
C. M Penney	General Electric Corporation
Wolfgang Renger	German Aerospace Establishment, West Germany
Philip B. Russell	SRI International
Robert K. Seals, Jr.	NASA Headquarters
Gary Swenson	NASA Marshall Space Flight Center

Lance Thomas	Appleton Laboratory, United Kingdom
Thomas D. Wilkerson	University of Maryland

Edward V. Browell, Project Scientist
Langley Research Center
National Aeronautics and Space Administration

CONTENTS

Page

PREFACE iii

INTRODUCTION 1

SCIENTIFIC INVESTIGATIONS WITH SHUTTLE LIDAR 4
  RATIONALE FOR LIDAR ON SPACE SHUTTLE 4
  SCIENTIFIC OBJECTIVES 7
    Introduction 7
    Scientific Objective 1: Global Flow of Water Vapor and Pollutants 10
    Scientific Objective 2: Stratospheric and Mesospheric Chemistry and Transport 24
    Scientific Objective 3: Radiative Models 34
    Scientific Objective 4: Meteorological Data 46
    Scientific Objective 5: Upper Atmospheric Waves 58
    Scientific Objective 6: Thermospheric Chemistry and Transport . . . 67
    Scientific Objective 7: Magnetospheric Sun and Weather Relationships 74
  CANDIDATE SHUTTLE LIDAR EXPERIMENTS 80

SHUTTLE ATMOSPHERIC LIDAR PROGRAM EVOLUTION 89

APPENDIX A - DESCRIPTIONS OF SHUTTLE BORNE LIDAR EXPERIMENTS 95

APPENDIX B - LASERS OF POTENTIAL USE FOR SHUTTLE LIDAR 163

APPENDIX C - TRANSMITTING AND RECEIVING OPTICS CONSIDERATIONS 175

APPENDIX D - SPECTRAL DISCRIMINATORS AND DETECTORS FOR SHUTTLE LIDAR 193

APPENDIX E - GLOSSARY 219

INTRODUCTION

A Multiuser Shuttle lidar facility is needed to provide unique and essential information about processes governing the composition, transformations, and dynamics of the Earth's atmosphere. It is well known that the concentrations of certain atmospheric constituents have been increasing steadily and that there are projections of concomitant changes in global temperature, climate, weather, and air quality. While some of these increases are due to natural causes, others result from the activities of mankind - to what extent we don't know. Since the consequences may seriously affect life on Earth, it is of the utmost importance that every technique which may bring us closer to an understanding of the Earth's atmosphere be explored.

One of the significant conclusions that has emerged from research conducted to date is that the classical way of viewing the atmosphere as independent layers, i.e., the troposphere, stratosphere, etc., is not suitable for studying current problems. These atmospheric layers are strongly coupled, and the understanding of any one requires knowledge about the others. This has led to the need to measure many parameters simultaneously, over an extended altitude range, with the global or synoptic coverage obtainable only by satellite.

Passive instruments are being developed for satellite-based remote sensing of the atmosphere; they include infrared radiometers, interferometers, heterodyne receivers, millimeter-wave spectrometers, and ultraviolet and visible spectrometers. Each of these instruments has limitations, and several operate only during solar sunrise or sunset transitions. Active laser systems on an orbiting satellite will provide capabilities not possible with passive sensors. Such laser systems are now being evaluated by experiments involving ground-based, aircraft, and balloon-borne platforms. Their potential for synoptic measurements with high sensitivity, high specificity, high spatial resolution, and day or night operation is evaluated in this report.

Space Shuttle provides the ideal platform for performing important lidar experiments: both for improving understanding of the Earth's atmosphere and for developing active laser systems that will eventually be placed on free-flying satellites. In order to develop the rationale for a Shuttle atmospheric lidar system, an international working group of scientists was convened by the National Aeronautics and Space Administration (NASA) in September 1977. Their charter included the definition of a general set of science and applications objectives and experiment classes that could be conducted with a Shuttle borne lidar. The working group assessed the current technology in the areas of lasers, receivers, and detectors and proposed a model for the sequence of lidar experiments. The key considerations and conclusions of the study, determined from the coordinated efforts of the NASA Atmospheric Lidar Working Group, are discussed in this report.

The primary goals of the Shuttle atmospheric lidar program are to contribute to an understanding of the processes governing the Earth's atmosphere and to evaluate atmospheric susceptibility to manmade and natural perturbations. Lidar measurements from space have a variety of features that are important to such a program. Among these are high spatial resolution, control of the source wavelength and intensity, and high measurement specificity. This report presents the rationale for exploiting these unique features from the Space Shuttle in pursuit of these goals.

Lidar can make an important contribution to seven major science and applications objectives identified by the working group:

(1) Determination of the global flow of water vapor and pollutants in the troposphere and lower stratosphere.

(2) Improvement of chemical and transport models of the stratosphere and mesosphere.

(3) Evaluation of radiative models of the atmosphere.

(4) Augmentation of the meteorological data base.

(5) Investigation of excitation, propagation, and dissipation of wave motions in the upper atmosphere.

(6) Investigation of chemistry and transport of thermospheric atomic species.

(7) Investigation of magnetospheric aspects of Sun/weather relationships.

Each of these objectives and their requirements are discussed in this report.

The working group also identified a set of 26 candidate experiment classes which significantly contribute to the seven science objectives:

(1) Cloud-top heights
(2) Tropospheric cloud and aerosol profiles
(3) Cirrus ice-water discrimination
(4) Noctilucent clouds and circumpolar particulate layer profiles
(5) Surface albedo
(6) Stratospheric aerosol profiles
(7) Alkali atom density profiles (Na, K, Li)
(8) Ionospheric metal ion distributions (Mg^+, Fe^+, Ca^+)
(9) Water-vapor profiles
(10) Trace species measurements (O_3, H_2O, NH_3, CFM's, etc.) - Total burden; rough profiles
(11) Chemical release diagnosis
(12) Stratospheric ozone profiles
(13) Upper atmosphere trace species profiles (two-satellite)
(14) Na temperature and winds
(15) Surface and cloud-top pressure measurements
(16) Tropospheric pressure profiles
(17) Tropospheric temperature profiles
(18) Trace species (O_3, H_2O, NH_3, C_2H_4, etc.) profiles

(19) Cloud-top winds
(20) Aerosol winds
(21) OH density profiles
(22) Metal atom/ion/oxide profile ($Mg/Mg^+/MgO$, 80 to 600 km)
(23) Tropospheric NO_2 burden profile
(24) Stratospheric aerosol composition
(25) NO density profiles (70 to 150 km)
(26) Atomic oxygen profiles (80 to 150 km)

These experiment classes serve as a basis for the establishment of requirements for a lidar system which would be flexible enough to permit a wide range of potential investigations. This report examines these experiment classes as to feasibility, uniqueness, and specialized requirements, as well as to how they address the science and applications objectives.

This report also describes an evolutionary program flow that incorporates realistic hardware development constraints into a coordinated sequence of lidar investigations to address the seven science objectives.

Appendixes A, B, C, and D contain detailed descriptions of each candidate experiment, as well as technology assessments of laser sources, transmitting and receiving optics, and detectors for potential use on Shuttle lidar. A glossary of acronyms, abbreviations, and symbols is included as appendix E.

Use of trade names or names of manufacturers in this report does not constitute an official endorsement of such products or manufacturers, either expressed or implied, by the National Aeronautics and Space Administration.

SCIENTIFIC INVESTIGATIONS WITH SHUTTLE LIDAR

RATIONALE FOR LIDAR ON SPACE SHUTTLE

Since the early 1960s, the development of atmospheric probing instrumentation incorporating lasers has led to a variety of lidar techniques for observing the atmosphere. The number of laser atmospheric studies has steadily increased since 1963 when the first measurements of atmospheric properties - lidar echoes from dust layers in the upper atmosphere - were reported. Rapid advances in the development of lasers and concomitant advances in electronics technology have contributed to the development of reliable, efficient lidar systems for use in atmospheric studies. The feasibility of making lidar measurements has now been firmly established in a wide variety of field measurement programs. Although the first lidar experiments were carried out from fixed ground-based sites, the advantages of operating a lidar system from a moving platform have been demonstrated by a number of lidar systems that have been developed and successfully operated from research aircraft, ships, and instrumented trailers or vans. The use of a space-borne platform would capitalize on the unique capabilities of the lidar technique to probe the atmosphere with high spatial resolution, providing global observations of certain species and atmospheric parameters on a continuous around-the-clock basis. For some experiments, such as those which examine the evolution of the atmosphere on a global scale, this ability to obtain an effectively instantaneous "snapshot" of the atmosphere is essential.

Although a variety of in situ and passive remote sensing techniques are available for measuring some of the atmospheric parameters needed for an understanding of the Earth's atmosphere, the combination of spatial resolution and sensitivity inherent in a Shuttle borne lidar can seldom be equalled by these other measurement systems. For the lidar technique, the vertical distribution of a species is derived directly from observations of the magnitude of the laser echo as a function of the time interval from laser pulsing; with passive remote sensors, on the other hand, vertical profiles must be inferred by using spectral or geometric inversion techniques. Typical laser pulse lengths of order 30 ns correspond to lidar range resolutions of less than 5 m. The horizontal resolution for a single laser pulse is also high. For example, the pulse diameter of a 1 mrad laser beam at a range of 300 km is only 300 m; the beam diameter can be made correspondingly narrower or wider by varying the divergence of the transmitted laser pulse. Frequently, a number of consecutive laser echoes will be averaged in order to achieve an adequate signal-to-noise ratio for a specific experiment; the horizontal resolution is then determined by the distance that the spacecraft travels while the required number of pulses are being transmitted. Many atmospheric experiments may not require the high vertical resolution inherent in the lidar technique. For such cases, simple trade-offs between horizontal and vertical resolution are accomplished by integrating individual laser echoes over much longer range intervals (e.g., over 500 m range increments) to achieve the required signal-to-noise ratio with fewer laser pulses. While certain in situ techniques may provide comparable spatial resolution in one dimension (e.g., vertical profiles of atmospheric constituents obtained by rocket-borne instruments), they cannot provide the nearly instantaneous two-dimensional cross sections that would be obtained with a Shuttle borne lidar.

In certain cases, such as for studies of cloud-top heights in the troposphere or studies of wave propagation through the sodium layer in the upper atmosphere, the superior vertical resolution made possible by the lidar technique is essential to the science objectives being addressed. Furthermore, the use of a space-borne lidar to obtain range-resolved vertical profiles appears to be the only technique that can provide global observations of tropospheric aerosol particles, tenuous cirrus clouds, and surface reflection characteristics. The range resolution inherent in the pulsed-lidar technique is also needed when it becomes necessary to characterize the three-dimensional distribution of a target such as the product of a chemical release; although passive observations can provide some range information by triangulation, this is usually done at the expense of operational convenience and data quality. For other experiments, such as in studies of the horizontal inhomogeneity of aerosol layers on scales of less than 200 km, passive limb scanning sensors are not able to provide the required information at all, and passive nadir-viewing sensors have neither the vertical resolution nor the sensitivity that lidar can provide. In general, the spatial and spectral characteristics of the laser can often be tailored to provide a measurement sensitivity which is superior to that of passive techniques. For example, this is the case when pulsed lasers are used to locate and measure subvisible cirrus clouds and aerosol layers and when tuned lasers are used to generate narrow spectral lines to access strong absorption features associated with infrared-active molecules that would not otherwise be detected by conventional solar-absorption or thermal-emission sensors.

A space-borne lidar can carry out measurements involving radiation at wavelengths that cannot effectively be propagated through the lower atmosphere. For example, the ultraviolet wavelengths required for measurements of metal-ion species in the mesosphere and for two-photon atomic oxygen experiments in the upper atmosphere are severely attenuated by absorption in the lower atmosphere, and the experiments are not possible from the ground. Furthermore, since lidar provides its own illumination source, it can often perform the observations in both daytime or nighttime conditions, in contrast to many of the passive sensors which require sunlight or twilight conditions for operation. Actually, nighttime is the favorable period for the many lidar experiments that use wavelengths in the solar spectrum and must overcome sunlight background. Even though many of these experiments may be restricted to nighttime operation, they still deliver a greater concentration of data than twilight experiments. Lidar can also provide data that are complementary to the passive daytime data with the possibility of improved resolution and other benefits mentioned above. Other space-borne experiments for which a lidar system would provide a unique observational capability include direct measurements of alkali-atom densities in the upper atmosphere, discrimination between ice crystals and water droplets in clouds by polarization-sensitive backscatter, remote measurements of the surface pressure, and direct measurements of tropospheric, stratospheric, and mesospheric winds by Doppler sensitive active probing.

Coordinated measurements with other Shuttle experiments would also be possible and are highly recommended; the multi-instrument design of the Shuttle provides an opportunity for synergistic experiments involving lidar and other sensor systems located on the same spacecraft. As an example, simultaneous lidar and passive infrared measurements of cloud-top heights would provide both a means for testing conventional measurement techniques and the necessary data for improving passive analysis algorithms. Active perturbation experiments involving excitation by the lidar beam and detection by other sensors are also attractive possibilities.

At its present stage of evolution, lidar instrumentation is relatively large and requires a large fraction of the power available on the Shuttle. Improvements in size and efficiency are steadily being made, however, and the multiple-reflight nature of the NASA Shuttle program is ideal for an instrument of this type, permitting the evolutionary process to occur with a wide variety of initial experiments and with the implementation of more advanced systems with greater flexibility and measurement effectiveness for subsequent flight programs.

SCIENTIFIC OBJECTIVES

Introduction

In identifying those problems which are best addressed by an orbiting lidar system, the special features of the lidar must be considered. These features are

(1) The ability to actively probe the atmosphere

(2) Very good vertical resolution when used in the pulsed mode

(3) Fine horizontal resolution with the capability to probe the troposphere between the clouds

(4) Very high sensitivity in aerosol and thin-cloud detection

(5) The ability to select atmospheric constituents by narrow spectral features, such as in resonant scatter or in absorption

(6) The ability to measure temperatures of these constituents by the spectral shape of the features, given adequate spectral purity of the laser

(7) The possibility of measuring the spectrum of the lidar return either by high-resolution interferometry or by heterodyne detection, with sufficient resolution to determine the Doppler shift; thence, after eliminating the satellite motion, to deduce the atmospheric motion field

(8) The ability to obtain global-scale data rapidly

(9) The ability to point the lidar system in any direction, subject to the restriction of slew rate and scattered sunlight

The scientific objectives presented in this section, while of great interest and significance themselves, are not the entire range of scientific problems of interest in the atmosphere. Rather, they are a set of very important problems to which the orbiting lidar can make a unique contribution - problems that cannot be solved by other techniques alone. Some of them can be addressed by lidar itself without any accompanying observations; in other cases, complementary observations by passive techniques, in situ probes from balloons or rockets, or radio probing from the ground are needed to obtain the maximum scientific benefit. These correlative observations are indicated for each objective.

As a consequence of special features (2) and (3) given above, an orbiting lidar will have a view of the troposphere that is unique among spaceborne sensors. That is, although passive limb scanners can have quite good vertical resolution, their view of the troposphere is usually blocked by clouds; on the other hand, passive nadir viewing sensors, which can view between the clouds, have less vertical resolution and often less sensitivity. Lidar's unmatched ability to probe between clouds with good vertical resolution opens up a whole class of global tropospheric studies that only spaceborne experiments can provide. Examples of these studies are mentioned below and elaborated on in later sections.

It also happens that the capabilities of orbiting lidar make it particularly suitable for studies of the stratosphere and mesosphere. This region, between 10 and 100 km altitude, is known as the "middle atmosphere." The scientific problems for this region were studied at a 1976 conference in Urbana, Illinois, and are documented in the Middle Atmosphere Program Planning Document (1976). Further discussions of the problems are contained in the Upper Atmosphere Research Satellite planning document (1978) and in "Upper Atmosphere Research in the 1980's - Ground-Based Rocket and Airborne Techniques," a document in preparation by the Committee on Solar Terrestrial Research, National Academy of Sciences - National Research Council, Washington, DC 20418.

As a result of strong international scientific interest, the Middle Atmosphere Program (MAP) has been approved by the International Council of Scientific Unions as a program of cooperative research in the period 1982-1985, with the participation of four scientific unions, the Scientific Committees on Space Research and on Solar-Terrestrial Physics, and the World Meteorological Organization.

One of the questions of prime scientific concern in the middle atmosphere is the mechanism by which long-lived chemical compounds and particulates make their way from the Earth's surface into the middle atmosphere. Simplified one- or two-dimensional models parameterize this flow in terms of an eddy transport coefficient. However, the situation in the real atmosphere is much more complex. Not only are the sources unevenly distributed over the surface of the globe, but the vertical transport is dominated by troposphere/stratosphere exchange like that found in the tropics and that associated with tropopause folding at medium latitudes. Scientific objective 1 addresses itself to the problem of tracing the actual paths followed by various tracers and relating it to the general circulation. If the Spacelab lidar is operational during the period of MAP from 1982 to 1985, it will be able to make a substantial contribution to this international cooperative effort.

The global distribution of natural and artificial minor constituents in the middle atmosphere is of great importance in determining the chemistry of ozone. The Spacelab lidar will be capable of measuring ozone and other related chemical species and can make a substantial contribution to the knowledge of ozone chemistry. As described under scientific objective 2, the scientific yield from the lidar measurements will be greatly enhanced by combining them with passive measurements from space, balloon, and rocket measurements of minor constituent concentrations.

All models of the terrestrial climate involve assumptions about radiative parameters of the atmosphere. Since a lidar system is capable of measuring a wide range of radiatively active constituents with precision in altitude, it can provide a new data base for global radiative models, as described in scientific objective 3. In fact, since the largest amounts of radiatively active constituents (e.g., aerosols, water vapor, CO_2) are located in the troposphere, lidar's unique view of this atmospheric layer (mentioned above) is especially applicable to this objective. As an example, the unique ability of Shuttle lidar to make global measurements of tropospheric aerosols with the required vertical resolution and sensitivity has been cited in the planning document, "Guidelines for the Aerosol Climatic Effects Special Study: An Element of the NASA Climate Research Program" (1979).

The Global Atmospheric Research Program (GARP), which is intended to provide data to test new global circulation models of the atmosphere, can benefit from certain limited but important measurements of temperature, pressure, and cloud-top height which will be derived from the Spacelab lidar program. The benefits and limitations of these data are explored under scientific objective 4.

Scientific objectives 5, 6, and 7 relate to a number of problems in the atmosphere above the stratosphere accessible to neither balloons nor satellites. In this region, scatter from aerosols is much less frequent and Rayleigh scatter by air molecules is too weak for use by lidar. However, a number of species are present which can scatter resonantly, for example, atmospheric metals, metal ions, and hydroxyl. These will be used as tracers to study thermospheric dynamics (objective 5), chemistry (objective 6), and electrodynamic coupling to the solar-terrestrial environment (objective 7). Together with ground-based optical and radar probing and the use of rockets where appropriate, lidar is expected to give a new perspective on the physics and chemistry of this interesting and complex part of the atmosphere.

References

Middle Atmosphere Program Planning Document. Dep. Elect. Eng., Univ. Illinois, June 1976.

Upper Atmosphere Research Satellite Program - Final Report of the Science Working Group. JPL Publ. 78-54, NAS7-100, July 15, 1978. (Available as NASA CR-157558.)

Guidelines for the Aerosol Climatic Effects Special Study: An Element of the NASA Climate Research Program. NASA TM-78554, 1979.

Scientific Objective 1: Global Flow of Water Vapor and Pollutants

The purpose of scientific objective 1 is to trace the global flow of water vapor and pollutants in the troposphere and lower stratosphere.

Introduction

Understanding atmospheric transport processes requires understanding the transformation and flow of water vapor and pollutants from local chemical and microphysical processes through the general circulation of the atmosphere itself. In recent years, the atmosphere has increasingly been viewed as one of our natural resources, and the possibility that it would suffer from contamination by anthropogenic pollutants has increased our interest in the transport of such impurities over long distances by atmospheric motions. The understanding of transport processes is therefore of vital interest, not only for local air pollution control and planning but also for studies of global contamination of the atmosphere by widespread application of fertilizers, by the use of CFM's in aerosol spray cans, by nuclear experiments, by aviation, and by space technology.

The use of trace constituents of the atmosphere for establishing the effects of the general circulation on the transport of pollutants has been actively pursued. The global nature of the problem, however, requires new approaches to augment our understanding of global transport processes in the atmosphere and of the general circulation, especially outside and above the radiosonde networks. In particular, it appears possible to use a lidar on Shuttle or some other spacecraft to trace the global motion of particulates and gaseous pollutants which react only slowly with the surrounding constituents of the atmosphere or with the Earth's surface and which are generated in specific source regions. Ground-based lidars have already been used, for example, to document the time history of the changes in the height and concentration of aerosol particles in the stratosphere after the eruption of the Mt. Agung volcano in Bali in 1963 and after the eruption of the Fuego volcano in 1975. These observations, made at various times and locations by a number of different lidar groups, have been used to study stratospheric transport processes (e.g., Cadle et al., 1976). It would be extremely interesting to carry out a similar series of global observations of stratospheric aerosols from Shuttle for a 2- or 3-year period when another major volcanic eruption occurs. It is not necessary, of course, to wait for dramatic natural events such as a large volcanic eruption to study atmospheric transport processes. Measurements of dust particles transported in distinct layers over large distances from desert regions in Africa and Asia would provide data for use in studying tropospheric transport processes. Also, measurements of aerosol particles or gaseous pollutants such as O_3, SO_2, or the CFM's downwind of major urban areas could be used as input for testing and validating models of atmospheric dispersion by mesoscale flow fields.

There are a number of other problems that are of current interest in the scientific community. One is that of understanding the mechanisms for troposphere-stratosphere exchange processes involving such phenomena as the intrusion of ozone from the stratosphere to the troposphere in extremely thin (e.g., 1/2 km) layers or the injection into the stratosphere of tropospheric air with relatively high concentrations of water vapor in the vicinity of thunderstorms (Kuhn et al., 1971). Another subject having considerable current interest is that of atmospheric CO_2. The increase in the CO_2 content of the atmosphere has been well documented since 1958; however, the increase is equivalent to only about 50 percent of that known to have been produced by fossil fuel burning during the same period. Controversy exists on the process responsible for removing the excess CO_2. Accurate measurements of the concentration (or mixing ratio) of CO_2 near the Earth's surface might help to identify important sources and sinks of the molecule and thereby contribute to a resolution of that debate.

Previous Lidar Research

The presence of aerosol layers near or below the mesopause has been established by numerous visual observations of noctilucent clouds. Lidar measurements have been conducted at high latitudes where noctilucent clouds are observed (Fiocco and Grams, 1966 and 1969). The measurements indicate that the altitude region between 60 and 70 km contains an appreciable amount of particulate material during periods of noctilucent cloud activity; observations of transient features of a noctilucent cloud were also obtained during those experiments. Lidars have also detected mesospheric scattering layers at lower latitudes. During October and November of 1966 in England, Bain and Sandford (1966) detected layers at about 71 km with scattering 2.5 times that expected from a molecular atmosphere. McCormick et al. (1967) observed echoes from the 65 to 85 km region during February 1967 in Maryland. Latitudinal and seasonal changes in the vertical distribution of extraterrestrial aerosols below 100 km have been related to the general circulation of the upper atmosphere (Fiocco and Grams, 1971). The aerosol layers observed near 70 km are presumably of extraterrestrial origin. Estimates of the mass flux of extraterrestrial dust based on lidar data obtained at high latitudes (Fiocco and Grams, 1969) are in agreement with results obtained by other techniques (summarized, for example, by Parkin and Tilles, 1968).

The layer of aerosols found in the interval from about 15 to 25 km has also been observed extensively by Lidar. The existence of the layer was confirmed in the early 1960's by Junge and his collaborators (Junge and Manson, 1961; Chagnon and Junge, 1961; Junge et al., 1961) using balloon-borne impactors. Gruner and Kleinert (1927) and Gruner (1942) had previously concluded from twilight observations that there was dust above the tropopause, as had Bigg (1956) and Volz and Goody (1962) from more sophisticated twilight sky intensity measurements. The "Junge layer" has since been verified and studied extensively by many investigators employing both in situ and remote sensing techniques. The first lidar observations of the layer were reported by Fiocco and Grams (1964). These investigators carried out a 2-year study of the layer in 1964-65 in Massachusetts (Grams and Fiocco, 1967). The lidar profiles indicated a layer in the 15 to 20 km region for which the backscattering was almost twice as large as that expected from a dust-free molecular atmosphere; i.e., the backscattering from the aerosols and molecules was approximately equal. Comparisons between these results and those obtained earlier by other techniques indicated that the stratospheric aerosol concentration was about one order of magnitude higher, presumably because of the eruption of Mt. Agung in March 1963.

Since then, other investigators have used lidars for stratospheric aerosol studies. These results indicate a long-term trend toward decreasing aerosol concentrations after the Mt. Agung eruption which continued until late 1974, when high backscattering ratios were again observed following the eruption of the Fuego volcano. The temporal variation of the lidar returns from the stratospheric aerosol layer is summarized in figure 1. Results obtained with balloon-borne photoelectric particle counters are also shown for comparison. The lidar results shown in figure 1 appear to bracket the natural variability of the backscattering cross section of the stratospheric aerosol, with the exception of times and locations very close to volcanic injections.

The trapping of aerosol particles below temperature inversions is an effect that can be detected by lidar and used in boundary-layer studies. For example, a vertically pointing laser radar operated at a fixed location to determine time-height data on aerosol concentration can define the height of the boundary layer continuously throughout the diurnal cycle, as demonstrated by Uthe (1972) and Russell et al. (1974) and illustrated in figure 2. Alternatively, spatial variations of boundary-layer height have been obtained with a ground-based scanning lidar measuring two- or three-dimensional aerosol concentration profiles (Collis, 1969; Olsson et al., 1974) and with an airborne lidar looking downward (Grams et al., 1975; Melfi et al., 1974), as illustrated in figure 3. Lidar applications involving the acquisition of data on pollutant particles have been discussed by a number of authors, including Johnson (1969 and 1971), Barrett and Ben-Dov (1967), Hamilton (1966, 1967, and 1969), and Ruppersberg and Renger (1976).

Shuttle Studies

The above discussion underlines the fact that lidar observations of aerosol layers in the atmosphere are of considerable scientific interest. While many of the reported studies were obtained with ground-based systems, a number of experiments using airborne lidars have also been carried out. These studies reflect an interest in using lidars for mapping the spatial distribution of the airborne particles over large geographic areas to study, for example, the dispersion of pollution particles in the urban boundary layer (Melfi et al., 1974) or the meridional distribution of particulates in the stratospheric aerosol layer (Fox et al., 1973). It is apparent that the ability of the Shuttle lidar to detect and trace the global flow of aerosol particles in the mesosphere, stratosphere, and troposphere will attract the interest of the scientific community. While other satellite techniques can obtain data above the tropopause (e.g., the SAM II or SAGE solar occultation measurements), the ability of an active lidar system to operate continuously along the Shuttle orbit provides a unique ability to obtain high-resolution horizontal aerosol data for use in models of aerosol transport. Furthermore, lidar represents the only technique available for studying aerosol vertical distributions in the troposphere from an orbiting platform. Table I summarizes the parameters to be measured for experiments to trace the global flow of pollutants. The table lists the accuracies and resolutions required for each measurement.

Large-scale transport of atmospheric aerosol layers.- In considering the use of the Shuttle lidar for studies of aerosol transport, it is noteworthy that there are a number of interesting research topics associated with aerosol particles generated in specific source regions and transported in distinct layers for distances measured in thousands of kilometers. The most notable examples in the troposphere are the dust layers generated in vast desert regions such as the Saharan desert in Africa and the Takla Makan and Gobi deserts of eastern Asia. In the stratosphere, as discussed earlier, large amounts of volcanic ash and gases can be injected by violent volcanic eruption; the ash and particles formed from gases such as SO_2 or COS are then dispersed by atmospheric transport processes over the entire globe.

The existence of lidar data on the temporal and spatial distribution of stratospheric aerosol particles after the eruption of the Mt. Agung and Fuego volcanos has already led to quantitative studies of the dispersion in the stratosphere. Cadle et al. (1976) used lidar data obtained over a 2-year period in Massachusetts (Grams and Fiocco, 1967) after the eruption of Mt. Agung to test a two-dimensional stratospheric transport model. Figure 4 (from Cadle et al., 1976) shows a comparison between predicted aerosol concentrations at 18 km altitude and the corresponding temporal variation of concentration determined from lidar observations after the Mt. Agung eruption. Figure 5 shows the meridional distribution of stratospheric aerosol particles at various times after the Mt. Agung eruption as predicted by the model of Cadle and his colleagues.

Dust layers from the Saharan and Asian deserts are interesting examples of cases for testing models for long-range transport of particulates in the troposphere. One of the most striking examples of long-range transport of atmospheric particulates is the layer of particles observed over the northern tropical Atlantic Ocean during the summer months. The major fraction of the aerosols in this layer is composed of mineral particles originating in the arid and semiarid regions of West Africa (Savoie and Prospero, 1977) and transported into the oceanic area in large-scale Saharan air outbreaks (Prospero and Carlson, 1972). These massive outbreaks are known to carry large amounts of dust from the west coast of Africa to the Caribbean (Prospero et al., 1970). Figure 6 shows a vertical profile of the aerosol concentration as measured by Kondratyev et al. (1976) with aerosol-particle counters operated on an aircraft over the Atlantic during the GATE program in summer 1974. The Saharan dust layer is typically several kilometers thick, with the base of the dust layer located some 1 to 1.5 km above the ocean surface. The high concentrations of dust in the layer cause considerable attenuation of solar radiation, with the optical thickness often exceeding unity. The dust cloud significantly increases the albedo of the Earth atmosphere system, and the Saharan dust outbreaks are clearly visible in satellite photographs as large bright areas over the ocean with horizontal dimensions often greater than 1000 km. Such layers would easily be detected by the Shuttle lidar and, along with photographic images from geosynchronous satellites, would significantly increase our ability to understand long-range transport processes by mapping the vertical and horizontal dispersion of the dust layer as it moves across the Atlantic.

Recently, Rahn et al. (1977) suggested that some Arctic haze layers were, in fact, dust layers transported over long distances (9000 to 12 000 km) from the Takla Makan and Gobi deserts in eastern Asia. The term "Arctic haze" refers to turbid layers of air found regularly over the pack ice north of Alaska during periods of clear weather. These layers are hundreds to thousands of kilometers wide, 1 to 3 km thick, and can occur as single or multiple bands of haze at nearly any level of the troposphere. Although they are generally difficult to detect visually from the ground, they can be viewed from aircraft since horizontal and slant visibilities within the layer can be as small as 3 to 8 km. An observation program involving the operation of surface stations and an air-borne sampling program by the Universities of Alaska and Rhode Island (Rahn et al., 1977), Shuttle lidar observations of the temporal variation in the vertical distribution and horizontal extent of the Arctic haze layers, and an appropriate three-dimensional transport modeling effort could form the basis for a comprehensive study of the transport of tropospheric dust over long distances.

Boundary-layer aerosol morphology.- Observing aerosol particles associated with smaller scales of atmospheric motion will require additional levels of sophistication for both the lidar system and the supporting modeling efforts. In particular, higher horizontal resolution would be desired for studies of mesoscale transport processes. Figure 7 shows the results of analyzing the surface visibility in the vicinity of St. Louis, Missouri, during the METROMEX program (Shea and Auer, 1978). It is apparent that studies of the downwind transport of urban pollution particles would be possible when horizontal measurements of high spatial resolution (e.g., 10 km) are available.

Sources and transport of tropospheric species.- The techniques described for studying aerosol transport can be applied to gaseous constituents when lidar techniques such as DIAL become operational. For example, ozone distributions display maximum concentration values downwind of pollution sources in urban areas. Figure 8 shows a mesoscale analysis of ozone concentration (in parts per billion by volume) in southern Ontario (Chung, 1977).

Quantification of transport models for tropospheric and stratospheric pollutants using wind and temperature measurements.- All the transport studies described above would have to rely on data obtained by other techniques such as analysis of data from the existing network of meteorological stations or special measurement programs carried out as part of a specific Shuttle experiment as input to the dispersion models. The spatial resolution of this data may not be adequate, especially over the oceans and other data-sparse regions. The transport studies will be able to take advantage of more sophisticated modeling efforts with a more complete set of data, including lidar temperature profiles and data on wind speed and direction as well as the lidar observations of the spatial and temporal distribution of the pollutant particles or gases.

Extension of pollutant transport models to include profiles of additional trace species.- New insight into the fate of atmospheric pollutants would follow from studies involving a number of atmospheric constituents that can react with each other during the transport process. Thus, simultaneous measurements of SO_2 concentrations and aerosol concentrations downwind of an extended urban source region may provide new information on the rate of conversion of SO_2 to sulfate particles. Studies of this type would necessarily require a considerable amount of confidence in the transport model, as well as the amount and quality of the concentration data used as input for predicting the long-range transport of aerosols and gases, before gas-to-particle conversion rates could be deduced.

References

Bain, W. C.; and Sandford, M. C. W.: Light Scatter From a Laser Beam at Heights Above 40 km. J. Atmos. & Terrest. Phys., vol. 28, no. 6/7, pp. 543-552, June/July 1966.

Barrett, Earl W.; and Ben-Dov, Oded: Application of the Lidar to Air Pollution Measurements. J. Appl. Meteorol., vol. 6, no. 3, pp. 500-515, June 1967.

Bigg, E. K.: The Detection of Atmospheric Dust and Temperature Inversions by Twilight Scattering. J. Meteorol., vol. 13, no. 3, pp. 262-268, June 1956.

Cadle, R. D.; Kiang, C. S.; and Louis, J.-F.: The Global Scale Dispersion of the Eruption Clouds From Major Volcanic Eruptions. J. Geophys. Res., vol. 81, no. 18, pp. 3125-3132, June 20, 1976.

Chagnon, Charles W.; and Junge, Christian E.: The Vertical Distribution of Sub-micron Particles in the Stratosphere. J. Meteorol., vol. 18, no. 6, pp. 746-752, Dec. 1961.

Chung, Y.-S.: Ground-Level Ozone and Regional Transport of Air Pollutants. J. Appl. Meteorol., vol. 16, no. 11, pp. 1127-1136, Nov. 1977.

Collis, R. T. H.: Lidar. Vol. 13 of Advances in Geophysics, H. E. Landsberg and J. Van Mieghem, eds., Academic Press, pp. 113-139, 1969.

Fiocco, G.; and Grams, G.: Observations of the Aerosol Layer at 20 km by Optical Radar. J. Atmos. Sci., vol. 21, no. 3, pp. 323-324, May 1964.

Fiocco, G.; and Grams, G.: Observations of the Upper Atmosphere by Optical Radar in Alaska and Sweden During the Summer 1964. Tellus, vol. 18, no. 1, pp. 34-38, Feb. 1966.

Fiocco, G.; and Grams, G.: On the Origin of Noctilucent Clouds: Extraterrestrial Dust and Trapped Water Molecules. J. Atmos. & Terrest. Phys., vol. 33, no. 5, pp. 815-824, May 1971.

Fiocco, Giorgio; and Grams, Gerald: Optical Radar Observations of Mesospheric Aerosols in Norway During the Summer 1966. J. Geophys. Res., vol. 74, no. 10, pp. 2453-2458, May 15, 1969.

Fox, R. J.; Grams, G. W.; Schuster, B. G.; and Weinman, J. A.: Measurements of Stratospheric Aerosols by Airborne Laser Radar. J. Geophys. Res., vol. 7, no. 33, pp. 7789-7801, Nov. 20, 1973.

Grams, G. W.: Optical Techniques for Probing the Boundary Layer. Atmos. Technol., no. 7, pp. 50-59, Fall 1975.

Grams, Gerald; and Fiocco, Giorgio: Stratospheric Aerosol Layer During 1964 and 1965. J. Geophys. Res., vol. 72, no. 14, pp. 3523-3541, July 15, 1967.

Grams, G. W.; and Rosen, J. M.: Instrumentation for In-Situ Measurements of the Optical Properties of Stratospheric Aerosol Particles. Atmos. Technol., no. 7, pp. 35-54, Spring 1978.

Grams, G. W.; Patterson, E. M.; and Wyman, C. M.: Airborne Laser Radar for Mapping Two-Dimensional Contours of Aerosol Concentration. Opt. & Quantum Electron., vol. 7, no. 3, pp. 187-191, May 1975.

Gruner, P.: Dämmerungserscheinungen, Handbuch Geophys., Bd. 8, Borntraeger (Berlin), pp. 432-526, 1942.

Gruner, P.; and Kleinert, H.: Die Dammerungserscheinungen, Probleme der Kosmischen Physik, Bd. 10, Henri Grand (Hamburg), 1927.

Hamilton, P. M.: The Application of a Pulsed-Light Rangefinder (Lidar) to the Study of Chimney Plumes. Philos. Trans. R. Soc. London, ser. A., vol. 265, no. 1161, pp. 153-172, Nov. 13, 1969.

Hamilton, P. M.: Paper III: Plume Height Measurements at Northfleet and Tilbury Power Stations. Atmos. Environ., vol. 1, no. 4, pp. 379-387, July 1967.

Hamilton, P. M.: Use of Lidar in Air Pollution Studies. Air & Water Pollut., vol. 10, no. 6-7, pp. 327-334, June-July 1966.

Johnson, W. B.: Lidar Applications in Air Pollution Research and Control. J. Air Pollut. Control Assoc., vol. 19, no. 3, pp. 176-180, Mar. 1969.

Johnson, Warren B.: Lidar Measurements of Plume Diffusion and Aerosol Structure. Conference on Air Pollution Meteorology - Preprints of Papers, American Meteorol. Soc., pp. 55-61, 1971.

Junge, Christian E.; and Manson, James E.: Stratospheric Aerosol Studies. J. Geophys. Res., vol. 66, no. 7, pp. 2163-2182, July 1961.

Junge, Christian E.; Chagnon, Charles W.; and Manson, James E.: Stratospheric Aerosols. J. Meteorol., vol. 18, no. 1, pp. 81-108, Feb. 1961.

Kondratyev, K. Ya.; Barteneva, O. D.; Chapursky, L. I.; Chernenko, A. P.; Grishechkin, V. S.; Ivlev, L. S.; Ivanov, V. A.; Korzov, V. I.; Lipatov, V. B.; Prokofyev, M. A.; Tolkatchey, V. K.; Vasiliev, O. B.; and Zhvalev, V. F.: Aerosol in the GATE Area and Its Radiative Properties. Atmos. Sci. Paper No. 247 (Contract NOAA-C4-6-158-44036), Colorado State Univ., June 1976. (Available from NTIS as PB-265 264.)

Kuhn, P. M.; Lojko, M. S.; and Petersen, E. V.: Water Vapor: Stratospheric Injection by Thunderstorms. Science, vol. 174, no. 4016, pp. 1319-1321, Dec. 24, 1971.

McCormick, P. D.; Silverberg, E. C.; Poultney, S. K.; Van Wijk, U.; Alley, C. O.; and Bettinger, R. T.: Optical Radar Detection of Backscattering From the Upper Atmosphere. Nature, vol. 215, no. 5107, pp. 1262-1263, Sept. 16, 1967.

Melfi, S. H.; Bundy, D.; Eckert, J.; Guagliardo, J.; and McElroy, J. L.: Boundary-Layer Investigations Using a Down-Looking Airborne Lidar System. 1974 International Laser Radar Conference - Conference Abstracts American Meteorol. Soc., Sept. 1974.

Olsson, L. E.; McCormick, M. P.; Elliott, W. P.; and Melfi, S. H.: An Observational Study of the Mixing Layer in Western Oregon. Atmos. Environ., vol. 8, no. 3, pp. 241-252, Mar. 1974.

Parkin, David W.; and Tilles, David: Influx Measurements of Extraterrestrial Material. Science, vol. 159, no. 3818, pp. 936-946, Mar. 1, 1968.

Prospero, Joseph M.; and Carlson, Toby N.: Vertical and Areal Distribution of Saharan Dust Over the Western Equatorial North Atlantic Ocean. J. Geophys. Res., vol. 77, no. 27, pp. 5255-5265, Sept. 20, 1972.

Prospero, J. M. et al.: Dust in the Caribbean Atmosphere Traced to an African Dust Storm. Earth & Planet. Sci. Lett., vol. 9, no. 3, pp. 287-293, Oct. 1970.

Rahn, Kenneth A.; Borys, Randolph D.; and Shaw, Glenn E.: The Asian Source of Arctic Haze Bands. Nature, vol. 268, no. 5622, pp. 713-715, Aug. 25, 1977.

Ruppersberg, Gerhard H.; and Renger, Wolfgang: Monitoring of the Tropospherical Aerosol Using a Spacelab Borne Lidar System. Atmospheric Physics From Spacelab, J. J. Burger, A. Pedersen, and B. Battrick, eds., D. Reidel Pub. Co., pp. 297-313, c.1976.

Russell, Philip B.; Uthe, Edward E.; Ludwig, Francis L.; and Shaw, Neil A.: A Comparison of Atmospheric Structure as Observed With Monostatic Acoustic Sounder and Lidar Techniques. J. Geophys. Res., vol. 79, no. 36, pp. 5555-5566, Dec. 20, 1974.

Savoie, D. L.; and Prospero, J. M.: Aerosol Concentration Statistics for the Northern Tropical Atlantic. J. Geophys. Res., vol. 82, no. 37, pp. 5954-5964, Dec. 20, 1977.

Shea, D. M.; and Auer, A. H., Jr.: Thermodynamic Properties and Aerosol Patterns in the Plume Downwind of St. Louis. J. Appl. Meteorol., vol. 17, no. 5, pp. 689-698, May 1978.

Uthe, Edward E.: Lidar Observations of the Urban Aerosol Structure. Bull. American Meteorol. Soc., vol. 53, no. 4, pp. 358-360, Apr. 1972.

Volz, F. E.; and Goody, R. M.: The Intensity of the Twilight and Upper Atmospheric Dust. J. Atmos. Sci., vol. 19, no. 5, pp. 385-406, Sept. 1962.

TABLE I.- PARAMETERS TO BE MEASURED TO TRACE GLOBAL FLOW OF POLLUTANTS

Parameter	Height range, km	Δx, km (a)	Δz, km (b)	Remarks	Lidar experiment
Aerosols	0 to 10	100	1	20 percent, haze layers, thin cirrus, Saharan and Asian dust	2, 3
	10 to 30	500	2	20 percent, stratospheric aerosols	6, 24
H_2O	0 to 10	100	1	20 percent	9, 10
	10 to 20	500	2	20 percent	
	Total	100	---	20 percent	
O_3	0 to 10	100	1	20 percent	10, 12
	10 to 30	500	2	20 percent	18, 17
XY: e.g., SO_2, CH_4, NH_3, NO_2, N_2O, CFM's, etc.	0 to 10	100	1	20 percent	10, 18, 23
	10 to 50	500	3	20 percent	
	Total	100	---	20 percent	
Temperature	0 to 3	100	0.2	1 K; define boundary layer	17
	5 to 20	500	1	2 K; define tropopause	
V_x	0 to 10	100	1	5 m/s	19, 20
	10 to 50	500	2	10 m/s	
V_z	0 to 10	100	1	5 cm/s	
	10 to 50	500	2	10 cm/s	
CO_2 mixing ratio	0 to 3	100	3	1 percent; identify sources and sinks	

[a] Horizontal resolution.
[b] Vertical resolution.

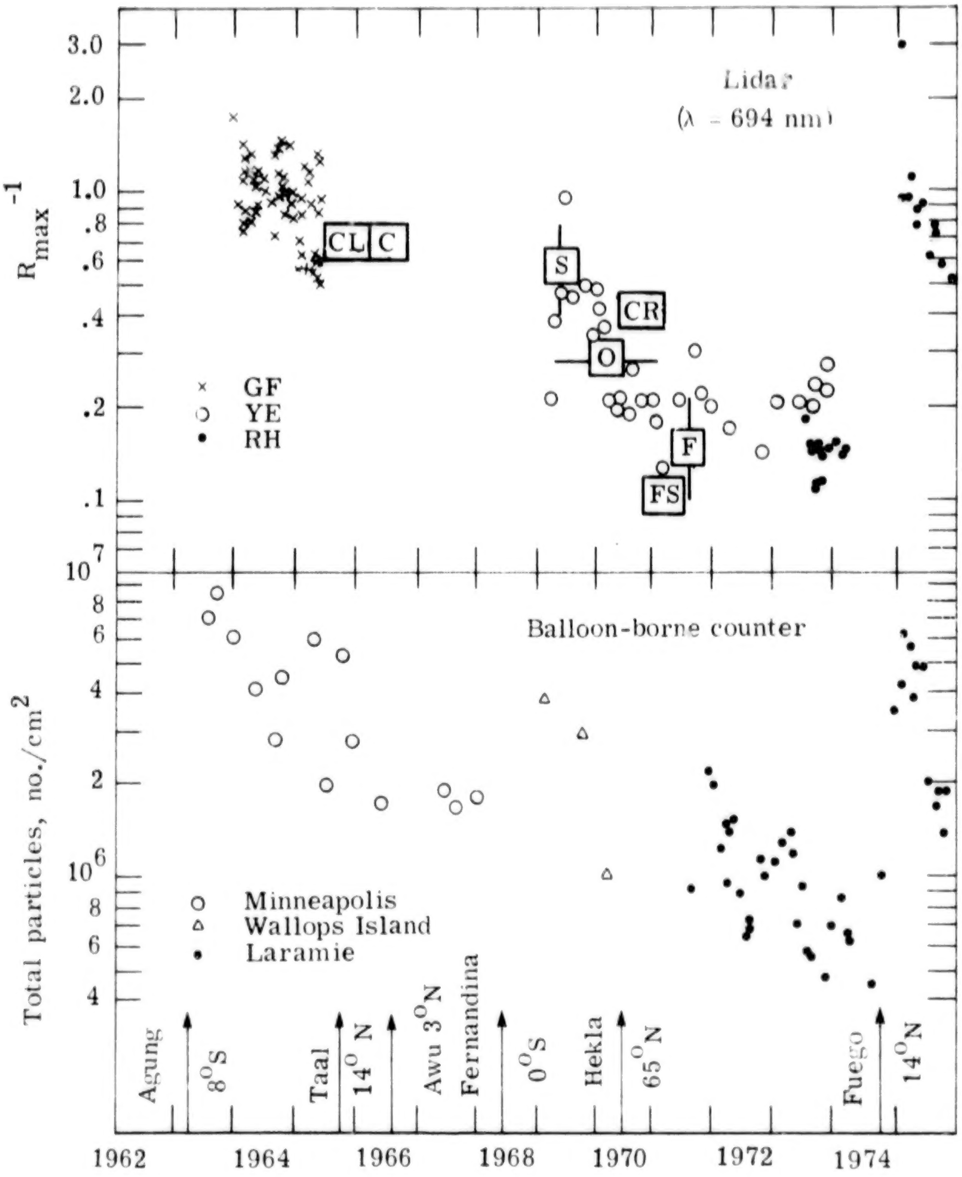

Figure 1.- Comparison of stratospheric aerosol measurements obtained by lidar and balloon-borne dustsondes between 1962 and 1975. Lidar observations obtained by:

GF (Grams and Fiocco), Mass.
CL (Collis and Ligda), Calif.
C (Clemesha et al.), Jamaica
CR (Grams and Rosen)
S (Schuster), Colo.
O (Ottway), Jamaica
FS (Frush and Schuster), Colo.
F (Fox et al.), Hawaii and Bermuda
YE (Young and Elford), Australia
RH (Russell and Hake)

(From Grams and Rosen, 1978, courtesy National Center for Atmospheric Research)

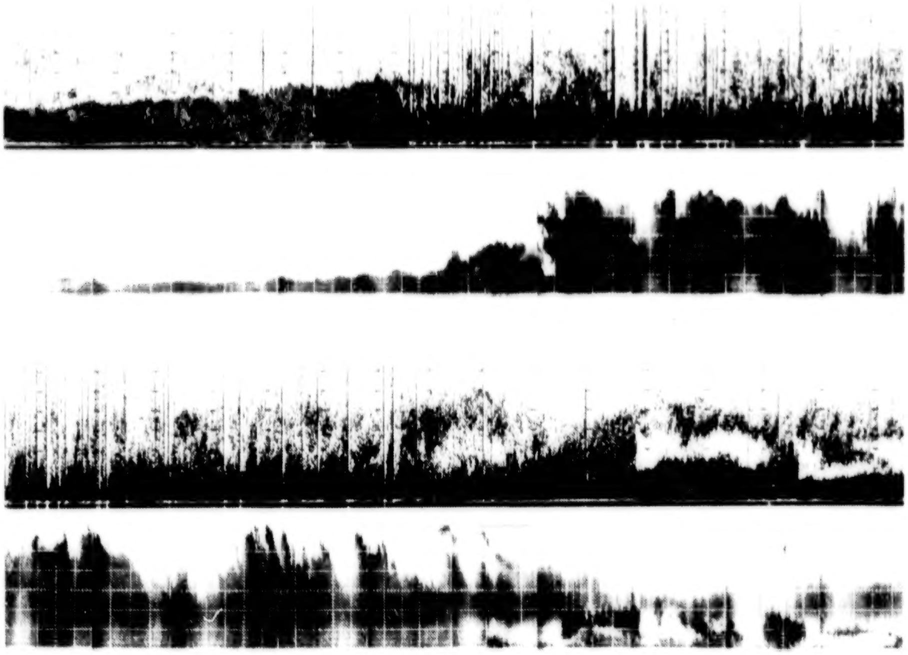

Figure 2.- Comparison of atmospheric time sections obtained by lidar and acoustic sounders at St. Louis, Missouri, on Aug. 14, 1972. Darkest areas are associated with strongest echoes. (From Russell et al., 1974)

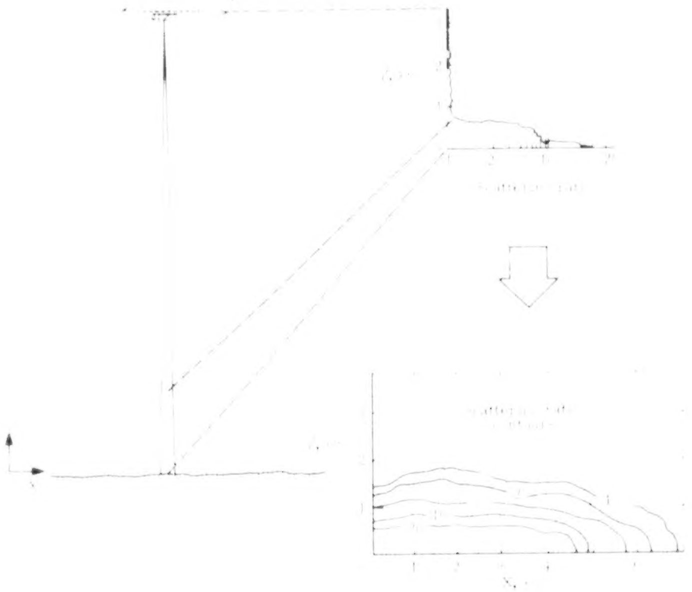

Figure 3.- Concept for observations of boundary-layer height using airborne lidar. Scattering ratio is obtained by dividing observed backscattering intensities by those expected from a dust-free atmosphere, with appropriate transmission corrections. (From Grams, 1975, courtesy National Center for Atmospheric Research)

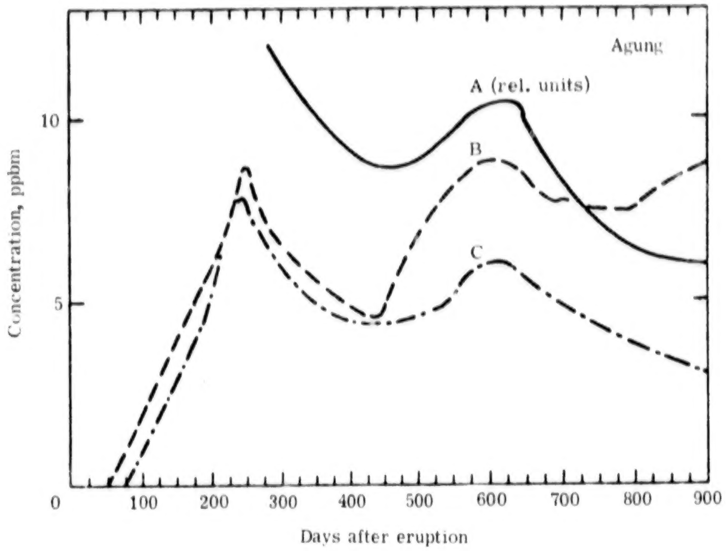

Figure 4.- Comparison between model calculations and lidar observations for temporal variation of aerosol concentration in lower stratosphere. Curve A shows lidar observations of Grams and Fiocco (1967) at the altitude of peak scattering ratio; curve B shows calculated maximum concentrations of H_2SO_4 droplets; curve C shows H_2SO_4 concentration at 18 km altitude. (From Cadle et al., 1976, courtesy American Geophysical Union)

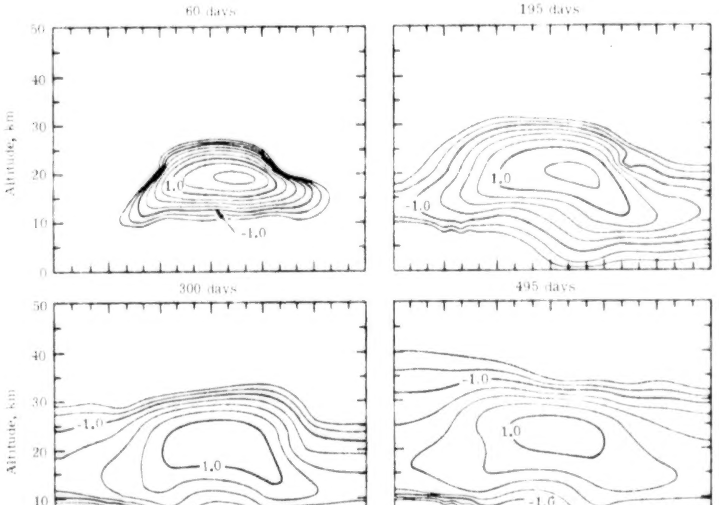

Figure 5.- Aerosol concentration isopleths (in log parts per billion by mass) from model calculations for Agung eruption. Days shown are after eruption. (From Cadle et al., 1976, courtesy American Geophysical Union)

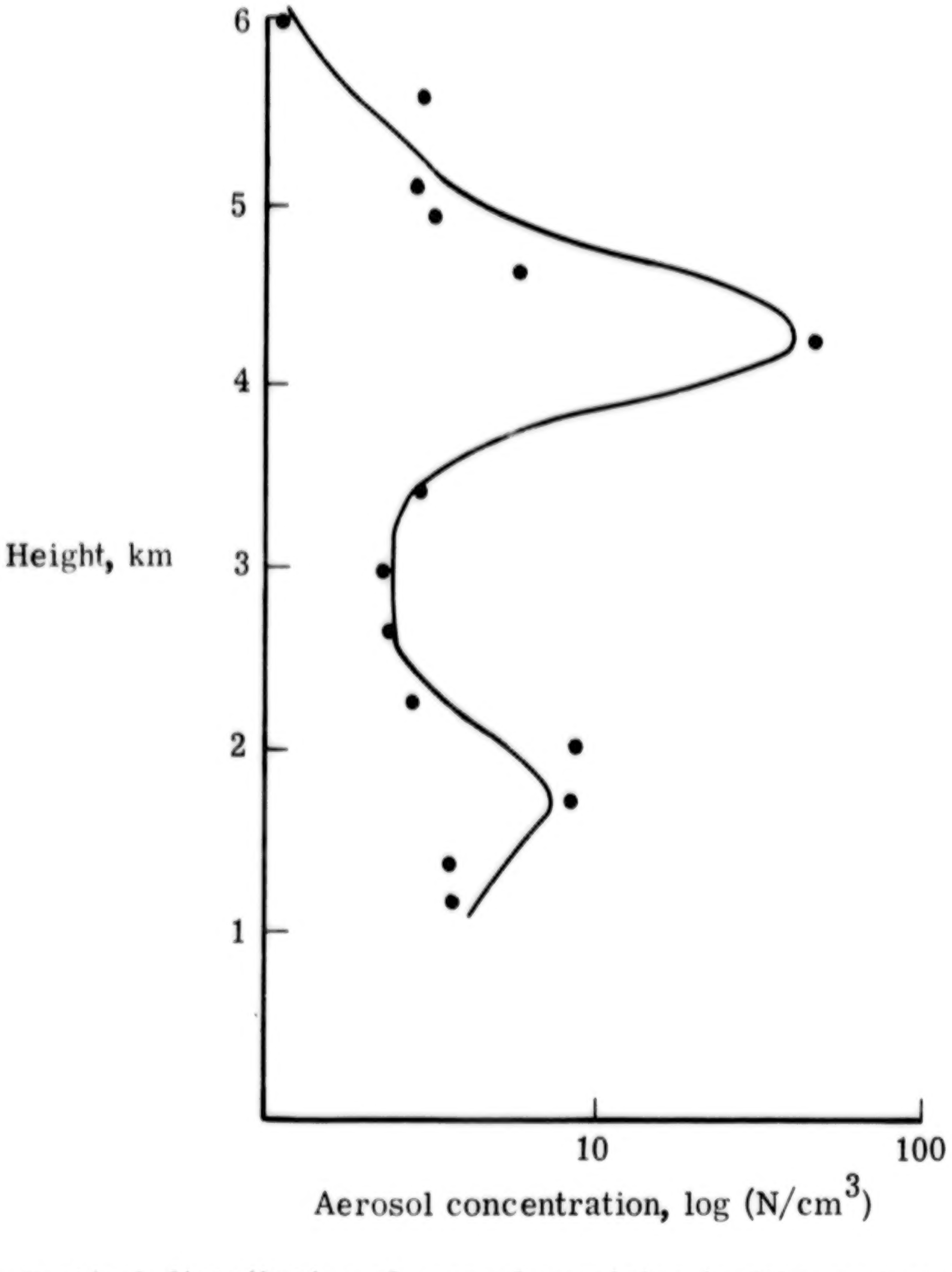

Figure 6.- Vertical distribution of aerosol particles in Saharan dust layer as observed with photoelectric particle counters during 1974 GATE program. (From Kondratyev et al., 1976)

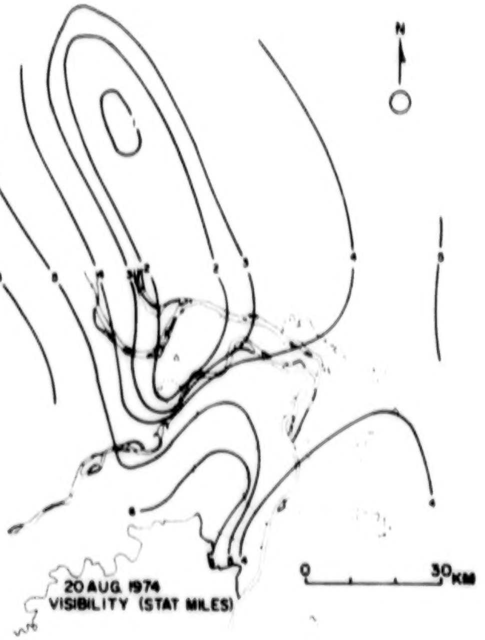
N
0
30 KM
20 AUG 1974
VISIBILITY (STAT MILES)

Figure 7.- Surface visibility in vicinity of St. Louis, Missouri, during METROMEX program in August 1974. (From Shea and Auer, 1978, courtesy American Meteorological Society)

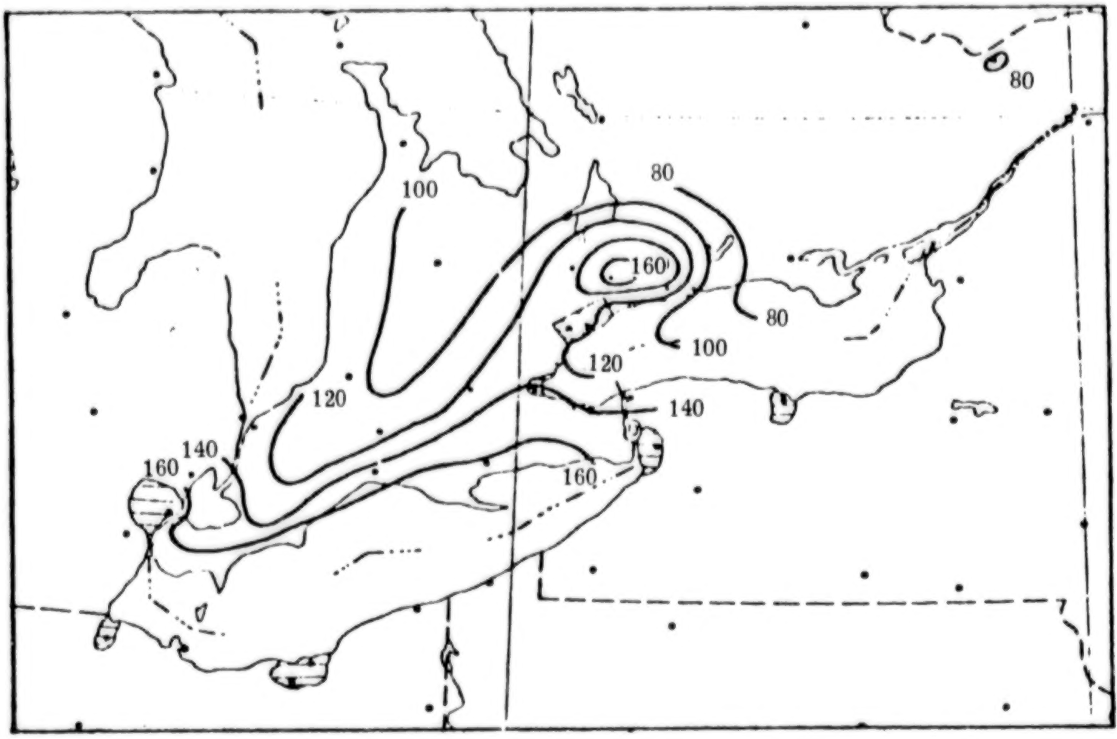
80
80
100
160
80
100
120
120
140
140
160
160

Figure 8.- Average afternoon ozone maximums (in ppb) for high ozone situations during August 1976 in southern Ontario. (From Chung, 1977, courtesy American Meteorological Society)

Scientific Objective 2: Stratospheric and Mesospheric Chemistry and Transport

The purpose of scientific objective 2 is to test and improve models of stratospheric and mesospheric chemistry and transport.

Introduction

Within the past few years, concern has been expressed as to the ability of man to inadvertently modify the upper atmosphere and, in particular, the ozone content (Molina and Rowland, 1974; Johnston et al., 1976). Any estimates of the impact of anthropogenic emissions on the ozone content must be made with sophisticated atmospheric models (Climatic Impact Committee, 1975; Panel on Atmospheric Chemistry, 1976; Hudson, 1977). The fundamental limits on the accuracies of these estimates are not the reactions or concentrations of the pollutants themselves but rather the knowledge of the many different processes which influence the overall chemical composition, energy budget, and dynamic behavior of the natural atmosphere - as well as the ability to model these complex processes.

Of necessity, therefore, the models employed must use approximations and simplifications in order to make such predictions. The purpose of objective 2 is to provide the information required to test these simplifications and improve the models.

Present Understanding

The structure of the stratosphere and mesosphere is the result of an intricate interplay among a large number of processes which, for simplicity, can be subdivided into the categories of radiation, chemistry, and dynamics. In this section, we will consider the latter two; radiation is considered in objective 3.

In general, a qualitative understanding of the chemistry of the sources, sinks, and budgets of most of the known upper atmospheric constituents now exists. Discussion of upper atmospheric chemistry can be divided into studies of a few families of constituents such as those containing nitrogen, hydrogen, chlorine, and sulfur (Crutzen et al., 1978). These families contain three basic types of species: source molecules (relatively stable compounds), radicals (short-lived derivatives of the source molecules), and sink molecules (more stable forms into which the radicals can be recombined). Concentration profiles of selected upper-atmosphere trace species are shown in figure 1 (Upper Atmosphere Research Satellite Program, 1978).

Stratospheric odd nitrogen, NO_x, is thought to come mainly from the attack of $O(^1D)$ on N_2O which is produced by bacterial denitrification in soils and the ocean (Liu et al., 1977; McElroy et al., 1976). The major sinks for NO_x should be diffusion to the troposphere, followed by rainout of soluble HNO_3 and photodissociation of NO in the upper stratosphere, followed by reaction of $N(^4S)$

with NO to form N_2. Mesospheric odd nitrogen is produced from a variety of ionization and dissociation processes and also from direct dissociation of N_2.

The hydrogen oxide budget is thought to be driven by a near photochemical equilibrium between formation by reaction of $O(^1D)$ and H_2O and destruction (mainly) by reaction of OH and HO_2 to reform H_2O (Liu et al., 1976; Luther and Duewer, 1978). The water budget is probably controlled by two main processes: transport from the troposphere and oxidation of CH_4. Rainout in the troposphere leads to significant reduction of water-vapor concentration with increasing altitudes. Thus, only a small residual penetrates the "cold trap" at the tropopause where a deep minimum in the temperature profile is found. The loss processes are condensation in the troposphere and dissociation in the upper mesosphere, followed by escape of a fraction of the H atoms.

The budget of chlorine is less well-known. The major sources are thought to be CCl_4 and CH_3Cl which are transported to the stratosphere where photolysis produces Cl atoms (Crutzen et al., 1978). Direct injection of HCl into the stratosphere is thought to be less important because of its high solubility in water. Manmade $CFCl_3$ and CF_2Cl_2, photolyzed in the stratosphere, supply an increasing fraction of the injected chlorine. Other halocarbons such as CH_3CCl_3 (methyl chloroform) may be significant sources. The only known sink for the resultant Cl_x is diffusion to the troposphere followed by rainout of HCl.

The atmospheric sulfur cycle is not well understood. Theories suggest that sulfur compounds emitted at ground level in both natural and anthropogenic processes diffuse into the stratosphere where they are oxidized, giving sulfur trioxide which later reacts in the presence of water to form sulfuric acid. It is believed that clusters of sulfuric acid molecules can act as condensation nuclei leading to the growth of stratospheric aerosols which are observed to exist in a 75-percent solution with water and are the principal components of the Junge layer. The sink for sulfur occurs when the heavier aerosols settle out of the stratosphere into the troposphere forming a dilute "acid rain."

The dynamics of the stratosphere below 25 to 30 km are at least crudely characterized and understood from studies of the transport tracers and the extension of tropospheric global circulation models (Johnston et al., 1976; Mahlman and Moxim, 1978). The dynamics of the atmosphere above 30 km is poorly characterized due to the lack of suitable experimental data for testing calculations. Most three-dimensional global circulation models extend to about 30 km; above this altitude, velocity fields are usually deduced from observed pressure and temperature fields or from sparse wind data. Suitable tracers are not available for testing because this is a region of coupled dynamics and chemistry.

The mean meridional winds are toroidal circulations, characterized, for example, at solstice by two cells between equator and pole in the stratosphere, connecting to a single pole-to-pole cell in the mesosphere. The direct cells in the tropics are driven by absorption of solar radiation in the troposphere, with the resulting motions extending high into the stratosphere. The mesospheric cell is similarly generated; thus, both these cells are indirect in that sinking motions take place in the warmer regions. (See fig. 2, from

Cunnold et al., 1975). These motions are clearly the result of a driving force and convert kinetic to potential energy.

The Coriolis torque acting on these meridional motions gives rise to the mean zonal motions. Unlike the meridional motions, these mean zonal motions are in geostrophic balance; that is, the Coriolis force is balanced by the mean horizontal-pressure gradient. As such, they can be deduced from the density field. These zonal motions are not constant in time; the winds have an annual change of direction as the winter and summer poles change places. In addition, a semiannual oscillation in the zonal flow is observed, with maximum westerlies occurring just after the equinoxes and maximum easterlies occurring just after the solstices. There is also a very strong oscillation of the mean zonal wind in the lower tropical stratosphere with a somewhat irregular period that averages out to about 26 months, the so-called "quasi-biennial oscillation." In addition to these cyclic variations, there are a number of irregular short-term and year-to-year variations.

In many respects the testing of both the chemical and the transport models should proceed concurrently. In practice, tests of the models can be devised that will verify either independently. Thus, the basic photochemistry can be tested at altitudes where photochemical equilibrium exists; i.e., the transport lifetimes are short compared to the chemical lifetimes. Measurements of the altitude profile of ozone density can, for example, be used to test photochemical theories above 30 km altitude and used to test the transport models below 30 km.

Currently Available Measurements

Measurements are currently being made in the stratosphere and mesosphere by satellite, balloon, rocket, aircraft, and ground-based experiments. Here we will discuss the satellite measurements only. Current satellite experiments for long-duration observation are focused on the measurement of aerosols and gases involved in the ozone-nitrogen chemistry of the stratosphere. These experiments include the Limb Infrared Monitor of the Stratosphere (LIMS), the Stratosphere and Mesosphere Sounder (SAMS), the Solar Backscatter Ultraviolet/ Total Ozone Mapping System (SBUV/TOMS), the Stratospheric Aerosol Measurement II (SAM II), and the Stratospheric Aerosol and Gas Experiment (SAGE). The first four experiments are part of the Nimbus G spacecraft and the last is a Scout launched solo payload. In addition, the SBUV is planned for operational use by the National Oceanic and Atmospheric Administration (NOAA) on the Tiros N payload. Each of these experiments measures a specific parameter or set of gases. The parameters to be measured, the instrument/experiment approach, and the schedule are given in table I.

The Atmospheric Trace Molecules Observed by Spectroscopy (ATMOS) is planned for flight on Spacelab 1. Unlike the others, ATMOS employs a survey instrument technique capable of providing data on a wide range of molecules including the NO_x, HO_x, ClO_x, and O_3 chemistry. However, as it only obtains data at solar occultation, its spatial coverage is limited. The Cryogenic Limb-Scanning Interferometer and Radiometer (CLIR) on the other hand is a limb scanning instrument and will provide global coverage with greater density and time.

Future satellite experiments include the Halogen Occultation Experiment (HALOE), Laser Heterodyne Spectrometer (LHS), and Solar Mesosphere Explorer (SME), followed by the Upper Atmosphere Research Satellite (UARS) experiment to bring together the O_3, NO_x, ClO_x, and solar flux measurements in a simultaneous data set.

Science Requirements

At present, some models treat chemistry and transport independently, whereas others combine these effects. In general the relative emphasis for the latter models will favor one of the processes. Thus, the one-dimensional models contain full chemistry but average all transport using a one-dimensional diffusion constant, while the full global-circulation models have little or no chemistry. Thus the science requirements are varied.

To study the chemistry, we can conveniently look at the families of species. To study those species in photochemical equilibrium, more than one species in the family needs to be measured. In addition, considerably more information can be obtained if the diurnal variation of these species is measured.

Transport in the models can be verified in two ways: first, by observing the densities of conserved quantities such as CH_4, O_3, and N_2O and aerosols below 30 km or the sodium atom above 80 km, and second, by direct observation of the horizontal winds.

Table II (from Upper Atmosphere Research Satellite Program, 1978) gives a list of those species that can be used for the verification of chemistry/transport models, with the required accuracies and spatial resolutions.

Shuttle Lidar Contribution

Table III gives a list of those species that are proposed for measurement in the experiments sections. In most cases, the resolution and accuracies meet or exceed the requirements given in table II.

References

Climatic Impact Committee, Natl. Res. Council: Environmental Impact of Stratospheric Flight: Biological and Climatic Effects of Aircraft Emissions in the Stratosphere. Natl. Acad. Sci., 1975.

Crutzen, Paul J.; Isaksen, Ivar S. A.; and McAfee, John R.: The Impact of the Chlorocarbon Industry on the Ozone Layer. J. Geophys. Res., vol. 83, no. C1, pp. 345-363, Jan. 20, 1978.

Cunnold, D.; Alyea, F.; Phillips, N.; and Prinn, R.: A Three-Dimensional Dynamical-Chemical Model of Atmospheric Ozone. J. Atmos. Sci., vol. 32, no. 1, pp. 170-194, Jan. 1975.

Hudson, Robert D., ed.: Chlorofluoromethanes and the Stratosphere. NASA RP-1010, 1977.

Johnston, Harold S.; Kattenhorn, David; and Whitten, Gary: Use of Excess Carbon 14 Data to Calibrate Models of Stratospheric Ozone Depletion by Supersonic Transports. J. Geophys. Res., vol. 81, no. 3, pp. 368-380, Jan. 20, 1976.

Liu, S. C.; Cicerone, R. J.; Donahue, T. M.; and Chameides, W. L.: Sources and Sinks of Atmospheric N_2O and the Possible Ozone Reduction Due to Industrial Fixed Nitrogen Fertilizers. Tellus, vol. 29, no. 3, pp. 251-263, June 1977.

Liu, S. C.; Donahue, T. M.; Cicerone, R. J.; and Chameides, W. L.: Effect of Water Vapor on the Destruction of Ozone in the Stratosphere Perturbed by Cl_x or NO_x Pollutants. J. Geophys. Res., vol. 81, no. 18, pp. 3111-3118, June 20, 1976.

Luther, Frederick M.; and Duewer, William H.: Effect of Changes in Stratospheric Water Vapor on Ozone Reduction Estimates. J. Geophys. Res., vol. 83, no. C5, pp. 2395-2402, May 20, 1978.

Mahlman, J. D.; and Moxim, W. J.: Tracer Simulation Using a Global General Circulation Model: Results From a Midlatitude Instantaneous Source Experiment. J. Atmos. Sci., vol. 35, no. 8, pp. 1340-1374, Aug. 1978.

McElroy, Michael B.; Elkins, James W.; Wofsy, Steven C.; and Yung, Yuk Ling: Sources and Sinks for Atmospheric N_2O. Rev. Geophys. & Space Phys., vol. 14, no. 2, pp. 143-150, May 1976.

Molina, Mario J.; and Rowland, F. S.: Stratospheric Sink for Chlorofluoromethanes: Chlorine Atomc-atalysed Destruction of Ozone. Nature, vol. 249, no. 5460, pp. 810-812, June 28, 1974.

Panel on Atmospheric Chemistry, Natl. Res. Council: Halocarbons: Effect on Stratospheric Ozone. Natl. Acad. Sci., 1976.

Upper Atmosphere Research Satellite Program - Final Report of the Science Working Group. JPL Publ. 78-54, NAS7-100, July 15, 1978. (Available as NASA CR-157558.)

TABLE I.- MEASUREMENTS, APPROACH, AND SCHEDULE OF SATELLITE EXPERIMENTS

RELEVANT TO SCIENTIFIC OBJECTIVE 2

Satellite experiment	Measurements	Instrument/experiment approach	Schedule
LIMS	O_3, H_2O, NO_2, HNO_3, temperature (2 to 4 km resolution; 10 to 70 km altitude)	Limb emission radiometry (6 to 17 μm)	Nimbus G, 1978
SAMS	CO, NO, N_2O, CH_4, H_2O, temperature, wind (15 to 90 km altitude)	Limb emission pressure modulated radiometer (2 to 16 μm)	Nimbus G, 1978
SBUV/TOMS	O_3 (vertical profile greater than 30 km; 5 km resolution; total O_3 maps)	Nadir solar backscatter	Nimbus G, 1978; Tiros N, 1981
SAM II	Aerosol extinction (1 km resolution; 8 to 50 km altitude)	Limb occultation photometer (1 μm)	Nimbus G, 1978
SAGE	O_3, aerosol, NO_2 extinction (1 km resolution; 8 to 65 km altitude)	Limb occultation photometer (0.3 to 1 μm)	AEM-II, 1979
ATMOS	Survey (2 km resolution; 10 to 100 km altitude)	Limb occultation interferometer (2 to 15 μm)	Spacelab 1, 1980; Spacelab 3, 1981
CLIR	Multiple species (2 km resolution; 20 to 140 km altitude)	Limb emission spectrometer/radiometer	Space Shuttle, 1984
UARS	Chemistry; radiation; transport	Variety of instruments	Launch, 1984
HALOE	O_3, HCl, HF, NO, CH_4, H_2O, CF_2, Cl_2, pressure (2 km resolution; 10 to 70 km altitude)	Limb occultation gas filter and broad band radiometer (2 to 11 μm)	Spacelab 3, 1981; ERBSS-A, 1983
LHS	O_3, HNO_3, CF_2Cl_2, $CFCl_3$ (2 km resolution; 10 to 70 km altitude)	Limb occultation laser heterodyne radiometry (9 to 12 μm)	Space Shuttle, 1984

TABLE II.- SCIENCE REQUIREMENTS

Parameter	Altitude range, km	Δx, km	Δz, km	Accuracy, percent
O_3	10 to 60	500	1	10
	60 to 90		3	25
NO	25 to 100	500	3	10
NO_2	25 to 60	500	3	10
HNO_3	20 to 30	500	3	10
N_2O	10 to 40	500	3	20
OH	25 to 40	500	3	10
	60 to 90			25
H_2O	10 to 70	500	3	10
H_2O_2	25 to 50	500	3	10
HO_2	25 to 50	500	3	10
HCl	20 to 50	500	3	10
ClO	25 to 40	500	3	10
$ClONO_2$	20 to 30	500	3	10
CH_4	10 to 60	500	3	20
CFM's	10 to 40	500	3	20
Na	80 to 100	100	1	10
Aerosols	10 to 100	500	1	30
Wind	15 to 60	1000	3	2 m/s
	65 to 100	1000	3	10 m/s

TABLE III.- SHUTTLE LIDAR CONTRIBUTION

Parameter	Altitude range, km	Altitude resolution, km	Accuracy, percent	Lidar experiment
O_3	Stratosphere burden		8	10
	10 to 70	1	2	13
NO	45 to 55	1	20	13
	70 to 150	3	20	25
NO_2	35 to 45	1	10	13
HNO_3	10 to 20	1	10	13
N_2O	Stratosphere burden		1	10
OH	50 to 60	1	20	13
	35 to 100	3	10	21
H_2O	10 to 30	1	2	13
	10 to 40	1 to 5	10 to 20	9
H_2O_2	25 to 35	1	----------	13
HO_2	25 to 35	1	20	13
HCl	Stratosphere burden		10	10
	20 to 30	1	5	13
ClO	30 to 35		20	13
$ClONO_2$	20 to 30		----------	13
CH_4	10 to 20	1	5	13
CFM's	Stratosphere burden		1	10
	10 to 20	1	10	13
Na	80 to 100	1	10	7
Aerosol	10 to 30	1	30	6
Wind	80 to 100	1	5.5 m/s	14
	10 to 30	1	2 to 3 m/s	20

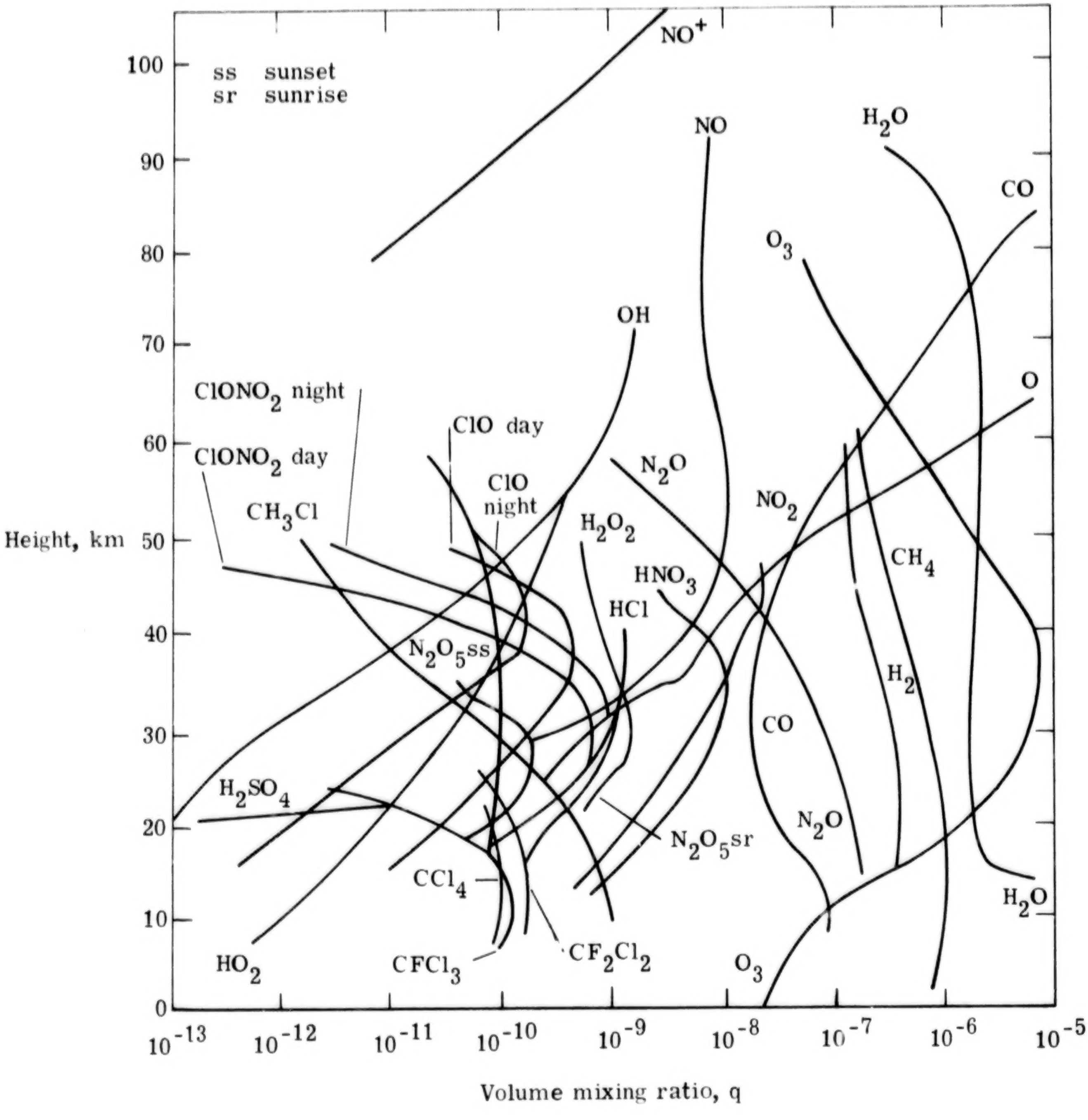

Figure 1.- Concentration profiles of minor species. (From Upper Atmosphere Research Satellite Program, 1978)

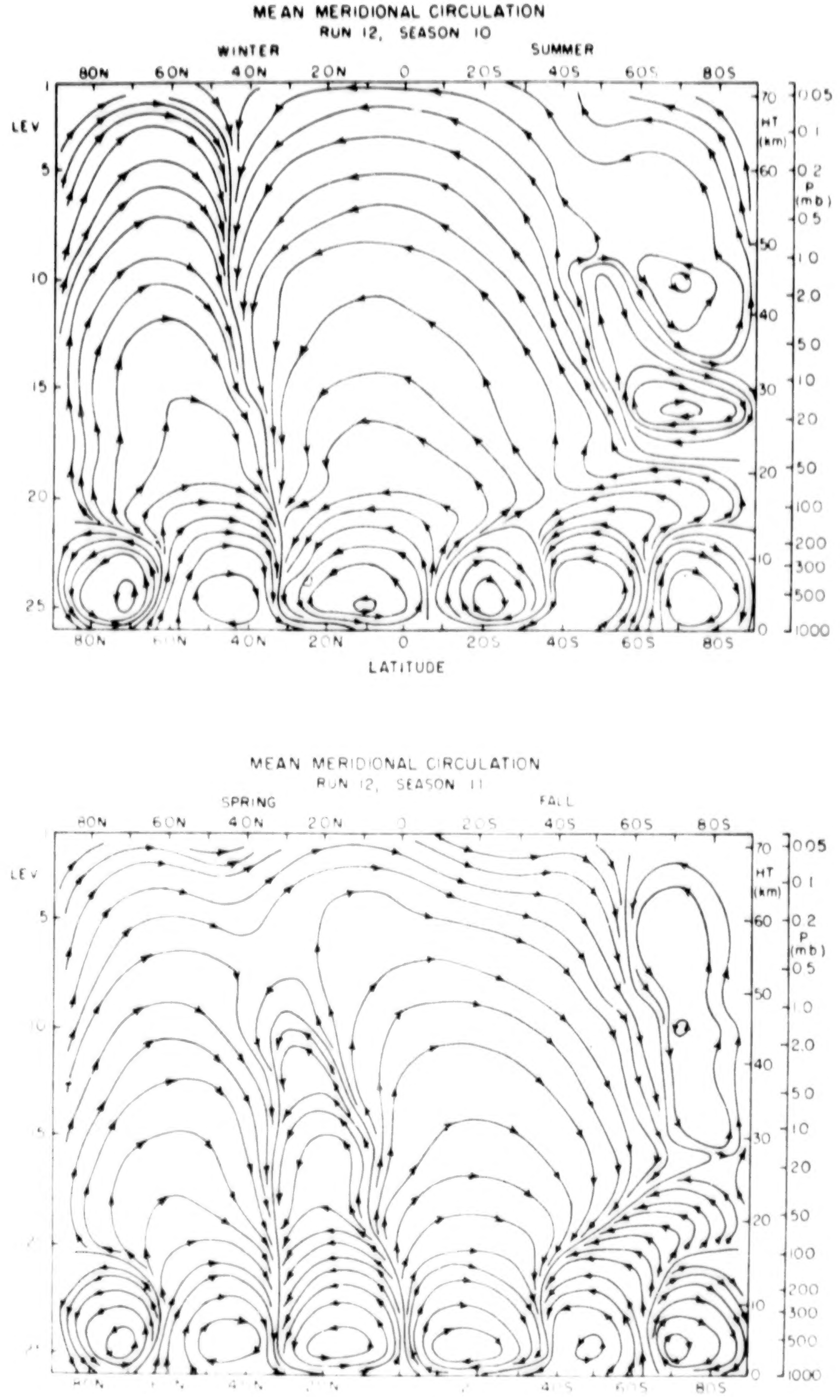

Figure 2.- Mean meridional circulation patterns for the solstices and equinox. (From Cunnold et al., 1975, courtesy American Meteorological Society)

Scientific Objective 3: Radiative Models

The purpose of scientific objective 3 is to test and improve atmospheric models of radiation, radiatively active substances, and radiative effects.

Introduction

Scientific objective 3 encompasses two major research areas. The first is that of providing input data for models which describe radiative energy exchange in the Earth's atmosphere and the effects on this exchange of altered atmospheric composition. The second is that of providing input data for studies which test the basic assumptions used to analyze data from passive remote sensors. Here again, changes in atmospheric constituents (aerosol particles or thin cirrus, for example) may affect the values of the atmospheric parameters inferred from the data.

A major reason for the current interest in radiative energy exchange is that alterations in this exchange can in turn alter the climate. Within the past few years, public concern for problems associated with climatic fluctuations has increased dramatically. The impact of climate variability has been vividly demonstrated by the effects of record cold winters on energy demands; the loss of life and property caused by record snowfalls, extreme flood events, mudflows, and landslides; and the effect on food and water supplies of droughts in England, the U.S.S.R., Africa, and the Western United States. We are also aware that man's activities, in part by altering atmospheric composition and surface albedo, have already affected local and regional climates and may affect the global climate as well.

A growing concensus and sense of urgency concerning the Nation's needs for understanding and anticipating climatic changes has led to the development of A United States Climate Program Plan (1977) by the Interdepartmental Committee for the Atmospheric Sciences, which calls for the development and coordination of needed climate research and services by the Federal Government. In response to this call, the NASA Goddard Space Flight Center developed a Proposed NASA Contribution to the Climate Program in 1977, which shows how our practical understanding of the behavior of the climate system could be advanced by concerted use of space-based global observations and by application of NASA's data management, analysis, and coordination capabilities. Shuttle lidar could play an important role in this process by providing unique data on atmospheric constituents and surface properties that affect the radiation budget, while coordinated measurements could document the radiative quantities per se. (See examples in the section "Earth Radiation Budget Studies.")

In parallel with the current interest in radiative effects on climate, there is an ongoing interest in the effects of minor atmospheric constituents on passive remote sensors. This interest derives from the major and growing role that these passive sensors play in a variety of applications. For example, data from passive, nadir-viewing temperature sounders are routinely used in operational weather forecasts, and the impact of these data is expected to increase as more and better sounders are flown. (See scientific objective 4.) Also, current and future limb-emission radiometers are expected to provide data on minor constituents (e.g., O_3, H_2O, NO_x, and CFM's) that are vital to our understanding of the ozone depletion threat and other fundamental problems. (See scientific objective 2.) The outputs of both these types of radiometers can be affected by emissions from aerosol and cloud particles within the field of view. These effects, if significant, must be properly accounted for in reducing the radiometric data. However, this has been very difficult in the past because of the highly variable nature of aerosol and cloud particles, and the attendant difficulty in determining the presence, height, and effects of particles in specific data sets. Here again, data from a Shuttle borne or free-flying lidar, obtained with simultaneous data from the passive sensors, could provide unique advances in resolving some of these important questions. (See section entitled "Effects on Passive Sensors.")

Table I summarizes the measurements needed to provide significant advances in verifying radiative models for both the climatic and remote-sensing applications. The table lists the required accuracies and resolutions and relates these needs to specific lidar experiments and correlative sensor types. One parameter in table I that requires special mention is $\sigma_v(\lambda)$. This parameter is used to identify the collective effects of aerosol or cloud particles on the transfer of solar and terrestrial radiation as required in a particular study. Thus, $\sigma_v(\lambda)$ could represent the spatial distribution of extinction or absorption cross section as a function of wavelength λ, or the scattering cross section as a function of scattering angle (i.e., the phase function), or a combination of these. (None of these cross sections is measured directly by lidar, but with careful use of conversion factors, lidar can often provide the best remotely sensed data available; we will return to this point below.) To characterize the radiation field sufficiently, the models also require information on gaseous constituents for the same location as the aerosol and cloud data. These important gases are also listed in table I. In each case, accuracies and vertical resolutions are varied with altitude in a manner that reflects the importance of the contribution of each constituent to variations in the total radiation field. Temperature profiles are also required, both as inputs to infrared radiative calculations and to verify the heating profiles that the calculations yield. It does not appear necessary to specify profiles of CO_2 directly since temperature data and the common assumption that the CO_2 mixing ratio is constant above the boundary layer can be used to calculate a sufficiently accurate CO_2 concentration profile.

The final entries in table I reflect the need of radiative climate models for data on the albedo of the Earth's surface or the albedo of the Earth's atmosphere underlying a height of interest. Proper treatment of information on clouds, such as the fractional cloud cover, cloud heights, and the presence of thin cirrus layers, is also very important in both the radiative climate models and the analysis of passive sounding data.

With reference to the parameter $\sigma_v(\lambda)$, it was mentioned above that lidar does not directly measure the particulate extinction, absorption, and angular scattering coefficients required by the radiative models. While this is strictly true, it is also true that occasional, carefully designed correlative studies using in situ or passive remote sensors in conjunction with ground-, air-, or space-based lidar can yield reliable factors for converting lidar-measured backscattering to certain of the desired quantities. This procedure has already been used with good success in the case of the stratospheric aerosol (e.g., Northam et al., 1974; Russell et al., 1976). These correlative studies yield optical models on which the conversion factors are based. For a given subsequent lidar observation, the optical model is never certain, but it can often be sufficiently bounded (by using multiwavelength lidar data, expected variabilities from intermittent correlative measurements, information on the source, height, and temperature of observed particles, etc.) so that conversion uncertainties are understood and are minimized. When such carefully bounded conversion factors are combined with the unique spatial resolution and high sensitivity of lidar, the resulting description of particulate radiative parameters is usually more accurate than can be obtained by any other downward-looking remote-sensing technique (as must be used for global coverage of the troposphere). This is especially so because aerosol and cloud concentrations can be highly variable in space and time and are often confined to narrow layers. Thus in many cases, lidar-derived particulate radiative parameters do not need to be highly accurate to represent a significant and useful improvement over what is otherwise available. Examples of such cases include tenuous (often subvisible) cirrus clouds and Saharan, Mongolian, or urban haze layers.

In the following sections, we present more specific examples of important studies in which a Shuttle borne lidar could provide important data not attainable by other means.

Earth Radiation Budget Studies

Because of the widespread concern regarding possible climate change, many investigators (e.g., Charlson and Pilat, 1969; Atwater, 1970; Ensor et al., 1971; Rasool and Schneider, 1971; Mitchell, 1971; Barrett, 1971; Neumann and Cohen, 1972; Yamamoto and Tanaka, 1972; Braslau and Dave, 1973a and 1973b; Chýlek and Coakley, 1974; Shettle and Green, 1974; Harshvardhan and Cess, 1976; Coakley and Grams, 1976; Luther, 1976; Pollack, et al., 1976; Fiocco et al., 1976 and 1977) have developed models to assess the possibilities quantitatively. These models describe the radiative energy exchange in the Earth atmosphere system and what might be the effects on this exchange of changing aerosol, cloud, and trace-gas amounts, as well as changing surface albedos.

The well-documented effects of the injection of volcanic dust into the Earth's stratosphere by the Mt. Agung eruption of 1963 (see scientific objective 1) can be used to test a number of the climate theories. Following the eruption, anomalous increases in the stratospheric temperature were attributed to the presence of volcanic dust (e.g., Newell, 1971). One figure from Newell's paper is reproduced here as figure 1. It shows the difference in stratospheric temperature between January 1963 and January 1964 as a function of geographical location at an altitude of about 19 km. A large temperature increase is evident in the latitude strip between 0° and $20^{\circ}S$, with maximums around central Africa and New Guinea and over South America. Mugnai, et al. (1978) calculated stratospheric heating rates induced by aerosol particles at the 19 km level using data on the mean winter-time values of the planetary albedo as a function of latitude and longitude obtained from satellite observations (Vonder Haar and Ellis, 1974), the concentration and composition of aerosol particles at the 19 km level predicted by a two-dimensional model of global-scale dispersion of the volcanic debris (Cadle et al., 1976), and data on temperature and concentration profiles for O_3, CO_2, and H_2O from the U.S. Standard Atmosphere Supplements, 1966. The results are shown in figure 2. A very high degree of correlation between the temperature differences in figure 1 and the heating rates in figure 2 is evident. Maximum heating rates of about 0.4 K per day are associated with temperature differences of about 8 K, thereby suggesting radiative relaxation time constants on the order of 20 days at the 19 km level.

In another test of the climatic perturbation of the Mt. Agung volcano, Hansen et al. (1978) computed the vertical temperature profile at low latitudes using a one-dimensional radiative-convective model. Their results, computed as a function of time before and after the eruption, also show good agreement with observations. Results for the stratosphere and the troposphere are shown in figures 3 and 4, respectively.

Although these models have provided many valuable new insights, a persistent lack of suitable global input data and of model verification has prevented predictions of future radiative-climatic conditions. In part because of this situation, a major parallel effort has been mounted to monitor the radiation budget directly on a global scale. Satellite-borne radiometers, such as the Earth Radiation Budget (ERB) sensors on Nimbus 6 and Nimbus 7, provide a powerful means of doing this. More complete data will be provided in the future by the multisatellite Earth Radiation Budget Satellite System (ERBSS). (See, e.g., Woerner and Cooper, 1977; Woerner, 1978.) Whereas the data from these sensors will by themselves be very instructive, they will be most beneficial when used with the radiation models mentioned above, and with simultaneous data on the radiatively important atmospheric constituents and surface properties. Coordinated studies of this sort can provide well-constrained checks of the mutual consistency of atmospheric constituent measurements, radiative calculations, and measured radiative effects. It is in this way that the most rapid progress will be made toward a reliable capability to predict future changes in Earth radiation balance and climate resulting from natural and manmade factors. For example, much could be learned from measuring and modeling the change in the Earth atmosphere albedo along a track passing from the South Atlantic, through the region of the Atlantic Saharan dust layer (see scientific objective 1), and into the North Atlantic, with the model constrained by simultaneously measured input data on the aerosol heights and densities and the surface reflectivity.

An attractive means of obtaining these coordinated data sets is by flying, along with ERB sensors, other sensors that measure the important atmospheric constituents and surface properties in the same region as viewed by the ERB sensors, and at the same time. Unfortunately, passive nadir-viewing sensors cannot provide aerosol and gas data with the required vertical resolution and accuracy, nor can they unambiguously separate surface from atmospheric effects; moreover, passive limb-scanning sensors are largely limited to the stratosphere and above, and cannot view the ERB sensed area simultaneously with ERB. These shortcomings are critical since the bulk of many radiatively important constituents (e.g., aerosols, tenuous clouds, and water vapor) is usually confined to thin layers in the troposphere, and rapid changes in these constituents often provide the most instructive and least ambiguous tests of radiative models (e.g., Russell et al., 1979).

The lidar data could include aerosol and cloud particle backscattering coefficients and H_2O, O_3, and other gas concentrations, all with a vertical resolution equal to or better than that specified in table I. Also, total gas density profiles, or temperature profiles (using a more advanced lidar), could be measured and used to specify the CO_2 vertical profile. Surface reflectivity could be simultaneously monitored, and this, coupled with suitable models and "ground-truth" measurements, could provide a useful input on surface albedo to the radiative calculations.

Another lidar-measured parameter of value to the radiative calculations is the top height of opaque clouds within the ERB FOV. As noted in table I, variations in the height by as little as 0.1 km can be important in determining radiative fields and equilibrium temperatures; this is an accuracy that cannot be provided by passive sensors but can be achieved by lidar.

The unique ability of lidar to detect subvisible cirrus clouds is also worthy of mention. Previous ground-based and airborne lidar studies have detected tenuous cirrus clouds with water (ice) contents that were at least two orders of magnitude less than those associated with visible cirrus layers. Repeated lidar measurements in many latitudes have suggested that these subvisible cirrus layers are quite prevalent, but the lidar measurements to date have been too sporadic to provide a useful global or regional census. Also, these tenuous cirrus layers cannot be globally monitored by satellite multispectral radiometers since they are difficult to resolve unambiguously against complex backgrounds and are not discernible in the visible spectral ranges. Such tenuous clouds could produce measurable effects in certain ERB channels and, if widespread and persistent, could significantly perturb the global radiation budget. Only a space-borne lidar, co-aligned with an ERB sensor, could determine whether subvisible cirrus clouds were present in the ERB FOV during times of measured albedo changes. Such a space-borne lidar could also provide the first global census of the occurrence, height, density, and thickness of these tenuous clouds.

Effects on Passive Sensors

Both visible and subvisible clouds can influence the retrieval of temperature profiles from nadir-viewing multispectral infrared radiance measurements (e.g., Smith et al., 1972; Chahine, 1974). Procedures for adjusting for the influence of visible clouds have been developed, but they require an appropriately scaled specification of the height and amount of the clouds. Uncertainties in passively inferred cloud heights can thus introduce error into these procedures. Simulations by Halem and Chow (1976) indicate that the profile errors become significant for errors in the heights of high clouds with coverage of more than 50 percent. Although these simulations cannot be considered definitive because of persistent uncertainties in their treatment of cloud radiative properties, they nonetheless point to the need for improved cloud measurements, both as a check on the simulations and as an aid in developing improved analysis methods. A Shuttle borne lidar, co-aligned with a temperature-sounding radiometer so that the fields of view of the radiometer and lidar are coincident, could provide the height information on visible clouds for this purpose, as well as height, thickness, and density information on subvisible clouds; these latter clouds are not accounted for in current data-reduction schemes (as their presence is not detectable), but their emissivities may make them significant contributors to the measured radiances and hence a significant source of error.

Dave (1978) has reported the results of an investigation aimed at estimating the effect of stratospheric and tropospheric particulate pollutants on total ozone measurements obtained from the Backscatter Ultraviolet (BUV) spectrometer aboard the Nimbus 4 satellite. His study showed that the total ozone in an atmospheric column could be in error by about ±2 percent due to particulate contamination encountered in the terrestrial atmosphere under average conditions and that the error could be expected to rise to about ±8 percent under strong particulate contamination conditions. A Shuttle borne lidar, co-aligned with a BUV instrument, could be used to test these predictions by obtaining simultaneous data on the vertical distribution of aerosol particles and ozone.

A variety of other experiments could also be performed to test other possible effects of aerosol particles on the passive sensors used to infer concentrations of various molecular constituents. Limb-scanning radiometers that infer stratospheric and mesospheric constituent profiles from measured infrared emissions can also be influenced by subvisible aerosol layers. For example, the Limb Radiance Inversion Radiometer (LRIR) on Nimbus 6 and the Limb Infrared Monitor of the Stratosphere (LIMS) on Nimbus 7 both determine ozone profiles by observing the infrared radiation emitted in the spectral interval from about 9 to 10 μm. Although the composition of the stratospheric aerosol layer is still quite uncertain, a number of investigators (e.g., Rosen, 1971; Toon and Pollack, 1973; Russell et al., 1976) have suggested that the stratospheric particles are a 75 percent by weight mixture of sulfuric acid in water. Figure 5 (from Mugnai et al., 1978) shows absorption cross sections for the 75-percent sulfuric-acid mixture that may be large enough to affect the 9 to 10 μm radiation detected by the limb-scanning radiometers for strong aerosol loading in the stratosphere - such as after the Mt. Agung and Fuego volcanic eruptions. Future detailed studies of this problem, and other similar problems involving the effects of infrared aerosol absorption or emission on concentrations of minor species detected by satellite sensors, may suggest additional Shuttle borne lidar experiments for testing and improving our techniques for obtaining data on atmospheric constituents.

References

Atwater, Marshall A.: Planetary Albedo Changes Due to Aerosols. Science, vol. 170, no. 3953, pp. 64-66, Oct. 2, 1970.

Barrett, Earl W.: Depletion of Short-Wave Irradiance at the Ground by Particles Suspended in the Atmosphere. Sol. Energy, vol. 13, no. 3, pp. 323-337, Nov. 1971.

Braslau, Norman; and Dave, J. V.: Effect of Aerosols on the Transfer of Solar Energy Through Realistic Model Atmospheres. Part I: Non-Absorbing Aerosols. J. Appl. Meteorol., vol. 12, no. 4, pp. 601-615, June 1973a.

Braslau, Norman; and Dave, J. V.: Effect of Aerosols on the Transfer of Solar Energy Through Realistic Model Atmospheres. Part II: Partly-Absorbing Aerosols. J. Appl. Meteorol., vol. 12, no. 4, pp. 616-619, June 1973b.

Cadle, R. D.; Kiang, C. S.; and Louis, J.-F.: The Global Scale Dispersion of the Eruption Clouds From Major Volcanic Eruptions. J. Geophys. Res., vol. 81, no. 18, pp. 3125-3132, June 20, 1976.

Chahine, Moustafa T.: Remote Sounding of Cloudy Atmospheres. I. The Single Cloud Layer. J. Atmos. Sci., vol. 31, no. 1, pp. 233-243, Jan. 1974.

Charlson, R. J.; and Pilat, M. J.: Climate: The Influence of Aerosols. J. Appl. Meteorol., vol. 8, no. 6, pp. 1001-1002, Dec. 1969.

Chýlek, Petr; and Coakley, James A., Jr.: Aerosols and Climate. Science, vol. 183, no. 4120, pp. 75-77, Jan. 11, 1974.

Coakley, J. A., Jr.; and Grams, G. W.: Relative Influence of Visible and Infrared Optical Properties of a Stratospheric Aerosol Layer on the Global Climate. J. Appl. Meteorol., vol. 15, no. 7, pp. 679-691, July 1976.

Dave, J. V.: Effect of Aerosols on the Estimation of Total Ozone in an Atmospheric Column From the Measurements of Its Ultraviolet Radiance. J. Atmos. Sci., vol. 35, no. 5, pp. 899-911, May 1978.

Ensor, David S.; Porch, William M.; Pilat, Michael J.; and Charlson, Robert J.: Influence of the Atmospheric Aerosol on Albedo. J. App. Meteorol., vol. 10, no. 6, pp. 1303-1306, Dec. 1971.

Fiocco, G.; Grams, G.; and Mugnai, A.: Energy Exchange and Equilibrium Temperature of Aerosols in the Earth's Atmosphere. Radiation in the Atmosphere, H.-J. Bolle, ed., Science Press, Princeton, pp. 74-78, c.1977.

Fiocco, Giorgio; Grams, Gerald; and Mugnai, Alberto: Energy Exchange and Temperature of Aerosols in the Earth's Atmosphere (0-60 km). J. Atmos. Sci., vol. 33, no. 12, pp. 2415-2424, Dec. 1976.

Halem, Milton; and Chow, Ming-Dah: Sounder Design Considerations in the Selection of Temperature Sensing Channels. J. Appl. Meteorol., vol. 15, no. 4, pp. 394-401, Apr. 1976.

Hansen, James E.; Wang, Wei-Chyung; and Lacis, Andrew A.: Mount Agung Eruption Provides Test of a Global Climatic Perturbation. Science, vol. 199, no. 4333, pp. 1065-1068, Mar. 10, 1978.

Harshvardhan; and Cess, R. D.: Stratospheric Aerosols: Effect Upon Atmospheric Temperature and Global Climate. Tellus, vol. 28, no. 1, pp. 1-10, 1976.

Luther, Frederick M.: Relative Influence of Stratospheric Aerosols on Solar and Longwave Radiative Fluxes for a Tropical Atmosphere. J. Appl. Meteorol., vol. 15, no. 9, pp. 951-955, Sept. 1976.

Mitchell, J. Murray, Jr.: The Effect of Atmospheric Aerosols on Climate With Special Reference to Temperature Near the Earth's Surface. J. Appl. Meteorol., vol. 10, no. 4, pp. 703-714, Aug. 1971.

Mugnai, A.; Fiocco, G.; and Grams, G.: Effects of Aerosol Optical Properties and Size Distributions on Heating Rates Induced by Stratospheric Aerosols. Q. J. R. Meteorol. Soc., vol. 104, no. 441, pp. 783-796, July 1978.

Neumann, Jehuda; and Cohen, Ariel: Climatic Effects of Aerosol Layers in Relation to Solar Radiation. J. Appl. Meteorol., vol. 11, no. 4, pp. 651-657, June 1972.

Newell, Reginald E.: The Global Circulation of Atmospheric Pollutants. Sci. American, vol. 224, no. 1, pp. 32-42, Jan. 1971.

Northam, G. Burton; Rosen, James M.; Melfi, S. Harvey; Pepin, T. J.; McCormick, M. P.; Hofmann, D. J.; and Fuller, William H., Jr.: Dustsonde and Lidar Measurements of Stratospheric Aerosols: A Comparison. Appl. Opt., vol. 13, no. 10, pp. 2416-2421, Oct. 1974.

Pollack, James B.; Toon, Owen B.; Summers, Audrey; Van Camp, Warren; and Baldwin, Betty: Estimates of the Climatic Impact of Aerosols Produced by Space Shuttles, SST's, and Other High Flying Aircraft. J. Appl. Meteorol., vol. 15, no. 3, pp. 247-258, Mar. 1976.

Rasool, S. I.; and Schneider, S. H.: Atmospheric Carbon Dioxide and Aerosols: Effects of Large Increases on Global Climate. Science, vol. 173, no. 3992, pp. 138-141, July 9, 1971.

Rosen, James M.: The Boiling Point of Stratospheric Aerosols. J. Appl. Meteorol., vol. 10, no. 5, pp. 1044-1046, Oct. 1971.

Russell, P. B.; Livingston, J. M.; and Uthe, E. E.: Aerosol-Induced Albedo Change: Measurement and Modeling of an Incident. J. Atmos. Sci., vol. 36, no. 8, Aug. 1979.

Russell, P. B.; Viezee, W.; Hake, R. D., Jr.; and Collis, R. T. H.: Lidar Observations of the Stratospheric Aerosol: California, October 1972 to March 1974. Q. J. R. Meteorol. Soc., vol. 102, no. 433, pp. 675-695, July 1976.

Shettle, E. P.; and Green, A. E. S.: Multiple Scattering Calculation of the Middle Ultraviolet Reaching the Ground. Appl. Opt., vol. 13, no. 7, pp. 1567-1581, July 1974.

Smith, W. L.; Woolf, H. M.; and Fleming, H. E.: Retrieval of Atmospheric Temperature Profiles From Satellite Measurements for Dynamical Forecasting. J. Appl. Meteorol., vol. 11, no. 1, pp. 113-122, Feb. 1972.

Toon, Owen B.; and Pollack, James B.: Physical Properties of the Stratospheric Aerosols. J. Geophys. Res., vol. 78, no. 30, pp. 7051-7056, Oct. 20, 1973.

A United States Climate Program Plan. ICAS 20b-FY1977, Off. Sci. Technol. Policy, July 1977. (Available from NTIS as PB-295 946.)

Vonder Haar, Thomas H.; and Ellis, James S.: Atlas of Radiation Budget Measurements From Satellites (1962-1970). NASA Grant NGR-06-002-102, Colorado State Univ., [1974]. (Available as NASA CR-142676.)

Woerner, C. V.: The Earth Radiation Budget Satellite System - An Overview. Proceedings of the Third National Conference on Aerospace Meteorology, American Meteorol. Soc., pp. 345-348, June 28-30, 1978.

Woerner, Charles V.; and Cooper, John E.: Earth Radiation Budget Satellite System Studies. NASA TM X-72776, 1977.

Yamamoto, Giichi; and Tanaka, Masayuki: Increase of Global Albedo Due to Air Pollution. J. Atmos. Sci., vol. 29, no. 8, pp. 1405-1412, Nov. 1972.

TABLE I.- SUMMARY OF MEASUREMENTS TO VERIFY RADIATIVE MODELS

Parameter	Height range, km	Δx, km	Δz, km	Remarks	Correlative sensors	Lidar experiment
$\sigma_v(\lambda)$[a]	0 to tropopause	100	0.5 to 1	10 percent to factor 3; haze, clouds, dust layers, thin cirrus	ERB sensor[c]; temperature and H_2O sounders[d]	1, 2, 3
	Tropopause to 100	200	2 to 4	10 percent to factor 5; stratospheric aerosols, mesospheric aerosols, noctilucent clouds	ERB sensor[c]; temperature and H_2O sounders[d]	4, 6, 24
H_2O	0 to tropopause	500	2	20 percent	ERB sensor[c]; temperature and H_2O sounders[d]	9, 10, 18
	Tropopause to 30	500	3	50 percent to factor 2		
O_3	0 to tropopause	500	3	20 percent (5 percent of total O_3)	ERB sensor[c]; BUV sensor[d]	10, 18
	Tropopause to 50	500	3	10 percent		10, 12
CO_2	------------------	----	--------	10 percent below 50 km; can be obtained from T(z)	ERB sensor[c]; temperature and H_2O sounders[d]	
CO_2 mixing ratios	70 to 100	1000	5	20 percent needed for input on radiative transfer for non-noctilucent conditions		13
Minor species (e.g., CFM's)	0 to tropopause	500	2	20 percent		10, 18
	Tropopause to 50	500	3	20 percent		
Temperature	0 to tropopause	500	2	1 K		17
	Tropopause to 30	500	3	2 K		17
	30 to 100	1000	3	5 K		17
Albedo	Surface	500	--------	0.01	ERB sensor	2
Cloud-top heights	0 to tropopause	[b]500	0.1		ERB sensor[c]; cloud-height radiometer	1

[a] Particulate scattering and extinction cross sections, as function of wavelength (or angle for scattering).

[b] Averaged quantity.

[c] For Earth Radiation Budget studies.

[d] For effects on passive sensors.

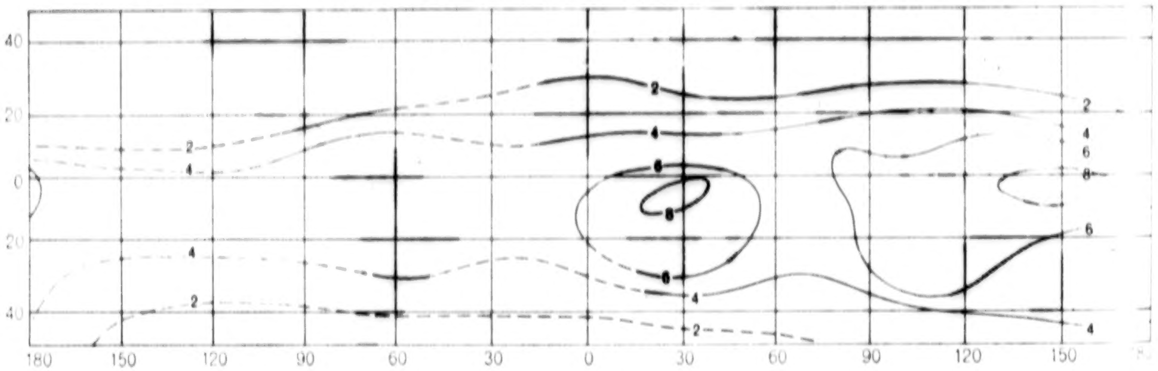

HEATING EFFECT after Mount Agung is mapped. The isotherms give the increase in mean temperature at about 19 kilometers, in degrees Celsias, from January before the eruption to one year later (Broken lines indicate uncertainty due to scarcity of observations.

Figure 1.- Increase in temperature at 19 km altitude from January 1963 to January 1964. (From Newell, 1971: The Global Circulation of Atmospheric Pollutants. Copyright © 1970 by Scientific American, Inc. All rights reserved)

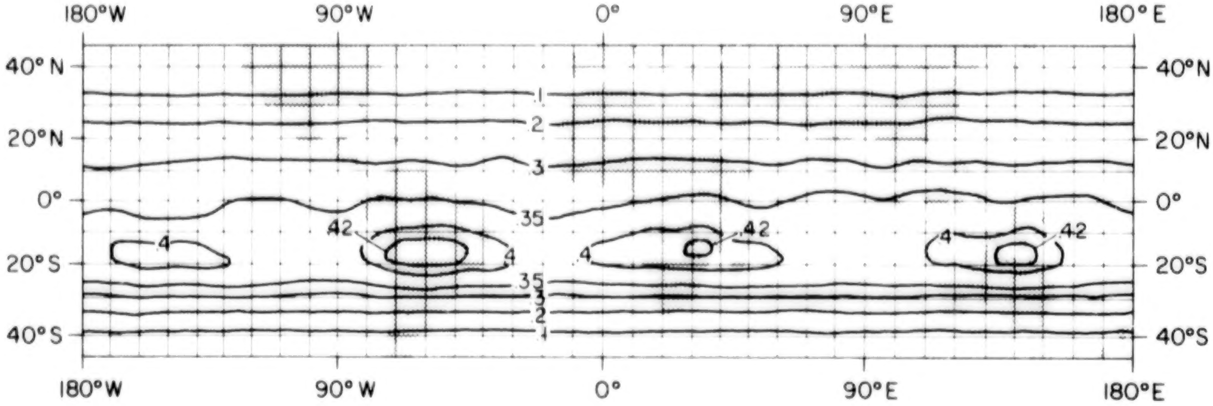

Figure 2.- Daily average heating rates (in K per day) at 19 km altitude for fine ash and impure sulfuric acid droplets 300 days following Mt. Agung eruption. (From Fiocco et al., 1977)

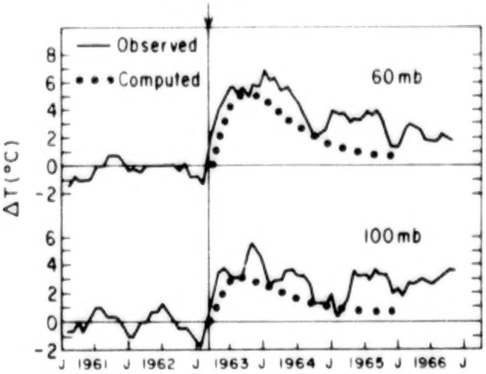

Figure 3.- Comparison between stratospheric temperatures before and after eruption of Mt. Agung as observed over Australia and as computed using a radiative-convective climate model. (From Hansen et al., 1978)

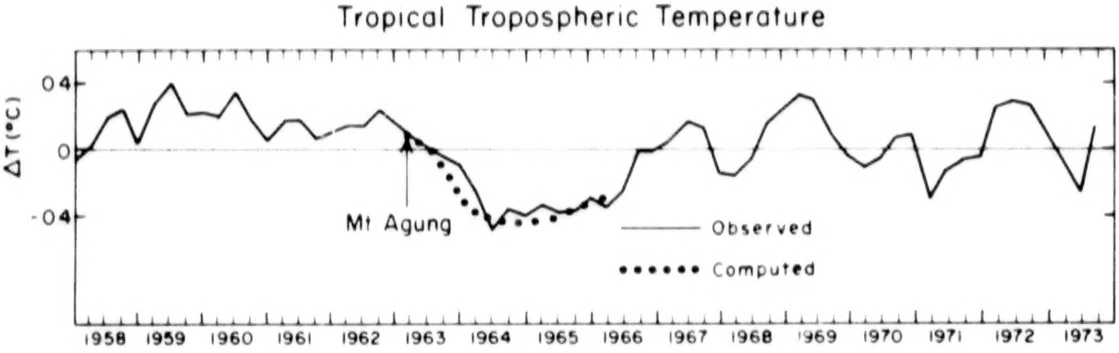

Figure 4.- Comparison between tropospheric temperatures before and after eruption of Mt. Agung as observed between 30°N and 30°S and as computed using a radiative-convective model. (From Hansen et al., 1978)

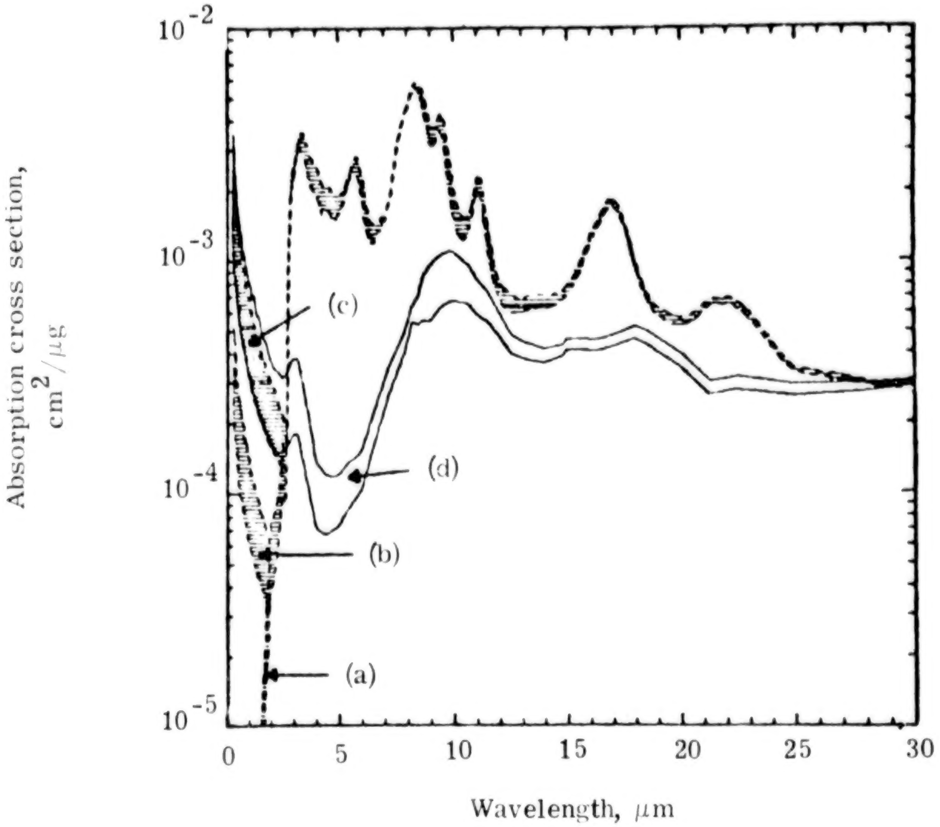

Figure 5.- Spectral variation of aerosol absorption cross section per unit mass for three models of a 75 percent by weight mixture of sulfuric acid and water (labeled (a), (b), and (c)) and for a volcanic ash model (labeled (d)). Each set of curves represents upper and lower bounds on cross sections for all particle radii between 0.01 and 1 μm. (From Mugnai et al., 1978, courtesy Royal Meteorological Society)

Scientific Objective 4: Meteorological Data

The purpose of scientific objective 4 is to augment the meteorological data base.

Introduction

Although it is often thought that modern society is becoming less vulnerable to the weather, in many respects the reverse is true. For example, weather is still the dominant factor in determining annual changes in global and regional food production, a fact made more important by recent declines in grain reserves. (These reserves now barely cover annual variations in production caused by weather.) In addition, many economies (including our own) are becoming increasingly dependent on international transport of products and resources; furthermore, an increasing portion of oil and other resources is being derived from off-shore operations. As a result, changes in weather and sea state have become more important in determining the performance of related sectors of the economy. These are but three examples of the many aspects of modern societies and economies that are sensitive to the weather. Another contributing factor is the growing scale of man's activities, which have reached the point of inadvertently affecting the weather. All of these trends have increased the importance of accurate weather measurements and predictions, not only in major population centers but also in more remote areas such as ocean shipping lanes and major agricultural regions (Committee on Atmospheric Sci., Natl. Res. Council, 1977).

In recent decades the advent of weather radar, weather satellites, and increasingly powerful computers has led to tremendous advances in our ability to monitor weather and to understand it. However, the relatively modest accompanying gains in forecasting skill (Phillips, 1976; Halem, 1976; Tracton and McPherson, 1977; Baer and Boudra, 1977) point to the fact that much room for improvement remains. For example, improved warnings of severe storms and increased skill in predicting weather statistics in specific growing regions and seasons could yield benefits measured in the hundreds of millions of dollars (e.g., Committee on Atmospheric Sci., Natl. Res. Council, 1977).

Improvements in the observational data base, along with improvements in numerical prediction models and computers, are thought to hold the key to improved skill in weather prediction. Careful consideration of these factors has been made, and several studies have specified resolutions and accuracies for various observations that are considered necessary for fundamental improvements in forecast accuracy (e.g., The Physical Basis of Climate and Climate Modelling in 1974, U.S. Committee for Global Atmospheric Res. Program in 1978, and Proposed NASA Contribution to the Climate Program in 1977).* These requirements are summarized in table I. The parameters in the body of the table describe the needs for global or hemispheric numerical weather prediction models. As noted above, current global prediction models have not benefitted significantly from the uses made of satellite weather data, particularly remotely sensed temperature soundings. This is partly due to the skillful use of all the older types of weather data, including land, ship, and aircraft reports. The current Northern Hemisphere satellite sounding data set adds only small nuances to the conventional data set. Although the satellite data can have a large impact on individual situations, current global prediction models are usually insensitive to the small nuances in initial state that the satellites provide (Phillips, 1976; Tracton and McPherson, 1977). Also, intercomparison of models shows that differences in the analyses and forecasts of different models can be far greater than the differences produced by satellite data. Hence, model errors can still dominate, and this prevents a general demonstration of a positive impact of satellite data on global-scale or hemispheric-scale numerical prediction.

---

*These documents are not formally published and are therefore not in the reference list.

Partially as a result of this situation, fine-mesh prediction models are now being developed to give improved short-range (1 to 2 days) predictions, particularly of weather phenomena of interest to the public - namely winds, rain, thunderstorms, snow, etc. (e.g., Shuman, 1978). Figure 1 shows the horizontal area and grid spacing for several types of fine-mesh models in comparison to the hemispheric model of the U.S. National Meteorological Center (NMC). The fine-mesh models require initial data with finer spatial and temporal resolution than do the global models, and perhaps with better accuracy. (See the footnote in table I for details). Also, the fine-mesh models are sensitive to factors not important for the large-scale circulation. These include moisture, latent heat release, radiation effects of clouds, and vertical wind components. Current satellite observing systems cannot measure all of these quantities to the required accuracies and resolutions. However, improved satellite instruments, including lidar, have the potential to make the required measurements, so that satellite data will become increasingly more important to numerical weather prediction as time goes on.

Specific Problems

The following sections discuss the basis for the specific requirements in table I and the ability of lidar and other sensors to satisfy them. The section "Summary of Needs and Expected Capabilities" summarizes the requirements and their relation to the expected performance of various lidar measurements. (See also appendix A.)

Temperature.- The development of satellite temperature sounders and their application in understanding and forecasting weather have been and continue to be a major thrust of the NASA meteorology program. The emphasis on the development of current sounders such as the Vertical Temperature Profile Radiometer (VTPR), the High Resolution Infra-Red Sounder (HIRS), and the Scanning Microwave Sounder (SCAMS) provides ample evidence of this thrust. In the mid- and high-latitude section of table I, temperatures are listed first (before winds) because in these latitudes it has been common practice to derive winds from temperatures using balance relationships. (Note, however, the discussion in the "Winds" section.)

General circulation models have now developed to the point where data at as many as seven independent tropospheric levels are required, whereas even the most advanced passive sounder currently under study is expected to provide no more than four independent levels. In addition, evaluation studies of sounding accuracy by both the National Meteorological Center and the Goddard Institute for Space Studies show that current passive sounding techniques can provide an accuracy of only about 1.5 to 3.5 K, depending upon level. Figure 2 shows an example of the result of this type of evaluation study. In the Northern Hemisphere this accuracy is not sufficient to produce more than small improvements in the forecast accuracy achieved on the basis of surface, radiosonde, and aircraft measurements alone.

Hence, the requirements for temperature profiles specified in table I markedly exceed the present capabilities of passive temperature sounders. Table I thus clearly establishes a need for sounders with greatly improved accuracy relative to current capabilities (1 K vs. 1.5 to 3.5 K). With regard to accuracy, it should also be noted that thin clouds and aerosol layers can introduce substantial errors into passive temperature soundings. However, the extent of these errors and the best methods to correct them have not been satisfactorily established because of (1) the approximate theoretical treatment of cloud and aerosol layers and (2) the current difficulty in documenting thin cloud and aerosol layer height, density, or even occurrence within the passive profiler field of view. Differences of 3 to 4 K and larger between satellite and radiosonde temperature profiles have been observed near the antarctic tropopause (Asgeirsson and Stanford, 1977); it is possible that subvisible cirrus clouds are responsible for these differences, but without further data this is only speculation.

Lidar measurements from space could be used to improve temperature soundings in two ways. In the near future, they could be used to document cloud and aerosol layer heights and densities within the FOV of co-aligned passive profilers. The resulting data set could clarify the effects of particulate layers as a function of location and season and lead to improved analysis methods or instrumentation, which would improve the accuracy of the data product produced by passive sounders. Also, for thick clouds, combining an infrared window measurement with a lidar height measurement could yield the temperature at a well-defined height. With further development it appears that lidar differential absorption or Doppler measurements could provide direct measurements of the complete temperature profile with extremely high vertical resolution. In addition, the use of the lidar technique will allow the temperature of specified layers to be measured in a direct manner, rather than requiring the use of inversion techniques as must currently be done in order to use the data from passive profilers. Finally, mathematical analysis indicates that a lidar temperature profile experiment could meet the 1 K temperature accuracy requirement while simultaneously meeting the vertical resolution requirement of 2 km.

Winds.- In the tropics, horizontal wind is considered the most important observational variable because the synoptic-scale temperature and pressure gradients are weak; hence, the wind is only weakly coupled to the mass field and may not be satisfactorily derived from other parameters. Moreover, in extratropical regions, even though geostrophic wind can be derived from other parameters, nongeostrophic wind components near the tropopause and in the lower levels are important for the diagnosis and prediction of weather development, and these cannot be derived from the temperature field alone. Thus there is a need for horizontal wind measurements at all latitudes, but the need is greatest in the tropics. There is also a need for vertical-wind measurements and their associated regions of convergence, divergence, and instability. These needs are summarized in table I.

Wind information is currently derived from radiosondes launched once every 12 hours from points about 350 km apart in developed countries, with much larger gaps over the oceans. Cloud motions derived from satellite photographs are another source of wind data, but this method, though very valuable, is limited as it cannot provide the wind field at cloud-free levels or locations. There are also questions regarding the possible differences between apparent cloud motions and the true wind and, more fundamentally, difficulties with assigning heights to the derived cloud-motion vectors. The cloud-height problem is especially difficult for cirrus clouds (typical errors of 1 to 2 km or more - see Shenk et al., 1975; Reynolds and Vonder Haar, 1977; Minzner et al., 1978) and for cumulus clouds that penetrate the tropopause and may have temperatures that differ from their surroundings. (See also "Clouds" below.) With regard to the vertical-wind component, it should be noted that there is currently no satellite method for measuring it.

Space-borne lidar has the potential to improve wind measurements in two main ways. In the near term, cloud-top height measurements could be made to well within the accuracy specified in table I, and this, combined with concurrent passive radiometric data, could aid in testing and refining passive height-assignment strategies. (Current tests of passively derived heights are not so direct as those permitted by space-borne lidar.) In the longer term, Doppler lidar measurements could possibly provide a direct measure of both vertical and horizontal winds in all areas unobscured by thick clouds.

Pressure.- The pressure field is the most fundamental variable in weather prediction and atmospheric circulation studies. Surface pressure and 500 mb heights are used by the operational meteorologist to determine mass movement; the three-dimensional pressure field is also the principal variable used in general circulation models for mid-range and long-range forecasting. It may be noted that the pressure profile can be used directly to specify both the temperature profile and the "balanced" wind. In contrast, the derivation of a pressure profile from a temperature profile is not possible without specifying pressure at a reference height.

Currently, remote-sensing techniques for the direct measurement of the pressure profile and even for the surface pressure have not yet been developed; moreover, the lack of an accurate pressure reference level hinders derivation of pressure profiles from radiometrically sensed temperature profiles. As a result, measurements of the pressure profile are available only at radiosonde locations and where satellite temperature profiles and a surface pressure measurement coincide.

The lidar technique combined with the method of differential absorption could permit the direct measurement of either the surface pressure (using ground-based reflection) or cloud pressure heights (using cloud-top returns).

Specification of a reference pressure and the height at which the reference pressure is obtained is a basic requirement of the NASA climate plan as well as for the GARP program. The requirements for this measurement for the above programs are an accuracy of 0.3 percent and a horizontal resolution of 500 km, which it is believed could be met or exceeded by a lidar measurement.

The lidar-measurement technique may also be used in conjunction with returns from aerosol and molecular scattering to obtain a direct measurement of the pressure profile in the lower troposphere. For this measurement, mathematical analysis shows that accuracies in the range of 0.2 percent for altitudes less than 2 km, and accuracies of better than 0.4 percent for altitudes up to 5 km, are potentially obtainable with a vertical resolution of 1 km and a horizontal resolution of 500 km. This measurement of the pressure profile would provide information which must currently be derived from a combination of measurements of the temperature profile, at much poorer vertical resolution, and ground-based measurements of surface pressure.

Humidity.- Until recently, atmospheric humidity (whether in vapor or liquid form) has not been considered very important as initial data for global numerical weather prediction. However, the thrust to develop fine-mesh prediction models has changed this, both because of the importance of clouds and rain to mesoscale processes and because humidity is a very sensitive indicator of horizontal convergence or divergence (particularly in the lower atmosphere). The divergence patterns in turn relate to vertical air currents that are important in energy transformations, which are involved in the formation of storms such as cyclones, squall lines, and hurricanes. Another potential application of humidity data from geosynchronous satellites is in the determination of winds in cloud-free areas (Endlich et al., 1972). This method is similar to tracking clouds to determine winds since humidity patterns on isentropic surfaces are tracers of air motions. Data of sufficient accuracy and detail to permit application of this method have been obtained very recently by the European geosynchronous satellite Meteosat and are currently being studied. (See the example in fig. 3.) Although microwave instruments flown on recent satellites (e.g., the ESMR on Nimbus 5 and the SCAMS on Nimbus 6) have given promising results in measuring humidity, the vertical resolution has not been sufficient to meet the requirements of table I. Calculations indicate that differential absorption lidar measurements from space could meet the requirements of the table.

Clouds.- As mentioned above, satellite cloud observations are currently a major source of wind data, but more accurate determinations of cloud-top heights are needed. The changing height of a cloud top is also a measure of the intensity of its upward vertical motion and thus is related to the low-level convergence, subsequent release of latent heat, and eventually to the intensity of rainfall and the degree of storm severity. Thus, improved measurements of cloud-top heights could aid severe-storm prediction in two ways: through improved height assignments to cloud-motion vectors and through more accurate inference of storm intensity. The latter aspect is especially in need of improved measurement techniques because the tops of towering cumulus, which may penetrate the tropopause and be much colder than the surrounding air, yield large height errors when measured by some passive radiometric techniques.

Another cloud parameter that is of value in meteorological analyses is the thermodynamic phase (ice vs. water). Lidar measurements of backscattered polarization can provide information on particle shape and, by inference, on phase. As with cloud height measurements, limited numbers of lidar flights could have a positive impact on operational cloud determinations if passive radiometers (e.g., Kyle, et al., 1978) are co-aligned with the lidar and the lidar data are used to improve the data analysis procedures for the passive sensors (which could be flown more frequently and in geosynchronous orbits).

Summary of Needs and Expected Capabilities

Table II summarizes the resolutions and accuracies required of various parameters for improvements in weather forecasting and the performance that is expected from various lidar experiments. The experiments are described in the section "Candidate Shuttle Lidar Experiments" and in more detail in appendix A where they are grouped according to their probability for success and their complexity; roughly speaking, the smaller the experiment serial number, the greater the feasibility of the experiment. Thus it can be seen that the most feasible lidar experiments (experiments 1 and 2) do not yield direct data on temperature, wind, pressure, or humidity; rather, they are intended to aid current passive methodologies through identifying cloud-top heights and the effects of thin clouds and aerosols on passive profilers. The higher numbered experiments are expected to provide direct measurements of the meteorological parameters with resolutions and accuracies that are often markedly superior to those of current systems. In general, the outstanding advantage expected from the lidar measurements is an ability to provide tropospheric profile data with vertical resolution of order 1 km.

References

Asgeirsson, Vigfus; and Stanford, John L.: Systematic Deviations of Nimbus-5 Atmospheric Temperature Fields From Radiosonde Data Over the Winter Antarctic. Geophys. Res. Lett., vol. 4, no. 10, pp. 445-448, Oct. 1977.

Baer, F.; and Boudra, D.: Numerical Prediction and Modification of Cyclone-Scale Precipitation. Mon. Weather Rev., vol. 105, no. 5, pp. 603-617, May 1977.

Committee on Atmospheric Sci., Natl. Res. Council: The Atmospheric Sciences. Problems and Applications. Natl. Acad. Sci., 1977.

Endlich, R. M.; Mancuso, R. L.; and Nagle, R. E.: A Proposed Method for Determining Winds in Cloud-Free Regions by Isentropic Analysis of Temperature and Water Vapor Profiles. J. Appl. Meteorol., vol. 11, no. 6, pp. 1019-1021, Sept. 1972.

Halem, M.: Report on a Four-Dimensional DST Temperature Sounding Impact Test. Proceedings of the Symposium on Meteorological Observations From Space: Their Contribution to the First GARP Global Experiment, J. I. Kelley and S. Ruttenberg, eds., NCAR/5101-76-1, pp. 405-412, Sept. 1976. (Available from NTIS as PB 262 530.)

Kyle, H. L.; Curran, R. J.; Barnes, W. L.; and Escoe, D.: A Cloud Physics Radiometer. Third Conference on Atmospheric Radiation - Preprints, American Meteorol. Soc., pp. 107-109, June 1978.

Minzner, R. A.; Shenk, W. E.; Teagle, R. D.; and Steranka, J.: Stereographic Cloud Heights From Imagery of SMS/GOES Satellites. Geophys. Res. Lett., vol. 5, no. 1, pp. 21-24, Jan. 1978.

Morel, Pierre; Desbois, Michel; and Szejwach, Gérard: A New Insight Into the Troposphere With the Water Vapor Channel of Meteosat. Bull. American Meteorol. Soc., vol. 59, no. 6, pp. 711-714, June 1978.

Phillips, Norman A.: The Impact of Synoptic Observing and Analysis Systems on Flow Pattern Forecasts. Bull. American Meteorol. Soc., vol. 57, no. 9, pp. 1225-1240, Sept. 1976.

Reynolds, David W.; and Vonder Haar, Thomas A.: A Bispectral Method for Cloud Parameter Determination. Mon. Weather Rev., vol. 105, no. 4, pp. 446-457, Apr. 1977.

Shenk, William E.; Holub, Robert J.; Neff, Robert A.: Stereographic Cloud Analysis From Apollo-6 Photographs Over a Cold Front. Bull. American Meteorol. Soc., vol. 56, no. 1, pp. 4-16, Jan. 1975.

Shuman, Frederick G.: Numerical Weather Prediction. Bull. American Meteorol. Soc., vol. 59, no. 1, pp. 5-17, Jan. 1978.

Smith, W. L.; and Woolf, H. M.: The Use of Eigenvectors of Statistical Covariance Matrices for Interpreting Satellite Sounding Radiometer Observations. J. Atmos. Sci., vol. 33, no. 7, pp. 1127-1140, July 1976.

Tracton, M. Steven; and McPherson, Ronald D.: On the Impact of Radiometric Sounding Data Upon Operational Numerical Weather Prediction at NMC. Bull. American Meteorol. Soc., vol. 58, no. 11, pp. 1201-1209, Nov. 1977.

TABLE 1.- MEASUREMENT NEEDS TO AUGMENT THE METEOROLOGICAL DATA BASE[a]

Parameter (b)	Δt, hr	Δx, km	Δz		Accuracy	Remarks
			Troposphere	Stratosphere		
Mid and high latitudes						
Temperature	12 to 24	250 to 500	4 levels (2 km)	3 levels (4 km)	±1 K	
Wind:						
Horizontal	12 to 24	250 to 500	4 levels (2 km)	3 levels (4 km)	±2 m/s	
Cloud motion vector	12 to 24	(c)	---------------	---------------	±2 m/s	Height must be known to 0.5 km
Vertical	12 to 24	250	4 levels (2 km)	3 levels (4 km)	≈1 cm/s	For individual cloud scale 1 m/s may be useful
Relative humidity	12 to 24	250	4 levels (2 km)	3 levels (4 km)	±30 percent	
Sea surface temperature	12 to 24	250	---------------	---------------	±1 K	
Pressure:						
Surface (or reference level)	12 to 24	250	---------------	---------------	±0.3 percent	
Profile	12 to 24	250	4 levels (2 km)	3 levels (4 km)	±0.3 percent	
Tropics						
Wind:						
Horizontal	12 to 24	250	4 levels (2 km)	3 levels (4 km)	±2 m/s	
Cloud motion vectors	12 to 24	(c)	---------------	---------------	±2 m/s	Height must be known to 0.5 km
Vertical	12 to 24	250	4 levels (2 km)	3 levels (4 km)	≈1 cm/s	For individual cloud scale 1 m/s may be useful
Temperature	12 to 24	500	4 levels (2 km)	3 levels (4 km)	±1 K	
Relative humidity	12 to 24	250	4 levels (2 km)	3 levels (4 km)	±30 percent	
Sea surface temperature	12 to 24	250	---------------	---------------	±1 K	

[a] Values listed in body of table for Δt, Δx, and Δz apply to inputs for global or hemispheric models. For fine-mesh models, required Δx is 100 km, Δt is somewhat smaller than shown, and Δz can be a factor of 2 finer than that shown.

[b] Additional parameters: cloud, snow, and ice cover; precipitation areas and soil moisture; reflected, scattered, and emitted radiation, albedo and radiation balance.

[c] Needed at 200 km intervals in cloudy regions.

TABLE II.- REQUIRED AND EXPECTED PERFORMANCE FOR LIDAR MEASUREMENTS THAT ADDRESS METEOROLOGICAL OBJECTIVES

Parameter	Required performance								Lidar experiment	Expected performance		
	Global models				Fine-mesh models							
	Δt, hr	Δx, km	Δz, km	Accuracy	Δt, hr	Δx, km	Δz, km	Accuracy		Δx, km	Δz, km	Accuracy
Temperature	12 to 24 12 to 24	500 500	2 to 4 2 to 4	±1 K ±1 K	6 to 12 6 to 12	100 100	1 to 2 1 to 2	±1 K ±1 K	[c]2 17	2 500	1 2	(c) 0.7 to 2 K
Wind	12 to 24 12 to 24 12 to 24	500 500 500	[a]2 to 4 [a]2 to 4 [a]2 to 4	±3 m/s ±3 m/s ±3 m/s	6 to 12 6 to 12 6 to 12	100 100 100	[a]1 to 2 [a]1 to 2 [a]1 to 2	[b]±3 m/s [b]±3 m/s [b]±3 m/s	[c]1 19 20	[c]≈1 0.1 100	0.15 .15 1	(c) ±2 m/s ±2 m/s
Pressure at reference level	12 to 24	500		±0.3 percent	6 to 12	100	1 to 2	[b]±0.3 percent	15	17 to 100	0.1	0.2 percent
Pressure profile	12 to 24	500	2 to 4	±.3 percent	6 to 12	100	1 to 2		16	500	1	0.1 to 0.5 percent
Relative humidity	12 to 24 12 to 24	500 500	2 to 4 2 to 4	±30 percent ±30 percent	6 to 12 6 to 12	100 100	1 to 2 1 to 2	[b]±30 percent	9 10 18	50 to 250 10 160	2 Column content 1	5 to 35 percent ±1 percent 10 percent
Cloud-top height			0.5						1	0.36	0.15	0.15 km
Cloud-droplet phase									3	0.36	0.15	

[a] Cloud motion vector height must be known to 0.5 km.
[b] Better accuracy may be needed for some applications.
[c] Cloud or aerosol measurement to aid passive methodology.

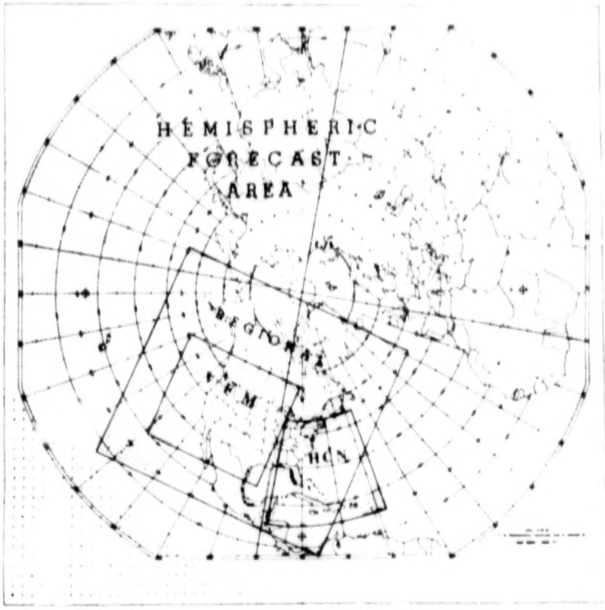

Figure 1.- Horizontal area and sample of grids for several numerical weather prediction models of the U.S. National Meteorological Center. Grid samples for hemispheric, regional, experimental VFM, and HCN models are shown by dot patterns in a corner of each area. (From Shuman, 1978)

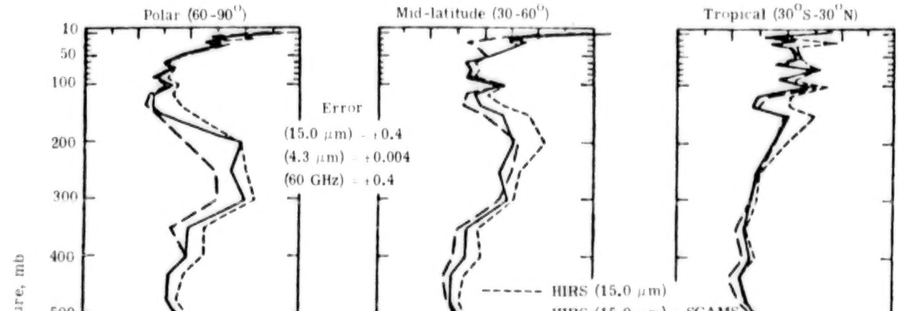

Figure 2.- Comparisons of root-mean-square (rms) temperature errors obtained from simulations using an eigenvector method to process radiances from different channels of infrared and microwave sounding spectrometers. (From Smith and Woolf, 1976)

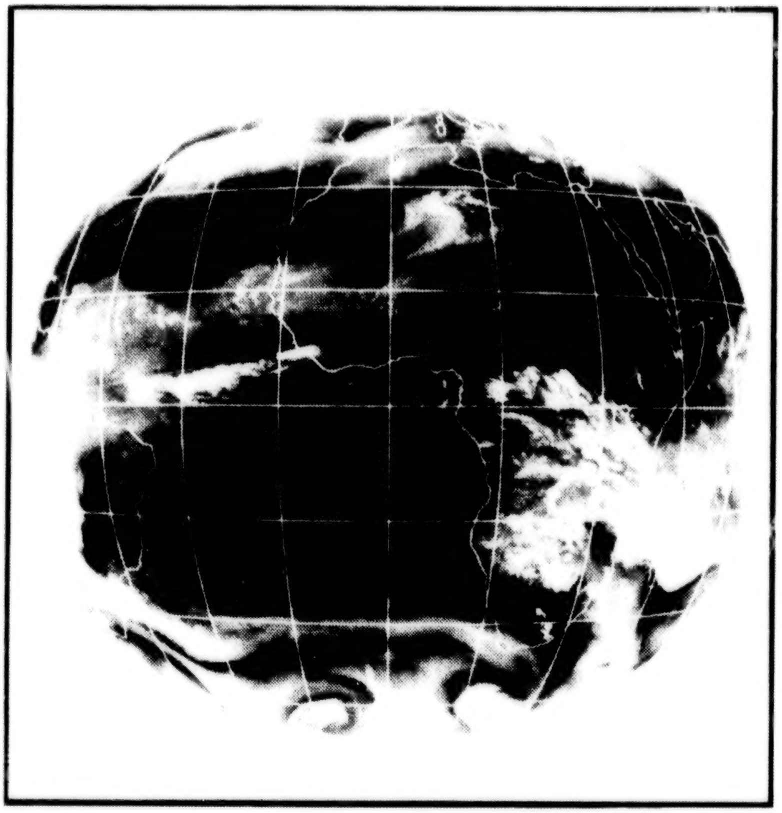

Figure 3.- Typical image of upper-tropospheric water-vapor structure obtained from 5.7 to 7.1 um channel of Meteosat, the European meteorological geostationary satellite. White (dark) indicates relatively large (small) moisture content. (From Morel et al., 1978, courtesy American Meteorological Society)

Scientific Objective 5: Upper Atmospheric Waves

The purpose of scientific objective 5 is to study excitation, propagation, and dissipation of wave motions in the upper atmosphere. Scientific objective 5 is further divided into the four sections "Global Morphology of Mesospheric and Thermospheric Waves," "Wave Motions of All Scales from 80 to 100 km Altitude," "Global Morphology of Lower Mesospheric Waves Using OH Radical," and "Wave Motions of All Scales in Stratosphere and Their Sources."

Global Morphology of Mesospheric and Thermospheric Waves

Introduction.- The motion of the atmosphere above about 60 km can be described in terms of a prevailing wind, tidal oscillations, an irregular component due to internal gravity waves, and turbulence. The tidal and gravity wave fields contain as much energy as the longer time scale geostrophically balanced motions and make a major contribution to the global balance of energy and momentum at these heights.

The sources of the tidal oscillations are believed to be heating by absorption of solar radiation by ozone and water vapor (Butler and Small, 1963; Lindzen, 1967). However, the latitudinal variation of the diurnal and semidiurnal tides, the seasonal variations of these components, and the influence of the latitude variation of the mean wind and temperature on tidal wave propagation are far from understood; and studies of all these aspects require a greater world-wide observational coverage than is presently available. For gravity waves the identification of the source is more problematic since excitation by tropospheric interactions, by changes associated with the auroral electrojet, and by nonlinear interactions of tidal oscillations is expected to be capable of generating such waves. It is evident that information on the global morphology of atmospheric oscillations will also help to identify the roles of these different sources.

On the basis of studies of the propagation characteristics of extratropical planetary waves (e.g., Charney and Drazin, 1961), it would be expected that such waves will only propagate through the stratosphere and be detected at mesospheric heights in the presence of a relatively weak westerly flow. However, in view of the possible role of such waves in the transport of trace species, in addition to that arising from turbulent mixing, every attempt should be made to identify and study planetary scale structures in the mesosphere and at even greater heights.

Present status.- For the present heights of interest, the greatest contribution to the study of atmospheric tides has been made by meteor radar observations (e.g., Greenhow and Neufeld, 1961) but these have been limited to the 80 to 105 km height range. Greenhow and Neufeld have shown that the diurnal component of the tidal wind is dominant at low latitudes and the semidiurnal component is dominant at high latitudes (Spizzichino, 1969). Recent incoherent scatter observations at Arecibo by Harper (1977) have confirmed that the diurnal variation is dominant below 110 km but the semidiurnal component is strongest at 150 to 170 km. Amplitudes of both oscillations can reach 100 m/s at

100 km, with 30 km being a reasonable estimate for the vertical wavelength of the component.

For studies of gravity waves a number of ground-based techniques have been used. Radio and radar probing (Manson et al., 1976; Woodman and Guillen, 1974) and meteor drift studies (Geller et al., 1977) have all contributed to information on waves below about 105 km, as have observations of airglow emissions (Krassovsky and Shagaev, 1974). A major number of the disturbances observed at mesospheric heights are believed to originate at lower levels. At thermospheric heights, radio probing studies (e.g., Munro, 1950) have provided considerable information on traveling ionospheric disturbances, which represent the response of the F-region plasma to the driving force of gravity waves, under the control of the Earth's magnetic fields. There is considerable evidence to associate the disturbances of medium or large scales (100 to 1000 km wavelengths) with polar disturbances (Georges, 1967), but the generation mechanism is not established. Even at these thermospheric levels, a less coherent type of disturbance sometimes observed is believed to originate at lower levels (Georges, 1968).

Relevance to lidar.- Series studies of atmospheric tides at the heights of interest by lidar techniques have been limited to the work of Kent et al. (1972). This was based on the fluctuations of molecular densities measured by Rayleigh scattering using a very sensitive system.

A number of ground-based systems have been used to observe the mesospheric sodium layer using resonance scattering. These have operated with vertical pointing laser beams and have commonly shown large variations in the shape of the vertical height distribution in a single night (e.g., Sandford and Gibson, 1970); in these variations a downward propagating wave has been identified (Blamont et al., 1972; Rowlett et al., 1978). In addition, observations with a steerable beam have shown the presence of small scale structure and also a horizontal variation over distances of about 80 km, such a variation persisting for over an hour (Thomas et al., 1976 and 1977).

For thermospheric levels, metal atoms and ions provide suitable tracers for studies of motions. However, resonance scatter from these constituents occurs at ultraviolet wavelengths and this approach has not been possible from the ground because of atmospheric absorption of these wavelengths.

A comparison of the horizontal structures of sodium and neutral magnesium will provide information on the vertical phase progression of gravity waves. Furthermore, a similar comparison of the neutral and ionized magnesium measurements for as high an altitude in the lower thermosphere as possible will demonstrate the influence of the Earth's magnetic field on traveling ionospheric disturbances commonly observed by radio techniques.

The extension of the measurements to yield height profiles will reduce the horizontal resolution but will also provide information on the vertical phase progression of waves. Thus, for the sodium layer the horizontal resolution expected for profile data will be about 50 km in daytime, but this will still be sufficient to observe the larger gravity wave structures and those arising from tidal oscillations and planetary waves. The combination of the sodium and neutral magnesium height profiles could provide detailed information over the

80 to 180 km region to enable vertical wavelengths for gravity waves (10 km), tides (30 km), and also planetary waves to be identified. The measurement of the Mg^+ profile within sporadic E-layer would enable the downward transport of metal ions by gravity waves to be recognized.

Wave Motions of All Scales From 80 to 100 km Altitude

Introduction.- It is expected that in the 80 to 100 km height range the major wave phenomena and effects will arise from gravity-wave and tidal-scale disturbances. On the basis of theoretical predictions, the amplitudes of planetary-scale disturbances will be small because of interactions with the zonal wind field at stratospheric heights (Charney and Drazin, 1961), but these effects might still be important especially in the transport of trace constituents.

For tidal oscillations and gravity waves originating at lower heights, it is expected that the perturbations increase with height as $\rho^{-1/2}$ (where ρ is mean density), but this growth is countered at the upper levels of the present heights of interest by enhanced dissipation arising from large values of kinematic viscosity and thermal conductivity. Such dissipation is believed to be responsible for a significant heating at these and higher levels (Hines, 1965). Marked attenuation of gravity waves can also be seen at critical levels where the horizontal phase velocity is equal to the velocity of the mean wind (Booker and Bretherton, 1967). The transfer of moment of momentum to the wind at such levels can influence the atmospheric circulation (Jones and Houghton, 1971), and nonlinear interactions can give rise to turbulent layers at such levels (Fritts, 1978). The generation of turbulence by gravity waves and tidal oscillations in the present height of interest is of considerable interest both in relation to small-scale accuracy of atmospheric constituents (Lindzen, 1971) and also in controlling the circulation at these levels (Houghton, 1978).

Present status.- The information currently available on wave motions in the 80 to 100 km region has been derived largely from ground-based techniques. The meteor radar method has made a major contribution to tidal studies in recognizing the predominance of the diurnal component at low latitudes and semidiurnal component at high latitudes (Spizzichino, 1969) and has demonstrated that the amplitudes of each component can reach 100 m/s at 100 km. This approach has also been used to identify some of the characteristics of gravity waves and has also identified longer term oscillations which have been attributed to planetary waves. Very-high-frequency Doppler radar measurements have illustrated the propagation of gravity waves to mesospheric heights from below (Woodman and Guillen, 1974) and have shown a growth in amplitude and dissipation with increasing height. The influence of gravity waves in the 80 to 100 km region has been demonstrated in airflow observations of intensities and temperatures (Krassovsky and Shagaev, 1974). Recent results of Noxon (1978) have revealed very large temperature oscillations which will facilitate the observation of such waves but will also demand a nonlinear treatment in investigations at these heights.

Relevance to lidar.- Because of the relatively small molecular densities existing in the 80 to 100 km region, Rayleigh scattering does not lend itself readily to studies of wave motions at these altitudes, although some results on tidal oscillations have been obtained using a large, sensitive receiving system (Kent et al., 1972). In contrast, observations of the mesospheric sodium layer by resonance scattering have successfully demonstrated gravity-wave activity. Large variations have been observed in the vertical height distributions (e.g., Sandford and Gibson, 1970), and evidence for a downward propagation wave has been found (Blamont et al., 1972). In addition, measurements of profiles at two points separated by about 15 km have shown oscillations similar to those expected for gravity waves, and evidence for a horizontal variation over distances of about 80 km has been obtained (Thomas et al., 1976 and 1977); if this variation is attributed to wave action, its persistence of about an hour would seem to imply a standing-wave pattern.

These results indicate that the detailed height information available from lidar experiments combined with the latitude coverage provided by a satellite experiment could provide the necessary information for the present wave studies.

The development of the ground-based method for studying the mesospheric sodium layer provides the best basis for lidar measurements of waves in the 80 to 100 km region; Rayleigh scattering studies for this height range will not be feasible. Further development will be directed towards the incorporation of temperature measurements from observations of the Doppler broadening of the sodium line profile and of wind measurements from the Doppler shift imposed on this profile.

Global Morphology of Lower Mesospheric Waves Using OH Radical

Introduction.- As with the lower thermosphere, the 60 to 80 km height region should contain disturbances of gravity-wave, tidal-oscillation, and planetary-wave scales. However, for gravity waves and tides the amplitudes at the lower heights will be reduced in proportion to ρ^{-1} (where ρ is mean density) and will, therefore, be more difficult to detect. Thus, direct observations of these waves at a 60 km height, based on temperature or wind measurements, will require accuracies of about 1 K and 2 m/s, respectively. For planetary waves, the amplitudes should be larger in the 60 to 80 km region than in the lower thermosphere, but the above measurement accuracies will still be required.

The 60 to 80 km height range is of interest because, on the basis of present ideas, it does not represent a major source region of waves and is still below the region of major dissipation of gravity waves and tides.

Present status.- The study of atmospheric waves in the 60 to 80 km height range has not attracted the same attention as at other heights. Observations with rocketsondes have terminated at the lower height limit, and the meteor radar technique can only provide information above 80 km. Some information on motions in the upper part of the height range has been given by observations of partial reflections of MF radio waves pulses (e.g., Manson et al., 1976), and large VHF facilities (e.g., Woodman and Guillen, 1974) are particularly useful for observations of the smaller-scale disturbances. Information on planetary waves has been provided since 1975 by measurements of temperature structure using the Pressure Modulator Radiometer and the Limb Radiance Inversion Radiometer on a Nimbus 6 satellite, and such instruments could in the future be also used for wind measurements.

Relevance to lidar.- Observations of the 60 to 80 km height region of the atmosphere are rendered difficult by the absence of any suitable scattering constituent. Rayleigh scattering has been used for observing tidal oscillations (Kent et al., 1972) but has required a very sensitive system.

Both theoretical (Thomas and Bowman, 1972) and experimental treatments (Anderson, 1971a and 1971b) have indicated concentrations of the OH radical in excess of 10^6 cm^{-3} at heights between about 60 and 75 km, the concentration decreasing rapidly with further increase in height. No lidar observation of this constituent has been made at these heights. However, it can be shown that resonance scattering of lines in the OH ($^2\Sigma$ - $^2\Pi$) band system near 300 nm will exceed Rayleigh scattering; and when account is taken of quenching of the $^2\Sigma^+$ state, it is found that the scattering efficiency is greater than 80 percent above about 60 km. Thus the OH radical could provide a suitable tracer for studying the 60 to 80 km region by a lidar technique.

Wave Motions of All Scales in Stratosphere and Their Sources

Introduction.- Although a number of atmospheric oscillations are expected at stratospheric heights, some of these do not lend themselves to observations during Spacelab flights limited in duration to one or two weeks. They include the annual periodicity, the quasi-biennial oscillation commonly observed below 35 km, the semiannual oscillations most evident above this height, and the periodicity of about 14 days observed in the amplitude of planetary waves. Thus the present consideration of Spacelab observations of the stratosphere will be confined to planetary waves, gravity waves, and tides. However, future operations with a power module might make the observation of some longer-term oscillations possible.

For planetary waves, it is considered that the differential solar heating over oceans and continents dominates the production of waves in the middle stratosphere, with wind flow over orographic features being capable of generating waves at lower heights (Beer, 1974). A study of planetary-wave activity at a series of heights in the stratosphere in relation to the distribution of continents, oceans, and mountain ranges might help identify these sources, as well as the role of baroclinic instability in the excitation of waves at heights above about 30 km.

For gravity waves, the lee waves generated by the passage of winds over extensive chains of mountains provide specific sources capable of study from world-wide observations of the stratosphere. Furthermore, the production of such waves by the supersonic movement of the terminator should be more easily detectable at stratospheric heights than at ground level.

For both types of waves, interaction with the mean flow is known to be of major importance. In particular, the presence of critical layers, in which the horizontal phase velocity is equal to that of the mean wind (e.g., Booker and

Bretherton, 1967), can cause marked attenuation. Consequently, the interpretation of changes in the wave amplitudes with height will need to take account of this effect as well as the possibility of reflection from features in the wind and temperature profiles.

For tidal oscillations, the sources mechanisms are believed to be heating caused by absorption of solar radiations, of ozone in the upper stratosphere (Butler and Small, 1963), and of water vapor at lower heights (Lindzen, 1967). The detection of tidal oscillations at stratospheric heights will be relevant to the confirmation of these ideas.

Present status.- The greatest information on atmospheric waves at stratospheric heights probably relates to planetary scale effects. Hirota (1975) and Hirota and Sato (1969) have shown that traveling waves of few meters per second amplitude in summer, and considerably larger amplitude in winter, are frequently observed; and corresponding temperature fluctuations have been detected from Nimbus satellites in summer (about 1 K) and winter (about 10 K). The planetary-wave effects associated with stratospheric warmings can be considerably larger (Labitzke, 1972).

Both theoretical and experimental studies on tidal oscillations at stratospheric heights have indicated small amplitudes. Thus for the diurnal component, Reed et al. (1969) have shown from observations and Lindzen (1967) from theoretical analysis that an amplitude of 1 m/s is representative of 30 km altitude.

Similar small amplitudes are also to be expected for gravity waves. According to the results of the meteorological rocket network (Justus and Woodrum, 1973) and measurements with VHF radar (Woodman and Guillen, 1974; Rüster et al., 1978), amplitudes less than 1 m/s are to be normally expected near 20 km.

It is evident that the detection of such small changes in wind or temperature for studies of the wave field at stratospheric heights will be very challenging.

Relevance to lidar.- The objective of examining planetary wave activity at different heights in the stratosphere, in order to identify the proposed source mechanisms, could be realized with the good height resolution characteristic of the lidar technique. This feature could also lend itself to the identification of vertical wavelengths of atmospheric oscillations in the stratosphere.

To date, no lidar observations of the wind field, or of the detailed temperature structure at stratospheric heights have been reported. The measurement of the Doppler shift imposed on laser radiation from moving atmospheric aerosols has been demonstrated for tropospheric heights by Benedetti-Michelangeli et al. (1972). Their experiment made use of a stabilized, chopped argon ion laser operating at 633.8 nm with photon counting being used in the receiver system. In addition, the general capability of a coherent infrared lidar technique for accurate wind measurement has been demonstrated by Huffaker, 1975.

References

Anderson, James G.: Rocket-Borne Ultraviolet Spectrometer Measurement of OH Resonance Fluorescence With a Diffusive Transport Model for Mesospheric Photochemistry. J. Geophys. Res., vol. 76, no. 19, pp. 4634-4652, July 1, 1971a.

Anderson, James G.: Rocket Measurement of OH in the Mesosphere. J. Geophys. Res., vol. 76, no. 31, pp. 7820-7824, Nov. 1, 1971b.

Beer, Tom: Atmospheric Waves. John Wiley & Sons, 1974.

Benedetti-Michelangeli, G.; Congeduti, F.; and Fiocco, G.: Measurement of Aerosol Motion and Wind Velocity in the Lower Troposphere by Doppler Optical Radar. J. Atmos. Sci., vol. 29, no. 5, pp. 906-910, July 1972.

Blamont, J. E.; Chanin, M. L.; and Megie, G.: Vertical Distribution and Temperature Profile of the Night Time Atmospheric Sodium Layer Obtained by Laser Backscatter. Ann. Geophys., t. 28, nr. 4, pp. 833-838, 1972.

Booker, John R.; and Bretherton, Frances P.: The Critical Layer for Internal Gravity Waves in a Shear Flow. J. Fluid Mech., vol. 27, pt. 3, pp. 513-539, Feb. 24, 1967.

Butler, S. T.; and Small, K. A.: The Excitation of Atmospheric Oscillations. Proc. R. Soc. London, ser. A, vol. 274, no. 1356, pp. 91-121, June 25, 1963.

Charney, J. G.; and Drazin, P. G.: Propagation of Planetary-Scale Disturbances From the Lower Into the Upper Atmosphere. J. Geophys. Res., vol. 66, no. 1, pp. 83-108, Jan. 1961.

Fritts, David C.: The Nonlinear Gravity Wave-Critical Level Interaction. J. Atmos. Sci., vol. 35, no. 3, pp. 397-413, Mar. 1978.

Geller, M. A.; Bowhill, S. A.; and Hess, G. C.: A Description of the University of Illinois Meteor Radar System and Some First Results. J. Atmos. & Terrest. Phys., vol. 39, no. 1, pp. 15-24, Jan. 1977.

Georges, T. M.: HF Doppler Studies of Traveling Ionospheric Disturbances. J. Atmos. & Terrest. Phys., vol. 30, no. 5, pp. 735-746, May 1968.

Georges, T. M.: Ionospheric Effects of Atmospheric Waves. ESSA Tech. Rep. IER 57-ITSA 54, U.S. Gov. Print. Off., 1967.

Greenhow, J. S.; and Neufeld, E. L.: Winds in the Upper Atmosphere. Q. J. R. Meteorol. Soc., vol. 87, no. 374, pp. 472-489, Oct. 1961.

Harper, R. M.: A Comparison of Ionospheric Currents, Magnetic Variations, and Electric Fields at Arecibo. J. Geophys. Res., vol. 82, no. 22, pp. 3233-3242, Aug. 1, 1977.

Hines, C. O.: Dynamical Heating of the Upper Atmosphere. J. Geophys. Res., vol. 70, no. 1, pp. 177-183, Jan. 1, 1965.

Hirota, I.: Spectral Analysis of Planetary Waves in the Summer Stratosphere and Mesosphere. J. Meteorol. Soc. Japan, vol. 53, pp. 33-44, 1975.

Hirota, I.; and Sato, Y.: Periodic Variation of the Winter Stratospheric Circulation and Intermittent Vertical Propagation of Planetary Waves. J. Meteorol. Soc. Japan, vol. 47, no. 5, pp. 390-402, Oct. 1969.

Houghton, J. T.: The Stratosphere and Mesosphere. Q. J. R. Meteorol. Soc., vol. 104, no. 439, pp. 1-29, Jan. 1978.

Huffaker, R. M.: CO_2 Laser Doppler Systems for the Measurement of Atmospheric Winds and Turbulence. Atmos. Technol., no. 9, pp. 71-76, Feb. 1975.

Jones, Walter L.; and Houghton, David D.: The Coupling of Momentum Between Internal Gravity Waves and Mean Flow: A Numerical Study. J. Atmos. Sci., vol. 28, no. 4, pp. 604-608, May 1971.

Justus, C. G.; and Woodrum, Arthur: Upper Atmospheric Planetary-Wave and Gravity-Wave Observations. J. Atmos. Sci., vol. 30, no. 7, pp. 1267-1275, Oct. 1973.

Kent, G. S.; Keenliside, W.; Sandford, M. C. W.; and Wright, R. W. H.: Laser Radar Observations of Atmospheric Tides in the 70-100 km Height Region. J. Atmos. & Terrest. Phys., vol. 34, no. 3, pp. 373-386, Mar. 1972.

Krassovsky, V. I.; and Shagaev, M. V.: Inhomogeneities and Wavelike Variations of the Rotational Temperature of Atmospheric Hydroxyl. Planet. & Space Sci., vol. 22, no. 9, pp. 1334-1337, Sept. 1974.

Labitzke, Karin: Temperature Changes in the Mesosphere and Stratosphere Connected With Circulation Changes in Winter. J. Atmos. Sci., vol. 29, no. 4, pp. 756-766, May 1972.

Lindzen, R. S.: Thermally Driven Diurnal Tide in the Atmosphere. Q. J. R. Meteorol. Soc., vol. 93, no. 395, pp. 18-42, Jan. 1967.

Lindzen, R. S.: Tides and Gravity Waves in the Upper Atmosphere. Mesospheric Models and Related Experiments, G. Fiocco, ed., Springer-Verlag, pp. 122-130, 1971.

Manson, A. H.; Gregory, J. B.; and Stephenson, D. G.: Gravity Waves in the Lower Thermosphere. J. Atmos. & Terrest. Phys., vol. 38, no. 2, pp. 143-148, Feb. 1976.

Munro, G. H.: Travelling Disturbances in the Ionosphere. Proc. R. Soc. London, ser. A, vol. 202, no. 1068, pp. 208-223, June 22, 1950.

Noxon, J. F.: Effect of Internal Gravity Waves Upon Night Airglow Temperatures. Geophys. Res. Lett., vol. 5, no. 1, pp. 25-27, Jan. 1978.

Reed, Richard J.; Oard, Michael J.; and Sieminski, Marya: A Comparison of Observed and Theoretical Diurnal Tidal Motions Between 30 and 60 Kilometers. Mon. Weather Rev., vol. 97, no. 6, pp. 456-459, June 1969.

Rowlett, J. R.; Gardner, C. S.; Richter, E. S.; and Sechrist, C. F., Jr.: Lidar Observations of Wave-Like Structure in the Atmospheric Sodium Layer. Geophys. Res. Lett., vol. 5, no. 8, pp. 683-686, Aug. 1978.

Rüster, R.; Röttger, J.; and Woodman, R. F.: Radar Measurements of Waves in the Lower Stratosphere. Geophys. Res. Lett., vol. 5, no. 2, pp. 119-122, Feb. 1978.

Sandford, M. C. W.; and Gibson, A. J.: Laser Radar Measurements of the Atmospheric Sodium Layer. J. Atmos. & Terrest. Phys., vol. 32, no. 8, pp. 1423-1430, Aug. 1970.

Spizzichino, A.: Étude éxperimentale des vents dans la haute atmosphere. Ann. Geophys., t. 25, fasc. 3, pp. 697-720, 1969.

Thomas, L.; and Bowman, M. R.: The Diurnal Variations of Hydrogen and Oxygen Constituents in the Mesosphere and Lower Thermosphere. J. Atmos. & Terrest. Phys., vol. 34, no. 11, pp. 1843-1858, Nov. 1972.

Thomas, L.; Gibson, A. J.; and Bhattacharyya, S. K.: Lidar Observations of a Horizontal Variation in the Atmospheric Sodium Layer. J. Atmos. & Terrest. Phys., vol. 39, no. 11/12, pp. 1405-1409, Nov./Dec. 1977.

Thomas, L.; Gibson, A. J.; and Bhattacharyya, S. K.: Spatial and Temporal Variations of the Atmospheric Sodium Layer Observed With a Steerable Laser Radar. Nature, vol. 263, no. 5573, pp. 115-116, Sept. 9, 1976.

Woodman, Ronald F.; and Guillen, Alberto: Radar Observations of Winds and Turbulence in the Stratosphere and Mesosphere. J. Atmos. Sci., vol. 31, no. 2, pp. 493-505, Mar. 1974.

Scientific Objective 6: Thermospheric Chemistry and Transport

The purpose of scientific objective 6 is to study the chemistry and transport of thermospheric atomic species.

Introduction

Above 80 km, the molecular constituents which were predominant below that level are broken into atomic species by the intense solar ultraviolet radiation. The photodissociation of molecular oxygen into atomic oxygen is especially effective in the thermosphere; and the study of the oxygen cycle, its formation, its transport by molecular and eddy diffusion or by global circulation, and its recombination into molecular oxygen are determinant factors in the composition and thermal structure of the thermosphere.

The presence of oxygen either in molecular or atomic form is responsible for a large number of chemical reactions. For example, N atoms and H atoms undergo oxidation reactions to produce NO and OH, respectively, and metals and alkalis which are present in the lower thermosphere are limited by their oxidation.

It should also be mentioned that the far ultraviolet solar photons lead to the photoionization of the major thermospheric neutral components N_2, O_2, and O, as well as minor constituents, alkalis, and metal atoms and oxides. This equilibrium between neutral and excited species is very unstable due to collisions and interactions with fast photoelectrons, and de-excitation leads either to optical emissions or thermal energy production.

The equilibrium of most of those species cannot be understood without taking into account transport processes, whether they are global scale circulation or tidal and planetary waves. Vertical transport and eddy diffusion at the level of the mesopause ($\approx$90 km) play an important role in the energy transport from the thermosphere to the mesosphere, and they affect the distribution of most of the thermospheric atoms H, He, Ar, and O.

A simultaneous global coverage of several of those species together with the measurement of the dynamical parameters responsible for their transport would be helpful in the understanding of the equilibrium of atomic species in the lower thermosphere.

Such a program cannot be completely fulfilled by lidar alone and should be based on simultaneous use of active and passive techniques. A valuable feature of using the lidar technique to study the atmosphere is the possibility of obtaining good vertical resolution ($\leqq$1 km). It is then possible to observe the spatial and/or temporal evolution of structures and inhomogeneities which have already been proven to exist in most species around the mesopause level.

Specific Problems

Lower thermosphere eddy diffusion coefficient.- It is now generally recognized that eddy diffusion plays a major role in the energy transport through the mesopause level. Measurements of the eddy diffusion coefficient are too few and too scattered in space and time to give an accurate idea of its variation. The usual techniques have used the observation of meteorites, artificial clouds, and mass spectrograph ratio measurements of Ar to N_2. A recent review of our present knowledge of the eddy diffusion coefficient is given by Roper (1977). More recently, the vertical distribution of sodium atoms has led to an evaluation of the eddy diffusion coefficient (Megie and Blamont, 1977) by studying the temporal evolution of the topside scale height of the sodium layer in the absence of any source. An estimate of this coefficient can also be obtained from the presence or absence of structures in the sodium layer as an increase in the eddy turbulence tends to make those structures vanish. Such information can be easily obtained using lidar to measure the vertical distribution of the sodium layer on a global scale. Even such a rough estimate (within a factor of 5) should be of great help if obtained on a global scale. More accurate measurements of the evolution of the topside scale height require a large series of measurements on many orbits in order to obtain the temporal variation at the places where the orbits cross each other.

The scientific requirements are obviously more ambitious than that which is proposed in the following table for the measurement of the eddy diffusion coefficient K (mainly because the measurement will be limited to the topside of the layer from 95 to 100 km), but no other method seems to be available to perform such a measurement on a global scale.

Parameter, cm^2/s	Altitude range, km	Resolution		Accuracy, percent
		Δx, km	Δz, km	
Scientific requirement				
K	80 to 105	≈100	5	≈100
Proposed achievement				
K	95 to 100	≈10 km	5	A few
K	95 to 100	A few measurements	5	10

Morphology of Na abundances.- Sodium airglow has been observed for over 50 years; but with the exception of a few rocket measurements which gave sporadic information, it has only been a decade since accurate vertical distributions have been provided using the lidar technique.

Increased spatial resolution using the lidar technique, and the possibility of continuous observation during night and twilight, has led to a better understanding of the sources and sinks of these atoms. Dynamical effects have also been studied, and the structures observed in the layer have been attributed to gravity or tidal waves propagating downwards with a speed of one to a few kilometers per hour. The measurements are yet limited to a few geographic locations, and the latitudinal variation cannot be deduced from the available data (Blamont et al., 1972; Gibson and Sandford, 1971; Hake et al., 1972; Kirchhoff and Clemesha, 1973).

A global coverage with a good horizontal resolution could be obtained from the Spacelab which will provide a global view of the general shape and structure of the layer. Such information will not only help to understand the existence of those atoms but, because they can be used as tracers of motions, they will provide information on local and global circulation.

Such an objective can be fulfilled with the available technology. A comparison between the scientific requirement and the proposed achievement in the measurement of Na is given in the following table:

Parameter	Altitude range, km	Resolution		Accuracy, percent
		Δx, km	Δz, km	
Scientific requirement				
Na	80 to 100	100	0, 5	20
Proposed achievement				
Na	80 to 100	10 at night; 100 during day	0, 5	20

Stratospheric-mesospheric coupling using Na.- A significant correlation has been observed at high latitudes between sodium abundances and stratospheric warmings (Hunten and Godson, 1967). The breakdown in the stratospheric circulation pattern occurring from the rapid cooling of the polar stratosphere could produce vertical mixing which would carry salt particles up to the mesopause. A simultaneous study of stratospheric warmings, vertical transport, and sodium abundances could give a clearer insight into the stratospheric-mesospheric coupling. A measurement of the time delay between stratospheric warmings and the Na abundance increase would be of a great interest. It was also suggested (Hunten and Godson, 1967) that the vertical mixing associated with stratospheric warmings would increase the NO concentration. And, as NO is the principal source of electrons in the D-region, this will lead to a similar increase of the recombination processes producing neutral sodium from bimolecular ions. Simultaneous measurements of NO and sodium ions would be worth associating with the above suggested measurements.

In a first phase, the lidar would only be used to obtain the sodium abundance and vertical distribution; stratospheric temperature could be provided by an infrared radiometer from CO_2 absorption around 15μm with an accuracy of ±1 K. Measurements of NO by passive techniques (γ-band dayglow or infrared absorption), even though they involve integration over a path length, would be useful until an NO density profile could be obtained by resonant fluorescence lidar in the γ-bands (205 to 210 nm). This ultraviolet lidar still needs laser development and will only be available for future missions. The results are summarized as follows:

Parameter	Altitude range, km	Resolution		Accuracy, percent
		Δx, km	Δz, km	
Scientific requirement				
Na	80 to 110	100	10	A few
Possible achievement				
Na	80 to 110	10 at night; 100 during day	10	A few
Scientific requirement				
NO	100 to 130	500	5	10
Possible achievement				
NO	70 to 150	100	3	20
Passive measurements required: Stratospheric temperature, ±1 K Vertical transport Preliminary NO total content Na^+ from 80 to 100 km				

Origin of Na and K in upper atmosphere.- The simultaneous measurement of the altitude distribution of Na and K by lidar (Megie et al., 1978) has shown that the abundance ratio presents a seasonal variation; that is, it varies between a minimum value compatible with a meteoritic origin (≈10) and a maximum value compatible with a terrestrial source (40 to 50). These measurements imply two different origins for the alkalis in the upper atmosphere: meteoric and terrestrial. Measurements of this abundance ratio at different latitudes could confirm this hypothesis because it is assumed that the terrestrial source of sodium is due to the vertical transport of salt particles at high latitude during stratospheric warming.

Such an experiment can be performed with a laser pumping two different dyes using a technology which is well developed now and is already used on the ground. The performance of both detectors, even though degraded by an order of magnitude for K, is sufficient to satisfy the science requirements. In a later stage, it would be possible to extend this study to other metals and alkalis such as Mg, Li, Ca, Fe, etc.

Simultaneous observations of metallic atom, ion, and oxide distribution.- The equilibrium of metallic constituents from either terrestrial or meteoritic origin (or from both origins) is regulated by photochemistry, photoionization, and dynamics. The neutral species are subject to ionization and oxidation occurring at the top and at the bottom of the neutral layer, respectively, and vertical distribution of the neutral constituent. The presence in the atmosphere of a specific constituent can be better traced if it is possible to observe simultaneously the atom, the ion, and the oxide of the same metal. Vertical profiles and latitudinal distribution will provide valuable information on sources and sinks, as well as on thermospheric and ionospheric circulation.

Two sets of metallic constituents could be traced with the available technology: Mg, Mg^+, and MgO; Fe, Fe^+, and FeO.

The presence of Mg^+ at the level of the E- and F-layers would be of particular interest, as mentioned in scientific objective 5 in the study of ionospheric plasma dynamics.

Global distribution of atomic oxygen between 80 and 150 km.- The importance of measuring atomic oxygen and, mainly, its vertical profile to understand the oxygen cycle and the relative role of photochemistry and diffusion was previously mentioned in the general statement. Such a study will be more valuable if molecular species such as O_2, N_2, or even O_3 and OH could be performed simultaneously either by active or passive techniques. Lidar offers the only way to obtain a global map of the altitude distribution of atomic oxygen. At this stage, it requires laser development in order to be able to make this measurement (McIlrath et al., 1979). Potential solutions are in view; and such a possibility, even not available for the first missions, should be considered.

The scientific requirements and proposed experiments are summarized as follows:

Parameter	Altitude range, km	Resolution		Accuracy, percent
		Δx, km	Δz, km	
Scientific requirement				
O	80 to 200	500	5	10
Proposed experiment				
O	80 to 180	8000 to 300	3	10
Scientific requirement				
OH	80 to 100	500	5	20
Proposed experiment				
OH	35 to 100	100 during day	3	10
Simultaneous passive experiments required: global coverage of O_2, N_2, and O_3 in same range of altitude				

References

Blamont, J. E.; Chanin, M. L.; and Megie, G.: Vertical Distribution and Temperature Profile of the Night Time Atmospheric Sodium Layer Obtained by Laser Backscatter. Ann. Geophys., t. 28, nr. 4, pp. 833-838, 1972.

Gibson, A. J.; and Sandford, M. C. W.: The Seasonal Variation of the Night-Time Sodium Layer. J. Atmos. & Terrest. Phys., vol. 33, no. 11, pp. 1675-1684, Nov. 1971.

Hake, R. D., Jr.; Arnold, D. E.; Jackson, D. W.; Evans, W. E.; Ficklen, B. P.; and Long, R. A.: Dye-Laser Observations of the Nighttime Atomic Sodium Layer. J. Geophys. Res., vol. 77, no. 34, pp. 6839-6848, Dec. 1, 1972.

Hunten, D. M.; and Godson, W. L.: Upper-Atmospheric Sodium and Stratospheric Warmings at High Latitudes. J. Atmos. Sci., vol. 24, no. 1, pp. 80-87, Jan. 1967.

Kirchhoff, V. W. J. H.; and Clemesha, B. R.: Atmospheric Sodium Measurements at 23°S. J. Atmos. & Terrest. Phys., vol. 35, no. 8, pp. 1493-1498, Aug. 1973.

McIlrath, T. J.; Hudson, R.; Aikin, A.; and Wilkerson, T. D.: Two-Photon Lidar Technique for Remote Sensing of Atomic Oxygen. Appl. Opt., vol. 18, no. 3, pp. 316-319, Feb. 1979.

Megie, G.; and Blamont, J. E.: Laser Sounding of Atmospheric Sodium - Interpretation in Terms of Global Atmospheric Parameters. Planet. & Space Sci., vol. 25, no. 12, pp. 1093-1109, Dec. 1977.

Megie, G.; Bos, F.; Blamont, J. E.; and Chanin, M. L.: Simultaneous Nighttime Lidar Measurements of Atmospheric Sodium and Potassium. Planet. & Space Sci., vol. 26, no. 1, pp. 27-35, Jan. 1978.

Roper, R. G.: Turbulence in the Lower Thermosphere. The Upper Atmosphere and Magnetosphere, Natl. Acad. Sci. - Natl. Res. Counc., pp. 117-129, 1977.

Scientific Objective 7: Magnetospheric Sun and Weather Relationships

The purpose of scientific objective 7 is to study the magnetospheric aspects related to Sun and weather relationships.

Introduction

The subject of a possible relationship between solar activity and meteorological variables has intrigued scientific investigators for many years. A recent report [Shapley and Kroehl, 1979] lists over 1300 references to relatively recent papers alone. Unfortunately, it is difficult to test such relationships with certainty because of the high level of random variability in the meteorological quantities of prime concern and the relative infrequency of large solar events.

Modern interest in the subject dates from the work of Roberts and Olson (1973a and 1973b) when they introduced the vorticity area index and showed a correlation with geomagnetic activity. Wilcox et al. (1973 and 1974) showed how the index that represents the area of most intense vorticity in troughs in the Northern Hemisphere north of 20°N reaches a minimum about a day after a sector boundary crossing, which is a well-defined solar-terrestrial event. (See fig. 1.) These data have been reanalyzed by Shapiro (1976) and by Hines and Halevy (1975) with the conclusion that the association, while not as great as first suggested by Wilcox, does appear to be real.

The influence of solar activity on weather has been viewed with skepticism in the absence of widely accepted physical mechanisms. At two conferences in 1978 (Yosemite, California, February 8-11; Columbus, Ohio, July 24-28), the merits of various mechanisms have been debated at length. None has prevailed up to now, through the lack of evidence establishing the intermediate links in the causative chain. It is therefore important to study possible mechanisms for solar effects on weather in as quantitative a manner as possible so that those mechanisms that are not found to be viable can be discarded.

The relationships between solar disturbances and changes in atmospheric structure are best studied by prolonged observational programs involving geostationary satellites, for instance, rather than by experiments on relatively brief sortie missions. However, there are several magnetospheric aspects which involve the processes by which the energy is deposited in the atmosphere, where a lidar experiment may play a significant role, if accompanied by an extensive supporting program of ground, rocket, and balloon measurements. The probable availability of the Upper Atmosphere Research Satellite during at least some of the lidar missions offers the possibility of extending in time some of the global measurements associated with this problem.

Possible Mechanisms

There is no lack of suggestions as to ways in which short-term solar variability may affect the atmosphere. They include those mechanisms in which solar effects on the thermosphere are transmitted to lower levels and those in which the troposphere or stratosphere is affected directly.

Roberts and Olson (1973a) suggested that penetrating ionizing radiation might produce ions in the middle atmosphere that could form condensation nuclei and produce subvisible cirrus, which would then affect the radiative balance and hence the vorticity. Lidar measurements could play a key role in testing this idea.

Another possibility would arise when energetic particles are deposited in the high-latitude thermosphere and produce strong heating which excites a disturbed thermospheric wind field. This disturbed wind field will couple with the ionization present throughout the thermosphere and with the Earth's magnetic field and will produce electric fields and currents that are characteristic of the disturbed dynamo current system. This same electric field is responsible for the magnetospheric convection of ionization and of trace constituents such as metal ions deposited by meteor trails in the lower thermosphere. It is further known from balloon measurements that these magnetospheric electric fields are conducted into the stratosphere; and it is possible that they may produce nucleation effects, having implications for the energetics of the troposphere-stratosphere system. It is also possible that their disturbance of the normal global stratospheric current system may impinge on thunderstorm electrification and therefore indirectly on cyclogenesis.

It seems unlikely that the dynamic effect of the disturbed circulation would penetrate to lower altitudes, as the energy fluxes involved are quite small compared with those required to affect the stratosphere or troposphere.

A final thermospheric effect that might be relevant is the augmentation of minor thermospheric species such as nitric oxide by particle input. Such constituents can make their way into the mesosphere where they may well profoundly affect the chemistry of other constituents such as ozone. Thermal perturbations will result from changes in absorption of near-ultraviolet radiation by the ozone, and these thermal effects may impinge on the transmission or reflection of tropospherically generated planetary-wave propagation through the mesosphere. For example, a reflected planetary wave has a large energy content in the mesosphere and might have a significant effect on cyclogenesis when it reappears in the upper troposphere.

As far as those effects involving the troposphere or stratosphere directly are concerned, most of these involve ozone in one way or another. Enhanced fluxes of solar protons associated with solar-wind sector boundaries can produce strong enhancements of the ozone layer; these will be quite nonuniform over the globe and will produce strong dynamical effects. Excess absorption of solar ultraviolet radiation will produce thermal forcing of stratospheric planetary waves whose energy may suffice to perturb the lower stratosphere sufficiently to affect synoptic-scale processes. An alternate suggestion is that short-term changes in the composition of solar near-ultraviolet radiation may change the ozone layer and produce a similar forcing effect.

A final direct effect on the stratosphere may be the energetic particle effect on its ionization content, and therefore its conductivity. Through the current system associated with the fair-weather electric field mentioned above, this may again affect thunderstorm electrification processes. This does not by any means exhaust the list of suggested mechanisms, but suffices to show the importance of measurements of thermospheric and stratospheric chemistry and dynamics.

Magnetospheric Convection Patterns of Mg^+

One tracer for the electric-field pattern in the low-altitude magnetosphere is the distribution of alkali metals such as Mg^+. These are convected from the low-latitude E-region to much higher altitudes and latitudes, where they have been seen by satellite probes [Hanson and Sanatani, 1971] and by ultraviolet photometry of their resonant fluorescence in sunlight [Gérard, 1976]. The lidar (experiment 8) is capable of observing these metals, and the orbit-to-orbit change in their distribution will give a measure of the magnitude and variability of the electric fields.

Correlative measurements include in situ measurements of the field from satellites, measurements of the field in the stratosphere from balloons, the magnetic variations at ground level arising from the ionospheric current system, and incoherent scatter measurements at several latitudes of the ionospheric drift velocity.

Chemical Coupling From Thermosphere to Mesosphere

Large amounts of nitric oxide are known to be produced in the auroral zone during intense auroral activity (such as that associated with a substorm). This long-lived constituent is carried to lower latitudes and down into the D-region, where it is thought to be responsible for the "winter anomaly" in D-region ionization. The catalytic destruction of ozone by nitric oxide may be one link in the chain by which atmospheric dynamics is finally affected.

Nitric oxide has been observed by resonance fluorescence in the γ-bands both by rocket and by satellite; however, the former lacks horizontal coverage while the latter is incapable of producing an accurate vertical profile because of Rayleigh scattering and other effects. An ultraviolet lidar (experiment 25) would provide new results on the association of the global spread of nitric oxide with substorms and sector crossings, particularly in conjunction with ground and rocket measurements of the D-region. Mesospheric temperatures measured by a sodium lidar (experiment 14) would show resultant thermal perturbations.

Ozone Heating Effects on Circulation

Changes in the circulation of the atmosphere are usually associated with the forcing of planetary waves or tides, depending on the global nature of the change. Ozone heating can produce such changes at high altitudes, which communicate kinetic energy downwards into the lower atmosphere, perhaps by modifying either the polar night jet or the propagation of planetary waves from the troposphere. Here, measurements by lidar of the atmospheric and thermospheric velocity field, using aerosols (experiment 20) and sodium (experiment 14), for example, should show the propagation processes at work. The temperature field should be mapped simultaneously; and meteorological rockets, meteor radars, partial-reflection drift experiments, and mesosphere/stratosphere/troposphere (MST) VHF radars will supplement conventional rawinsondes to give the atmospheric state on a coarser scale for comparison. Measurements by lidar of ozone and other constituents by DIAL (experiment 18) or occultation (experiment 13) would be needed to evaluate the ozone coupling effect.

The following table summarizes the requirements for scientific objective 7:

Parameter	Altitude range, km	Δx, km	Δz, km	Accuracy	Experiment
E	100 to 500	200	20	1 mV/m	8, 11
NO	60 to 150	200	5	20 percent	13, 25
NO	[a]25 to 150	200	5	20 percent	13, 25
V_x	60 to 150	200	10	10 m/s	14
V_x	[b]80 to 150	500	20	20 m/s	14
O	100 to 200	500	10	10 percent	26
O_3	30 to 90	200	5	10 percent	12, 13
T	50 to 150	1000	5	10 K	14

[a] During polar-cap absorption event.
[b] During geomagnetic disturbances.

References

Gerard, Jean-Claude: Satellite Measurements of High-Altitude Twilight Mg^+ Emission. J. Geophys. Res., vol. 81, no. 1, pp. 83-87, Jan. 1, 1976.

Hanson, W. B.; and Sanatani, S.: Relationship Between Fe^+ Ions and Equatorial Spread F. J. Geophys. Res., vol. 76, no. 31, pp. 7761-7768, Nov. 1, 1971.

Hines, C. O.; and Halevy, I.: Reality and Nature of a Sun-Weather Correlation. Nature, vol. 258, no. 5533, pp. 313-314, Nov. 27, 1975.

Roberts, Walter Orr; and Olson, Roger H.: Geomagnetic Storms and Wintertime 300-mb Trough Development in the North Pacific-North America Area. J. Atmos. Sci., vol. 30, no. 1, pp. 135-140, Jan. 1973a.

Roberts, Walter Orr; and Olson, Roger H.: New Evidence for Effects of Variable Solar Corpuscular Emission on the Weather. Rev. Geophys. & Space Phys., vol. 11, no. 3, pp. 731-740, Aug. 1973b.

Shapiro, Ralph: Solar Magnetic Sector Structure and Terrestrial Atmospheric Vorticity. J. Atmos. Sci., vol. 33, no. 5, pp. 865-870, May 1976.

Shapley, A. H.; and Kroehl, H. W., eds.: Solar-Terrestrial Physics and Meteorology. STP Working Doc. III, Scientific Committee on Solar-Terrestrial Physics, Natl. Acad. Sci., May 1979.

Wilcox, John M.; Scherrer, Philip H.; Svalgaard, Leif; Roberts, Walter Orr; and Olson, Roger H.: Solar Magnetic Sector Structure: Relation to Circulation of the Earth's Atmosphere. Science, vol. 180, no. 4082, pp. 185-186, Apr. 13, 1973.

Wilcox, John M.; Scherrer, Philip H.; Svalgaard, Leif; Roberts, Walter Orr; Olson, Roger H.; and Jenne, Roy L.: Influence of Solar Magnetic Sector Structure on Terrestrial Atmospheric Vorticity. J. Atmos. Sci., vol. 31, no. 2, pp. 581-588, Mar. 1974.

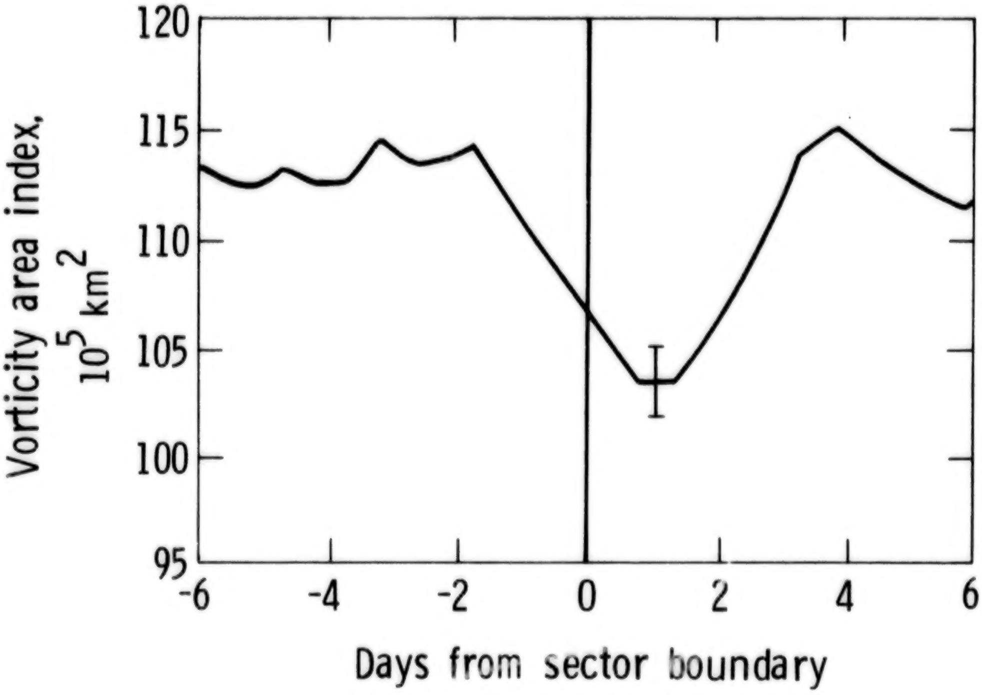

Figure 1.- Average response of vorticity area index to solar magnetic sector structure during winter period. Sector boundaries were carried past Earth by solar wind on day zero. (From Wilcox et al., 1974, courtesy American Meteorological Society)

CANDIDATE SHUTTLE LIDAR EXPERIMENTS

A set of representative experiments for a Shuttle atmospheric lidar system is described in this section. This set of experiment descriptions is intended to satisfy two objectives. The first objective is to set forth specific measurements that address the science objectives given in the preceding section, with each measurement documented in enough detail to establish its relative degree of feasibility, probable measurement accuracy, and particular contributions to the relevant science objective. The second objective is to establish a hardware envelope for the Shuttle lidar that will permit high-confidence operation for those measurements whose operation is well defined and will also provide the growth potential for the generations of lidar measurements whose techniques are still under development. In accordance with these objectives, a wide range of experiments has been included, from the simple and reliable experiments to those that are more complex and challenging.

Feasibility Rating

Because heavy emphasis was placed on obtaining a realistic assessment of space-borne lidar potential and because lidar is still an emerging technology whose techniques are changing rapidly, a rating system was developed to reflect both the degree of hardware complexity involved in an experiment and the degree to which the measurement concept has already been proven in field operation. This rating system is discussed here because the experiments are listed in order of decreasing feasibility.

Each experiment has been assigned a feasibility rating containing a numerical and an alphabetical descriptor. The numerical descriptor (indicating probability of success) has been determined primarily by the depth of prior hardware experience, and the alphabetical descriptor (indicating complexity) has been determined from the hardware complexity or size, which ultimately bears on the cost of the experiment. The experiment feasibility ratings are tabulated as follows:

Success probability:

1 High confidence: Field experience with actual hardware usually including aircraft flight experience; well-developed analytical techniques

2 Good confidence: Limited field experience with prototype hardware; straightforward development needed in experiment and/or analysis

3 Medium confidence: Demonstrated potential in laboratory; no field experience; no major anticipated obstacles although substantial development or proof-of-principle demonstrations needed

4 Uncertain: Scientifically worth attempting but measurement technique is still under investigation; success probability cannot yet be assessed

Complexity:

A Least complex, can be done with minimal hardware set

B Moderately complex, but does not stress Shuttle capability

C Complexity near full Shuttle capability, or requires pointing system

The set of experiments described here spans the complete range of feasibility. Some of the experiments can be carried out with a very high probability of success because they use flight-proven hardware which has a long history of lidar operation and does not stress the Shuttle capabilities. The class of experiments next in feasibility and ease of implementation uses less thoroughly demonstrated and more complex lidar hardware, such as the frequency-narrowed dye laser or a CW CO_2 lidar system with heterodyne detection, but can still be planned with confidence because of prior ground experience. These experiments will provide data of even greater scientific interest and applications utility. For some of these experiments, such as those involving UV, the measurement can only be made from space. Finally, where the technique is still under development, some experiments are included to indicate the kind of experiments that are likely to emerge as Shuttle lidar candidates during the next decade.

Experiment Evaluation

In order to assess the value of each experiment in the Shuttle lidar context, each experiment was evaluated in sufficient detail to make evident its probable performance and current level of development. These evaluations in their entirety are given in appendix A for each experiment and contain the following sections:

Description gives a brief overview of the experiment purpose and technique.

Implementation contains numerical values of the hardware parameters needed; determines the measurement accuracy obtainable with these parameters; gives limiting factors, unique features, and supporting evidence for experiment viability.

Feasibility provides rating and rationale for rating.

Needed Development defines critical areas which must be addressed before regarding the experiment as ready for Shuttle use.

Discussion presents the relation to science objectives, the uniqueness of a Shuttle lidar measurement, and particular correlative or supportive measurements needed.

One aim of the implementation section was to address the objective of defining a Shuttle lidar hardware envelope. The measurement accuracies were computed using simulation techniques that have proven accurate in describing the actual performance capabilities of existing ground-based and aircraft-borne lidar systems. Many of the simulations were based on a hardware set with the characteristics given in the following tabulation:

Laser:	
Nd:YAG	1 J/pulse; 10 Hz; 15 ns pulse; <0.1 nm line width; 5-percent amplitude stability
Nd derivatives (energy conversion efficiency listed as percent of Nd:YAG energy)	Nd×2, 30 percent; Nd×3, 10 percent; Nd×4, 6 percent; visible dye (D), 30 percent (0.1 nm) or 10 percent (5 pm); UV dye (D×2, frequency-doubled dye) 3 percent (0.1 nm) or 1 percent (5 pm)
CO_2	CW, 10 W output; line tunable; 1 MHz bandwidth Pulsed, 10 J/pulse at 15 Hz; 2 to 3 μs pulsewidth with transform-limited bandwidth
Receiver:	1 m diameter; useful from 0.2 to 12 μm; diffraction limited at 10 μm

Other simulations did not use the exact laser characteristics given in this standard hardware set, but in most cases they can be scaled to be compatible with the standard set. Experiments that require lidar capabilities beyond those given in the standard set have their additional requirements stated in the feasibility section. It should be emphasized that the standard hardware set served only as a starting point for Shuttle lidar design and was not optimized for an experiment or set of experiments. The actual Shuttle lidar hardware set will be based upon detailed analysis of the needs and scientific value of each of the experiments and upon the sequence of their implementation.

A secondary aim of the implementation section was to serve as a source document showing lidar capabilities in the various experiment areas. Simple scaling laws can be applied to the measurement accuracies to discover the result of performing the experiment with hardware parameters different from those assumed in the simulations.

Experiment Set

Tabulation

A condensed list of the set of lidar experiments is given in table I. This table shows some of the pertinent details for each experiment, as well as giving a cross-reference to the science objectives addressed by each experiment.

Description

Detailed descriptions of the 26 Shuttle lidar experiments are given in appendix A. A brief description of each experiment follows.

Experiment 1: Cloud-top heights.- Measure cloud top heights with lidar while co-aligned passive sensors view the same area. Use lidar data to improve passive analysis techniques. Accurate measurements of cloud heights are needed to assign heights to cloud-motion vectors and to determine emissivities and radiation balance.

Experiment 2: Tropospheric clouds and aerosols.- Measure the presence, geometrical profiles, and backscattering of thin clouds and aerosols. Convert to optical thickness using models and 2λ backscatter information. Co-aligned Earth radiation budget sensor would measure flux and albedo changes; co-aligned passive temperature and humidity sensors would allow assessment of cloud and aerosol effects on passive profilers. Data would document the locations and extent of aerosol effects and clouds and permit correlation with radiation changes detected by passive sensors. This information is essential for verifying the ability of satellite-borne sensors to monitor aerosol-induced albedo changes. The existence of pollution and dust clouds (e.g., Saharan dust) over large areas could be monitored and mapped.

Experiment 3: Cirrus ice/water discrimination.- Two polarization components of the backscattered signal (for a linearly polarized transmitted signal) from cloud layers are used to discriminate between spherical water droplets and ice crystals in cirrus clouds. These measurements will be very useful in ascertaining the radiative transfer characteristics of cirrus clouds. The presence of ice-crystal layers admixed with water-droplet layers can lead to large errors in the interpretation of current passive radiometric measurements.

Experiment 4: Profiles of noctilucent clouds, circumpolar particulate layers, and mesospheric particulates.- Determine presence, structure, and density of noctilucent clouds and particulate layers near the Summer mesopause by elastic (Mie) backscatter to evaluate radiative effects of the layers and use them as tracers of atmospheric dynamics.

Experiment 5: Surface reflectance measurements.- Measure surface reflectance at several wavelengths while Earth radiation budget sensors view the same area. This experiment could be coupled with others such as 1, 2, and 6, deriving surface reflectance from surface-return signal and attenuation corrections. In appendix A this experiment has been incorporated into experiment 2.

Experiment 6: Stratospheric aerosol backscatter profiles.- Measurement of stratospheric aerosol from orbital altitudes using particulate backscattering at wavelengths of 530 nm and 1060 nm in order to obtain global-scale information on their distribution. These data are important because of their potential effect on the Earth's climate and environment and on passive O_3 measurements.

Experiment 7: Alkali-atom density profiles.- Determine altitude profiles of the free sodium atoms in the layer from 80 to 110 km by observation of sodium resonance fluorescence excited by a pulsed tunable dye laser. Spatial variations in these profiles provide information about circulation, wave motions, and diffusion characteristics in the upper atmosphere. Lithium and potassium profiles can be determined with the same technique.

Experiment 8: Ionospheric metal ion distributions.- Use laser resonant scattering to obtain altitude profiles of Mg^+ density from 80 to 500 km to study ionospheric irregularities (which affect communications systems), lower thermospheric neutral wind patterns, and general ionospheric circulation patterns. The technique can also be applied to measurements of ambient Fe^+ and Ca^+.

Experiment 9: Water-vapor profiles.- Measure water-vapor profiles in the troposphere using the 720 or 820 nm bands of H_2O, or in the region of the tropopause and lower stratosphere using the 940 nm band, with a differential absorption technique (DIAL). Demonstrate that lidar can meet accuracy and resolution requirements for GARP and NASA climate plan and can assess H_2O profiles and transport over large land and sea areas for which evaporation is important. Water-vapor total burden can be obtained using ground reflection.

Experiment 10: Atmospheric species measurements using CW/IR laser ground and cloud returns.- Measure concentrations of a variety of species such as O_3, H_2O, NH_3, the CFM's, CCl_4, C_2H_4, and C_2H_3Cl using CO_2 lasers; or CH_4, CO_2, N_2O, CO, and HCl with other IR lasers (doubled CO_2, CO, etc.). Species total burdens in the troposphere and stratosphere and species profiles with 3 to 4 km vertical resolution would be obtained using reflection from the Earth's surface and from clouds. The experiment offers a large potential for growth in atmospheric species measurements since the infrared is richer in molecular absorption spectra than the UV or visible. This approach would address a variety of needs in species transport, source and sink studies, meteorology, and environmental quality.

Experiment 11: Chemical release diagnosis.- Use laser resonant scattering to measure motion, internal structure, and dissipation of artificial chemical releases (e.g., Na, Ba, and Ba^+) for diagnosis of ionospheric fields and dynamics.

Experiment 12: Stratospheric ozone concentration profiles.- Measurement of stratospheric ozone concentration between 15 and 50 km using differential range absorption techniques at UV wavelengths in order to provide global-scale information on ozone vertical distribution. Data address a number of science objectives in the climate and environmental areas.

Experiment 13: Upper atmospheric trace species measurements using two-satellite occultation.- Trace species having absorption bands in the 3.5 to 15.0 μm region are measured with high accuracy, day or night, by direct absorption of IR laser radiation transmitted between two satellites. Typical species include O_3, ClO, $ClONO_2$, H_2O, H_2O_2, the CFM's, C_2H_3Cl, C_2H_4, CCl_4, HNO_3, NH_3, etc. Use of a retroreflector or detection system on the "passive" satellite allows highly sensitive measurements over long path lengths. Such measurements are important in providing data for evaluating stratospheric/mesospheric models and in studying the coupling of dynamical, chemical, and radiative processes. Laser power requirements are low since a cooperative target is used, and a variety of tunable lasers may eventually be used to reach nearly all desired species.

Experiment 14: Sodium-layer temperature and winds.- Doppler sensitive detection of the resonance backscattered signal from the Na layer near 90 km to determine the altitude distribution of sodium, its temperature, and winds in the sodium layer. Nighttime and daytime measurements will provide information concerning the dynamics of an important region of the atmosphere about which little is known.

Experiment 15: Surface pressure and cloud-top pressure and height measurements.- Accurate measurement of atmospheric pressure at the Earth's surface and of pressure and altitude at cloud tops using surface and cloud returns of laser radiation tuned to the O_2 A-band absorption lines. Surface pressure is a fundamental meteorological variable needed in weather forecasting and in general circulation models. Cloud-top pressure can also be used similarly.

Experiment 16: Vertical profiles of atmospheric pressure.- Height-resolved tropospheric pressure profiles will be measured using a differential absorption method employing larger spatial resolution elements than in experiment 15. The emphasis in Shuttle measurements will be on testing and refining the technique for ultimate operational use. The pressure profile is a basic meteorological quantity needed both in weather forecasting and in general circulation modeling.

Experiment 17: Temperature profile.- Measure the (height-resolved) temperature profile in the troposphere or in the region of the tropopause with a DIAL technique. Demonstrate that lidar can meet the accuracy and vertical resolution requirements on temperature profile measurements for the NASA climate program and GARP and for stratosphere or troposphere exchange studies.

Experiment 18: Altitude distribution of atmospheric constituents using IR DIAL - Tropospheric profiles of gases such as O_3, H_2O, NH_3, and C_2H_4, and stratospheric O_3 profiles, will be measured using differential absorption lidar (DIAL) based on scattering of CO_2 laser radiation pulses by atmospheric aerosols. Heterodyne detection provides high-detection sensitivity to the scattered light and relative insensitivity to daylight background. Knowledge of the altitude distribution of O_3 will help define the roles of downward diffusion from the stratosphere and ground-level sources and sinks. Weather forecasting can benefit from information on the vertical distribution of H_2O vapor.

Experiment 19: Cloud-top winds.- Measure the wind at the top of clouds, during the day and at night, with an uncertainty in the measurement of ±2 m/s by Doppler sensitive detection of cloud-top returns. Both incoherent detection of Nd laser radiation and coherent detection of CO_2 laser radiation are considered. These measurements are important in determining wind components in the tropics and other latitudes which cannot be derived from the temperature field.

Experiment 20: Aerosol winds.- Measure the height-resolved wind profile between ground and 30 km altitude by Doppler sensitive detection of molecular and aerosol-scattered returns at either Nd or CO_2 laser wavelengths. This experiment will provide the wind field with unambiguous altitude resolution and global coverage. These measurements will be important for the study of general atmospheric circulation and tropospheric-stratospheric interaction.

Experiment 21: OH density profile between 35 and 100 km altitude.- Determine the density of OH in the upper atmosphere by observing remote fluorescence from OH excited by a tuned laser with wavelength in the range 280 to 310 nm. Because OH is involved in many key chemical reactions and undergoes a strong diurnal variation, the measurements will lead to improved chemistry/transport models of the upper atmosphere. The OH measurements will also be useful for remote sounding of pressure and temperature, given improvements over present UV laser power.

Experiment 22: Simultaneous measurement of metallic atom, ion, and oxide profiles.- Use multiwavelength resonant scattering to obtain simultaneous altitude profiles of Mg, Mg^+, and MgO densities to provide information on the gross features of upper and lower thermospheric circulation.

Experiment 23: Tropospheric NO_2 concentration profile.- Measure tropospheric NO_2 density between 0 and 4 km and total NO_2 column using DIAL techniques in the 450 nm spectral region. The total burden measurement assumes scattering from the ground. These data are particularly important in ozone chemistry.

Experiment 24: Stratospheric aerosol composition.- Identify the chemical composition of stratospheric aerosols using pattern-recognition techniques with multiwavelength (infrared) aerosol backscattering (DISC differential scattering). This information would be important for determination of the climatic and environmental effects of stratospheric aerosols.

Experiment 25: NO density profiles between 70 and 150 km altitude.- Altitude profiles of NO will be measured by resonance scattering or fluorescence, using a tunable laser which is frequency-doubled into the NO γ-bands or suitable excimer lasers that may be developed in the future. Demonstration on the Shuttle is important for development of global monitoring of NO. The D-region of the ionosphere between 70 and 100 km altitude is formed largely through the ionization of NO by solar Lyman-α radiation. The abundance of NO and its transport at higher and lower altitudes are fundamental questions in the physics and chemistry of the atmosphere.

Experiment 26: Abundance and vertical profiles of atomic oxygen.- Altitude profiles of O will be measured by two-photon fluorescence spectroscopy, using very short pulses of tunable radiation at 225.6 nm. Knowing the distribution of atomic oxygen in the mesosphere and lower thermosphere is essential for understanding the photochemistry of oxygen and water and the transport processes occurring in the transition from turbulent mixing to diffusive separation. Development and testing of a two-photon method for measuring O from the Space Shuttle is an important step toward global measurements of species for which standard UV fluorescence techniques will not be applicable due to short range extinction.

Results

A comparison of the expected measurement accuracies with the needs given in the science objectives shows that lidar is indeed a useful remote-sensing tool in space. All of these experiments will provide a valuable data set in their own right during a 7 to 30 day sortie mission. In some cases, the data set will also increase the utility of ongoing free-flyer passive observations of similar phenomena, either by providing truth data or by revealing the extent of spatial fluctuations that may restrict the use of the passive data. For experiments such as pressure, temperature, and wind measurements, the Shuttle lidar observations will serve as the proof-of-principle demonstration needed before proceeding to a free-flyer meteorological monitoring system.

A comparison of the hardware requirements for successful Shuttle operation with the current state of the art in lasers, detectors, and telescopes shows that lidar is currently ready for Shuttle deployment. No high-risk engineering is required for implementation of at least the high-feasibility experiments. These high-feasibility experiments will in turn pave the way for more complex - but potentially more valuable - experiments, as shown in the following section on evolutionary lidar development.

TABLE I.- CANDIDATE EXPERIMENTS

Number	Feasibility	Description	Altitude region, km	Principle	Laser	Scientific objectives[a]
1	1A	Cloud-top heights	0 to 15	Elastic backscatter	Any	3, 4
2	1A	Profiling of tropospheric clouds and aerosols	0 to 15	Elastic backscatter	Any (0.5 to 2μm)	1, 3, 4
3	1B	Cirrus ice/water discrimination	5 to 15	Polarization sensitive elastic backscatter	Any	1, 3
4	1B	Profiles of noctilucent clouds and circumpolar particulate layers	60 to 80	Elastic backscatter	Any (0.5 to 2μm)	3, 5
5	1A	Surface reflectance	Ground	Surface scatter	Any	3
6	1B	Stratospheric aerosol backscatter profiles	10 to 50	Elastic backscatter	Any (0.5 to 2μm)	1, 2, 3
7	2B	Alkali-atom density profiles	80 to 120	Resonant scatter	Tuned dye	5, 6
8	2B	Ionospheric metal ion distributions	80 to 600	Resonant scatter	Tuned dye	6, 7
9	2B	Water-vapor profiles	0 to 20	DIAL	Tuned dye	1, 3, 4, 5
10	2B	Atmospheric species measurements using CW/IR laser ground and cloud returns	0 to 30	Long path absorption (column content)	Line tunable CW CO_2	1, 3, 4
11	2B	Chemical release diagnosis	90 to 50 000	Resonant scatter	Tuned dye	7
12	2B	Stratospheric ozone concentration profiles	20 to 60	Differential range absorption	Nd×4, and/or dye	1, 2, 3, 7
13	2C	Upper atmospheric trace species measurements using two-satellite occultation	10 to 50	Long path absorption	Tunable, mainly IR	2, 3, 7
14	3B	Sodium-layer temperature and winds	80 to 110	Doppler sensitive resonant scatter	Tuned dye	5, 6, 7
15	3B	Surface pressure and cloud-top pressure and height measurements	0 to 10	O_2 absorption (column content)	Tuned dye	4
16	3C	Vertical profiles of atmospheric pressure	0 to 10	O_2 absorption (range resolved)	Tuned dye	4
17	3C	Temperature profile	0 to 10	Temperature sensitive O_2 absorption	Tuned dye	1, 2, 3, 4
18	3B	Altitude distribution of atmospheric constituents using IR DIAL	0 to 15	DIAL	Line tunable pulsed CO_2	1, 3, 4
19	3C	Cloud-top winds	0 to 15	Doppler sensitive elastic backscatter	Any narrowband	1, 2, 4
20	3C	Aerosol winds	0 to 25	Doppler sensitive elastic backscatter	Any narrowband	1, 2, 4, 5
21	3C	OH density profile between 35 and 100 km altitude	35 to 100	Resonance fluorescence	Tuned dye	2, 5
22	3C	Simultaneous measurement of metallic atom, ion, and oxide profiles	80 to 600	Resonant scatter	Tuned dye	6
23	3C	Tropospheric NO_2 concentration profile and total burden of NO_2	0 to 15	DIAL	Tuned dye	1
24	4	Stratospheric aerosol composition	15 to 30	Differential scattering (DISC	Line tunable pulsed CO_2	1, 3
25	4	NO density profiles between 70 and 150 km altitude	70 to 150	Resonance fluorescence	Tuned dye	2, 7
26	4	Abundance and vertical profiles of atomic oxygen	80 to 500	Two-photon fluorescence	Tuned dye	6, 7

[a] Objective numbers denote the following:
1 Global flow of water vapor and pollutants
2 Stratospheric and mesospheric chemistry and transport
3 Radiative models
4 Meteorological data
5 Upper atmospheric waves
6 Thermospheric chemistry and transport
7 Magnetospheric Sun and weather relationships.

CONTENTS

Page

PREFACE . . . . iii 1/A5

INTRODUCTION 1 1/A8

SCIENTIFIC INVESTIGATIONS WITH SHUTTLE LIDAR 4 1/A11
  RATIONALE FOR LIDAR ON SPACE SHUTTLE 4 1/A11
  SCIENTIFIC OBJECTIVES 7 1/A14
    Introduction 7 1/A14
    Scientific Objective 1: Global Flow of Water Vapor and Pollutants 10 1/B3
    Scientific Objective 2: Stratospheric and Mesospheric Chemistry and Transport 24 1/C3
    Scientific Objective 3: Radiative Models 34 1/C13
    Scientific Objective 4: Meteorological Data 46 1/D12
    Scientific Objective 5: Upper Atmospheric Waves 58 1/E12
    Scientific Objective 6: Thermospheric Chemistry and Transport . . . 67 1/F7
    Scientific Objective 7: Magnetospheric Sun and Weather Relationships 74 1/F14
  CANDIDATE SHUTTLE LIDAR EXPERIMENTS 80 1/G6

SHUTTLE ATMOSPHERIC LIDAR PROGRAM EVOLUTION 89 2/A2

APPENDIX A - DESCRIPTIONS OF SHUTTLE BORNE LIDAR EXPERIMENTS 95 2/A8

APPENDIX B - LASERS OF POTENTIAL USE FOR SHUTTLE LIDAR 163 2/F7

APPENDIX C - TRANSMITTING AND RECEIVING OPTICS CONSIDERATIONS 175 2/G5

APPENDIX D - SPECTRAL DISCRIMINATORS AND DETECTORS FOR SHUTTLE LIDAR 193 3/A14

APPENDIX E - GLOSSARY 219 3/C13

SHUTTLE ATMOSPHERIC LIDAR PROGRAM EVOLUTION

The laser-radar technique has an inherent flexibility that allows a limited set of hardware components to perform measurements which involve a wide height range in the atmosphere and contribute to a diverse set of disciplines. It is apparent that many of the specific lidar measurements of interest in the late 1980's cannot be foreseen now. Furthermore, the laser and detector technology upon which the lidar program can draw is evolving quite rapidly; members of the lidar working group have seen new laser sources emerge even during the course of their deliberations. Accordingly, it is felt that the hardware approach to a Shuttle lidar system should incorporate (1) a building block, or modular, approach where the individual lidar components are readily interchangeable and can be replaced as appropriate to changing measurement needs and technology developments and (2) an evolutionary approach where the initial hardware complement for the simplest early experiments will be augmented by subsequent hardware additions to expand the lidar capability for more complex and more technologically demanding experiments. This section sets forth the considerations which led to the modular, evolutionary Shuttle lidar approach. It also describes a model set of hardware and the evolutionary development of a capability for performing most of the experiments described in appendix A.

MODULAR LIDAR APPROACH

The principal consideration leading to a modular lidar approach is that a lidar can quite naturally be divided into distinct components linked by well-defined and easily describable interfaces. These components are: the laser transmitter, the telescopic return-signal collector, the detector, and data-processing electronics.

The telescopic light collector is physically the largest of the components (for the one-meter class telescope being considered here) and has the most demanding physical tolerances. Since the telescope can be made in an all-reflective configuration capable of handling the complete range of interesting wavelengths, from 0.2 to 10 μm, it is appropriate to consider the telescope as the basic building block around which the other components can be attached. The output of the telescope can be configured to accommodate several detectors, either simultaneously through beam splitters or sequentially through beam switching optics.

The lasers needed for the measurements described herein fall into two classes (1) visible/near-visible lasers based on an Nd laser as the primary source and (2) CO_2 lasers. For the Nd-based lasers, the output beam can be directed to the lidar target through an auxiliary set of transmit optics. The CO_2 lasers will most likely be operated in a heterodyne configuration for maximum sensitivity with the lidar transmitter and receiver beams sharing the same set of large-aperture main-telescope optics. In either case, the interface between the laser and collector can be designed to accommodate a wide range of laser variants.

The detectors in the visible and near visible are mainly of the photometric type, where a change of photomultiplier and prefilter, leaving the detector optics and housing unchanged, is all that might be necessary to change from one wavelength to another. Special-purpose visible detectors, such as the sodium absorption cell for mesopause temperature measurements and the Fabry-Perot detector for wind and temperature measurements, can be designed to use the same telescope optical output configuration as the photometric type of detector. For the CO_2 laser experiments, the heterodyne detectors will most probably be built into the laser itself, with the laser and detector sharing the telescope optics through a special port.

The data-acquisition electronics for all of the photometric detectors are basically similar, having parallel analog-to-digital current mode and photon-counting mode capabilities to handle the wide dynamic range of a lidar return signal. Most of the measurements described herein require such a capability, often for two or more wavelengths simultaneously. The special-purpose detectors, visible Fabry-Perot and heterodyne, have their own data-processing requirements but eventually produce a serial data string for each lidar pulse that must be entered into the data-recording medium. The data volume varies from one experiment to the next, but a general-purpose processor can be designed that will handle all the different types of experiments.

The modular approach permits a flexible assembly of hardware for any given mission, because only those laser and detector components needed for a particular set of measurements need be attached to the receiver. Such a flexibility can result in considerable weight, power, and integration cost savings in the lidar payload for each individual mission.

EVOLUTIONARY LIDAR APPROACH

The principal consideration leading to an evolutionary approach to the Shuttle lidar design is that a very simple set of hardware can be used for the early measurements and then be supplemented with additional components to provide a capability for the more complex measurements. Such a design approach also provides a capability for incorporating advances in laser and detector technology into the lidar program. These advances might provide an improved capability for existing measurements or may extend the lidar capability into new areas.

A good example of this progressive hardware implementation is with the Nd laser and its derivatives. A basic Nd laser source with a photometric detector will provide valuable data on atmospheric clouds and aerosols. The capabilities of that laser can then be augmented by adding crystal doublers, triplers, and quadruplers to the beam path providing a wavelength set for more detailed aerosol data and data on high-altitude ozone distributions. The doubled, tripled, or quadrupled output can then be used to pump a tunable dye laser for most of the resonant-scatter and differential-absorption measurements listed herein.

An especially attractive feature of the evolutionary approach is that the set of hardware needed for the more complex measurements can be tested during a mission devoted primarily to acquiring a data set for a simpler experiment. For example, the tunable dye laser to be used for sodium-layer measurements can be flown on a mission whose primary objective is acquiring two-color (Nd and doubled Nd) aerosol data, with the dye laser performance being tested in the space environment during a small fraction of the lidar operational time. If the dye laser does not perform as well as expected, changes can then be made before a flight dedicated to sodium-layer data acquisition. Furthermore, if the dye laser hardware fails during a future sodium-layer mission, the fall-back position of acquiring aerosol data is readily available. Such an approach also means that operational experience can be gained while useful data are being acquired with a simple set of hardware, before the more complex hardware is used.

Another evolutionary process involves the CO_2 lasers and other infrared lasers for the detection of particular chemical species in the atmosphere. Continuous CO_2 lasers may be used initially for the detection of ozone and water vapor, with some height resolution, on a global basis; and with this capability will come the ability to detect other trace species such as the chlorofluoromethanes, hydrocarbons, nitric acid, etc., which are within the tuning range of CO_2 lasers. With the advancement of pulsed CO_2 lasers will come the capability to provide much better vertical resolution for species detection. Further developments of tunable lasers in other wavelength regions, which may involve CO_2 lasers as pump sources, will result in the capability to monitor a wide range of atmospheric species of interest.

When the complete set of lidar hardware is available, mission planners will have a great deal of flexibility in scheduling lidar operational time for quick-reaction response to sporadic geophysical events, such as volcanic eruptions which inject a cloud of aerosols into the stratosphere.

An especially complex consideration in the lidar-development schedule revolves around the question of when and how to include a flexible pointing capability in the hardware complement. While most of the lidar measurements can be performed with the system strapped down to the orbiter, it will eventually be desirable to have a fully steerable system. Vector wind measurements, chemical release tracking, and long-path-absorption limb measurements using a subsatellite retroreflector are some of the measurements needing various degrees of pointing capability. The lidar can be designed for hardware compatibility with the instrument pointing devices under consideration for Shuttle use.

EVOLUTIONARY FLOW

A model for the possible evolutionary flow of lidar experiments has been constructed to illustrate the evolution of a Shuttle lidar program. It should be emphasized that this model is intended only as a guide to the process and not as a measure of what the ultimate lidar scenario should be. A number of the assumptions used in deriving this model are listed as follows:

> The choice of experiment on any mission would be guided by scientific value to the mission and by probability of success with increasing emphasis on the former as the program matures.

A schedule of equipment and experiments would be sought such that each experiment would add capability to the overall system by building upon the equipment and techniques proven in previous experiments.

Experiments involving the more sophisticated wavelength-shifting devices would be tested in flight before becoming primary objectives.

The lidar system would include primary laser sources, several derivative devices for wavelength shifting (doubling crystal, dye laser, etc.), a large receiver telescope, and several detector packages.

The first laser modules would be

Nd	1 joule per pulse and 10 pps at 1.06 μm; twice diffraction limit; capability for doubling (30-percent conversion of 1.06 μm energy), tripling (10-percent conversion of 1.06 μm energy), and quadrupling (6-percent conversion of 1.06 μm energy); provision for narrowing 1.06 μm output to 0.1 pm (not necessarily implemented in initial stages)
Dye	Nd pumped; goal of 1 pm line width at 600 nm with 25-percent conversion efficiency of 530 nm pump energy; dye doubling (20-percent conversion of dye energy)
CO_2(1)	CW lasers with 10 W output each; 1 MHz bandwidth and stability for heterodyne detection
CO_2(2)	Pulsed laser; 10 J at 15 pps; transform-limited spectral width at 2 to 3 μs pulse length

The telescope would have a 1 m diameter primary, all reflecting optics useful from 0.2 to 12 μm, diffraction-limited operation at 10.6 μm, and would be rigidly attached to the Shuttle platform for initial experiments.

Table I shows a sample sequence of experiments based on the Nd laser, with the lidar capabilities evolving from Nd and doubled Nd measurements of atmospheric particles and albedo to the short wavelength (200 to 225 nm) measurements of NO and O atoms. Table II presents a similar flow for experiments using CO_2 lasers as they might evolve from CW experiments involving tropospheric species or from measurements of upper atmospheric minor species (using two-satellite occultation) to wind and DIAL species-profile measurements using high-energy pulsed CO_2 lasers.

TABLE I.- SAMPLE EXPERIMENT FLOW FOR Nd SYSTEMS

Experiment	Measurement	Laser	Comment
1 to 6	Atmospheric particles, reflectivity	Nd, Nd×2, Nd×3	
12	Stratospheric O_3 profiles	Nd×4, Nd×2→D×2	
7	Na profile	Nd×2→D (≈1 to 5 pm)	
14	Na profile, T	Nd×2→D (5 pm)	(a)
11	Chemical release (without pointing)	Nd×2→D (1 to 5 pm)	(b)
8, 21	Mg^+ and OH profiles	Nd×2→D×2 (0.5 pm)	
14	High altitude T and winds - Na	Nd×2→D (5 pm)	(c)
19, 20	Winds - troposphere/low stratosphere	Nd (0.1 pm)	(c), (d)
9, 15 to 17	Tropospheric H_2O, T, and pressure (surface pressure and profiles)	Nd×2→D (3 pm), 2 wavelength	
23	Tropospheric NO_2 burden and profile	Nd×3→D, 2 wavelength	
9	H_2O profile into lower stratosphere	Nd×2→D (≦1 pm), 2 wavelength	
22	$Mg/Mg^+/MgO$	Nd×2→D×2 (0.5 pm), multiwavelength	
25	Upper atmospheric NO profile	Nd×3→D×2 (0.5 pm)	(e)
26	Upper atmospheric O atom profile	Nd×3→D×2 (0.5 pm) or excimer	(f)

[a] Requires absorption cell or multispectral detection.

[b] Capability would exist, but coordination with release required.

[c] Requires pointing information accurate to 1 arc min.

[d] Depends upon successful Nd line-narrowing.

[e] Capability would exist but would be greatly enhanced by excimer laser.

[f] Same as (e) with addition of mode-locking capability.

TABLE II.- SAMPLE EXPERIMENT FLOW FOR CO_2 SYSTEMS

Experiment	Measurement	Laser	Comment
10	Trace species in troposphere and lower stratosphere (total burdens, rough altitude profiles)	CW CO_2	(a)
13	Trace species profiles in stratosphere and mesosphere	CW CO_2	(b)
1, 2, 18	Atmospheric particles; trace species profiles in troposphere and lower stratosphere (DIAL)	Pulsed CO_2	
19, 20	Winds - troposphere and lower stratosphere	Pulsed CO_2	(c)
24	Stratospheric aerosol composition	Pulsed CO_2	

[a] Altitude profiling requires multiple wavelengths or spectral tuning.

[b] Capability exists, but a subsatellite and pointing (≈2 → 10 μrad accuracy) are required.

[c] Requires pointing information accurate to 100 μrad.

APPENDIX A

DESCRIPTIONS OF SHUTTLE BORNE LIDAR EXPERIMENTS

Appendix A outlines each of the 26 candidate Shuttle borne lidar experiments.

Experiment 1: Cloud-Top Heights

Description.- Measure cloud-top heights with lidar while co-aligned passive sensors view the same area. Accurate measurements of cloud heights are needed to assign heights to cloud-motion vectors and to determine emissivities and radiation balance.

Implementation.- Standard Nd:YAG laser doubled to 530 nm with 2 mrad FOV, 0.5 nm FWHM filter, 20-percent quantum efficiency (QE) PMT detector, night or day operation. Cloud occurrence is detected by increase of lidar return above the ambient signal, and cloud-top height must be defined in terms of some predetermined threshold value of intensity level. Very dilute and diffuse cloud boundaries will have locations that depend to some extent on the criteria employed and the nature of the signal processing involved.

Figure A1 shows expected single-shot measurement errors for a range of cloud densities and heights, using 150 m range bins. In the vertical scale label, N_B and N_S are the numbers of background and signal photoelectrons at the detector. The night curves assume N_B for moonlit cloud (worst case, 6.1×10^5 photons/s); the day curves assume sunlit cloud (5.2×10^{11} photons/s). The figure can be used to judge cloud detectability in the following manner: We will say that a cloud is detectable when its return signal C exceeds that of the nearby clear air A (in the same profile) by the combined, 3σ, measurement errors. Hence, all clouds for which $C - A \geq 3(\sigma_C{}^2 + \sigma_A{}^2)^{1/2}$ are detectable. The arrows at the bottom of the figure show the result of solving this equation for these minimum detectable cloud strengths as a function of height and background light.

Using the top scale of figure A1, it can be seen that, for all heights, all visible clouds are detectable by night or day. (The distinction between visible and subvisible clouds is approximate, but it is based on numerous comparisons of human, satellite, and lidar observations made in the tropics and midlatitudes.)

Feasibility.- 1A. This rating is based on the availability of a large amount of experimental field data and the existence of good computation models. Hardware and techniques are well advanced, and confidence for success is very high.

Needed development.- No significant development needed. Criteria must be established for uniquely defining the cloud-top heights, particularly for diffuse clouds and for spatially inhomogeneous situations.

Discussion.- Lidar experiment 1 addresses scientific objectives 3 and 4 and is useful as a stand-alone system providing new data with very high spatial resolution ($\Delta Z = 150$ m; $\Delta X = 150$ m). It has the capability to measure clouds night and day and well down into the subvisual regime. It can be used with passive sensors such as radiometers and stereographic cameras to improve their capabilities for cloud-height determination and radiation balance analysis.

Bibliography

Davis, Paul A.: Applications of an Airborne Ruby Lidar During a BOMEX Program of Cirrus Observations. J. Appl. Meteorol., vol. 10, no. 6, pp. 1314-1323, Dec. 1971.

Evans, William E.: Remote Probing of High Cloud Cover via Satellite-Borne Lidar. Final Report. NASA CR-96893, 1968.

Platt, C. M. R.: Lidar and Radiometric Observations of Cirrus Clouds. J. Atmos. Sci., vol. 30, no. 6, pp. 1191-1204, Sept. 1973.

Schneider, Stephen H.: Cloudiness as a Global Climatic Feedback Mechanism: The Effects on the Radiation Balance and Surface Temperature of Variations in Cloudiness. J. Atmos. Sci., vol. 29, no. 8, pp. 1413-1422, Nov. 1972.

Viezee, W.; Endlich, R. M.; and Serebreny, S. M.: Satellite-Viewed Jet Stream Clouds in Relation to the Observed Wind Field. J. Appl. Meteorol., vol. 6, no. 5, pp. 929-935, Oct. 1967.

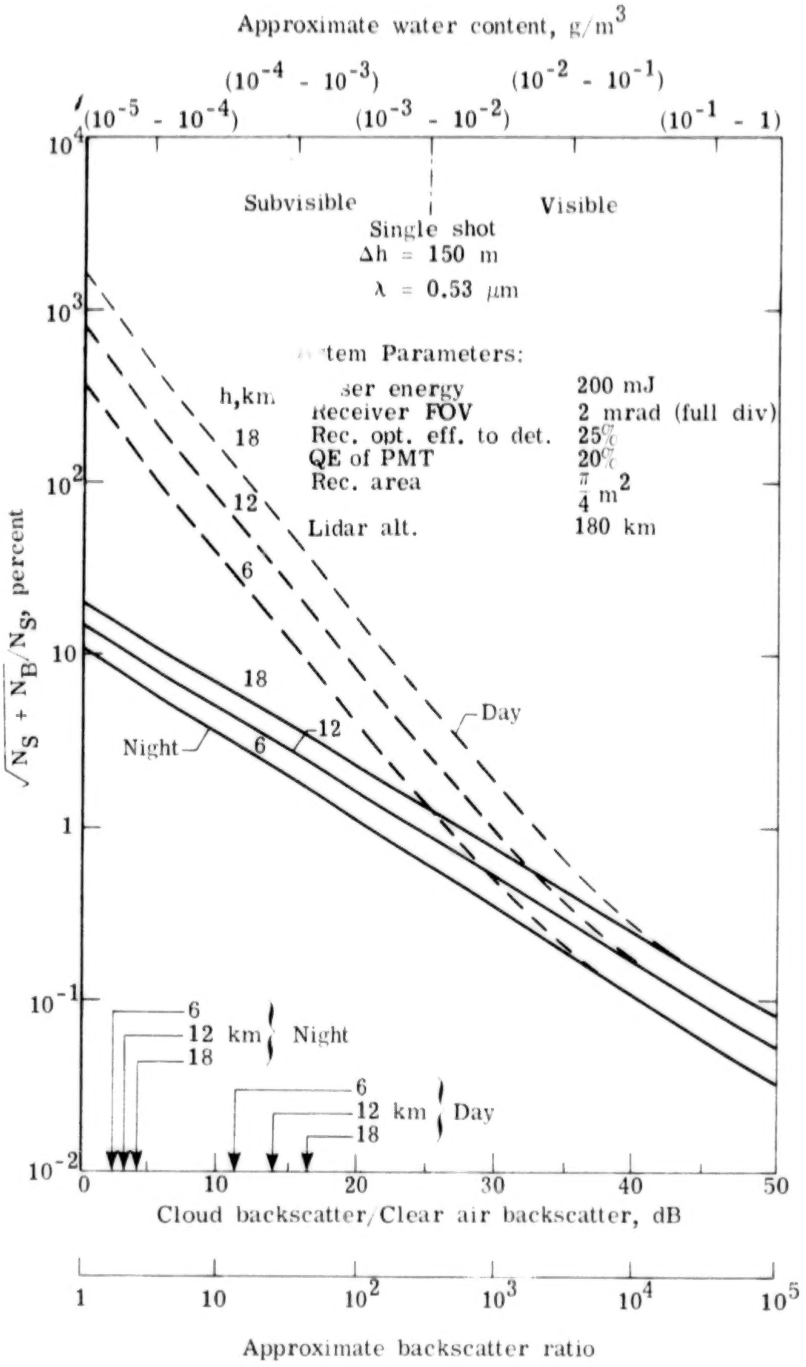

Figure A1.- Expected measurement errors for cloud density and height.

Experiment 2: Tropospheric Clouds and Aerosols and Surface Reflectance

Description.- Measure the presence, geometrical profiles, and backscattering of thin clouds and aerosols. Convert to optical thickness using models and 2λ backscatter information. Infer surface reflectance from surface return signal and attenuation corrections. Co-aligned Earth radiation budget sensor would measure flux and albedo changes; co-aligned passive temperature and humidity sensors would allow assessment of cloud and aerosol effects on passive profilers. Data would document the locations and extent of aerosols and clouds and permit correlation with radiation changes detected by passive sensors. This information is essential for verifying the ability of satellite-borne sensors to monitor aerosol-induced albedo changes. The existence of pollution and dust clouds (e.g., Saharan dust) over large areas could be monitored and mapped.

Implementation.- Standard Nd:YAG lidar operating at both 530 nm and 1060 nm with 2 mrad FOV, 2 PMT detectors (20-percent QE at 530 nm; 2-percent QE at 1060 nm). Third harmonic at 350 nm would also be useful though not essential. Night or day operation. Data system capable of generating spatial profile or return with height resolution of about 150 m. Some simulations are available and sample results are shown in figure A2 (lidar at 180 km, 0.1 J, Rayleigh atmosphere only) for expected single-shot errors. Simulations under development to include tropospheric aerosols, higher laser energy and multishot averaging show greatly improved signal to noise. System will be limited by signal levels for very low-density aerosols and clouds, and signal measurement errors will be a limiting factor. Achieving ±20-percent accuracy in conversion to optical thickness will be difficult a priori but will be aided by 2λ backscattering measurements. Since aerosol optical thickness is very poorly known at most global sites, and since this is a fundamental parameter in aerosol radiative models, even this limited accuracy will be very useful in many applications.

Feasibility.- 1A (530 nm), 1B (1060 nm). Experiment design information is available, and a moderate amount of ground-based field data is available in the visible region of the spectrum. The requirement for good range resolution at very low-signal levels increases the difficulty.

Discussion.- This experiment addresses scientific objectives 1, 3, and 4. At present, no other spaceborne system exists for measuring the full spatial distribution of subvisual tropospheric clouds and aerosols. Such data are vital for a more quantitative understanding of the radiation budget and of the operation of currently used passive sensors. In addition, monitoring the motions of the aerosols and clouds provides information on atmospheric transport and mixing processes.

Aerosols and thin clouds are currently being measured from space by three passive methods: (1) thermal emission from the atmospheric limb, (2) intensity and polarization of scattered solar radiation, and (3) solar occultation measurement of atmospheric extinction in the limb viewing orientation. These techniques offer less spatial resolution in both vertical and horizontal directions compared to the lidar. In addition, the limb viewing mode restricts the observation times and conditions. This is especially true in the troposphere where the limb viewing mode is usually blocked by clouds. Lidar offers capability not only for wide coverage in space and time but also the ability to probe between thick clouds and quantitatively measure subvisible aerosol and cloud features. The range resolution capability of lidar will also permit use of the ground return signal to obtain additional information on atmospheric extinction and surface reflectance characteristics.

Bibliography

Chahine, Moustafa T.: Remote Sounding of Cloudy Atmospheres. I. The Single Cloud Layer. J. Atmos. Sci., vol. 31, no. 1, pp. 233-243, Jan. 1974.

Halem, Milton; and Chow, Ming-Dah: Sounder Design Considerations in the Selection of Temperature Sensing Channels. J. Appl. Meteorol., vol. 15, no. 4, pp. 394-401, Apr. 1976.

Johnson, W. B.; and Uthe, E. E.: Lidar Observations of the Lower Troposphere During BOMEX. AT(04-3)-115, Stanford Res. Inst., Dec. 1969. (Available from NTIS.)

Pollack, James B.; Toon, Owen B.; Sagan, Carl; Summers, Audrey; Baldwin, Betty; and Van Camp, Warren: Volcanic Explosions and Climatic Change: A Theoretical Assessment. J. Geophys. Res., vol. 81, no. 6, pp. 1071-1083, Feb. 20, 1976.

Ruppersberg, Gerhard H.; and Renger, Wolfgang: Monitoring of the Tropospherical Aerosol Using a Spacelab Borne Lidar System. Atmospheric Physics From Spacelab, J. J. Burger, A. Pedersen, and B. Battrick, eds., D. Reidel Publishing Co., pp. 163-177, c.1976.

Russell, James M., III; and Remsberg, Ellis E.: The Effect of Aerosols on the Inference of Nitric Acid in the Stratosphere From Limb Emission Measurements at 11.2 μm. Second Conference on Atmospheric Radiation - Collection of Abstracts, American Meteorol. Soc., Oct. 1975.

Smith, W. L.; Woolf, H. M.; and Fleming, H. E.: Retrieval of Atmospheric Temperature Profiles From Satellite Measurements for Dynamical Forecasting. J. Appl. Meteorol., vol. 11, no. 1, pp. 113-122, Feb. 1972.

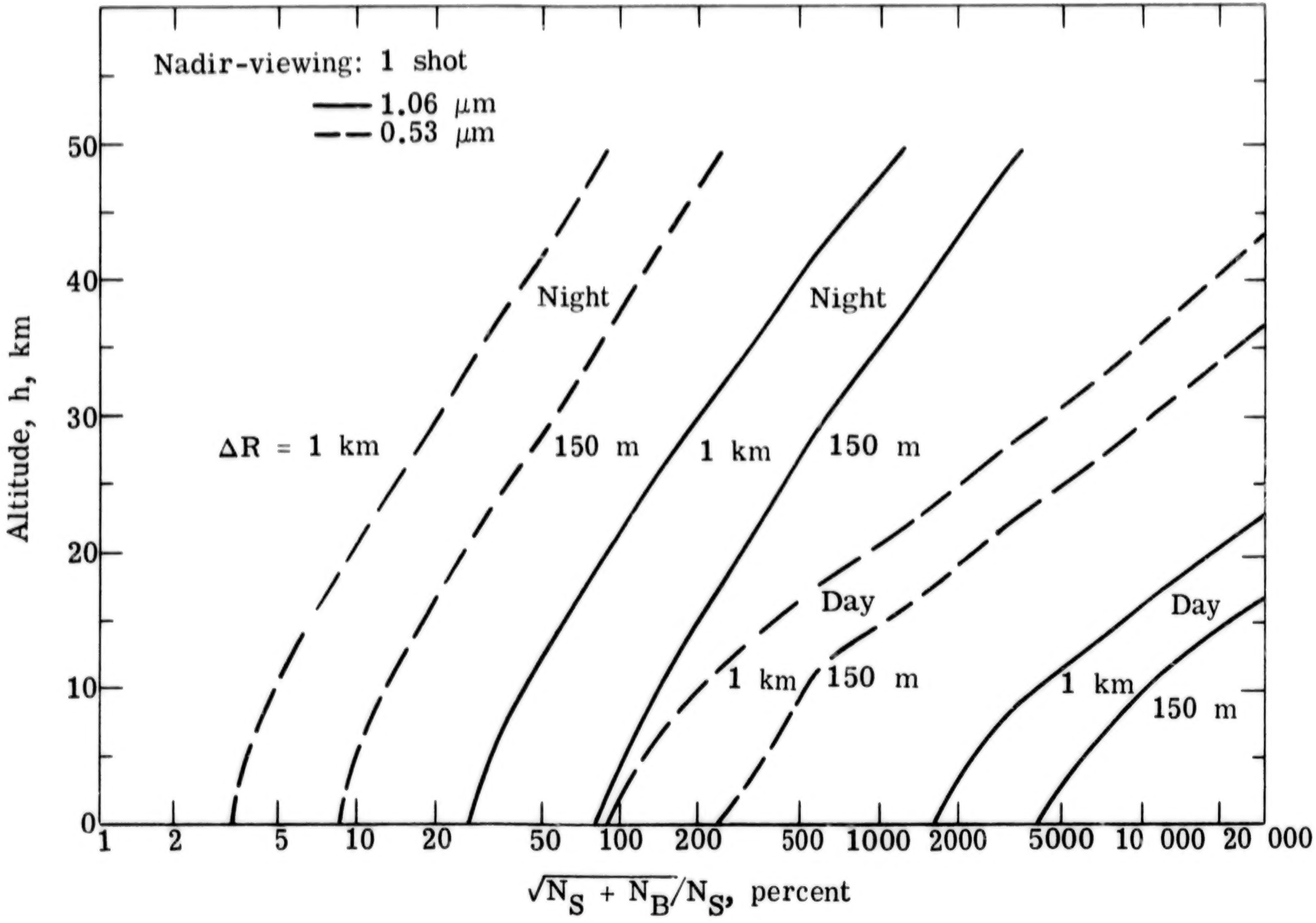

Figure A2.- Relative error in measurement of lidar signal for pure Rayleigh scattering (no particle) atmosphere. Same system parameters and background as given for experiment 1.

APPENDIX A

Experiment 3: Cirrus Ice-Water Discrimination

Description.- Two polarization components of the backscattered signal (for a linearly polarized transmitted signal) from cloud layers are used to discriminate between spherical water droplets and ice crystals in cirrus clouds. These measurements will be very useful in ascertaining the radiative transfer characteristics of cirrus clouds. The presence of ice-crystal layers admixed with water-droplet layers can lead to large errors in the interpretation of current passive radiometric measurements.

Implementation.- Standard Nd:YAG lidar (530 nm) with 1 mrad FOV, and a linear polarized output (to at least one part per thousand). One-meter receiver, with two-channel polarizing optics, possibly in the form of a polarizing beam splitter to monitor the components parallel and perpendicular to the direction of the transmitted linear polarization. Measurement requirements are similar to those involved in experiments 1 and 2 except that a two-channel receiver is required for the two polarization components. (These must be measured simultaneously.) Ground-based measurements indicate that the cross-polarized signal will typically have a magnitude of about 0.3 times the parallel polarized signal. (See fig. A3.) The vertical resolution required would be of the order of 150 m. This experiment would probably be best flown in conjunction with other passive systems for measuring cloud properties. There is some uncertainty with the backscatter cross sections for the various ice crystals.

Feasibility.- 1B. This experiment involves well-developed systems and techniques. Polarization requirements increase system complexity somewhat; however, all essential features have been demonstrated in ground-based systems. Polarization characteristics of the transmitting and receiving optics will have to be carefully designed and documented.

Needed development.- Some additional work on ice-crystal scattering is warranted to improve the quantitative capabilities of the data. Additional modeling calculations and measurements with ground-based laboratory and field systems would be useful.

Discussion.- Addresses scientific objectives 1, 3, and 4. Such measurements could be made with relatively little increase in complexity to the basic Shuttle lidar and would provide substantial new information. The data obtained is not available from passive systems now on satellites, and the measurements from Shuttle would provide broad coverage useful in examining the value of such information and the performance of new passive sensors.

No other technique presently permits the discrimination between ice and water in cirrus cloud layers. The lidar will provide this new information with excellent spatial resolution in both the horizontal and vertical directions (150 m). The possibility of detecting preferential alignments of ice crystals via polarization measurements is also available.

APPENDIX A

Bibliography

Kyle, H. L.; Curran, R. J.; Barnes, W. L.; and Escoe, D.: A Cloud Physics Radiometer. Third Conference on Atmospheric Radiation - Preprints, American Meteorol. Soc., pp. 107-109, June 1978.

Liou, Kuo-Nan; and Lahore, Henry: Laser Sensing of Cloud Composition: A Backscattered Depolarization Technique. J. Appl. Meteorol., vol. 13, no. 2, pp. 257-263, Mar. 1974.

Pal, S. R.; and Carswell, A. I.: The Polarization Characteristics of Lidar Scattering From Snow and Ice Crystals in the Atmosphere. J. Appl. Meteorol., vol. 16, no. 1, pp. 70-80, Jan. 1977.

Platt, C. M. R.: Lidar and Radiometric Observations of Cirrus Clouds. J. Atmos. Sci., vol. 30, no. 6, pp. 1191-1204, Sept. 1973.

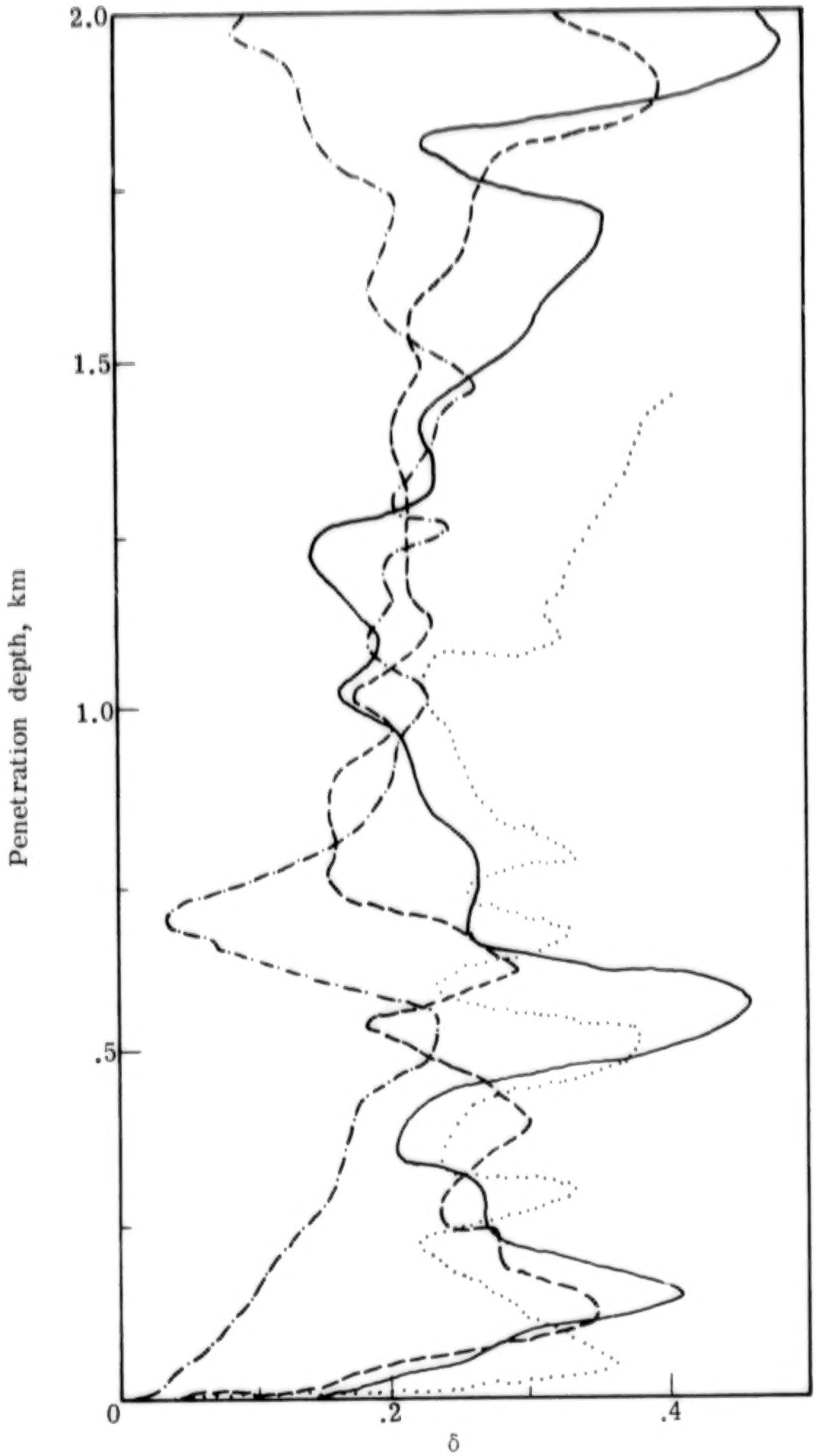

Figure A3.- Sample profiles of backscatter depolarization ratio, δ, for cirrus clouds from ground-based measurements at 694 nm.

APPENDIX A

Experiment 4: Profiles of Noctilucent Clouds, Circumpolar Particulate Layers, and Mesospheric Particulates

Description.- Determine presence, structure, and density of noctilucent clouds and particulate layers near the summer mesopause by elastic (Mie) backscatter to evaluate radiative effects of the layers and use them as tracers of atmospheric dynamics.

Implementation.- Standard doubled Nd:YAG or dye lidar with PMT detection, narrow-band receiver, and nadir-viewing geometry. An example of the ability of space-borne lidar to characterize the mesopause particulate layer is shown in figure A4. The calculations were done with the following lidar parameters:

> Wavelength, 530 nm; laser pulse energy, 0.35 J; receiver diameter, 1.0 m; receiver detection efficiency (including optics, filter, and PMT quantum efficiency), 0.08; receiver FOV, 0.2 mrad; filter passband, 0.04 nm; twilight background intensity, 3×10^9 photons nm^{-1} sr^{-1} s^{-1} cm^{-2}; Shuttle altitude, 280 km; number of laser pulses integrated, 1000 (700 km horizontal resolution at 10 Hz); vertical range bin, 5 km

The assumed particulate backscatter profile is appropriate to the relatively weak scatter from a nonvisible particulate layer near, but not in, a noctilucent cloud deck. Most of the plotted measurement uncertainty is due to photon-counting statistics, but a possible 10-percent error in the molecular backscatter contribution has also been included. The 10-percent overall measurement uncertainty is quite good enough to evaluate the gross radiative effects of these layers, and the assumed spatial resolution will suffice to assess their global morphology. Actual noctilucent clouds, however, as well as the intense circumpolar particulate layer observed by OGO-6, have backscatter strengths higher by one to two orders of magnitude than shown in figure A4. This will provide a strong enough signal so that the vertical and horizontal extent of the lidar data-integration volume can be substantially reduced from the values used in the figure (5 km and 700 km) to values more appropriate to the study of wave structures and fine-scale mesopause thermal effects of those features ($\approx$0.5 km vertical and $\leq$10 km horizontal resolution with reduced, but acceptable, measurement accuracy).

High inclination or polar orbits are required because the main circumpolar layer is confined to within 15° of the summer pole and noctilucent clouds are seldom seen more than 35° from the pole. Incoming data will be digitized at 5 MHz, and greatly compressed over most of the return, except for the 1 to 5 km altitude range where the clouds occur. Data will be cataloged by geographic location, peak return strength, and along-track duration.

Useful correlative measurements would include simultaneous lidar measurements of the sodium layer, low-light-level TV pictures of the layer to document the portion probed by the lidar, and photometer observations of OH emissions to detect mesopause temperature fluctuations associated with atmospheric wave passages.

Feasibility.- 1B. Requires only low-risk adaptation of existing hardware to Shuttle operation. Data quality limited primarily by available power-aperture product. Requires high inclination or polar orbit.

Needed development.- None.

Discussion.- This experiment directly addresses scientific objective 3 by supplying data on the opacity of the mesospheric aerosol features and scientific objective 5 where the spatial variations in the layers reflected the passage of waves. It also indirectly addresses scientific objectives 2 and 6 by documenting the existence of aerosols which may play an important role in atmospheric chemical processes.

Mesopause particulates, of which noctilucent clouds and the circumpolar particulate layer are high-latitude manifestations, occur in a region of dramatic ion-composition change. Their role in heterogeneous chemistry is unknown but could be significant. Likewise, the role of the circumpolar layer on the climatology of the summer pole is probably significant. More data are needed on the density, extent and duration of the layer, and on its impact on mesopause chemistry. The latter objective could be met by simultaneous observations of the mesopause particulates and the sodium layer. Wave structures in the particulate layers are indicative of the presence of gravity waves and hence can be used as a tracer for mesopause dynamics. Because the climatological implications of the layer are addressed by passive sensors, Shuttle lidar observations are useful primarily in conjunction with other Shuttle experiments (e.g., Na layer measurements) and to achieve the vertical and horizontal resolution and geographic coverage needed to exploit the layer as a tracer of mesopause dynamics. Since the lidar hardware associated with several other experiments (e.g., 3, 6, and 7) is capable of providing data for experiment 4, its operation should be included in the scenarios of these experiments, especially for high-latitude portions of the orbits.

Lidar can detect these layers in locations that are not sunlit, which passive devices cannot do. The superior spatial resolution of lidar (≈0.25 km vertical and ≈30 km horizontal for lidar; ≈2 km vertical and ≈300 km horizontal for passive devices; for typical circumpolar and noctilucent cloud layers) is needed to assess the chemical and local-thermal effects of the layers and to use the layers as tracers of atmospheric dynamics.

Bibliography

Donahue, T. M.; Guenther, B.; and Blamont, J. E.: Noctilucent Clouds in Daytime: Circumpolar Particulate Layers Near the Summer Mesopause. J. Atmos. Sci., vol. 29, no. 6, pp. 1205-1209, Sept. 1972.

Fiocco, Giorgio; and Grams, Gerald: Optical Radar Observations of Mesospheric Aerosols in Norway During the Summer 1966. J. Geophys. Res., vol. 74, no. 10, pp. 2453-2458, May 15, 1969.

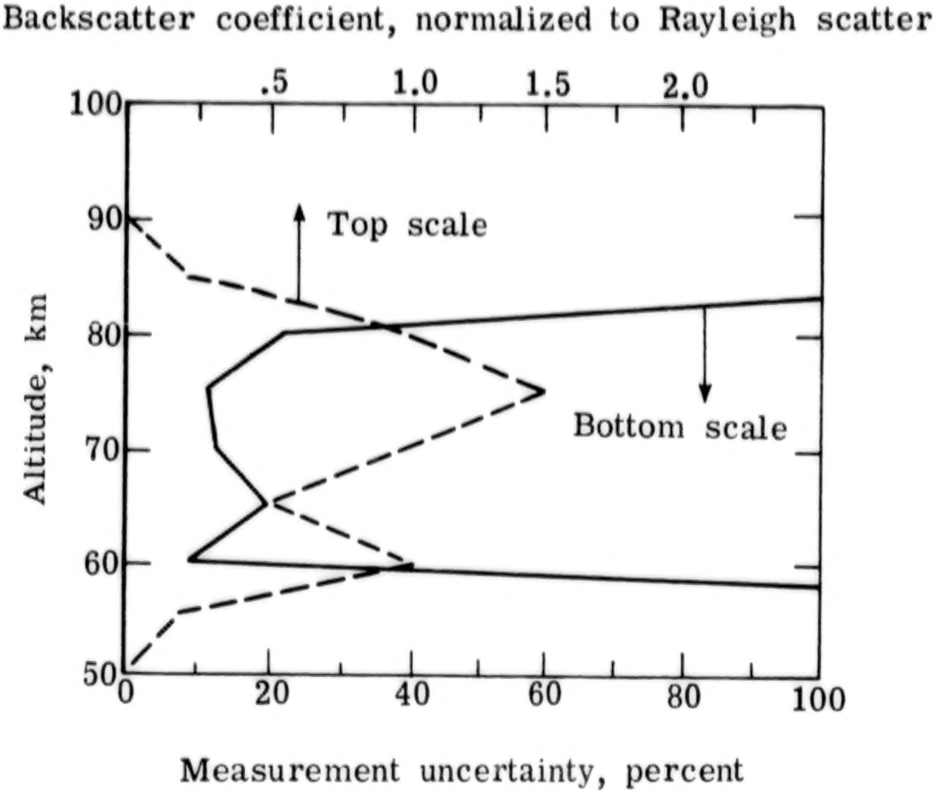

Figure A4.- Performance calculation for lidar measurement of mesospheric particulate layers. (Dashed line gives aerosol backscatter coefficient assumed in lidar-performance calculation, expressed as fraction of molecular Rayleigh backscatter at equivalent altitudes using the U.S. standard atmosphere; solid line gives percentage uncertainty with which that aerosol backscatter profile can be measured for lidar parameters given in text.)

Experiment 6: Stratospheric Aerosol Backscatter Profiles

Description.- Measurement of stratospheric aerosol from orbital altitudes using particulate backscattering at wavelengths of 530 nm and 1060 nm in order to obtain global-scale information on their distribution. These data are important because of their potential effect on the Earth's climate and environment.

Implementation.- Instrumentation includes a 1 m diameter receiver, standard Nd:YAG laser operating at energies of 1 J at 1060 nm and 0.35 J at 530 nm with 10 Hz repetition rate, a 1 mrad FOV, 1.0 nm FWHM wavelength filter, and system optical efficiency of 30 percent and PMT detectors with efficiencies of 20 percent at 530 nm and 2 percent at 1060 nm. This experiment can be readily performed from orbital altitudes of 300 km under nighttime viewing conditions. Data on aerosol backscattering are retrieved from the measured signal as well as from accurate descriptions of the relative contributions from molecular backscattering, lidar normalization, and atmospheric attenuation. Typical uncertainties in these latter parameters are included in the sensitivity analysis shown in figure A5. Assuming background stratospheric aerosol concentrations, the simulation indicates that at the peak of the aerosol concentrations (20 km) horizontal (along-track) resolutions of 75 km and vertical resolutions of 1 km are obtained with aerosol backscatter uncertainties of 20 percent or less at the 1060 nm wavelength (less than 10 percent for 300 km horizontal resolution). Aerosol backscatter information at 530 nm is retrieved with greater uncertainties since errors in the estimates of molecular backscattering contribute more significantly to the total error budget at this wavelength. Improvement in the accuracy can be obtained by adding the capability for utilizing tripled Nd:YAG output to reduce uncertainty in molecular density. Daytime measurements of stratospheric aerosols can be obtained with similar accuracies using longer integration times.

Feasibility.- 1B. Extensive measurements from existing ground (and airborne) lidar systems have clearly demonstrated the capability of quantitatively measuring stratospheric aerosols.

Needed development.- No significant development needed.

Discussion.- Detailed information on the spatial distribution and horizontal homogeneity of stratospheric aerosols relates to scientific objective 1 for stratospheric/tropospheric exchange studies, objective 2 for studies on stratospheric motions, and objective 3 for input data to radiative model calculations. Shuttle lidar measurements of stratospheric aerosols provide better horizontal resolution than passive sensors, have increased global coverage on the night side of the orbit, and provide opportunities for simultaneous tropospheric measurements - useful for subsequent stratospheric/tropospheric exchange studies. If multiple wavelengths are not available, supporting meteorological information on temperature/pressure profiles at the lidar measurement location is needed to define the molecular backscatter contributions to the measured signal.

APPENDIX A

Bibliography

Fiocco, G.; and Grams, G.: Observations of the Aerosol Layer at 20 km by Optical Radar. J. Atmos. Sci., vol. 21, no. 3, pp. 323-324, May 1964.

McCormick, M. P.; Swissler, T. J.; Chu, W. P.; and Fuller, W. H., Jr.: Post-Volcanic Stratospheric Aerosol Decay as Measured by Lidar. J. Atmos. Sci., vol. 35, no. 7, pp. 1296-1303, July 1978.

Russell, Philip B.; and Hake, Richard D., Jr.: The Post-Fuego Stratospheric Aerosol: Lidar Measurements, With Radiative and Thermal Implications. J. Atmos. Sci., vol. 34, no. 1, pp. 163-177, Jan. 1977.

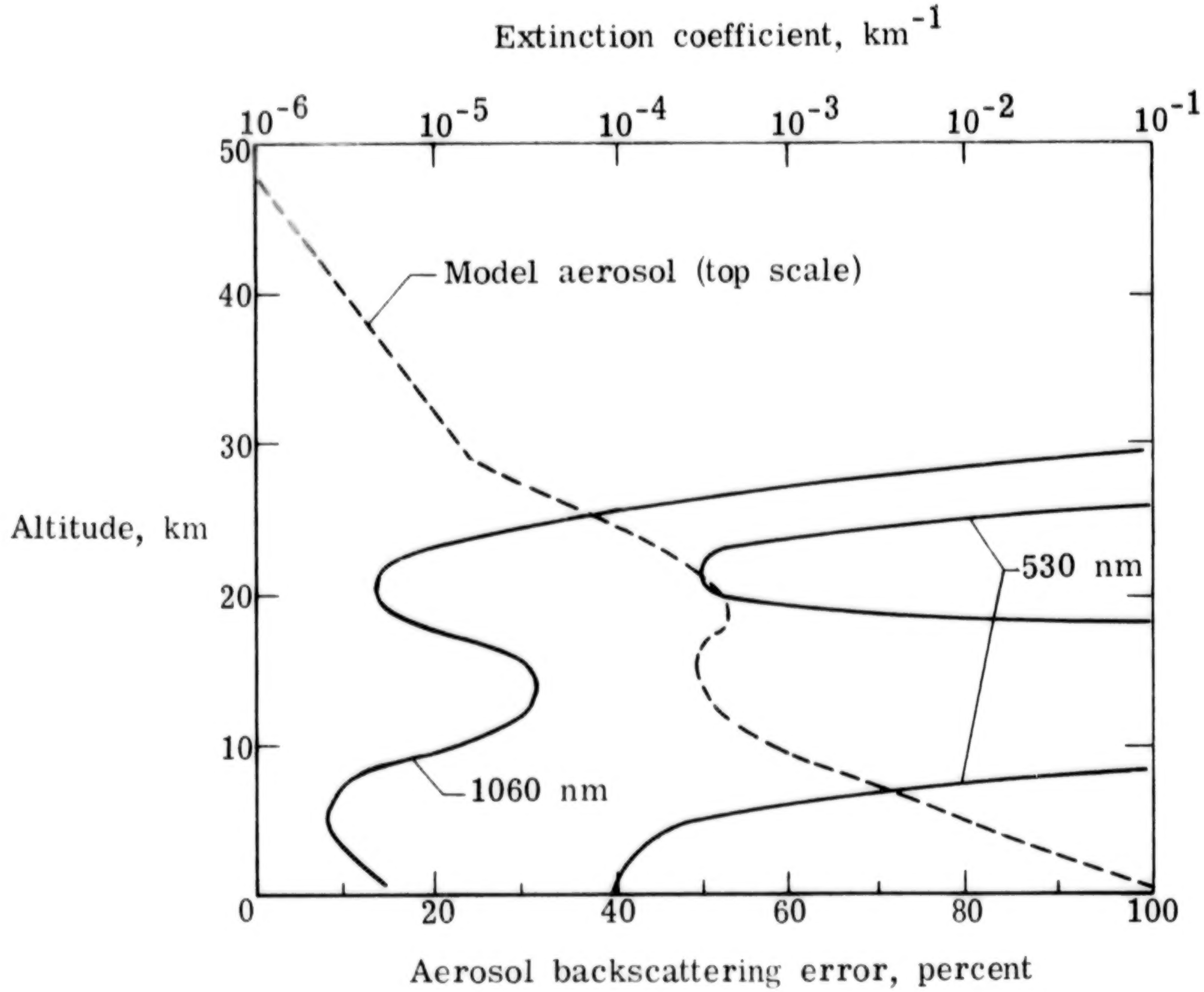

Figure A5.- Aerosol backscattering error.

APPENDIX A

Experiment 7: Alkali-Atom Density Profiles

Description.- Determine altitude profiles of the free sodium atoms in the layer from 80 to 110 km by observation of sodium resonance fluorescence excited by a pulsed tunable dye laser. Spatial variations in these profiles provide information about circulation, wave motions, and diffusion characteristics in the upper atmosphere. Lithium and potassium profiles can be determined with the same technique.

Implementation.- Resonance fluorescence excited using narrow-band frequency-tuned dye laser pumped by doubled Nd:YAG laser, with photon-counting PMT detection and nadir-viewing geometry. Return signal calculations have been performed using the following parameters:

> Wavelength, 589 nm; laser line width (Note 1), ≈1 pm; laser stability (Note 1), ≈0.2 pm; laser pulse energy, 0.02 J; laser pulse rate, 30 Hz; power consumed, 2 kW; Na backscatter cross section, 7×10^{-13} cm^2 atom^{-1} sr^{-1}; receiver area, 10^4 cm^2; receiver passband (Note 2), 0.04 nm; receiver detection efficiency, 0.03 (including optics, filter, and PMT quantum efficiency); receiver FOV (Note 2), 0.2 mrad; daytime background, 1.5×10^{13} photons s^{-1} nm^{-1} sr^{-1} cm^{-2} (Note 3); Shuttle altitude, 270 km

Note 1: Line width and stability values can be relaxed at the expense of a lower return signal and degraded measurement accuracy. The Doppler hyperfine sodium line width is ≈3.5 pm.

Note 2: The receiver requirements could have been made less demanding for the low-background nighttime scenario, actually requiring only a 1 mrad FOV and a 1 nm bandwidth filter to achieve the results shown.

Note 3: This value is 50 percent of continuum because of 0.04 nm filter width in Fraunhofer line.

The results of these calculations, expressed in terms of the amount of signal integration required to obtain a ±10-percent measurement uncertainty for the specified sodium densities, are shown in figure A6. A comparison of the vertical and horizontal resolutions given in the figure to the spatial characteristics of the geophysical processes of interest (gravity, tidal, and planetary waves, diurnal variation of eddy-diffusion coefficient) shows the high value of such lidar observations.

High-spatial-resolution measurements would be carried out during successive orbital passes through the same ≈10° orbital interval, and medium spatial resolution measurements throughout several complete orbits. All orbit inclinations are useful, with high-inclination orbits desired in order to gain access to the atmospheric perturbations in the auroral zone. The data will be acquired at a high rate during the mission and integrated post event to permit whatever combination of measurement uncertainty and spatial resolution is appropriate to the particular science investigations.

Feasibility.- 2B. Extensive ground-based measurements have been successfully carried out by several groups. Requires straightforward Shuttle adaptation of existing tunable dye laser technology.

Needed development.- None. Dye laser construction will require more effort than category 1 experiments, but will not require new technology development.

Discussion.- A study of the sodium layer dynamics addresses scientific objective 5, while a study of the morphology of the layer addresses scientific objective 6. Scientific objective 2 is addressed indirectly by this experiment providing information on large-scale, long-term vertical exchange in the atmosphere. The alkali layers are used as tracers of atmospheric dynamics in the critical turbopause region encompassing the transition from uniform (eddy) mixing to diffusive separation of the atmospheric gases. Observing the development of Na layer irregularities will provide information on the strength, movement, and origin of wave processes occurring in the turbopause region. Following the diurnal evolution of the topside scale height gives values of the eddy diffusion coefficients. Lidar provides the spatial resolution necessary to observe spatial fluctuations in the sodium layer. Spacecraft give the wide geographic coverage needed to define the layer patterns. The same lidar could also measure K (at 769.9 nm with 10 times less density than Na) or Li (at 670.7 nm with 100 times less density than Na) with degraded resolution. The geographic and seasonal variability of the Na/K ratio provides information on stratosphere/mesosphere/thermosphere exchange processes.

Lidar is the only technique for directly measuring alkali-atom densities. Dayglow photometer observations are somewhat ambiguous because of the impossibility of exactly correcting for resonance-radiation effects along the optically thick line-of-sight. Nightglow photometers measure only chemically excited radiations that are not simply related to sodium densities. Furthermore, the superior lidar spatial resolution (≈0.25 km vertical and ≈1 to 10 km horizontal, compared to ≈2 km vertical and ≈300 km horizontal for the limb-observing passive techniques) is needed to study the spatial effects produced by gravity waves passing through the layer.

APPENDIX A

Bibliography

Gibson, A. J.; and Sandford, M. C. W.: The Seasonal Variation of the Night-Time Sodium Layer. J. Atmos. & Terrest. Phys., vol. 33, no. 11, pp. 1675-1684, Nov. 1971.

Hake, R. D., Jr.; Arnold, D. E.; Jackson, D. W.; Evans, W. E.; Ficklin, B. P.; and Long, R. A.: Dye-Laser Observations of the Nighttime Atomic Sodium Layer. J. Geophys. Res., vol. 77, no. 34, pp. 6839-6848, Dec. 1, 1972.

Megie, G.; Bos, F.; Blamont, J. E.; and Chanin, M. L.: Simultaneous Nighttime Lidar Measurements of Atmospheric Sodium and Potassium. Planet. & Space Sci., vol. 26, no. 1, pp. 27-35, Jan. 1978.

Rowlett, J. R.; Gardner, C. S.; Richter, E. S.; and Sechrist, C. F., Jr.: Lidar Observations of Wave-Like Structure in the Atmospheric Sodium Layer. Geophys. Res. Lett., vol. 5, no. 8, pp. 683-686, Aug. 1978.

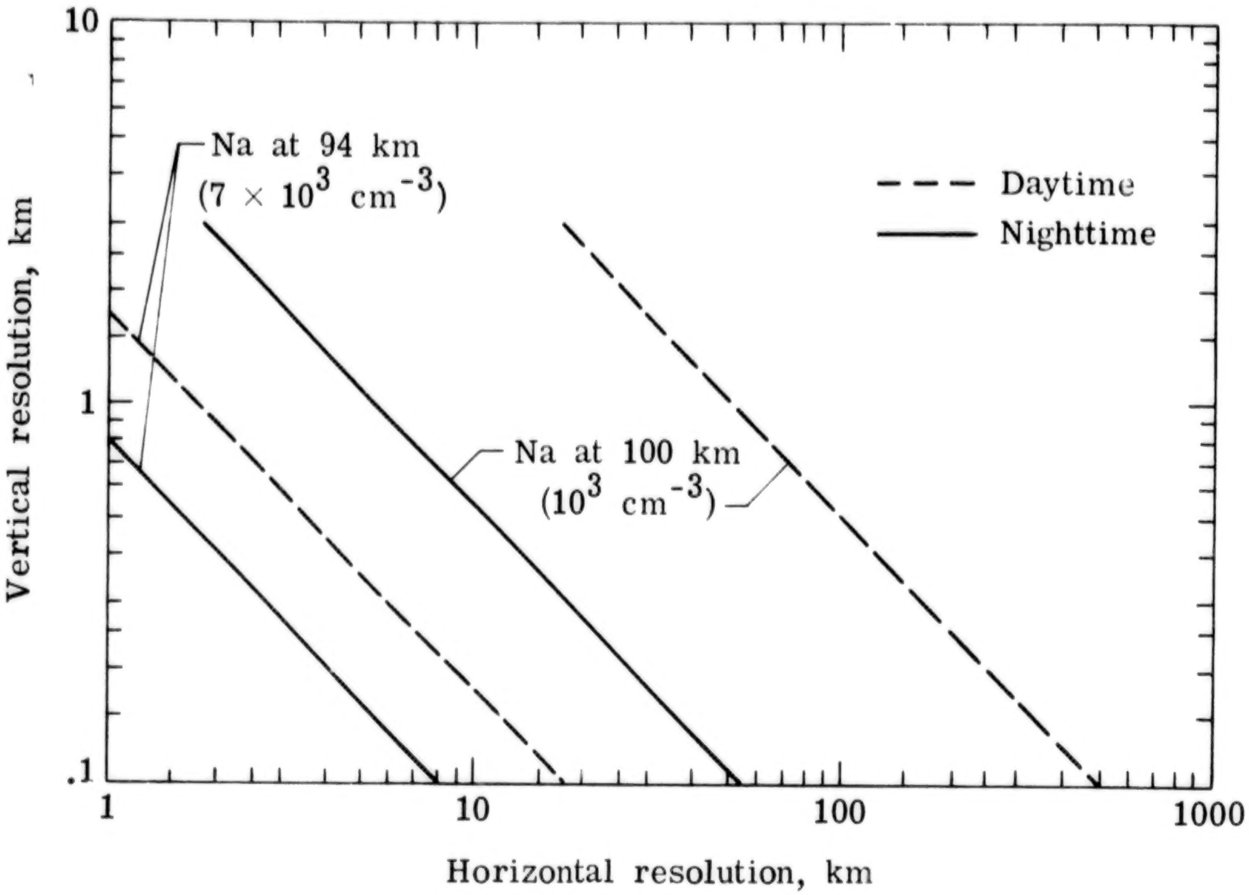

Figure A6.- Vertical/horizontal resolution trade-off for Shuttle lidar measurements of sodium layer. (Straight lines show trade-off between vertical resolution (range-bin size) and horizontal resolution (along-track integration distance) needed to give a ±10-percent measurement uncertainty under selected observing conditions. Assumed sodium-atom densities are given in parentheses.)

Experiment 8: Ionospheric Metal Ion Distributions

Description.- Use laser resonant scattering to obtain altitude profiles of Mg^+ density from 80 to 500 km to study ionospheric irregularities (which affect communications systems), lower thermospheric neutral wind patterns, and general ionospheric circulation patterns. The technique can also be applied to measurements of ambient Fe^+ and Ca^+.

Implementation.- Doubled narrow-band frequency-tuned dye laser pumped by doubled Nd laser, with PMT detection and nadir- and zenith-viewing geometry. Return-signal calculations have been performed using the following parameters:

> Wavelength, 279.6 nm; laser line width (Note 1), 0.6 pm; spectral stability (Note 1), 0.1 pm; laser pulse energy, $\geqq 0.001$ J; laser pulse rate, 30 Hz; power consumed, 2 kW; Mg^+ backscatter strength, 3.4×10^{-13} cm^2 ion^{-1} sr^{-1}; receiver area, 10^4 cm^2; receiver passband, 1.5 nm; receiver detection efficiency, 0.02; receiver FOV (Note 2), 0.2 mrad; daytime background (Note 3), 3×10^9 photons nm^{-1} sr^{-1} s^{-1} cm^{-2}; Shuttle altitude 270 km

Note 1: Line width and stability values can be relaxed at expense of lower return signal and degraded measurement accuracy. Doppler line width of Mg^+ ranges from 0.6 pm at 90 km to ≈1.3 pm in F-region.

Note 2: Nighttime requirement is less demanding, ≈1 mrad FOV.

Note 3: This value is 40 percent of continuum because of 1.5 nm filter width in Fraunhofer line.

The results of these calculations are shown in figure A7, presented in terms of the amount of signal integration required to obtain a ±10-percent measurement uncertainty for representative Mg^+ densities. An examination of this figure can give a feeling for which geophysical processes are capable of study with the assumed lidar, or, conversely, can reveal areas where the lidar sensitivity may need to be increased (or can stand to be decreased) based on the science objectives of concern. For instance, return signals from a strong sporadic E-layer ($Mg^+ = 3 \times 10^3$ cm^{-3}) will supply good data on the passage of gravity waves with horizontal periods above 50 to 100 km, but a diurnal study of the formation phase of these layers (initial densities: $Mg^+ < 10^3$ cm^{-3} at 100 to 120 km altitude) with an appropriate spatial resolution (≈2 km vertical, <100 km horizontal) will require a lidar of greater sensitivity.

All orbital inclinations are useful, but medium inclination orbits may be preferred in order to focus on postulated equatorial source regions and latitudinal structure. Measurements surrounding the period of a meteor shower would be especially valuable because of high-signal strength (enhanced Mg^+ densities) leading to better measurements of layer dynamics. Repetitive measurements in the same location on successive orbits are desirable. The data will be catalogued by geographic location and peak return strength and archived after compression in regions of low return.

Feasibility.- 2B. The required laser technology and the measurement technique have been well demonstrated in the laboratory, and by ground-based atmospheric measurements on similar species for which the measurement wavelength is not absorbed by ozone. Data quality will be limited primarily by the available power-aperture product.

Needed development.- None. The dye laser construction will require more effort than category 1 experiments, but will not require new-technology development.

Discussion.- The atmospheric dynamics observed in this experiment address the wave motions of scientific objective 5 and the morphological observations contribute directly to the understanding of thermospheric atomic species being pursued in scientific objective 6. The Sun/weather coupling question in scientific objective 7 is also addressed to the extent that ionosphere/magnetosphere plasma motions and electric fields can be determined either directly from the observations or by comparing the observations with predictions based on thermospheric electrodynamical models. High spatial resolution close to the Shuttle gives the location, strength, and power spectra of scintillation-producing ionospheric irregularities. Study of Mg^+ in sporadic E-layers reveals neutral wind patterns causing ionization motion in the lower thermosphere. Gross Mg^+ structure in the rest of the ionosphere shows plasma circulation patterns (the pileup at magnetic latitudes of 8° to 17° is of particular interest). Fe^+ has equal scientific value and would be a preferable species to Mg^+ because of its higher density but requires more laser development to reach the 259.6 nm operating wavelength. Ca^+ (resonance wavelength 396.5 nm) is another ion species known to exist in the ionosphere and for which a measurement need may arise. Direct observations of thermospheric electric fields can be made by observing the $E \times B$ velocity of Mg^+ by augmenting the lidar configuration of this experiment with the Fabry-Perot detector of experiment 14.

Competing techniques are rocket- and satellite-borne mass spectrometry and dayglow photometry. Although the spatial resolution of the mass spectrometers (<100 m) is superior to that of lidar ($\leqq 1$ km vertical, ≈10 to 50 km horizontal), the mass spectrometer techniques give only an in situ measurement, and not the instantaneous two-dimensional cross sectional cut given by the lidar, which is needed for the thermospheric dynamics studies. Dayglow photometry gives only column-content information and is not capable of nighttime measurements when much of the ion transport is occurring.

Bibliography

Anderson, James G.; and Barth, Charles A.: Rocket Investigation of the Mg I and Mg II Dayglow. J. Geophys. Res., vol. 76, no. 16, pp. 3723-3732, June 1, 1971.

Gérard, J.-C.; and Monfils, A.: Satellite Observations of the Equatorial Mg II Dayglow Intensity Distribution. J. Geophys. Res., vol. 79, no. 16, pp. 2544-2550, June 1, 1974.

Zbinden, P. A.; Hidalgo, M. A.; Eberhardt, P.; and Geiss, J.: Mass Spectrometer Measurements of the Positive Ion Composition in the D- and E-Regions of the Ionosphere. Planet. & Space Sci., vol. 23, no. 12, pp. 1621-1642, 1975.

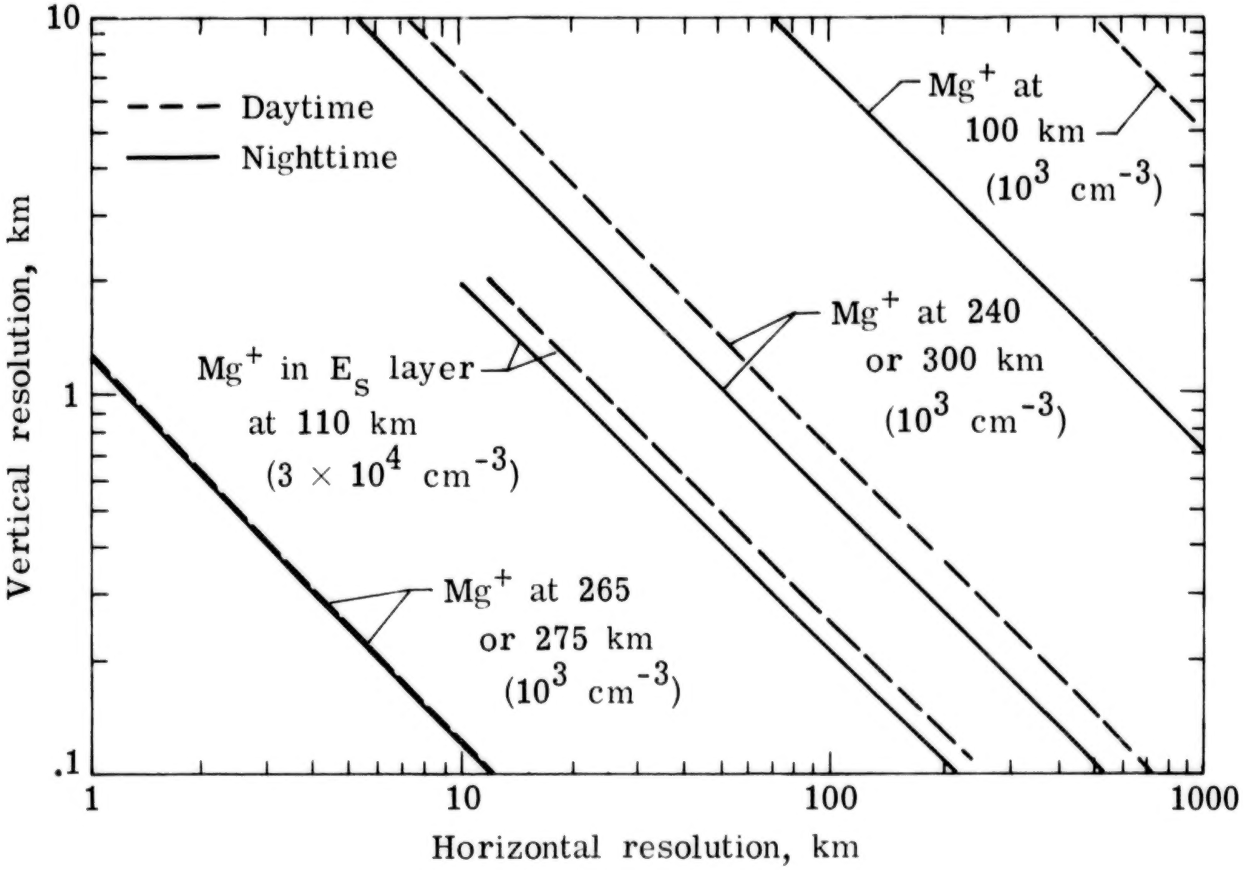

Figure A7.- Vertical/horizontal resolution trade-off for Shuttle lidar measurements of ionospheric magnesium ions. Straight lines show trade-off between vertical resolution (range-bin size) and horizontal resolution (along-track integration distance) needed to give ±10-percent measurement uncertainty under selected operating conditions. Assumed Mg^+ densities are given in parentheses.

APPENDIX A

Experiment 9: Water-Vapor Profiles

Description.- Measure water-vapor profiles in the troposphere using the 720 or 820 nm bands of H_2O, or in the region of the tropopause and lower stratosphere using the 940 nm band, with a differential absorption technique (DIAL). Demonstrate that lidar can meet accuracy and resolution requirements for GARP and NASA climate plan and can assess H_2O profiles and transport over large land and sea areas for which evaporation is important. Water-vapor total burden can be obtained using ground reflection.

Implementation.- Standard Nd:YAG (doubled) laser pumping near IR narrow-band dye laser (0.003 nm) giving pulse energies ranging from 60 mJ at 720 nm down to 20 mJ at 940 nm (10 pps). Overall receiver efficiencies of 10 percent and 2.5 percent assumed, for 720 and 940 nm regions using near IR PMT's. Nighttime operation with 1 mrad FOV and 10 nm detection bandwidth (daytime possible with 0.1 nm bandwidth and 0.1 mrad FOV). Humidity measurement accuracy dictated by vertical range resolution of lidar and total optical energy (number of pulses). Horizontal resolution resulting from pulse accumulation is 40 km (for 720 nm) up to 120 km (for 940 nm). Typical simulation choices for vertical resolution are 1, 2, and 5 km depending, for example, on whether the aim is to resolve the lower troposphere into 1 km thick layers or obtain greater accuracy at higher altitude by averaging H_2O over 5 km thick layers. In figure A8 the simulation for the 720 nm regions shows expected errors of order 10 percent near 10 km, assuming a Δz of 2 km and the use of the stronger H_2O line (dashed curve). Deeper penetration into the atmosphere is obtained using a weaker line so that the lower troposphere can be studied satisfactorily with $\Delta z = 1$ or 2 km (solid curves). Operation near 940 nm with narrower line width ($\approx$0.001 nm) is needed for better accuracy into the lower stratosphere; e.g., 20 to 30 percent for 15 to 20 km altitude. The off-line dye laser for H_2O DIAL need not be tuned and narrowed to the same degree as the on-line laser.

Feasibility.- 2B at 720 and 820 nm and 3B at 940 nm. Has been demonstrated with ground-based lidar at 724 nm; an airborne lidar is being developed for this wavelength. Laboratory systems suitable for lidar applications are being built and tested at 820 and 940 nm.

Needed development.- Accuracy of near IR lidar methods can be improved with more efficient laser dyes and detectors. A useful development would be to design the H_2O laser for adaptability to pressure and temperature measurements near 760 nm (experiments 15 to 17) on the same or later flights.

Discussion.- Water-vapor lidar data would contribute to objectives 1, 3, 4, and 7 through tracing of stratosphere/troposphere exchange processes, by providing knowledge needed for understanding radiative processes, and by providing inputs for meteorological investigations and forecast model work. Infrared and microwave instruments, such as those on Nimbus 7, can obtain some altitude profile data on H_2O (e.g., 15 to 60 km) and total column content. SME spectrometers are expected to give H_2O data between 30 and 70 km. Lidar profiles with 1 or 2 km vertical resolution in the lower troposphere would surpass present passive measurements which are essentially total burden. Present data on water-vapor concentrations in the 10 to 18 km region are quite limited, and lidar can potentially fill the gap.

APPENDIX A

Bibliography

Browell, E. V.; Brumfield, M. L.; Siviter, J. H., Jr.; Northam, G. B.; Wilkerson, T. D.; and McIlrath, T. J.: Development and Evaluation of a Near-IR H_2O Vapor DIAL System. Paper presented at Eighth International Laser Radar Conference (Drexel Univ., Philadelphia, Pa.), June 6-9, 1977.

Browell, E. V.; Wilkerson, T. D.; and McIlrath, T. J.: Water Vapor Differential Absorption Lidar Development and Evaluation. Appl. Opt., vol. 18, no. 20, Oct. 1979. (To be published.)

Remsberg, Ellis E.; and Gordley, Larry L.: Analysis of Differential Absorption Lidar From the Space Shuttle. Appl. Opt., vol. 17, no. 4, pp. 624-630, Feb. 1978.

Schotland, Richard M.: Errors in the Lidar Measurement of Atmospheric Gases by Differential Absorption. J. Appl. Meteorol., vol. 13, no. 1, pp. 71-77, Feb. 1974.

Schwemmer, G.; and Wilkerson, T.: Water Vapor Lidar Techniques Below 1 Micron Wavelength. Proceedings on a Workshop on Remote Sensing of the Marine Boundary Layer, Lothar H. Ruhnke, ed., NRL Memo. Rep. 3430, pp. 288-299, June 1977.

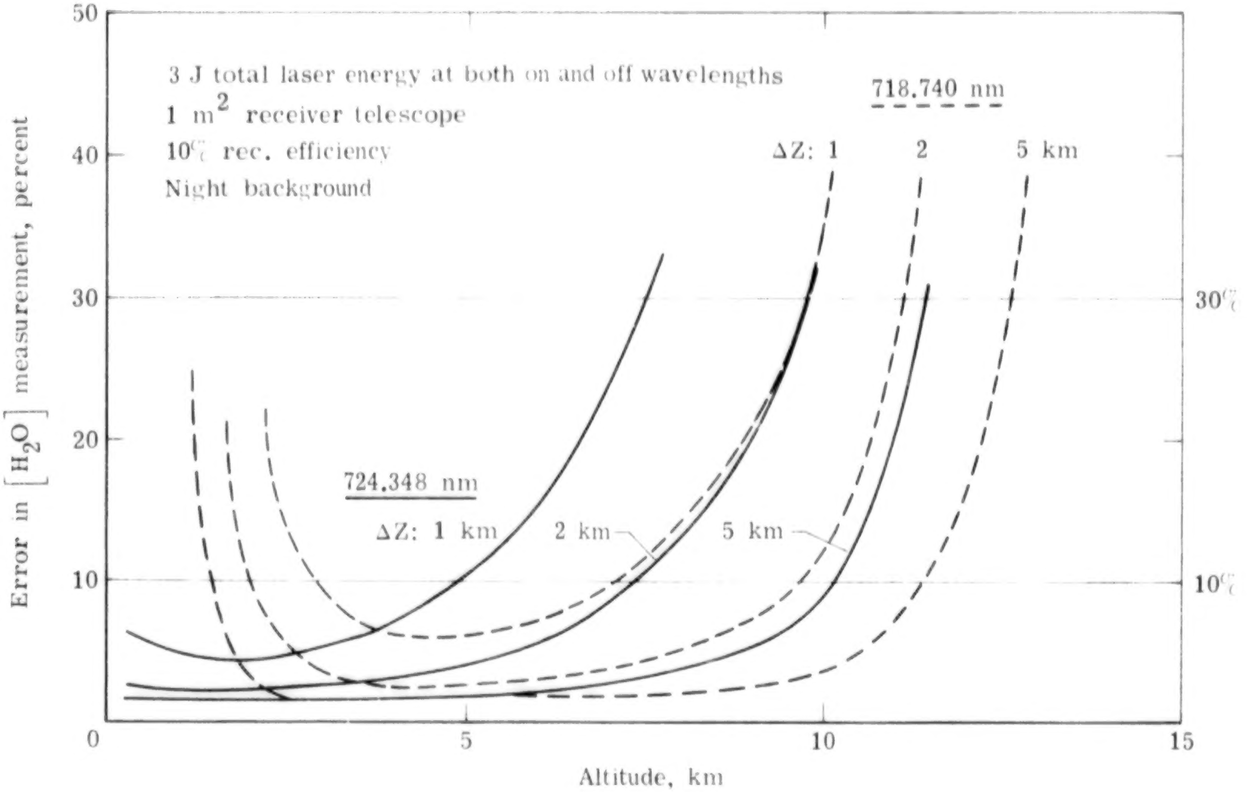

Figure A8.- Water-vapor lidar from Space Shuttle. Errors in H_2O vertical profile using 720 nm band.

APPENDIX A

Experiment 10: Atmospheric Species Measurements - IR Laser Ground and Cloud Returns

Description.- Measure concentrations of a variety of species such as O_3, H_2O, NH_3, the CFM's, CCl_4, C_2H_4, and C_2H_3Cl using CO_2 lasers; or CH_4, CO_2, N_2O, CO, and HCl with other IR lasers (doubled CO_2, CO, etc.). Species total burdens in the troposphere and stratosphere and species profiles with 3 to 4 km vertical resolution would be obtained using reflection from the Earth's surface and from clouds. This experiment offers a large potential for growth in atmospheric species measurements since the infrared is richer in molecular absorption spectra than the UV or visible. Sensitivity for most species mentioned above for a system using a CO_2 laser is approximately 0.002 atm-cm. This approach would address a variety of needs in species transport, source and sink studies, meteorology, and environmental quality.

Implementation.- CO_2 CW lasers operating at several discrete wavelengths, or tuned continuously over a characteristic absorption line of the species to be measured, would provide concentration data by differential absorption and vertical profiling by measured changes in the absorption line shape with pressure. Profiles with 3 to 4 km vertical resolution can be measured by discrete and/or continuous tuning over a major portion of a spectral line. (Line widths are typically ≈3 GHz near the ground and ≈750 MHz at the tropopause.) Two wavelength (on and off an absorption line) measurements provide total burden information. Extrapolation from aircraft measurements already performed to a Shuttle borne system (two CW CO_2 lasers each with 10 W output power at a specific wavelength, laser spectral purity of better than 10 MHz, 1 m diameter telescope receiver, IR heterodyne detection) leads to the following simulation examples: (1) the lower tropospheric H_2O burden can be measured to approximately ±1 percent, (2) the O_3 burden in the troposphere can be measured to ±0.002 atm-cm (±8 percent of the typical tropospheric burden), (3) total O_3 burden can be measured to ±0.003 atm-cm (±1 percent of total burden). The horizontal resolution would be 10 km for the tropospheric measurements and 250 km for the stratospheric measurements, either night or day. Multiple-wavelength pulsed lasers with comparable power, line width, and tunability are being developed and would allow extension of this experiment to DIAL measurements (see experiment 18). The following table shows the expected sensitivities for total burden measurements of several species using a CO_2 laser system:

Species	Sensitivity, atm-cm	Species	Sensitivity, atm-cm
O_3	0.002	C_6H_6	0.01
NH_3	.0002	CCl_3F	≈.001
C_2H_4	≈.001	CCl_2F_2	.0003
CCl_4	.002	$C_2Cl_3F_3$	≈.002
C_2H_3Cl	.004	CH_3OH	≈.002
HNO_3	≈.001	C_2Cl_4	≈.001

Feasibility.- 2B. This technique has been demonstrated in several successful aircraft measurements of O_3 in the troposphere, including some which simulated a Shuttle mission. These measurements used waveguide CO_2 lasers with 1-W CW power and <10 MHz bandwidth, in conjunction with IR heterodyne detection.

Needed development.- CO_2 CW lasers with spectral tuning and the stability needed for heterodyne detection must be upgraded to 10 to 25 W average power. The potential of matrix heterodyne detectors should be investigated. Simulations for many of the additional species capable of being measured are also needed.

Discussion.- Addresses objectives 1, 2, 3, and 4. The use of CO_2 and other IR lasers for species measurements is an open-ended area with good growth potential because of the rich spectral characteristics of the infrared. The experiments discussed here are potentially important as initial steps toward pulsed IR DIAL measurements as well as in their own right. O_3 measurements are important for information on tropospheric oxidant production and transport, and for global data on ozone burdens. H_2O measurements are important for meteorological models and for evaluating passive-sensor data. Measurements of other species, such as NH_3, the CFM's, and CCl_4, are important for understanding source/sink processes and the interactions of dynamics, radiation, and chemistry. The satellite data will provide global measurements of numerous species with resolution and reliability improved over those of passive or microwave techniques. Data processing is straightforward; and for Shuttle measurements, the data output will be wide-area maps of species concentrations. Heterodyne detection provides a sensitive measure of the backscattered laser radiation reducing even full daylight background to levels much smaller than the signal. A matrix of individual heterodyne detectors can, in principle, achieve nearly full heterodyne detection efficiency when a small transmitting aperture is used with a large receiving aperture. This approach may reduce power requirements since the full receiver mirror can be used. Averaging over speckle noise is accomplished by simultaneous multiple detection. These advantages are accompanied by an increase in detector complexity.

The measurement of atmospheric constituents using ground and cloud returns of scattered infrared laser radiation provides total burden and some vertical profile information over a region from ground level through the troposphere to the upper stratosphere. Global data of species concentrations in the troposphere are needed to understand large-scale regional transport and associated chemical transformations. Although microwave instruments can measure several of the species indicated above, they are not generally applicable to measurements in the lower atmosphere due to pressure broadening. Other passive instruments, such as the Fabry-Perot interferometer, pressure-modulated radiometer, and heterodyne radiometer, are also more suitable for upper atmospheric measurements. Moreover, since the active infrared laser system of experiment 10 can operate day or night, it permits measurements of solar-assisted chemical reactions to be observed much better than with solar-occultation techniques.

APPENDIX A

Bibliography

Menzies, R. T.: Laser Heterodyne Detection Techniques. Laser Monitoring of the Atmosphere, E. D. Hinkley, ed., Springer-Verlag, pp. 297-352, 1976.

Menzies, R. T.; and Shumate, M. S.: Tropospheric Ozone Distributions Measured With an Airborne Laser Absorption Spectrometer. J. Geophys. Res., vol. 83, no. C8, pp. 4039-4043, Aug. 20, 1978.

Shumate, M. S.; and Menzies, R. T.: The Airborne Laser Absorption Spectrometer - A New Instrument for Remote Measurement of Atmospheric Trace Gases. Proc. of Fourth Joint Conference on Sensing of Environmental Pollutants, American Chemical Soc., pp. 420-422, 1977.

Wiesemann, W.; Beck, R.; Englisch, W.; and Gürs, K.: In-Flight Test of a Continuous Laser Remote Sensing System. Appl. Phys., vol. 15, no. 3, pp. 257-260, Mar. 1978.

Experiment 11: Chemical Release Diagnosis

Description.- Measurement of motion, internal structure, and dissipation of artificial chemical releases (e.g., Na, Ba, Ba^+) to diagnose ionospheric fields and dynamics.

Implementation.- Resonant scattering using narrow-band, Nd:YAG pumped frequency-tuned dye laser with photon-counting PMT detection.

For one class of experiments the lidar could be hard mounted on the pallet (no pointing capability) and the Shuttle oriented such that the lidar line-of-sight cuts a swath across a previously deployed chemical release as the Shuttle passes nearby. For example, observations of the plasma structure in an ionized barium cloud could be carried out with a lidar system having the following parameters:

> Wavelength, 493.4 nm; laser line width, ≈1 pm (needed to selectively excite an optically thin Ba^+ line); laser stability, ≈0.2 pm; laser pulse energy, 0.02 J; repetition rate, 10 Hz; Ba^+ backscatter cross section, 2.4×10^{-14} cm^2 sr^{-1} ion^{-1} (for the odd mass, optically thin component of the 493.4 line); receiver diameter, 1 m; receiver FOV, 0.5 mrad; receiver detection efficiency, 0.12 (includes optics, filter, and PMT quantum efficiency); range to cloud, 100 km

The return signal for this case gives a single-pulse signal-to-noise ratio (SNR) of 4 for a 50 m thick (along the line-of-sight) plasma sheet with a Ba^+ density of 10^6 ions cm^{-3} appropriate to a 48 kg, 200 km barium release after 2 to 4 hr depending on wind velocity. Multipulse integration would permit longer range lidar observations, but at the expense of degraded spatial resolution.

For another class of experiments, the lidar could be provided with a high-accuracy pointing capability for mapping or following the evolution of chemical releases at long range. A steerable lidar with the parameters listed above (except for the receiver FOV of 0.1 mrad) could map a magnetospheric barium release at ranges beyond 10 000 km with a resolution of the order of 1 km in the transverse dimension and 30 km in the line-of-sight dimension. A 1 s integration time gives an SNR of 3, sufficient for mapping, for a cloud with an ion density of $\approx 10^4$ cm^{-3}, appropriate to a 16 kg magnetospheric barium release after 20 min. Such a cloud could be followed to later times, of the order of hours, with degraded spatial resolution. The pointing system for these experiments could be designed such that the orbiter provides gross pointing and the lidar mount provides only a vernier capability with a total excursion of a few (≈5) degrees and an absolute accuracy of 0.1 to 1 mrad, depending on the experiment. For release tracking the laser line width and stability requirements could be relaxed, at the expense of lower return signal.

All scenarios for this experiment are constrained by the limited viewing time per orbit and by the limited number of successive orbits during which the releases persist. Experiment data output and operating duration are extremely scenario dependent. The laser wavelength must be tuned in real time to compensate for the changing Doppler shift as the Shuttle moves by the release (maximum excursion ±0.015 nm with scenario-dependent tuning rates). Releases can be deployed from the Shuttle, ground-launched rockets, or the chemical-release satellite.

Feasibility.- 2B for hard-mounted system, 2C for the steerable system. The lidar technology is well proven by ground-based sodium-lidar experiments, but the steerable mounting and velocity-compensating wavelength controller will require a good deal of construction effort.

Needed development.- None for the hard-mounted system; pointing system development for the release-tracking version. Laser components will require construction effort but will not require new-technology development.

Discussion.- Chemical releases are effective tracers for neutral, plasma, electrodynamic, and magnetic processes occurring in the near Earth environment, contributing information on wave processes for scientific objective 5, species transport for scientific objective 6, and solar-induced effects for scientific objective 7. Dissipation mechanisms for ionospheric plasma structures, which interfere with communications systems, are not yet understood and can be derived from fly-by release diagnosis. Ion-cloud motions can be used to investigate the intensities and distributions of the Earth's electric and magnetic fields for both thermospheric and magnetospheric winds. The Ba^+ measurements discussed above are representative of a large class of release materials which could be observed by lidar. Na (589 nm), Ba (553.5 nm), AlO (484 nm), Li (670.7 nm), and Cs (852 nm) are other candidate release materials.

Further study is needed to determine those orbital/chemical-release scenarios where Shuttle mounting of the lidar is superior to ground operation of a similar system. In general, this will occur only where ground systems cannot be fielded or as part of a multiexperiment Shuttle investigation of magnetospheric/atmospheric processes.

Lidar provides the only technique for studying the 3-D power spectra of plasma irregularities in artificial releases. Lidar spatial resolution (≈50 m) is inferior to in situ rocket probes (≈1 m) and photography (≈10 m), but rocket probes provide only a single dimension of the cloud structure while photography (and photometry) provides only a measure of column content whose interpretation is subject to resonance-radiation transport contamination. Lidar also provides a unique nighttime tracking and diagnostic capability (for release locations and spatial scale lengths that are not suitable for observation by incoherent-scatter radar).

Bibliography

Adamson, D.; Fricke, C. L.; Long, S. A. T.; Landon, W. F.; and Ridge, D. L.: Preliminary Analysis of NASA Optical Data Obtained in Barium Ion Cloud Experiment of September 21, 1971. J. Geophys. Res., vol. 78, no. 25, pp. 5769-5784, Sept. 1, 1973.

Rees, D.; and Sandford, M. C. W.: Thermospheric Winds From Laser Tracking of Sodium Clouds. Nature, vol. 252, no. 5481, pp. 291-292, Nov. 22, 1974.

APPENDIX A

Experiment 12: Stratospheric Ozone Concentration Profiles

Description.- Measurement of stratospheric ozone concentration between 35 and 50 km and between 15 and 35 km from orbital altitudes using differential range absorption techniques at UV wavelengths in order to provide global scale information on ozone vertical distribution. Data address a number of science objectives in the climate and environmental areas.

Implementation.- Instrumentation: 1 m diameter receiver; standard Nd:YAG laser quadrupled to 265 nm at 0.10 J and 10 Hz; 1 mrad FOV; 0.1 nm FWHM wavelength filter; 15-percent system optical efficiency; and PMT detectors with QE approximately 20 percent. The experiment can be readily performed from orbital altitudes of 250 to 300 km at night. The simulations shown in figure A9 have been performed for a standard midlatitude ozone profile, 1000 km horizontal (along-track) and 2 km vertical resolution. The top curve of figure A9 indicates that for the quadrupled Nd laser (265 nm) the altitudes of better than 10-percent accuracy are 38 to 48 km (peak accuracy of ≈5 percent around 42 km). In addition, the doubled Nd:YAG output could be used to pump a dye whose output can be doubled into the 280 to 300 nm spectral region at 0.01 J and 10 Hz. Narrow spectral bandwidth and stability are not required for these experiments. Bandwidths of only ≦1 nm and stability of ≦0.5 nm are sufficient. Operational altitudes can be changed by using various dye wavelength combinations. As an example, the 290 nm simulation is shown as the lower curve in the figure. The altitude range is from 20 to 32 km (peak accuracy of ≈6 percent at an altitude of 24 km).

Feasibility.- 1B (quadrupled Nd:YAG)/2B (double dye). Ground-based UV DIAL measurements have demonstrated the viability of the experimental concept.

Needed development.- System development studies for functional dye or other laser output energies of 0.1 to 1 J at these wavelengths for a 10 Hz repetition rate. Experimental demonstration of hardware. Newer, more powerful lasers such as the krypton-fluoride laser could be used to generate four or five simultaneous discrete frequencies by Stokes tuning at output energies of 0.1 J at 10 Hz. With these energies, the same accuracies as above are obtained but for 100 km horizontal resolutions. In this manner, the entire stratosphere could be probed at once with high accuracy.

Discussion.- Information on ozone number density addresses the requirements of scientific objectives 2 and 7. Lower stratospheric ozone is useful as a tracer for studying stratospheric motions. Upper stratospheric ozone is most sensitive to photochemical changes arising from pollutants such as the CFM's and NO_X's. Shuttle lidar measurements of stratospheric ozone number density with 100 km horizontal resolution would provide better spatial resolution with approximately the same accuracy as passive sensors and would provide profile data at a much higher rate with greater geographic coverage per orbit throughout the night side of the orbit. Supporting meteorological data are necessary to define the contributions of the molecular backscattering to the retrieval of ozone number density profiles.

APPENDIX A

Bibliography

Gibson, A. J.; and Thomas, L.: Ultraviolet Laser Sounding of the Troposphere and Lower Stratosphere. Nature, vol. 256, no. 5518, pp. 561-563, Aug. 14, 1975.

Megie, G.; Allain, J. Y.; Chanin, M. L.; and Blamont, J. E.: Vertical Profile of Stratospheric Ozone by Lidar Sounding From the Ground. Nature, vol. 270, no. 5635, pp. 329-331, Nov. 24, 1977.

Uchino, O.; Maeda, M.; Kohno, J.-I.; Shibata, T.; Nagasawa, C.; and Hirono, M.: Observation of Stratospheric Ozone Layer by a XeCl Laser Radar. Appl. Phys. Lett., vol. 33, no. 5, pp. 807-809, Nov. 1978.

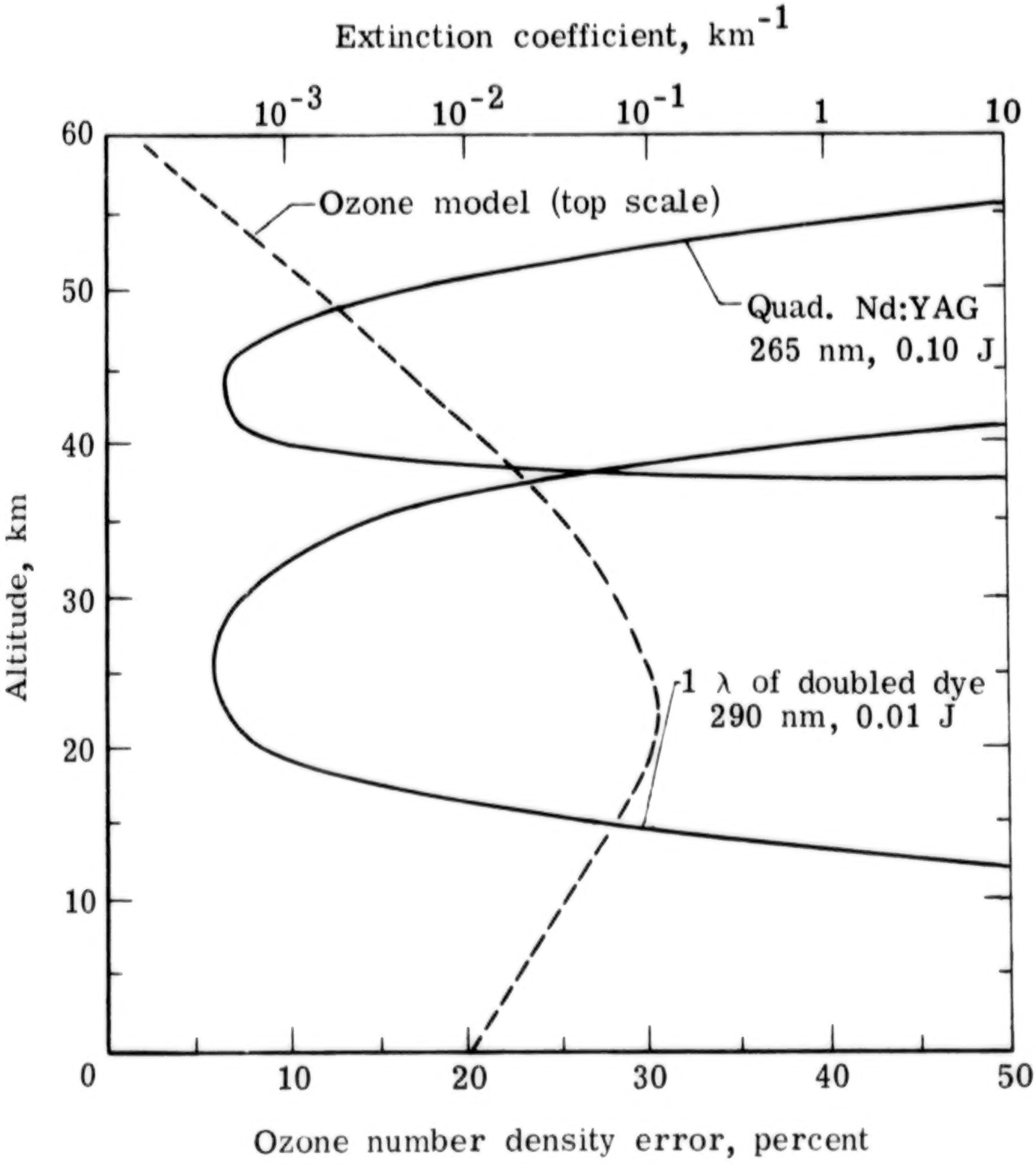

Figure A9.- Ozone number density error.

APPENDIX A

Experiment 13: Upper Atmospheric Trace Species Measurements Using Two-Satellite Occultation

Description.- Trace species having absorption bands in the 3.5 to 15.0 μm region are measured with high accuracy, day or night, by direct absorption of IR laser radiation transmitted between two satellites. Typical species include O_3, ClO, $ClONO_2$, H_2O, H_2O_2, the CFM's, C_2H_3Cl, C_2H_4, CCl_4, HNO_3, NH_3, etc. Use of a retroreflector or detection system on the "passive" satellite allows highly sensitive measurements over long path lengths. Such measurements are important in providing data for evaluating stratospheric/mesospheric models and in studying the coupling of dynamical, chemical, and radiative processes. Laser power requirements are low since a cooperative target is used, and a variety of tunable lasers may eventually be used to reach nearly all desired species. Figure A10 shows acceptable two-satellite transmitter power as a function of transmitter/receiver separation for several values of integration time from 10^{-3} to 1 s for a 25 cm telescope, transmitter/receiver system. Transmitted beam is diffraction limited for 25 cm diameter aperture, and a 1 m diameter retroreflector is assumed. Figure A11 shows two-satellite transmitted power as a function of transmitter/receiver diameter for a 4000 km separation, for integration times varying from 10^{-3} to 1 s. Transmitter powers in these cases do not exceed 25 mW, for telescope diameters up to 1 m.

Implementation.- A continuous-wave CO_2 laser could be used initially for limited trace species measurements to demonstrate feasibility for differential absorption using heterodyne measurements. Both Shuttle and daughter satellites could be placed in an orbit with the same inclination and in the same orbital plane. Rises and sets for occultation are slow, providing capability of relatively long integration times but with poor longitude-latitude resolution. The mission would provide continuous measurements at slowly varying altitudes, lasting on the order of one or more days, depending upon how the phasing maneuvers are accomplished. Scientific measurements would be directed toward those trace species requiring long integration times or those whose spatial distributions are not expected to show strong longitude-latitude or temporal variability. To accomplish more sophisticated scientific measurements, a noncoplanar geometry could be used with the same orbit inclination and altitude. For example, two satellites having an orbit inclination of 57° with an angular separation between the orbital plans of 150° and an altitude of 450 km would provide complete geographical coverage in a band from -5° to +5° latitude over a measurement time of 30 days. To increase latitude coverage for a dual satellite mission from ±5° to ±30°, an orbital mission with different orbit inclinations and altitudes can be implemented using noncoplanar geometry.

Needed development.- A mathematical inversion model should be developed to assess the effects of various measurement errors on the accuracy of the vertical profiles of trace species measured with the dual satellite technique. The model should be an end-to-end model converting the laser radiance collected by the optical receiver, processed by the optical receiver optics and electronics, and inverted to produce vertical profiles. Errors in the retrieved profiles can be due to the following uncertainties:

(1) Pointing effects: Compensation for beam steering effects due to atmospheric refraction; errors due to pointing and tracking jitter.

(2) Orbital effects: Doppler shift compensation; rise and set times for various orbital missions.

(3) Laser/receiver parameters: Requirements for laser line shape, position, and stability; data sampling errors; noise in heterodyne receivers; scanning versus fixed frequency; laser beam intensity distribution.

(4) Inversion effects: Target point pressure uncertainty; refraction effects; line selection criteria for reducing atmospheric interference effects.

A near-term design study should be performed to determine the trade-offs between pointing and tracking requirements for various orbital missions to assess rise/set times, simultaneous multispecies measurement strategy, and atmospheric refraction effects resulting in beam steering effects at the optical receiver.

Feasibility.- 2C/3C. An atmospheric inversion model of passive solar occultation experiments has been used to predict expected sensitivities in the vertical profile of a dual satellite, differential heterodyne measurement. Figure A12 shows the expected retrieval of a two-satellite measurement for O_3 from 10 to 60 km with an integration time of 0.1 s. Similar results have been obtained for ClO and HNO_3. Laser and detector requirements have already been demonstrated. However, pointing requirements near the limit of projected Shuttle capabilities make the rating 2C for a system using CW lasers. Utilizing tunable lasers (such as laser diodes) to enhance trace species detection capability would require a 3C rating. In addition, the rating would vary with the target species and orbital mission chosen. For example, in measurements of minor trace species such as ClO where absorption coefficients are relatively small, an orbital mission in which Shuttle and daughter satellite are in the same orbital plane inclination could provide the required integration time for measuring ClO to high precision and accuracy. For more sophisticated scientific missions requiring multispecies vertical profile measurements, trade-off studies must be conducted to interface species selection with the orbital mission parameters.

Discussion.- The two-satellite approach can address scientific objectives 1, 2, and 4. Listed in table AI are examples of species which could be measured, and expected measurement accuracies assuming the dominant error effects are shot-noise effects induced by the laser local oscillator of the heterodyne optical receiver. More detailed calculations considering other potential noise effects discussed previously should be performed to determine realistic retrieval accuracies of a two-satellite measurement. The most important advantages of the two-satellite measurement of species are the broad temporal and spatial coverages obtained by selecting different satellite orbits. Solar occultation measurements are restricted to only two local-time measurements during a mission. The integration time necessary for a solar occultation measurement to a certain accuracy is approximately a factor of 10 greater than the time necessary for the two-satellite measurement. Thus, for the same vertical resolution the two-satellite measurement has the potential of improving the measurement uncertainty by a factor of 3 for species such as O_3, ClO, and HNO_3.

Bibliography

Menzies, R. T.; and Shumate, M. S.: Tropospheric Ozone Distributions Measured With an Airborne Laser Absorption Spectrometer. J. Geophys. Res., vol. 83, no. C8, pp. 4039-4043, Aug. 20, 1978.

Peyton, B. J.; Lange, R. A.; Savage, M. G.; Seals, R. K.; and Allario, F.: Infrared Heterodyne Spectrometer Measurements of Vertical Profile of Tropospheric Ammonia and Ozone. AIAA Paper 77-73, Jan. 1977.

TABLE AI.- EXAMPLES OF SPECIES TO BE MEASURED

[Day or night operation; ΔX = 200 km; ΔZ = 1 km; satellite separation, 4000 km; typical absorption length, 200 km; collector diameter, 1 m; $P_n = 10^{-19}$ W/Hz]

Species	Typical altitude regions, km	Predicted error, percent (a)	Species	Typical altitude regions, km	Predicted error, percent (a)
Discretely tunable CW CO_2 laser			Tunable lasers in 2 to 9 μm region		
O_3	10 to 70	2	HCl	20 to 30	5
ClO	30 to 35	20	OH	50 to 60	20
$ClONO_2$	20 to 30	---	HO_2	25 to 35	20
H_2O	10 to 30	2	CH_4	10 to 20	5
H_2O_2	25 to 35	---	NO	45 to 55	[b]20
CFM's	10 to 20	20	NO_2	35 to 45	10
C_2H_3Cl	10 to 20	10	N_2O	10 to 30	[b]5
C_2H_4	10 to 20	10	CO_2	10 to 30	5
CCl_4	10 to 20	10		70 to 100	---
HNO_3	10 to 20	10			
NH_3	10 to 20	5			

[a] This represents average predicted error in gas concentration over altitude range indicated. Optimum available laser line was chosen for average gas concentration over specified altitude range.

[b] Can be reached with doubled CO_2.

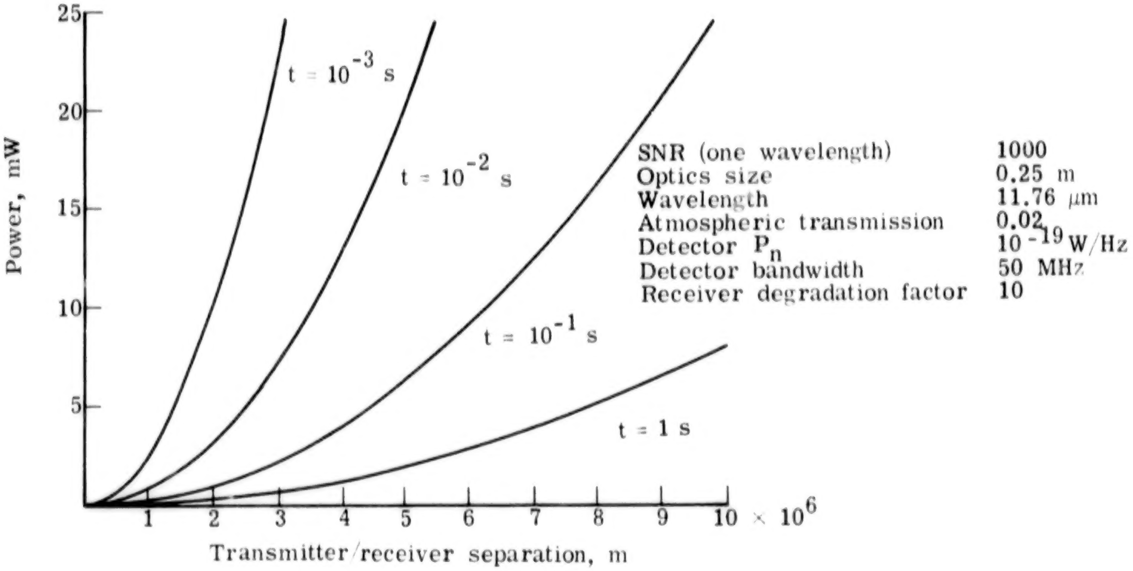

Figure A10.- Transmitted power as function of transmitter/receiver separation for two-satellite operation.

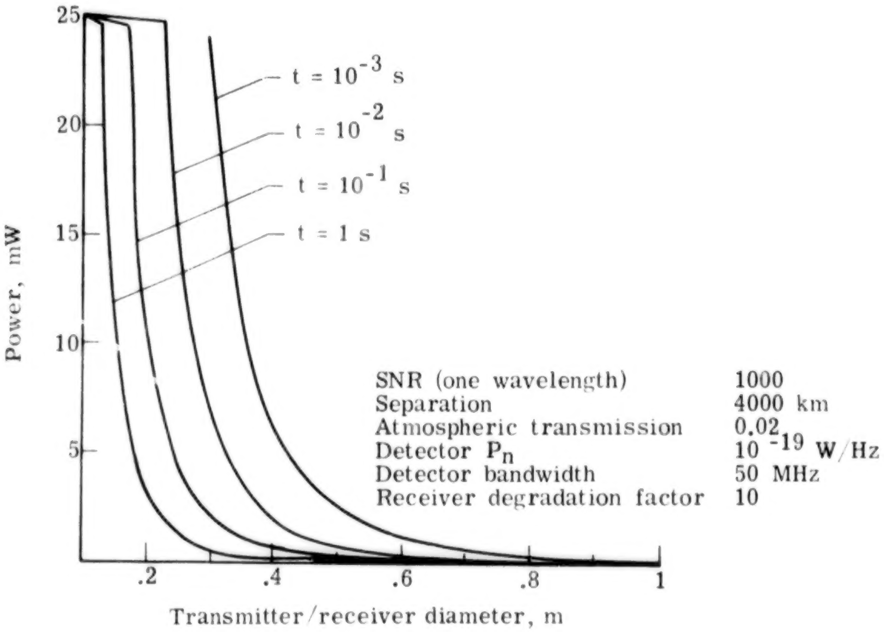

Figure A11.- Transmitted power as function of transmitter/receiver diameter for two-satellite operation.

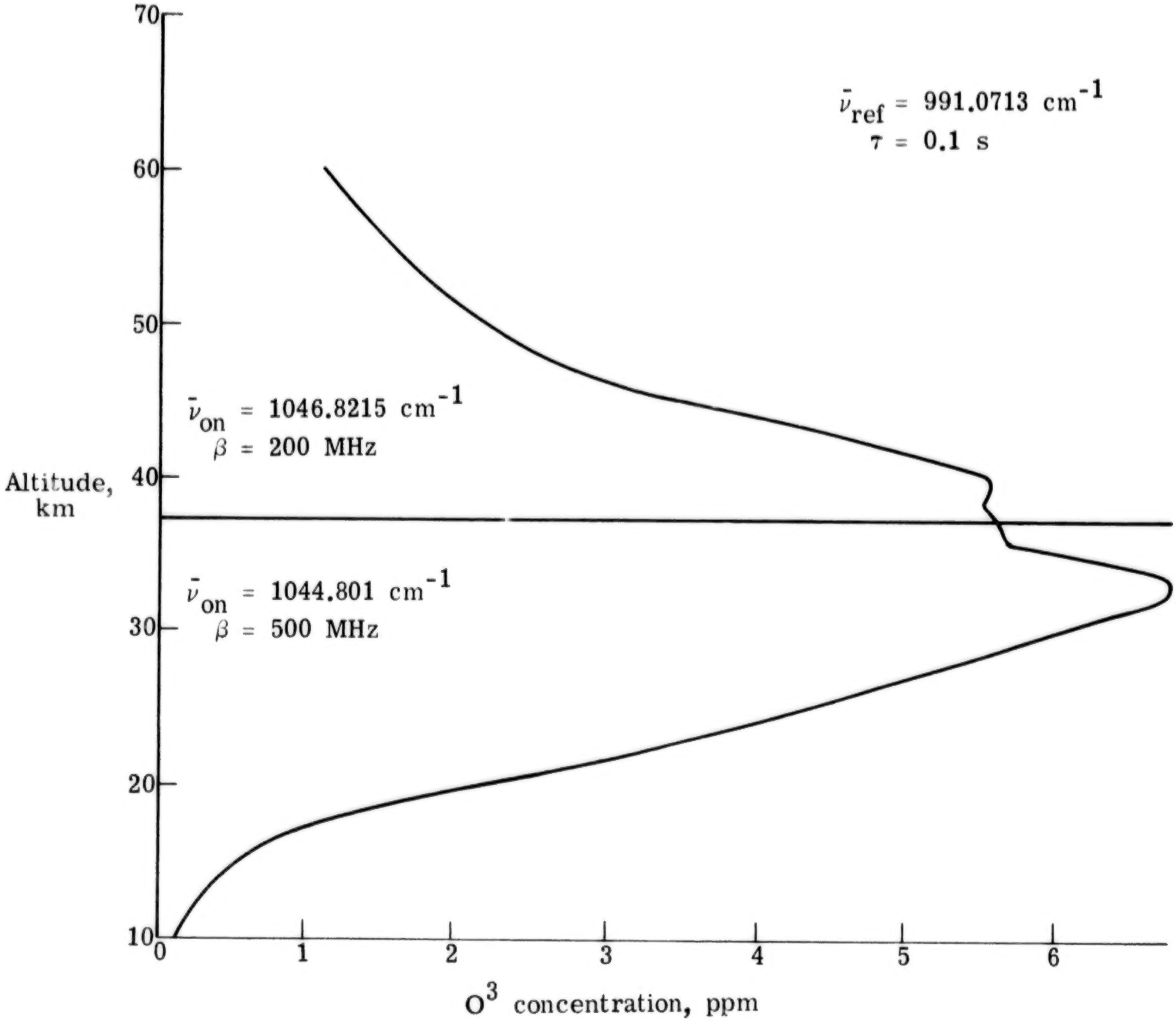

Figure A12.- Two-satellite measurement of O_3 from Shuttle lidar.

APPENDIX A

Experiment 14: Sodium Temperature and Winds

Description.- Analysis of the backscattered signal by resonance fluorescence techniques from the region near 90 km to determine the altitude distribution of sodium, its temperature, and winds in the sodium layer. Nighttime and daytime measurements will provide information concerning the dynamics of an important region of the atmosphere about which little is known.

Implementation for wind measurement.- A narrow-band ($\leq 10^{-3}$ nm) dye laser with standard Nd:YAG (doubled). The frequency stability of the laser should be $\leq 5 \times 10^{-4}$ nm for the wind measurement. The detector requires a high-resolution dispersive element. In order to measure two components of the wind vector, two different pointing directions will be needed. The accuracy with which the wind is measured depends on knowing the pointing direction a posteriori with an accuracy of 1 min of arc or better, or by using the ground return to determine a Doppler reference for the lidar. The error in the horizontal component of the wind has been determined to be 5 m/s for a nighttime measurement with the following parameters:

> Wavelength, 589 nm; laser pulse energy, 0.1 J; laser bandwidth, 10^{-3} nm; laser repetition rate, 10 Hz; Shuttle altitude, 250 km; telescope diameter, 1 m; vertical resolution, 1 km; horizontal resolution, 300 km; cross section 5.6×10^{-12} cm^2; Na density, 5×10^3 cm^{-3}; thermal line width^2 at 200 K, 1.23×10^{-3} nm; pointing accuracy, 2.4×10^{-5} rad (5 arc s)

The simulation was done with a Fabry-Perot interferometer and a 12 ring anode detector, with the following characteristics:

> Free spectral range, 1.37×10^{-2} nm; reflectivity 0.9; spectral scan, 1.37×10^{-2} nm; quantum efficiency, 10 percent; optical efficiency (other than Fabry-Perot), 0.05; detector resolution, 10^{-3} nm

The calculation was done with the line-of-sight at 45° with the vertical direction; the angle between the horizontal component of the line-of-sight and the velocity vector of the Shuttle was 45°. The accuracy with which the wind is measured depends on having a posteriori knowledge of the pointing direction. The ground return is useful in obtaining attitude knowledge. Due to the presence of clouds, however, the ground return information may not always be available.

Implementation for temperature measurement.- If one uses a laser emitter with a spectral width of 10^{-3} nm, successively centered on the maximum and the minimum of the absorption factor, one can deduce the temperature value from the backscattered intensity ratio. For an accuracy equal to 2.5 percent, the necessary photoelectron number is about 10^4. The laser line must be centered with an accuracy better than one-tenth of the emitted line width.

For the case of 0.1 J at 10 Hz, a 5 K accuracy can be obtained with 176 km horizontal resolution at night and 400 km during the daytime. The vertical resolution is 1 km. This is a conservative estimate since lasers with more power at narrower bandwidths are available which would improve the results considerably.

Feasibility.- 3B if only a temperature measurement is done; 3C if the wind measurement is included. The C-rating is given if a special pointing system is used.

Needed development.- The Fabry-Perot detection system needs design study based on current technology.

Discussion.- Addresses scientific objectives 5, 6, and 7. This is a measurement which provides information concerning the dynamics of an important region of the atmosphere about which very little is known.

Wind measurements in the mesosphere can be done passively with a Fabry-Perot interferometer or a gas correlation radiometer. These techniques involve limb scanning observations. A lidar technique, however, provides better spatial resolution, which is essential to achieve the scientific objectives of the measurement.

Bibliography

Abreu, Vincent J.: Wind Measurements From the Shuttle Using a Lidar System With Incoherent Detection: An Analysis. Appl. Opt., vol. 18, Sept. 1979. (To be published.)

Chamberlain, Joseph W.: Physics of the Aurora and Airglow. Academic Press, Inc., 1961.

APPENDIX A

Experiment 15: Surface Pressure and Cloud-Top Pressure and Height Measurement

Description.- Accurate measurement of atmospheric pressure at the Earth's surface and of pressure and altitude at cloud tops using O_2 A-band absorption lines. Surface pressure is a fundamental meteorological variable needed in weather forecasting and in general circulation models. Cloud-top pressure can also be used similarly.

Implementation.- Frequency-doubled Nd:YAG pumping a tunable, two-wavelength dye laser operating near 760 nm. A wavelength between two strong (and reasonably temperature-insensitive) O_2 absorption lines is used as shown in figure A13 in conjunction with a reference wavelength in an adjacent line-free region with a shift of 0.1 to 1 nm. Differences in the two lidar returns can be interpreted in terms of surface pressure and pressure profiles. (See experiment 16.) Cloud-top altitude is given by the time record of the lidar return. The outgoing laser pulse energy is measured in order to stabilize the amplitude of the lasers. Dual channel detection will be used to separate the two laser pulse returns. The simulation used the following parameters:

> Laser pulse energy, 0.05 J; repetition rate, 10 Hz; laser line width, 0.003 nm; laser frequency stability, 0.0005 nm; PM quantum yield, 0.12; optical efficiency, 0.35; receiver area, 10^4 cm^2; FOV, 10^{-6} sr; detector bandwidth, 1 nm; Earth albedo of 0.1; cloud albedo of 0.5; clouds, 0 to 8 km; O_2, 21 percent uniformly mixed; Shuttle altitude, 200 km

These simulations give surface pressure accuracy at 760.0263 nm of 0.2 percent for $\Delta X = 100$ km as shown in figure A14. The corresponding cloud-top pressure-height measurements yield pressure accuracies ranging from 0.2 percent at 0.5 km to 0.1 percent at 6.5 km for $\Delta X = 16$ km. Simulations also show that the spatial resolution of the surface pressure measurement can alternatively be improved to 5 km using the region at 760.11 nm while maintaining the surface pressure accuracy of 0.2 percent. The accuracy or spatial resolution of the cloud top and pressure profile experiments would, however, be degraded significantly. Both measurements would use both day and night operation. Range cells of 20 m are desirable (50 m required) for data acquisition in order to locate the altitude of pressure determinations to 5 m accuracy. The off-line laser can be broad band in either case (0.01 to 0.05 nm).

Feasibility.- 3B. On the basis of laser operation alone, this would be a 2-rated experiment due to similar requirements to experiment 9 in a similar spectral region. The 3-rating reflects the lack of a field demonstration needed for such a high-precision measurement.

Needed development.- Use of Nd:YAG (doubled) to pump a dye at 760 nm may require some development. Additional ground-based lidar tests are an essential prelude to flight measurements. Further numerical simulations should be carried out to clarify the advantages of narrow-band versus broad-band laser operation, including the influence of O_2 fluorescence and the different degrees of total extinction inherent in the two methods.

Discussion.- This experiment addresses objective 4 (Augmentation of the Meteorological Data Base). Surface pressure measurements allow temperature profiles obtained with IR sounders to be interpreted in terms of pressure profiles and thus circulation patterns.

Surface pressure and cloud-top pressure heights currently cannot be measured remotely. No passive method has been put forth that can make this measurement from a space platform. A microwave experiment for the measurement of surface pressure has been proposed and should be evaluated simultaneously with lidar. Comparison experiments between lidar and microwave would be a valuable use of Shuttle capability. Shuttle performance data will provide a good check on suitability of the method for operational use.

Bibliography

Burch, Darrell E.; and Gryvnak, David A.: Strengths, Widths, and Shapes of the Oxygen Lines Near 13,100 cm^{-1} (7620 Å). Appl. Opt., vol. 8, no. 7, pp. 1493-1499, July 1969.

Kalshoven, James Edward, Jr.; and Korb, Charles Laurence: Engineering a Laser Remote Sensor for Atmospheric Pressure and Temperature. NASA TM-79538, 1978.

Korb, C. Laurence: A Laser Technique for the Remote Measurement of Pressure in the Troposphere. Paper presented at Eighth International Laser Radar Conference (Drexel Univ., Philadelphia, Pa.), June 6-9, 1977.

Singer, S. Fred: Measurement of Atmospheric Surface Pressure With a Satellite-Borne Laser. Appl. Opt., vol. 7, no. 6, pp. 1125-1127, June 1968.

Wark, D. Q.; and Mercer, D. M.: Absorption in the Atmosphere by the Oxygen "A" Band. Appl. Opt., vol. 4, no. 7, pp. 839-844, July 1965.

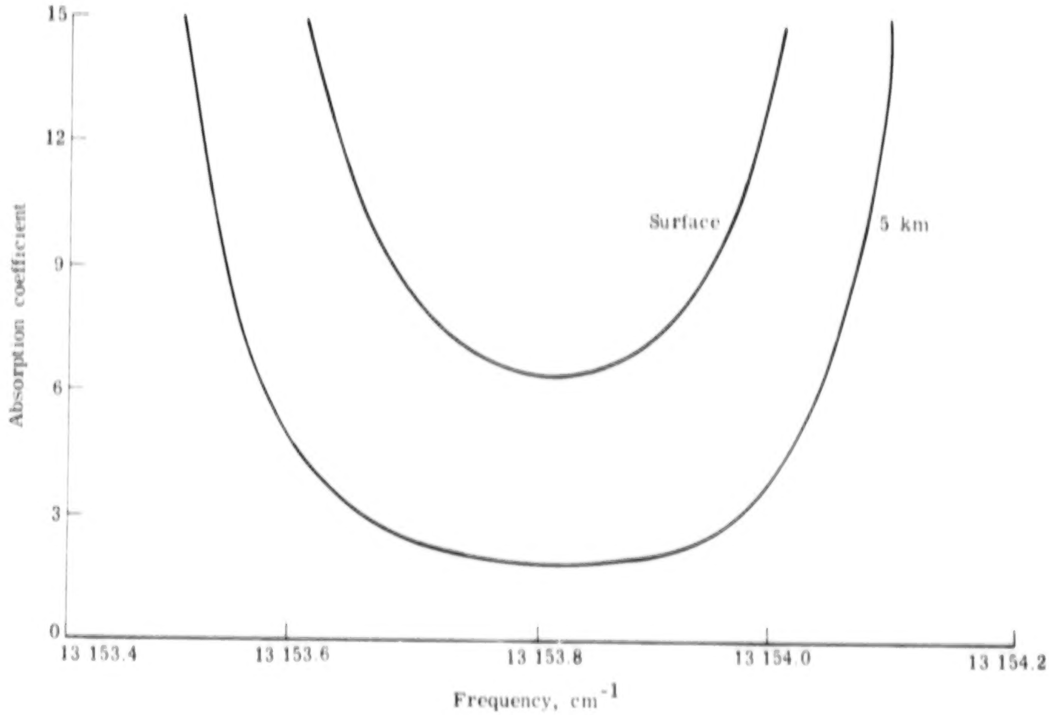

Figure A13.- Two-path atmospheric absorption coefficient for oxygen from Shuttle to Earth's surface and to 5 km altitude.

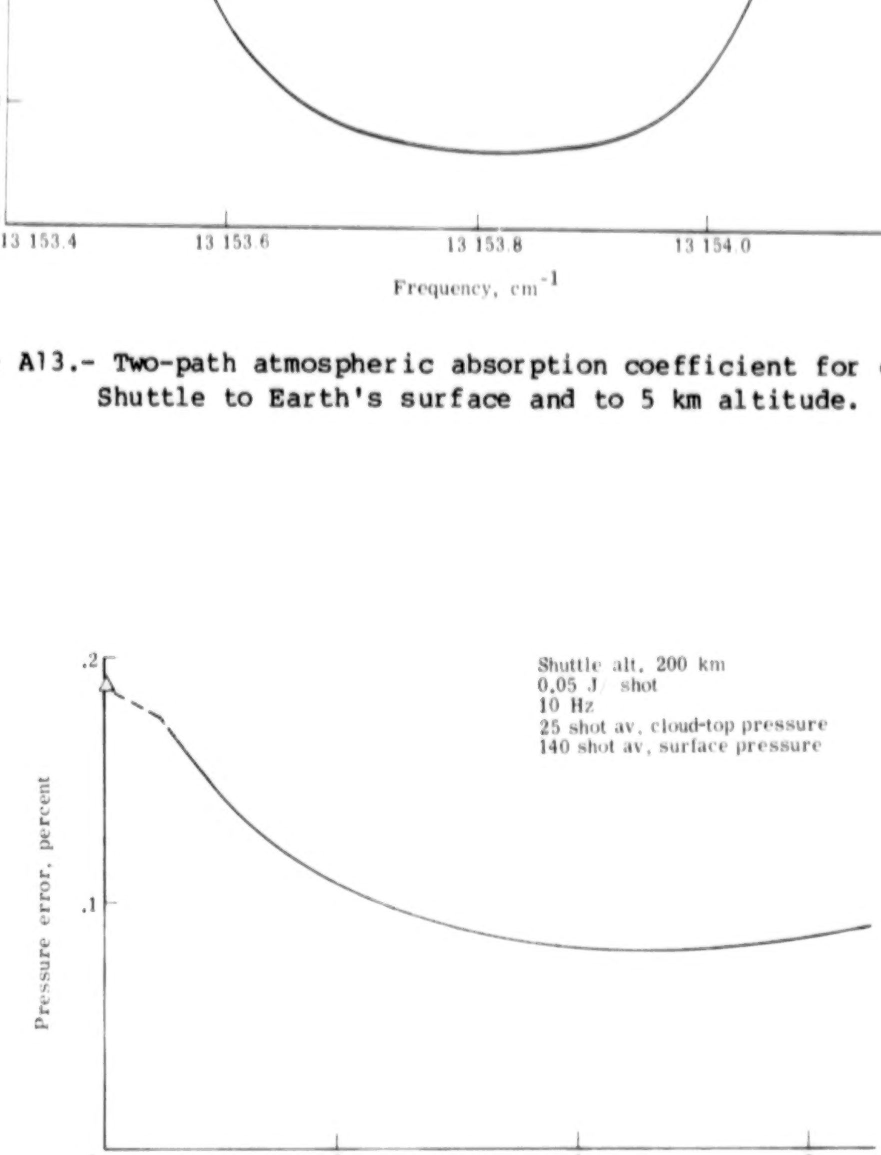

Figure A14.- Simulation of pressure measurement accuracy from Shuttle for surface pressure (100 km) and cloud-top pressure heights (16 km).

Experiment 16: Vertical Profiles of Atmospheric Pressure

Description.- Tropospheric pressure profiles will be measured using a differential absorption method employing larger spatial resolution elements than in experiment 15. The emphasis in Shuttle measurements will be on testing and refining the technique for ultimate operational use. The pressure profile is a basic meteorological quantity needed both in weather forecasting and in general circulation modeling.

Implementation.- A frequency doubled Nd:YAG laser is used to pump a tunable, two-wavelength dye laser operating near 760 nm. The measurements are similar to those of experiment 15 except that larger resolution elements permit sufficient pulse integration for DIAL measurements within the atmosphere. Nighttime operation certain, daytime operation possible with a 10^{-7} sr FOV and a 0.02 nm detection bandwidth. With a narrow-band laser method, the spatial resolution is $\Delta Z = 1$ km, $\Delta X = 500$ km. Shuttle simulation results given in figure A15 for a pressure sensitive wavelength of 760.0263 nm indicate that pressure measurement accuracies of 0.3 percent can be obtained for the lower troposphere using multipulse averaging techniques. The simulation used the following parameters:

> Laser pulse energy, 0.05 J; repetition rate, 10 Hz; laser line width, 0.003 nm; laser frequency stability, 0.0005 nm; PM quantum yield, 0.12; optical efficiency, 0.35; receiver area, 10^4 cm^2; FOV, 10^{-6} sr; detector bandwidth, 1 nm; Earth albedo, 0.1; cloud albedo, 0.5; clouds, 0 to 8 km; O_2, 21 percent uniformly mixed; Shuttle altitude, 200 km

For this experiment, range cells of 50 m are desirable (100 m required) in order to accurately locate the height of the pressure measurement. The off-line laser can be broad band (0.01 to 0.05 nm). Analytic models have been developed from which the pressure can be calculated, given calibration data. These models include desensitizing the measurements to the effects of temperature variations and changes in laser intensity and frequency.

Feasibility.- 3C. On the basis of laser operation alone, this would be a 2-rated experiment due to similar requirements to experiment 9 in a similar spectral region. The 3-rating reflects the lack of a field demonstration needed for such a high-precision measurement.

Needed development.- Use of Nd:YAG (doubled) to pump a dye at 760 nm may require some development. Additional ground-based lidar tests are an essential prelude to flight measurements. Further numerical simulations should be carried out to clarify the advantages of narrow-band versus broad-band laser operation, including the influence of O_2 fluorescence and the different degrees of total extinction inherent in the two methods.

Discussion.- This experiment addresses objective 4 (Augmentation of the Meteorological Data Base), objective 3 (Evaluation of Radiative Models of the Atmosphere), and provides correlative data for objective 7 (Magnetospheric

Aspects of Sun/Weather Relationships). Pressure profiles may be used to calculate temperature profiles and winds and are currently obtained only from radiosonde measurements.

Lidar offers the capability for remote sensing of the pressure profile in the lower troposphere to an accuracy of 0.3 percent. No other remote method has been proposed for this measurement. Moreover, remotely sensed pressure profiles would provide data suitable not only for temperature profile and wind determination but also for initialization of general circulation models and for weather prediction.

Bibliography

Burch, Darrell E.; and Gryvnak, David A.: Strengths, Widths, and Shapes of the Oxygen Lines Near 13,100 cm^{-1} (7620 Å). Appl. Opt., vol. 8, no. 7, pp. 1493-1499, July 1969.

Kalshoven, James Edward, Jr.; and Korb, Charles Laurence: Engineering a Laser Remote Sensor for Atmospheric Pressure and Temperature. NASA TM-79538, 1978.

Korb, C. Laurence: A Laser Technique for the Remote Measurement of Pressure in the Troposphere. Paper presented at Eighth International Laser Radar Conference (Drexel Univ., Philadelphia, Pa.), June 6-9, 1977.

Singer, S. Fred: Measurement of Atmospheric Surface Pressure With a Satellite-Borne Laser. Appl. Opt., vol. 7, no. 6, pp. 1125-1127, June 1968.

Wark, D. Q.; and Mercer, D. M.: Absorption in the Atmosphere by the Oxygen "A" Band. Appl. Opt., vol. 4, no. 7, pp. 839-844, July 1965.

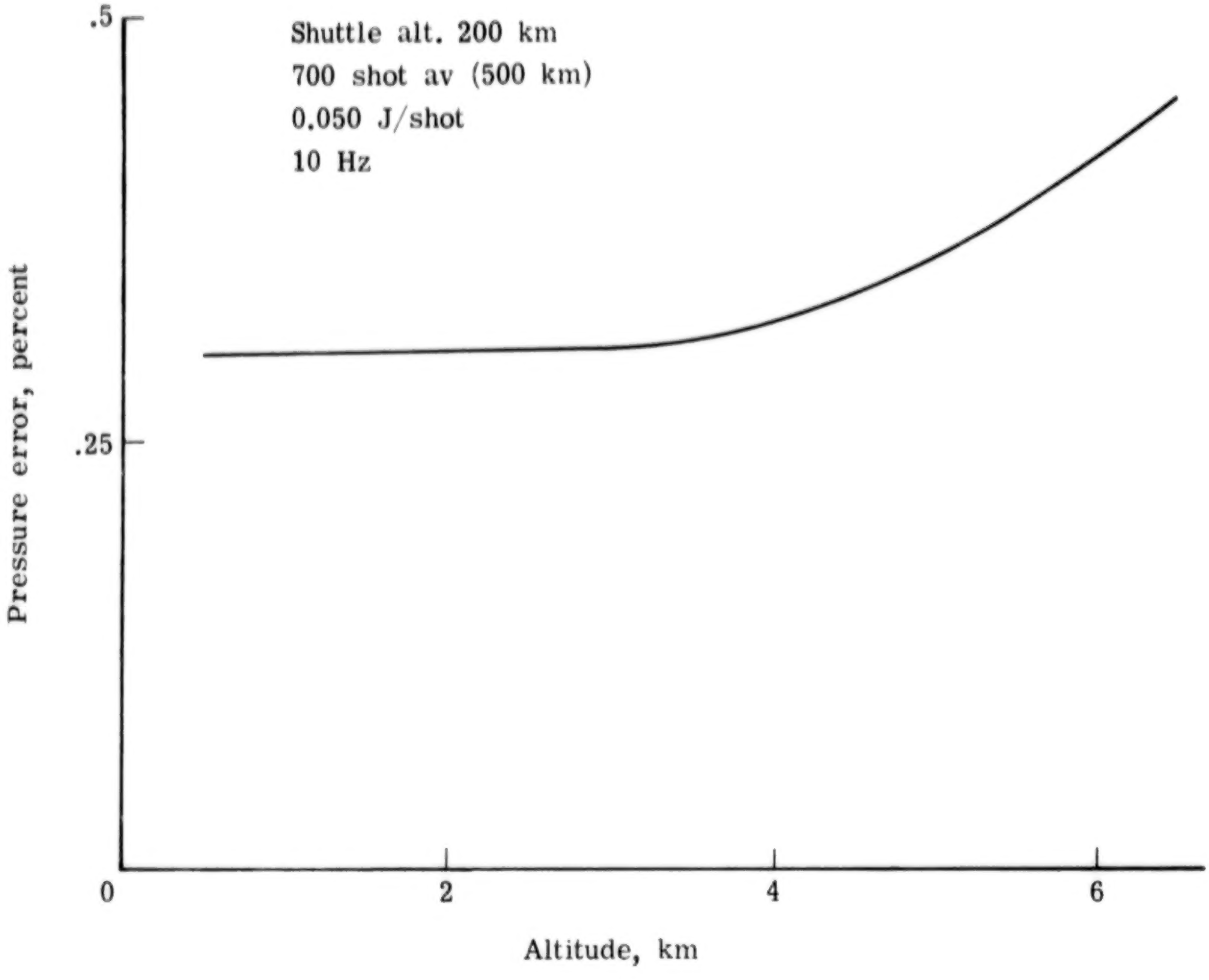

Figure A15.- Pressure profiling accuracy for Shuttle simulation at 760.0263 nm for vertical resolution of 1 km.

Experiment 17: Temperature Profile

Description.- Measure the temperature profile in the troposphere or in the region of the tropopause with a DIAL technique. Demonstrate that lidar can meet the accuracy and vertical resolution requirements on temperature profile measurements for the NASA climate program and GARP and for stratosphere/troposphere exchange studies.

Implementation.- A standard frequency doubled Nd:YAG laser is used to pump a tunable, two-wavelength dye laser operating near 770 nm. The experiment uses a high J rotational line in the oxygen A-band near 770 nm to obtain a strong dependence of absorption coefficient on temperature (as high as the sixth power of temperature) primarily through the dependence of the population of a state on temperature through the Boltzmann term. A second nearby wavelength with a bandwidth of 0.01 to 0.05 nm with a shift of 0.1 to 0.5 nm is used as a reference for the DIAL measurement. The use of a single temperature sensitive line for the measurement, rather than the use of a ratio of two temperature sensitive lines as has been discussed by Mason, leads to greatly increased experiment sensitivity. Simulations using the following parameters are shown in figures A16 and A17 for a spatial resolution of 500 km:

> Laser pulse energy, 0.05 J; repetition rate, 10 Hz; laser line width, 0.002 nm; laser frequency stability, 0.0005 nm; PM quantum yield, 0.12; optical efficiency, 0.35; receiver area, 10^4 cm^2; FOV, 10^{-6} sr; detector bandwidth, 1 nm; range bin, 100 m; Earth albedo of 0.1; cloud albedo of 0.5; clouds, 0 to 8 km; O_2, 21 percent uniformly mixed; Shuttle altitude, 200 km

Figure A16 shows that for the oxygen line located at a wavelength of 769.0215 nm temperature accuracies of the order of 1 K can be obtained for measurements in the troposphere with a vertical resolution of 2 km. The line strength used for this simulation was 2.0×10^{-3} g^{-1} cm^2 cm^{-1}. The results of a simulation at 768.380 are shown in figure A17 for vertical resolutions of 2 and 3 km. As shown, for a 3 km vertical resolution the measurements may be extended into the region of the tropopause and lower stratosphere with an accuracy as high as 1 K. The line strength used for this latter simulation was 4.1×10^{-3} g^{-1} cm^2 cm^{-1}. The above simulations pertain to nighttime background conditions. Daytime measurements may be feasible with a 10^{-7} sr FOV and a 0.02 nm detection bandwidth.

Feasibility.- 3C. Has not yet been experimentally demonstrated although water-vapor differential absorption measurements with comparable spectral resolution requirements have been performed in the same spectral region.

Needed development.- Use of Nd:YAG (doubled) to pump laser at 770 nm may require some development. Also, demonstration and testing of a ground-based lidar experiment is needed.

Discussion.- This experiment addresses objectives 1, 3, 4, and 7. Temperature profile measurements in the tropopause region can define the height of the tropopause and thus address the stratosphere/troposphere exchange problem (objective 1) and provide information for radiative transfer models (objective 3). Studies by both the Goddard Institute of Space Sciences and the

National Meteorological Center show that improved temperature accuracy and vertical resolution over those from current passive techniques are required for improved weather forecasts (objective 4).

Lidar has the capability for direct measurement of the temperature profile to accuracies of 1 K with a vertical resolution of 2 km for measurements in the troposphere, or 3 km in the region near the tropopause. In contrast, passive infrared and microwave temperature sounders are limited in vertical resolution to 5 to 10 km and have temperature profile accuracies of 2.5° although the accuracies are somewhat poorer near the Earth's surface and near the tropopause. In addition, the passive temperature sounding methods require the use of inversion techniques to recover the temperature profile, whereas lidar provides a direct measurement of the temperature profile.

Bibliography

Burch, Darrell E.; and Gryvnak, David A.: Strengths, Widths, and Shapes of the Oxygen Lines Near 13,100 cm^{-1} (7620 Å). Appl. Opt., vol. 8, no. 7, pp. 1493-1499, July 1969.

Kalshoven, James Edward, Jr.; and Korb, Charles Laurence: Engineering a Laser Remote Sensor for Atmospheric Pressure and Temperature. NASA TM-79538, 1978.

Mason, James B.: Lidar Measurement of Temperature: A New Approach. Appl. Opt., vol. 14, no. 1, pp. 76-78, Jan. 1975.

McClatchey, R. A.; Benedict, N. S.; Clough, S. A.; Burch, D. E.; Calfee, R. F.; Fox, K.; Rothman, L. S.; and Garing, J. S.: AFCRL Atmospheric Absorption Line Parameters Compilation. AFCRL-TR-73-0096, U.S. Air Force, Jan. 1973. (Available from DDC as AD 762 904.)

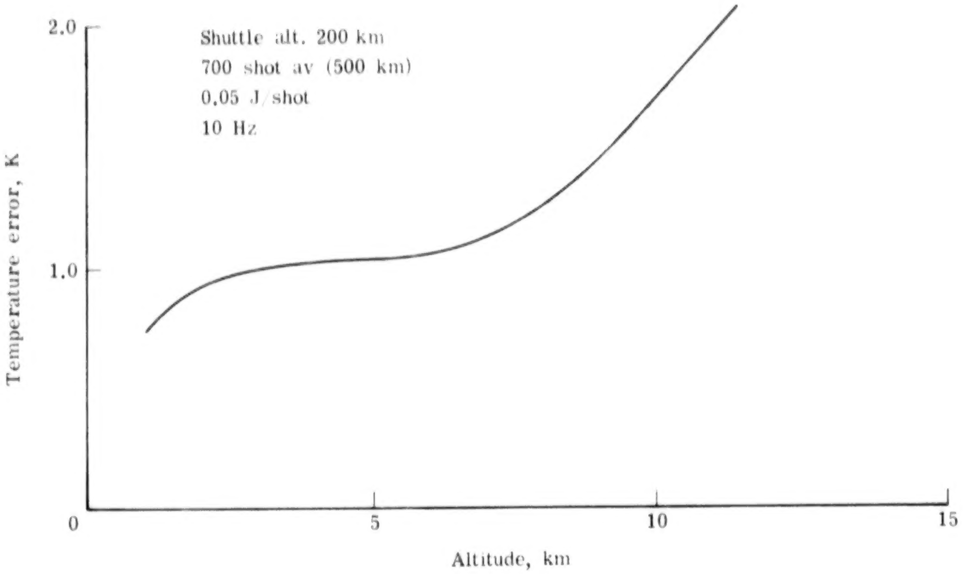

Figure A16.- Temperature profiling accuracy for Shuttle simulation at 769.021 nm for vertical resolution of 2 km.

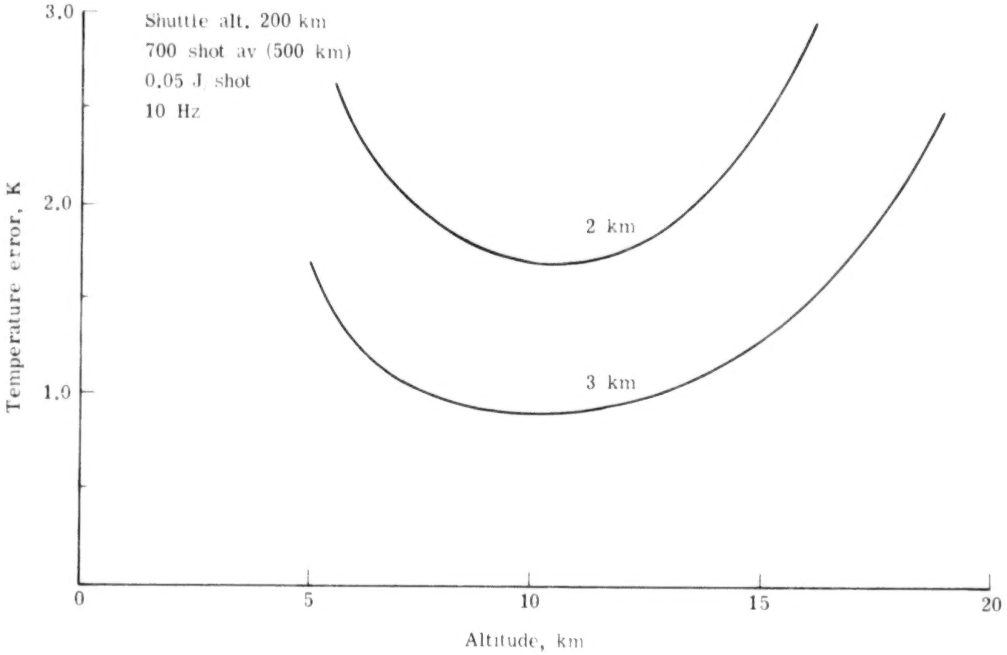

Figure A17.- Temperature profiling accuracy for Shuttle simulation at 768.380 nm for vertical resolution of 2 and 3 km.

Experiment 18: Altitude Distribution of Atmospheric Constituents - IR DIAL

Description.- Tropospheric profiles of gases such as O_3, H_2O, NH_3, and C_2H_4, and profiles of O_3 in the stratosphere, will be measured using differential absorption lidar (DIAL). The DIAL technique is based on the measurement of the intensity of pulses of laser radiation at selected wavelengths backscattered by atmospheric aerosols and differentially attenuated by the species whose concentration is to be measured. Heterodyne detection is used to provide high-detection sensitivity to the backscattered IR radiation, and makes the measurement relatively insensitive to the daylight background - thus day or night operation is possible. Knowledge of the altitude distribution of O_3 will help define the roles of downward diffusion from the stratosphere, and ground-level sources and sinks. Weather forecasting can benefit from information on the vertical distribution of water vapor. The vertical spatial resolution for the proposed DIAL measurement is 1 km.

Implementation.- High-average power lasers and efficient signal collection and detection (large mirror-heterodyne detection) will permit this experiment to achieve a horizontal resolution of about 160 km. Analysis shows that a multiline CO_2 laser with pulse energy of 2 J, pulse repetition rate of 15 Hz, and pulse duration of 4 μs is needed for the Shuttle DIAL experiment and that the spectral stability bandwidth of the laser radiation must be less than 10 MHz for heterodyne detection. The following results are based on a 1 m diameter telescope/receiver with an overall signal detection efficiency of 1 percent, a range of 200 km to the region being analyzed, and a minimum differential absorption sensitivity of 3 percent in a 1 km vertical range bin:

Species	CO_2 laser line	Absorption coefficient, $(atm\text{-}cm)^{-1}$ (a)	Sensitivity (SNR = 10)
O_3	P(14) 001-020	12.7	20 ppb
H_2O	Several lines	Various	10-percent relative humidity (300 K)
NH_3	R(30) 001-020	60	5 ppb
C_2H_4	P(14) 001-100	33	10 ppb

[a] At room temperature and atmospheric pressure.

Daylight background radiation effects are negligible because of the narrow bandwidth and FOV of heterodyne detection. The values of the absorption coefficients given above can be considered only approximate because variations will occur due to changes of pressure and temperature. For O_3, the laser wavelength must be away from line center in order for the beam to pass through the stratospheric ozone layer where the lines are much narrower than they are in the troposphere. The sensitivities shown in the above table are not necessarily optimum, and the list of species is not complete, but merely representative. Potentially, these sensitivities can be increased and other species can be measured using new tunable high-power lasers now under development. One of these, the high-pressure CO_2 laser appears particularly promising, although the ability to obtain laser radiation well away from line center with the necessary purity remains to be demonstrated. The major limiting factors are the need for appreciable absorption (≧3 percent) in a spatial resolution element, and a drop-off in aerosol scattering of infrared radiation with altitude. Simulations also indicate that O_3 in the lower stratosphere can be measured using a CO_2 DIAL system.

Feasibility.- 3B. Pulsed CO_2 lasers with capability of the order required have been demonstrated recently in the laboratory. Shuttle power requirements are intermediate to near maximum, depending on laser average power.

Needed development.- Multiline pulsed CO_2 lasers with pulse energies ≧2 J, average power ≧30 W (repetition rate of 15 Hz), spectral stability and line width less than 10 MHz. Recently demonstrated laboratory devices of this type must be space qualified. The use of heterodyne array detectors (see experiment 10) should be investigated, and detailed simulations for all potential species should be performed.

Discussion.- The DIAL experiment is relevant to scientific objectives 1, 2, 3, and 4 by providing global measurement of vertical and horizontal distributions of a number of important atmospheric constituents. These results can be analyzed in terms of atmospheric chemical transport and radiative models of the atmosphere. This experiment provides a unique combination of tropospheric spatial resolution and global coverage. The same equipment can perform laser absorption measurements using ground to cloud return (experiment 10) and "clear air" DIAL measurements. The detailed altitude resolution of the DIAL measurements will facilitate analysis of the ground to cloud returns which yield better horizontal resolution. Additional capability for measurement of profiles of CH_4, N_2O, and CO in the troposphere and lower stratosphere, with sensitivities and spatial resolutions comparable to the O_3 measurements, could be obtained with wavelengths in the 4 to 6 μm region (doubled CO_2 laser, CO laser, and others).

The approach proposed here permits the distributions of a variety of species to be measured in the troposphere and lower stratosphere with a spatial resolution (≦200 horizontal; ≈1 km vertical) which cannot be achieved with passive instruments.

Bibliography

Collis, R. T. H.; and Russell, P. B.: Lidar Measurement of Particles and Gases by Elastic Backscattering and Differential Absorption. Laser Monitoring of the Atmosphere, E. D. Hinkley, ed., Springer-Verlag, pp. 71-151, 1976.

Murray, Edward R.: Remote Measurement of Gases Using Differential-Absorption Lidar. Opt. Eng., vol. 17, no. 1, pp. 30-38, Jan.-Feb. 1978.

Remsberg, Ellis E.; and Gordley, Larry L.: Analysis of Differential Absorption Lidar From the Space Shuttle. App. Opt., vol. 17, no. 4, pp. 624-630, Feb. 1978.

APPENDIX A

Experiment 19: Cloud-Top Winds

Description.- The purpose of experiment 19 is to measure the wind at the top of clouds, during the day and the night, with an uncertainty in the measurement of ±2 m/s. This requires horizontal and vertical resolutions of 1 km and 0.15 km, respectively. The measurement is important in determining wind components in the tropics and other latitudes which cannot be derived from the temperature field. When the lidar beam is backscattered from a cloud top, it is scattered by individual ice or water droplets. These particles are small and are moving with the local wind velocity; consequently, the Doppler shift of the returned light beam determines the tropospheric wind velocity at the cloud tops.

Implementation for incoherent detection.- Nd:YAG or Nd:Glass laser with adequate frequency stability and a bandwidth of 10^{-4} nm; high-resolution dispersive element (Fabry-Perot interferometer) with an array-type detector. In order to measure two components of the wind vector, two different directions will be needed. The accuracy with which the wind is measured depends on having a posteriori knowledge of the pointing direction. The ground return, if available, is useful in obtaining attitude knowledge. The error in the horizontal component of the wind has been determined to be 1.7 m/s and 0.5 m/s for pointing accuracies of 1 arc min and 5 arc s, respectively. The parameters used in the measurement assessment were the following:

> Wavelength, 530 nm; laser pulse energy, 0.3 J; laser bandwidth, 10^{-4} nm; telescope diameter, 1 nm; number of pulses averaged, 1 pulse; altitude, 5 km; vertical resolution, 0.15 km; angle between line-of-sight and vertical direction, 45°; angle between horizontal component of line-of-sight and Shuttle velocity vector, 45°

The simulation was done for night conditions, assuming a Fabry-Perot interferometer and a 12-ring anode detector, with the following characteristics:

> Free spectral range, 3.8×10^{-3} nm; reflectivity, 0.9; spectral scan, 1.1×10^{-3} nm; quantum efficiency, 10 percent; optical efficiency (other than Fabry-Perot), 0.05; detector resolution, 1.27×10^{-4} nm.

Implementation for coherent detection.- In the CO_2 pulsed wind-measuring lidar, Doppler shifted backscatter from cloud tops is detected coherently. In order to measure the wind with an accuracy of ±1 m/s, laser energies of approximately 10 joules per pulse at a repetition rate of 15 Hz will be required. A pointing system is required whose readout would be accurate to approximately 100 μrad.

Feasibility.- 3C. The C-rating is given because of laser parameters and special pointing system (if required). Note that accurate knowledge of pointing direction is all that is required for a given component of the wind.

Needed development.- For coherent detection, hybrid TEA laser systems are required, with pulse energies of 10 J at a repetition rate of 15 Hz. For incoherent detection, high-energy narrow bandwidth ($\approx 10^{-4}$ nm) lasers need development. The detector system needs design study based on current technology. Diffuse penetration of laser light into clouds from above needs to be studied thoroughly.

Discussion.- Addresses scientific objectives 1, 2, and 4. This experiment has important applications in monitoring the development of tropical low-pressure systems which evolve into hurricanes, monitoring winds in frontal systems, and, in general, filling in the gaps in our radiosonde network in remote locations. Cloud-top winds cannot be measured using ground-based system, a passive system, or a microwave active system.

APPENDIX A

Experiment 20: Aerosol Winds

Description.- The objective of experiment 20 is to measure the wind or average translational velocity of aerosols within a vertical segment of the atmosphere between ground and 30 km altitude. The wind fields will be provided with unambiguous altitude resolution on a global basis. These measurements will be important for the study of general atmospheric circulation and tropospheric/stratospheric interactions.

Implementation.- Two types of measurement techniques are being considered for experiment 20. The first is based upon an Nd:YAG system which measures the Doppler shift in the backscattered laser pulse by means of a Fabry-Perot etalon. The second system utilizes a pulsed CO_2 laser, with the Doppler shifted frequency being measured by infrared heterodyne interferometry. The analyses given below are for a Shuttle altitude of 250 km and a telescope/receiver diameter of 1 m.

Incoherent detection: Nd:YAG (doubled) or Nd:Glass laser with a bandwidth of 10^{-4} nm or better. A high-resolution dispersive element (Fabry-Perot etalon) with an array-type detector is required to detect the Doppler frequency shift and reduce the integration time (which affects the spatial resolution in the horizontal direction). The following parameters were assumed for the mathematical simulation:

Wavelength, nm	550
Laser pulse energy at 10 Hz, J	0.3
Laser bandwidth, nm	0.0001
Laser pulse width, μs	<7
Backscatter coefficients	Elterman
Vertical resolution, km	1
Fabry-Perot detector characteristics:	
Free spectral range, nm	0.0038
Reflectivity	0.9
Spectral scan, nm	0.0011
Quantum efficiency, percent	10
Optical efficiency (other than Fabry-Perot)	0.05
Detector resolution, nm	0.00013

The incoherent-measurement curve shown in figure A18 was derived using the above parameters and a line-of-sight at 45° to the vertical direction and assumed a 45° angle between the velocity vector of the Shuttle and the horizontal component of the line-of-sight. The accuracy with which the wind is measured depends on having a posteriori knowledge of the pointing direction. In this simulation the pointing accuracy was assumed to be 2.4×10^{-5} rad (5 arc-s). It should be mentioned that the ground return signal is a useful way to obtain attitude knowledge; due to the presence of clouds, however, the ground-return information may not always be available. In order to measure the two horizontal components of the wind vector, it is necessary to point the laser beam in two directions.

Coherent detection: Using the pulsed CO_2 laser system, which operates in the 10 μm region of the infrared, the Doppler shifted backscattered signal can be measured directly by heterodyne techniques. Figure A18 shows the integration time (and resulting horizontal resolution) as a function of altitude for a measurement of the line-of-sight component of the aerosol wind. The following parameters were used in this simulation:

Wavelength, μm	10
Laser pulse energy at 15 Hz, J	10
Laser bandwidth, kHz	<50
Laser pulse width, μs	5
Backscatter coefficients	Collis and Russell
Atmospheric extinction coefficients	Elterman
Vertical resolution, km	1
System optical/detection efficiency, percent	1

Feasibility.- 3C. The C-rating is given because of the severe laser parameters and special pointing system requirements.

Needed development.- For incoherent detection, a high-energy, narrow-bandwidth (<0.0001 nm) laser must be developed which operates in the 500 nm region. For coherent detection, a TEA CO_2 laser system is needed with a pulse energy of 10 J, repetition rate of 15 Hz, and pulse width of >5 μs.

Discussion.- Addresses scientific objectives 1, 2, 4, and 5. Velocity fields over large geographical areas are important for the study of general atmospheric circulation and tropospheric/stratospheric interactions. These measurements can, in principle, yield unambiguous altitude resolution and improve the accuracy and lead-time of current numerical weather predictions by providing wind data in regions not presently covered. There is no passive technique that is capable of measuring winds on a global scale below 30 km altitude with the accuracy or spatial resolution given above.

Bibliography

Abreu, Vincent J.: Wind Measurements From the Shuttle Using a Lidar System With Incoherent Detection: An Analysis. Appl. Opt., vol. 18, Sept. 1979. (To be published.)

Collis, R. T. H.; and Russell, P. B.: Lidar Measurement of Particles and Gases by Elastic Backscattering and Differential Absorption. Laser Monitoring of the Atmosphere, E. D. Hinkley, ed., Springer-Verlag, pp. 71-151, 1976.

Elterman, L.: UV, Visible, and IR Attenuation for Altitudes to 50 km, 1968. AFCRL-68-0153, U.S. Air Force, Apr. 1968. (Available from DDC as AD 671 933.)

Huffaker, R. M.; Beran, D. W.; and Little, C. G.: Pulsed Coherent Lidar Systems for Airborne and Satellite Based Wind Field Measurement. Seventh Conference on Aerospace and Aeronautical Meteorology and Symposium on Remote Sensing From Satellites, American Meteorol. Soc., pp. 318-324, 1976.

Menzies, R. T.: Laser Heterodyne Detection Techniques. Laser Monitoring of the Atmosphere, E. D. Hinkley, ed., Springer-Verlag, pp. 297-352, 1976.

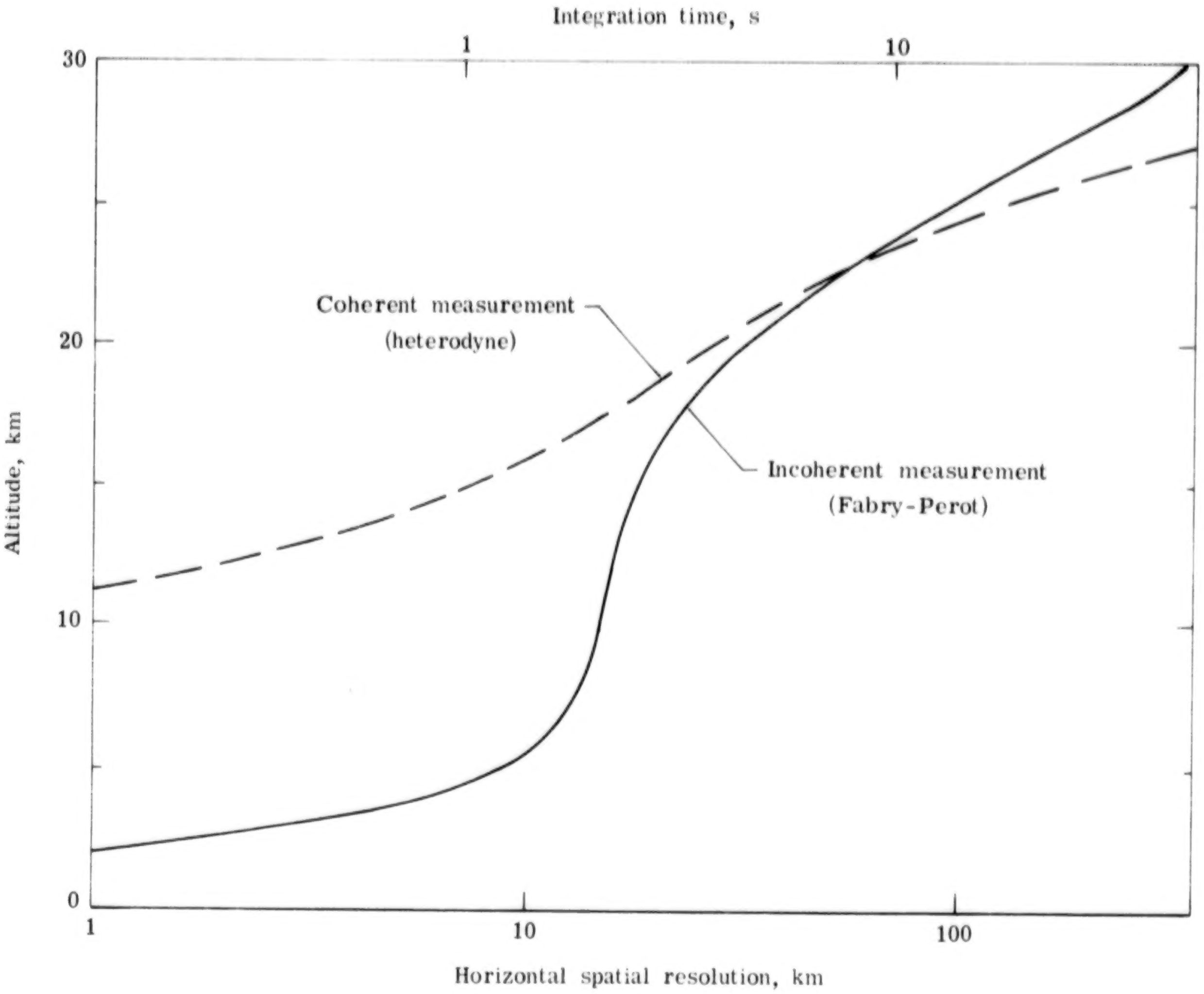

Figure A18.- Horizontal resolution (integration time) for 1 m/s wind accuracy as function of altitude and type of measurement.

APPENDIX A

Experiment 21: OH Density Profile

Description.- Determine the density of OH in the upper atmosphere by observing remote fluorescence from OH excited by a pulsed laser with wavelength in the range 280 to 310 nm. Because OH is involved in many key chemical reactions and undergoes a strong diurnal variation, the measurements will lead to improved chemistry/transport models of the upper atmosphere. Measurements of OH will also be useful for remote sounding of pressure and temperature, given improvements over present UV laser power.

Implementation.- A frequency-doubled dye laser pumped by a frequency-doubled Nd:YAG laser, with the dye laser line narrowed and tuned to $\Delta\lambda \leq 0.001$ nm. UV laser pulses of order 25 mJ are expected for the standard Nd pump laser operating at the level of 1 J/pulse at 10 pps. Several independent calculations of the number of detected photons due to OH fluorescence have been made assuming telescope collector areas of 1 m^2, Shuttle altitude of 200 km, vertical resolution of 5 km, and horizontal resolution of 100 km along the orbital path. Representative results are given in the table below, assuming in addition a PM quantum yield of 35 percent, telescope throughput of 60 percent, peak filter transmissions of 50 percent for 10 nm broad band for nighttime, and 10 percent for 0.001 nm narrow band for daylight conditions.

Z, km	Day (2% overall detection efficiency)		Night (10% overall detection efficiency)	
	OH number density, n cm^{-3}	Number of detected photons	OH number density, n cm^{-3}	Number of detected photons
40	3×10^7	500 ± 25	1.5×10^5	3 ± 1
80	4×10^5	30 ± 10	4×10^6	600 ± 25

These results also include corrections for quenching, ozone absorption, and differences in optical cross section and branching ratios for the various flourescence methods employed.

Thus it appears possible to monitor the broad daytime and nighttime maxima of OH - and the early stages of their change in response to solar illumination - with accuracies of order 5 percent within the spatial resolution element of $\Delta Z \, \Delta X$ = 5 km × 100 km. The major limitation affecting horizontal resolution and restricting nighttime measurements is light economy (laser power times collector throughput). An increase by a factor of 10 to 100 in laser pulse energy and average power (probably requiring a different laser such as an excimer laser) would augment confidence in daytime measurements and allow more comprehensive measurements at night. Higher spatial resolution along the orbital path would be very useful in studying the rapid changes in OH at the terminator.

Feasibility.- 3C. The required laser performance is within present capabilities and has not been entirely demonstrated in field operations. The technique has been used for in situ monitoring of ground level OH and in an aircraft experiment on OH at 11 km altitude requiring 0.001 nm line width. A balloon-borne OH lidar system with $\Delta\lambda = 0.001$ nm is being built for stratospheric measurements.

Needed development.- The assumed dye laser must be demonstrated and flight hardened. A more powerful (i.e., more efficient) laser system is desirable, and a factor of 10 improvement in UV laser energy is expected in the near future with eximer lasers. This would permit an OH measurement with a 10 km horizontal resolution and a 5 km vertical resolution. Greater power will also permit OH temperature and pressure measurements.

Discussion.- Experiment 21 addresses objectives 2 and 5. Information about the daytime maximum and altitude distribution and fluctuations is important for the development of upper atmosphere models. OH is intimately connected with catalytic cycles of ozone destruction involving chlorine and nitrogen oxides. It reacts with NO_2 to form HNO_3 thus removing the NO_2 molecule from the catalytic cycle. It reacts with HCl to release atomic chlorine, returning it to the ozone destruction cycle. The only upper atmosphere OH measurements are local, in situ measurements using resonance fluorescence.

It will be difficult to monitor upper atmospheric OH using ground-based lidar because the UV wavelengths involved are substantially absorbed by the stratospheric ozone layer. The combination of world-wide coverage and spatial resolution offered by the satellite-based UV lidar is not approached by any other proposed technique for the measurement of OH.

Bibliography

Anderson, J. G.: The Absolute Concentration of OH ($X^2\pi$) in the Earth's Stratosphere. Geophys. Res. Lett., vol. 3, no. 3, pp. 165-168, Mar. 1976.

Davis, D. D.; Heaps, W.; and McGee, T.: Direct Measurements of Natural Tropospheric Levels of OH via an Aircraft Borne Tunable Dye Laser. Geophys. Res. Lett., vol. 3, no. 6, pp. 331-333, June 1976.

Heaps, Wm. S.: Lifetime Effects in Remote Laser Induced Fluorescence. Paper presented at Eighth International Laser Radar Conference (Drexel Univ., Philadelphia, Pa.), June 6-9, 1977.

McGee, T. J.; and McIlrath, T. J.: Pressure and Temperature Determination From an OH Fluorescence Lidar Instrument. Paper presented at Eighth International Laser Radar Conference (Drexel Univ., Philadelphia, Pa.), June 6-9, 1977.

Nagy, A. F.; and Chameides, W. L.: Definition of Lidar Requirements for the AMPS Laboratory. NASA CR-150445, 1975.

Wang, Charles C.; Davis, L. I., Jr.; Wu, C. H.; Japar, S.; Niki, H.; and Weinstock, B.: Hydroxyl Radical Concentrations Measured in Ambient Air. Science, vol. 189, no. 4205, pp. 797-800, Sept. 5, 1975.

APPENDIX A

Experiment 22: Simultaneous Measurement of Metallic Atom, Ion, and Oxide Profiles

Description.- Use multiwavelength resonant scattering to obtain simultaneous altitude profiles of Mg, Mg^+, and MgO densities to provide information on the gross features of upper and lower thermospheric circulation.

Implementation.- Nd pumped dye laser with doubler, tuned simultaneously or sequentially to resonance lines of Mg, Mg^+, and MgO, with filtered receiver viewing the nadir or zenith. Return-signal calculations have been performed using the following parameters:

Laser wavelength	Species sensed	Backscatter cross section, cm^2 $atom^{-1}$ sr^{-1}	Laser pulse energy, J	Receiver passband, nm	Receiver efficiency (including optics, filter, and PMT)
500.0	MgO	$^a3 \times 10^{-15}$	0.020	0.04	0.03
285.2	Mg	9×10^{-13}	.002	1.5	.02
279.6	Mg^+	3×10^{-13}	.002	1.5	.02

[a] Effective cross section for absorption in one rotation line of the 0-0 (B → X) band and reemission in the same line.

Laser line width (Note 1, ≈1 pm; laser stability (Note 1), ≈0.2 pm; laser pulse rate, 30 Hz; receiver diameter, 1 m; receiver FOV, 0.2 mrad; sunlit Earth radiance, 3×10^{13} (visible), 8×10^9 (UV) photons nm^{-1} s^{-1} sr^{-1} cm^{-2}

Note 1: Laser line width and stability requirements can be relaxed at the expense of lower return signal and degraded measurement accuracy.

The results of these calculations for a measurement with ±20-percent accuracy of the average concentration in a 5 km range cell - all at a distance of 100 km from the Shuttle - are given in figure A19. The along-track integration needed for the measurement of representative densities of Mg (10^2 cm^{-3}), Mg^+ (10^3 cm^3), and MgO (10^3 cm^{-3}) is small enough to provide useful data on the mesoscale variability of all three species at night and on the variability of Mg and Mg^+ during the day. Note that all three wavelengths are assumed available simultaneously with the stated energies at 30 Hz. Sequential operation at each wavelength will increase the along-track integration distance in the figure inversely with the duty cycle of each wavelength. The scientific objectives require that the measurements of the different species be made at the same time, rather than on sequential orbits.

All orbital inclinations are useful, with low-latitude regions being of special interest to investigate the suggested equatorial origin of high-altitude metallic ions. Data can be compressed somewhat before being stored or transmitted, probably needing about one altitude profile per second for each species with 5 km height resolution. Receiver FOV and bandwidth requirements could be relaxed for a nighttime-only scenario.

Feasibility.- 3C because of multiple wavelengths and long operating times; 3B if only Mg and Mg^+ are measured using the same hardware as experiment 12.

Needed development.- Space qualification of narrow-band, frequency-agile dye laser.

Discussion.- This experiment addresses the upper atmospheric motions of concern in scientific objective 5, as well as the chemistry and transport of thermospheric species covered in scientific objective 6. The source function for magnesium is known to be localized near 90 km, and yet Mg^+ is found in substantial quantities above 500 km. The height and latitude distribution of the source function is known well enough that a measurement of the altitude and latitude partition among Mg, Mg^+, and MgO would provide information on the gross features of upper and lower thermospheric circulation. Measurements of Mg and Mg^+ only would also provide valuable information on ionospheric circulation but would not address the critical 70 to 120 km turbopause region where a substantial fraction of the magnesium inventory will be in the oxide form.

An alternative set of metallic constituents is the Fe (259.9 nm), Fe^+ (385.9 nm), FeO (579.0 nm) complex, which is present with roughly equal densities as the magnesium complex, and would provide data of equal scientific interest. Laser capabilities at the required wavelengths will determine which metallic complex is preferred for measurement. In either case, space-borne systems are needed because the UV lines are ozone shielded from ground observations.

Lidar is the only technique capable of measuring all three species simultaneously and the only technique capable of measuring Mg and Mg^+ simultaneously in the nighttime.

Bibliography

Anderson, James G.; and Barth, Charles A.: Rocket Investigation of the Mg I and Mg II Dayglow. J. Geophys. Res., vol. 76, no. 16, pp. 3723-3732, June 1, 1971.

Brown, Theodore L.: The Chemistry of Metallic Elements in the Ionosphere and Mesosphere. Chem. Rev., vol. 73, no. 6, pp. 645-667, Dec. 1973.

Gerard, J.-C.; and Monfils, A.: Satellite Observations of the Equatorial Mg II Dayglow Intensity Distribution. J. Geophys. Res., vol. 79, no. 16, pp. 2544-2550, June 1, 1974.

Zbinden, P. A.; Hidalgo, M. A.; Eberhardt, P.; and Geiss, J.: Mass Spectrometer Measurements of the Positive Ion Composition in the D- and E-Regions of the Ionosphere. Planet. & Space Sci., vol. 23, no. 12, pp. 1621-1642, 1975.

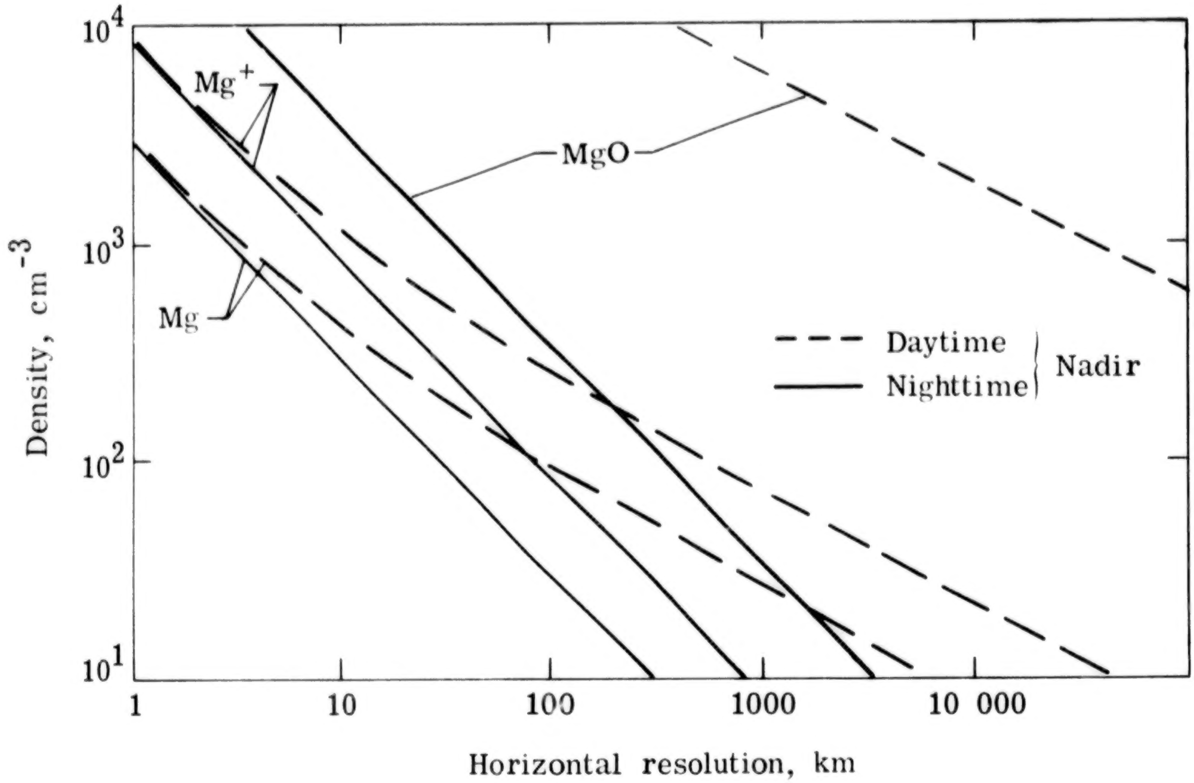

Figure A19.- Performance calculation for lidar measurement of metallic atom, ion, and oxide profiles. Curves show dependence of along-track integration distance needed for ±20 percent measurement accuracy on density of species at measurement point.

APPENDIX A

Experiment 23: Tropospheric NO_2 Concentration Profile

Description.- Measurement of tropospheric NO_2 density between 0 and 4 km and total NO_2 column using DIAL techniques in the 450 nm spectral region. The total burden measurement assumes scattering from the ground. These data are particularly important in ozone chemistry.

Implementation.- Experiment 23 is to be performed at orbital altitudes of 250 to 300 km under nighttime viewing conditions. Instrumentation includes: 1 m diameter receiver; standard Nd:YAG laser frequency doubled (tripled) to pump a dye with output near 450 nm at 0.01 J and 10 Hz; 1 mrad FOV; 0.5 nm FWHM wavelength filters; 10-percent system optical efficiency, and PMT detectors having a QE of about 20 percent. Spatial resolutions of 500 km horizontal (along-track) and 1 km vertical at accuracies less than or equal to 20 percent were set as goals for the 0 to 4 km altitude range, while the total burden goals are for 10-percent measurements with a 10 km horizontal resolution. Simulations have indicated that very long integration times are required in order to retrieve the NO_2 differential signal at these desired accuracies. Figure A20 shows simulated profile results for a similar lidar system, but one using DIAL wavelengths of 448.2 and 442.1 nm, laser output energies of 0.05 J at 10 Hz, and 20-percent optical throughput. The accuracies for 740 km horizontal resolution are at 0 km (10 ppb), 20 percent; at 1 km (30 ppb), 7 percent; at 4 km (3 ppb), 100 percent. These mixing ratios are typical of an urban center.

Feasibility.- 3C. Very low-signal levels. Enhanced signal-to-noise ratios are required.

Needed development.- System design studies, hardware testing, and aircraft based measurements for demonstrating experimental capabilities. Accurate simulations for total burden measurements are required.

Discussion.- Provides quantitative global scale mapping of tropospheric pollutants and addresses objective 1. Measurements of NO_2 concentrations in urban environments are extremely important for understanding tropospheric chemistry and for tracking downwind dispersal of urban pollution. Global measurements of tropospheric NO_2 are not available with any other technique.

Bibliography

Wright, M. L.; Proctor, E. K.; Gasiorek, L. S.; and Liston, E. M.: A Preliminary Study of Air-Pollution Measurement by Active Remote-Sensing Techniques. NASA CR-132724, 1975.

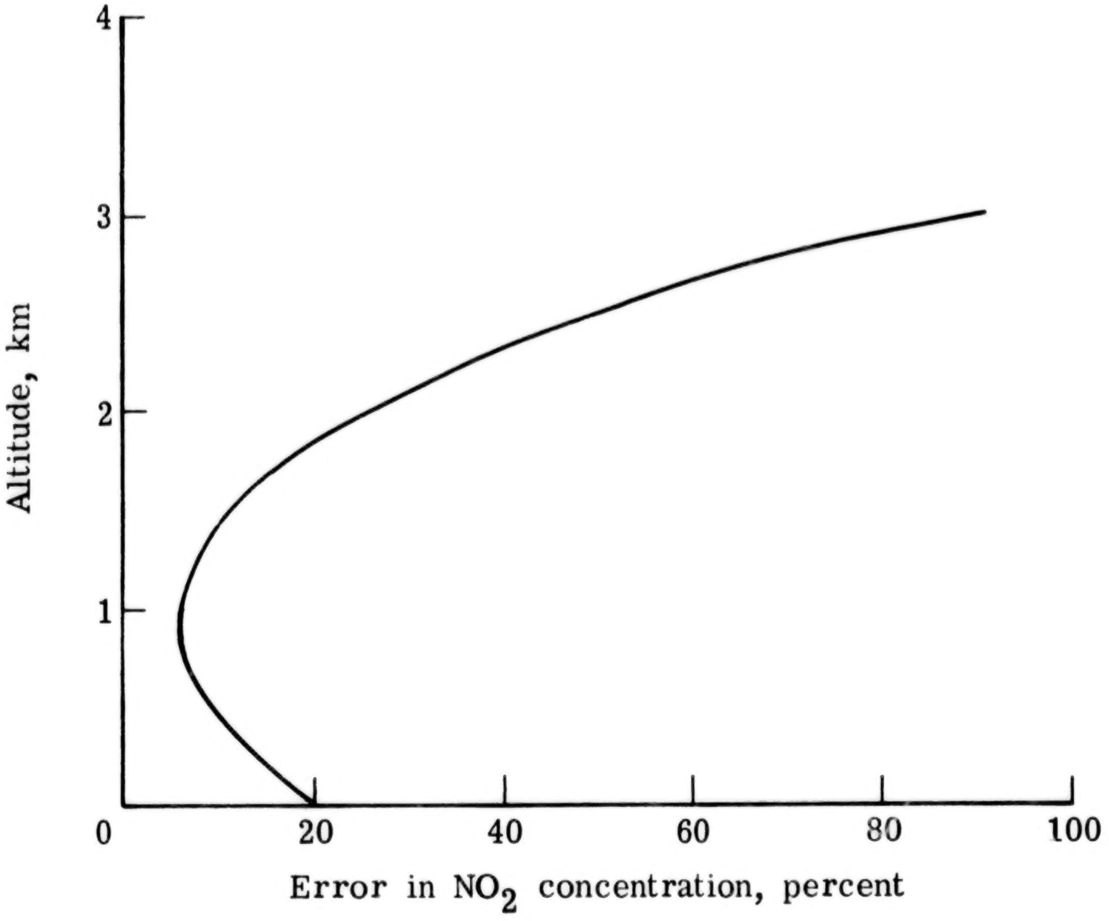

Figure A20.- Simulation of tropospheric NO_2 DIAL measurement. NO_2 urban model; spacecraft altitude of 300 km; 1000 shots (740 km horizontal, 1 km vertical); DIAL wavelengths of 442.1 nm and 448.2 nm; 0.05 J/pulse.

APPENDIX A

Experiment 24: Stratospheric Aerosol Composition

Description.- Identification of the chemical composition of stratospheric aerosols using pattern-recognition techniques with multiwavelength (infrared) aerosol backscattering (DISC differential scattering). This information would be important for determination of the climatic and environmental effects of stratospheric aerosols.

Implementation.- Experiment 24 can be performed under both nighttime and daytime viewing conditions. A preliminary study of instrumentation indicates that sufficient lidar sensitivity is obtained at a 220 km orbital altitude with a 1 m diameter receiver, standard line tunable (9 to 11 μm) CO_2 laser with a 20 J output at 1 Hz, ≈1 mrad FOV, and nitrogen cooled HgCdTe IR detection (or heterodyne detection). Measurement principle is based on the fact that aerosol backscatter coefficients show a dependence on wavelength that is characteristic of the aerosol composition, as shown in figure A21. Simulations indicate that pattern recognition techniques based upon a comparison of a measured backscatter with calculated backscatter will provide an identification of stratospheric-aerosol constituents. This analysis needs to be extended to include the problem of distinguishing backscattering from multiple aerosol constituents and the effects of interfering gases. The possibility of requiring a broader wavelength range than 9 to 11 μm is currently under investigation. Present simulations provide only very rough estimates of spatial resolution; present estimates are on the order of a few km vertical resolution, and a few hundred km horizontal resolution.

Feasibility.- 4. The DISC measurement principle is in a preliminary stage of concept development.

Needed development.- Conceptual development must be continued; sensitivity analysis on the aerosol composition must be extended; and the feasibility of the experimental technique must be demonstrated.

Discussion.- This experiment contributes to scientific objective 1 by providing data on the mass and global transport of certain pollutants in the aerosol phase; to objective 2 by characterizing the composition as a function of global location of the aerosol sink for stratospheric trace species; and to objective 3 by providing the bulk composition of the stratospheric aerosol for refined estimates of their radiative effect. Of special interest is the possibility of monitoring stratospheric aerosol composition changes during volcanic episodes and perhaps anthropogenic stratospheric pollution episodes such as the satellite solar power system construction phase. DISC could provide a powerful tool for tropospheric aerosol analysis as well if the backscatter signatures of different tropospheric aerosols are unique enough for the technique to work.

DISC offers the potential for a unique capability for remote sensing of the chemical composition of aerosols on a global scale.

APPENDIX A

Bibliography

Colburn, D. S.; and Pollack, J. B.: Infrared Backscatter Spectra for Differentiation of Stratospheric Aerosol Composition. 7th International Laser Radar Conference - Conference Abstracts. American Meteorol. Soc., Stanford Res. Inst., Nov. 4-7, 1975.

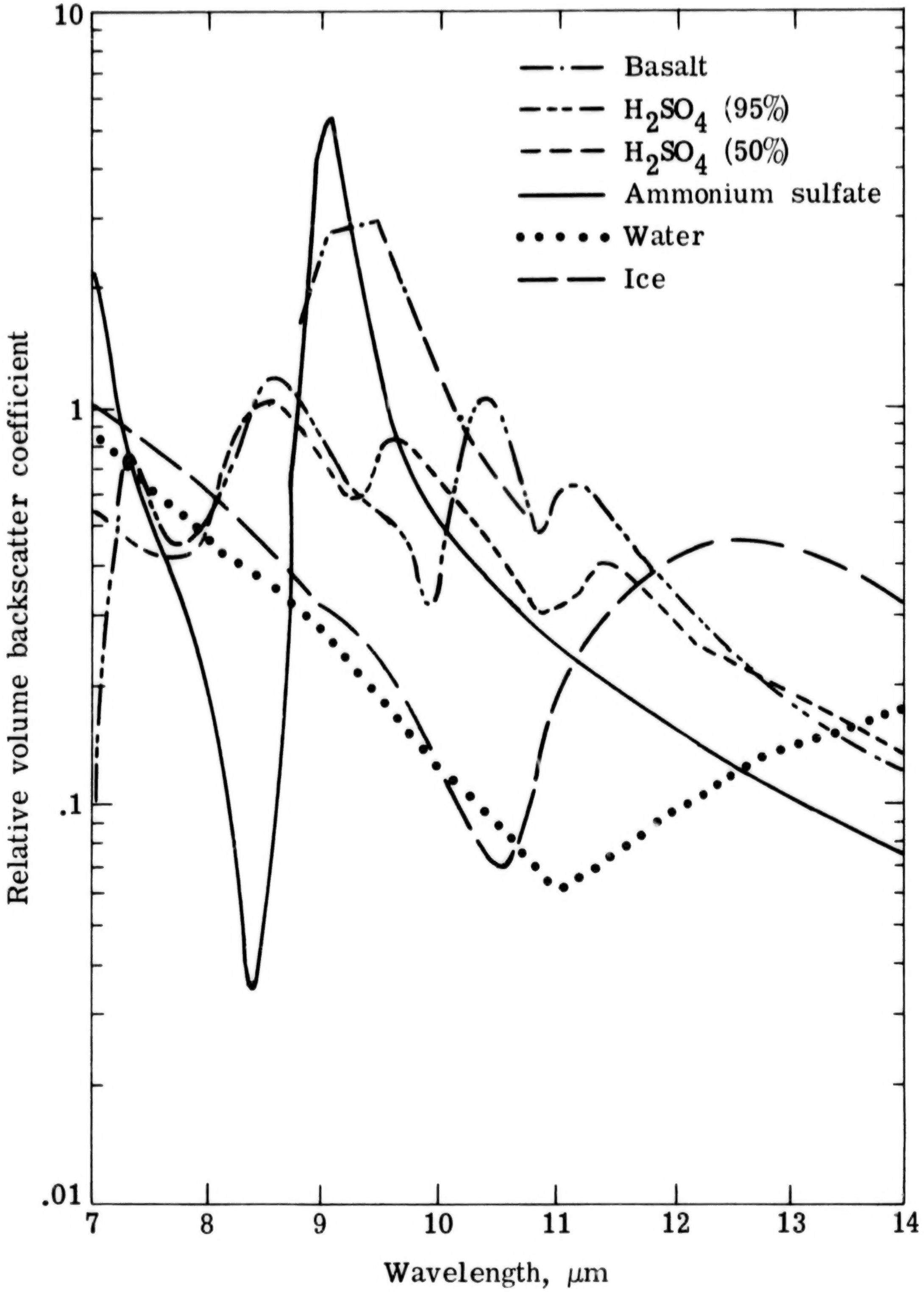

Figure A21.- Wavelength dependence of relative backscatter coefficient for several different aerosols possibly present in stratospheric aerosol layer.

APPENDIX A

Experiment 25: NO Density Profiles Between 70 and 150 km Altitude

Description.- Altitude profiles of NO will be measured by resonance scattering or fluorescence using a tunable laser which is frequency doubled into the NO γ-bands or suitable excimer lasers that may be developed in the future. Demonstration on the Shuttle is important for development of global monitoring of NO. The D-region of the ionosphere, between 70 and 100 km altitude, is formed largely through the ionization of NO by solar Lyman-α radiation. The abundance of NO and its transport at higher and lower altitudes are fundamental questions in the physics and chemistry of the atmosphere. A global, remote measuring technique for NO is highly desirable.

Implementation.- Nd:YAG, frequency tripled to 353.3 nm, pumping a tunable blue dye laser that, in turn, is frequency doubled into the NO γ-band region ($\approx$215 nm). With this laser design, NO density can be determined with 20-percent accuracy for $Z = 70$ km to 150 km, $\Delta Z = 3$ km, and $\Delta X = 100$ km. Several independent calculations of NO lidar performance have been made for 3 km deep segments of 100 km long swaths through the atmosphere below the Space Shuttle. Assumptions include (a) an overall electrical-to-optical conversion efficiency of 3×10^{-6} for $\lambda \approx 215$ nm, (b) detector efficiency of 10 percent, and (c) concentrations of $NO = 10^7/cm^3$ for $Z = 100$ km and $10^8/cm^3$ for $Z = 70$ km. No quenching corrections were made for collisions prior to reradiation of NO. The detected photon numbers are of order 25 for $Z = 70$ km and of order 20 for $Z = 100$ km, to within 1/2 order-of-magnitude discrepancies between the calculations. These are acceptable signals for detection but call for longer swaths in the range $\Delta X = 500$ km for decent measurements of NO. Greater accuracy and resolution will be possible if efficient UV lasers are developed for satellite applications.

Feasibility.- 4. The main question at present is the reliability of frequency doubling this far into the UV, given that the blue laser line width should be small (0.0005 nm). At present the excimer laser alternative appears to be at least as difficult as the proposed method.

Needed development.- Coherent ultraviolet light sources need considerable development for measurements of important atmospheric species. Improvements are greatly needed in UV frequency doubling and in the use of excimer systems both as oscillators and amplifiers. Nonlinear mixing techniques, using conventional solid materials, may make it possible to work at shorter wavelength ($\approx$190 nm) where the NO optical cross sections are larger than at 215 nm. This is a promising method that needs further work. Also, more accurate lidar simulations need to be calculated for a range of atmospheric models.

Discussion.- Measurement of NO relates to objectives 2, 6, and 7. Lidar provides the only remote sensing method for NO which would give spatial resolution simultaneously in all three dimensions. Existing methods are in situ (local ionization, chemiluminescence, IR laser absorption, ion composition) or passive remote sensing techniques involving integration over a path length (γ-band emission or absorption, IR absorption). On the Solar Maximum Mission (launch, Fall 1979) NO profiles from 80 to 120 km will be obtained at the terminator via UV solar occultation spectra to be taken with a Tandberg-Hanssen instrument. Also, the Solar Mesosphere Explorer now includes a spectrometer for measuring excited molecule emission above the Earth's limb in the altitude range 40 to 80 km; the NO γ-bands are included in this study.

Lidar fluorescence is based on a large optical cross section of order 10^{-16} cm^2 and an efficient placement of single-frequency excitation within an NO absorption band. In the mesosphere, NO is affected by transport above 100 km and by propagation of disturbances from the lower atmosphere. The transport of NO itself, both horizontally and to lower altitudes, may be important in the stratospheric abundance of odd nitrogen, but no information is available at this time. NO is created by charged particle deposition in the atmosphere and acts to deplete ozone in the upper stratosphere and mesosphere by means of the well-known catalytic cycle which converts odd oxygen into even oxygen species. This effect needs to be measured directly and in detail during charged particle events. Global maps of NO will be produced in the form of density contours as functions of latitude and altitude and in correlation with such species as O_3 and OH.

APPENDIX A

Bibliography

Ackerman, Marcel: NO, NO_2 and HNO_3 Below 35 km in the Atmosphere. J. Atmos. Sci., vol. 32, no. 9, pp. 1649-1657, Sept. 1975.

Alyea, Fred N.; Cunnold, Derek M.; and Prinn, Ronald G.: Stratospheric Ozone Destruction by Aircraft-Induced Nitrogen Oxides. Science, vol. 188, no. 4184, pp. 117-121, Apr. 11, 1975.

Baker, K. D.; Nagy, A. F.; Olsen, R. O.; Oran, E. S.; Randhawa, J.; Strobel, D. F.; and Tohmatsu, T.: Measurement of the Nitric Oxide Altitude Distribution in the Mid-Latitude Mesosphere. J. Geophys. Res., vol. 82, no. 22, pp. 3281-3286, Aug. 1, 1977.

Crutzen, Paul J.; Isaksen, Ivar S. A.; and Reid, George C.: Solar Proton Events: Stratospheric Sources of Nitric Oxide. Science, vol. 189, no. 4201, pp. 457-458, Aug. 8, 1975.

Nagy, A. F.; and Chameides, W. L.: Definition of Lidar Requirements for the AMPS Laboratory. NASA CR-150445, 1975.

Patel, C. K. N.: Spectroscopic Measurements of the Stratosphere Using Tunable Infrared Lasers. Opt. & Quantum Electron., vol. 8, no. 2, pp. 145-154, Mar. 1976.

Pontano, B. A.: Rocket Measurements of Nitric Oxide in the Lower D-Region of the Ionosphere. Sci. Rep. No. 347 (Contract DAHC04-68-C-0034; Grant NSF GP-5611), Ionosphere Res. Lab., Pennsylvania State Univ., Feb. 1970. (Available from DDC as AD 701 931.)

Reagan, J. B.: Ionization Processes. Dynamical and Chemical Coupling Between the Neutral and Ionized Atmosphere, B. Grandal and J. A. Holtet, eds., D. Reidel Pub. Co., pp. 145-160, c.1977.

Reagan, J. B.; and Imhof, W. L.: Detailed Profiles of the Ionization and Nitric Oxide Production in the Polar Mesosphere and Stratosphere During the August 1972 Solar Particle Events. EOS Trans., American Geophys. Union, vol. 57, no. 12, p. 972, Dec. 1976.

Swider, W.: Daytime Nitric Oxide at the Base of the Thermosphere. J. Geophys. Res., vol. 83, no. A9, pp. 4407-4410, Sept. 1, 1978.

Thorne, Richard Mansergh: Energetic Radiation Belt Electron Precipitation: A Natural Depletion Mechanism for Stratospheric Ozone. Science, vol. 195, no. 4275, pp. 287-289, Jan. 21, 1977.

Experiment 26: Abundance and Vertical Profiles of Atomic Oxygen

Description.- Altitude profiles of [O] will be measured by two-photon fluorescence spectroscopy, using very short pulses of tunable radiation at 225.6 nm. Atomic oxygen is a major constituent of the upper atmosphere. Knowing this distribution in the mesosphere and lower thermosphere is essential for understanding the photochemistry of oxygen and water and the transport processes occurring in the transition from turbulent mixing to diffusive separation. Development and testing of a two-photon method for measuring [O] from the Space Shuttle is an important step towards global measurements of species for which standard UV fluorescence techniques will not be applicable due to short range extinction.

Implementation.- Mode-locked Nd:YAG laser, frequency tripled to pump mode-locked dye laser near 450 nm. This output is doubled to 225.6 nm and amplified to the energy required. At present, 1 mJ at 225.6 nm is probably feasible using the baseline laser system and conventional amplifiers and doublers. A good measurement of [O] from the Shuttle will need a diffraction-limited, 1 J pulse; excimer amplification should be considered for these energies.

Two-photon excitation of $2p^3\ 3p\ ^3p$ state of atomic oxygen ($\sigma \approx 7 \times 10^{-36}$ cm^4 s) followed by fluorescence at 844.9 nm, which is detected using a 1 m^2 collecting telescope filtered to 0.01 nm spectral bandwidth. Figure A22 shows photon returns expected for a 1 J, 20 ps pulse at 226 nm and for a 1 km altitude resolution. Accuracies of order 5 to 10 percent in [O] can be obtained above 80 km. A major laser development effort is needed for this important experiment.

Feasibility.- 4. In addition to UV operation requiring the frequency-doubling as proposed, or an excimer equivalent, mode locking is needed for sufficient power density in the beam to have efficient excitation of [O]. Mode locking has been obtained with tunable pulsed systems in the blue.

Needed development.- Two levels of development are needed: one is the extension of relatively familiar methods leading to pulse energies of order 1 mJ at 225.6 nm and the second is to augment the first type of device with excimer amplification. A major program of UV laser development is needed to support the proposed type of geophysical measurement. A capability for single mode, 20 ps, 1 J pulses at 225.6 nm would make possible an [O] measurement having 5- to 10-percent accuracy down to 80 km with an altitude resolution $\Delta Z = 1$ km. A possible laser development direction for energetic UV pulses is the use of excimer systems to amplify from the 1 mJ level to the 0.1 to 1 J output required. This may require multipassing within the excimer amplifier because of the shortness of 20 ps pulses compared to relaxation times for the excimer system.

Discussion.- The measurement of [O] relates directly to objectives 6 and 7, and indirectly to objective 2. Lidar affords the only way to obtain a global map of the O-atom altitude distribution. A measure of the [O] profile between 80 and 150 km would provide knowledge of the photodissociation of molecular oxygen as well as eddy and molecular diffusion processes since the chemical lifetime of atomic oxygen is less than 1 day at 80 km and greater than 1 day at 95 km where diffusion becomes dominant. The study of [O] is essential to the understanding of the relative roles of photochemistry and diffusion and to the understanding of ozone and odd hydrogen photochemistry in the upper mesosphere. The measurement would be quite valuable when conducted simultaneously with a molecular species such as O_2 or N_2. Ozone, OH, and other photochemical products should be included in measurement programs focusing on photochemistry.

The two-photon method is necessary for lidar measurements of O-atoms. Ordinary resonance fluorescence of [O] at 130.4 nm is not useful beyond ≈100 m from the Shuttle due to absorption of the light. The two-photon cross section is fairly certain and should be verified by measurement.

Laser considerations are paramount. Given 10-percent efficiencies in each of the three stages following the generation of 20 ps, 1 J Nd:YAG pulses, one has 1 mJ pulses at 10 Hz to work with at 225.6 nm. Background and signal considerations lead one to believe that 10^4 such pulses are needed to give $SNR \approx 1$ for detection of [O] against optical background (nadir). For single-pulse measurement, ≈100 mJ would meet the same criterion; and a pulse energy of 1 J at 225.6 nm would make possible a very good determination of [O] down to 80 km. At the 1 mJ level of performance, then, $\Delta t \approx 1000$ s is required; hence, $\Delta X \approx 8000$ km or about 1/5 of the Earth's circumference. Though low-energy pulses are not useful for a Shuttle based geophysical experiment, they will serve to conduct more local measurements in the atmosphere during the laser development program. Other atomic species may prove susceptible to local atmospheric measurements using the fully developed UV short-pulse system for Shuttle measurements of [O].

Bibliography

Loudon, Rodney: Quantum Theory of Light. Oxford Univ. Press, Inc., 1973.

McIlrath, T. J.; Hudson, R.; Aikin, A.; and Wilkerson, T. D.: Two-Photon Lidar Technique for Remote Sensing of Atomic Oxygen. Appl. Opt., vol. 18, no. 3, pp. 316-319, Feb. 1979.

Pindzola, M. S.: Two-Photon Excitation of Atomic Oxygen. Phys. Rev. A, ser. 3, vol. 17, pp. 1021-1027, Mar. 1978.

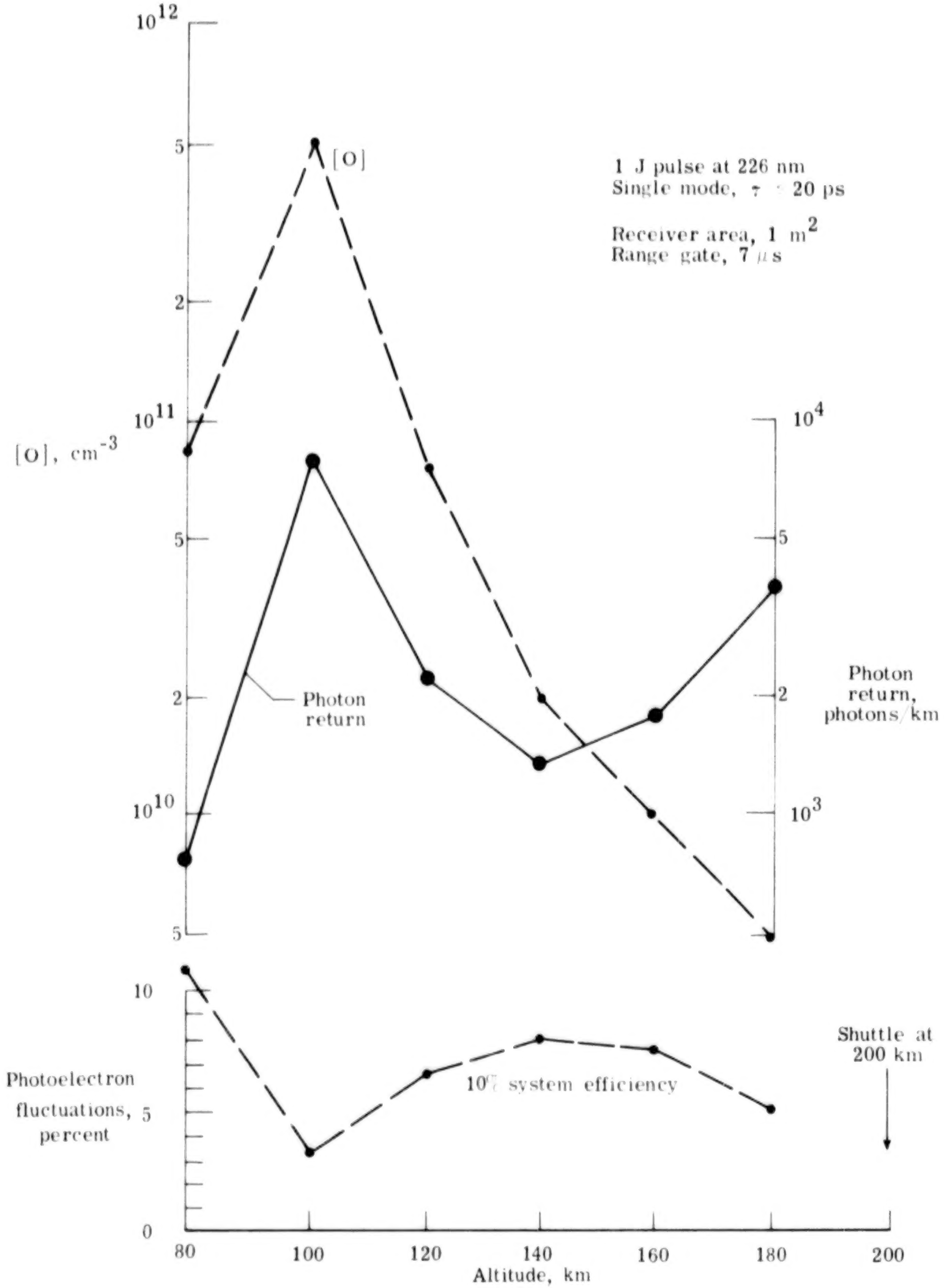

Figure A22.- Expected photon returns from various altitudes to Shuttle observatory at 200 km, with O-atom concentration assumed and indication of photon-statistical errors in [O] for reasonable optical system.

APPENDIX B

LASERS OF POTENTIAL USE FOR SHUTTLE LIDAR

INTRODUCTION

The remote identification of particulates as well as atomic and molecular species from the Space Shuttle platform requires pulsed lasers for active (lidar) detection or CW lasers for passive (heterodyne) detection. The detection of atomic species usually limits the laser source to the visible or ultraviolet spectral regions, while molecular species have many of their "spectral signatures" (vibrational-rotational transitions) in the mid-infrared (2 to 20 μm). The detection of particulates (clouds and aerosols) is best done using lasers which operate in the visible to the near infrared regions where elastic scattering cross sections are large.

It is necessary that any laser system be sufficiently developed to operate in the restricted environment of a Shuttle vehicle. In order to meet the goals of an early 1980's flight, the choice of lasers is probably limited to those that already have a demonstrated capability. Among those lasers are Nd:YAG and CO_2 which have already been extensively developed for airborne and military applications. Both of these lasers can operate either continuously or pulsed and have the best chance of producing results for the Shuttle program in its initial stages.

It should be pointed out that even if one restricts the choice of laser to Nd:YAG and CO_2, there is a wide range in the system design which may require a substantial development effort. The ultimate choice in system design depends upon what has to be detected. A careful assessment of how some realistic set of goals can be achieved with reliable laser technology must be made. It is important not to promise too much and to insure that the goals which are achieved will have a substantial impact on the political as well as scientific community. The real work on choice of the laser and detector technology will come when the specific tasks of remote detection from the Shuttle have been identified.

Nd:YAG LASER

The Nd:YAG laser has been extensively developed for military rangefinder and target designator applications. These devices are suitable for airborne applications and as man-portable devices. In the latter case, the entire package is only a couple of pounds in weight and can measure less than several inches on a side. In both cases, the lasers operate in the Q-switched mode with pulse widths of several nanoseconds and output energies ranging from a few to a few hundred millijoules. Operation conforms to standard "mil specs." The Nd:YAG laser can operate with about 1-percent overall efficiency at 1.06 μm and about half that efficiency in the frequency-doubled mode. It can also be frequency tripled and quadrupled to produce useful outputs in the ultraviolet, and it can be used to pump a dye laser in the visible and UV spectral regions. Commercially available devices can generate about 0.5 to 1 joule per pulse in

10^{-8} s at about 10 pulses per second at 1.06 μm in a fundamental spatial mode. Two basically different cavity configurations are used to achieve an output in a fundamental spatial mode. One of these is an unstable-resonator arrangement which has some advantages in extracting more fundamental mode energy than other configurations. Several companies offer various versions of this laser, see table BI as an example, and there should be no difficulty in space qualification. Normally, Nd:YAG lasers operate in a number of longitudinal modes with an envelope bandwidth of about 0.5 cm^{-1} due to spatial "hole-burning" in the laser medium. Recent results have shown that nearly all of the multimode output energy from a Q-switched Nd:YAG laser can be extracted in a single longitudinal mode. An intracavity electro-optic modulator together with two quarter-wave plates is used to hold off laser action until "super-radiant" line narrowing of the gain bandwidth to less than the axial mode spacing occurs. At that point, the modulator is opened and oscillation occurs on a single axial mode. While further work is necessary to improve the stability and reliability of this technique, such a device could greatly improve the sensitivity of some lidar systems by allowing use of coherent detection. A commercial version of this is apparently available from the Quanta-Ray Company. Local oscillators for such systems could be the quaternary diode lasers GaInAsP/InP which have demonstrated CW output powers of several milliwatts in a single axial mode when operated at room temperature. An advantage in using heterodyne detection at 1.06 μm is the greatly increased sensitivity from the reduced bandwidth (≈16 MHz for a 10^{-8} s transform limited pulse) over an optical transmission filter (bandwidth ≈0.5 nm) to reduce background photon noise. There is also an advantage in use of high-quantum efficiency photodiodes over photomultiplier tubes at 1.06 μm. The complexity of heterodyne detection is an obvious disadvantage. For remote wind measurements at 1 μm, a velocity of 1 m/s would require a laser pulse width longer than 160 ns in order to start to resolve the Doppler shifted signal. For a 10 μm laser, the comparable pulse length would be 1.6 μs. Of course, significantly longer pulse lengths are required to simplify the signal processing. Stretching out of Nd:YAG laser pulses, while not impossible, is difficult. Typical 1-J Q-switched output pulses from a Nd:glass laser are usually 30 to 50 ns, and the pulse stretching can be somewhat simpler than for Nd:YAG lasers.

The Nd:glass laser in a face-pumped slab configuration (see fig. B1) has been extensively developed by the General Electric Company and packaged into a compact form suitable for military airborne applications. The performance of this laser is at least as good as Nd:YAG lasers and can generate 1J at 10 to 30 pps in a 50 ns pulse width. A significant advantage of the Nd:glass laser is the ability to tune the laser itself over its spontaneous linewidth (≈200 cm^{-1}) using an intracavity tuning element. This could be a significant advantage for obtaining tunable frequencies in the UV and visible regions without the need for a dye laser. The Nd:glass laser output can be Raman frequency shifted with about 50 percent photon conversion efficiency using a large number of materials with various Raman frequencies. Subsequent frequency doubling, tripling, and quadrupling using conventional mixing crystals could cover all the wavelengths needed for the experiments defined in appendix A. A systems analysis would have to be performed in order to weigh the trade-offs between a Nd:YAG and a Nd:glass based system.

A large number of Nd transitions have been made to oscillate in the range 0.94 to 1.8 μm with individual transitions being tunable over a few wave numbers. Table BII lists some of the stronger transitions made to oscillate in Nd:YAG. In addition, Nd has been successfully used in other hosts such as YALO, SOAP, and the vanadates where the individual frequencies are slightly shifted. Use of such lasers may be considered where this is a fortuitous overlap of frequencies with some atomic or molecular transition but, in practice, may be impractical compared to other options.

The Er:YLF (erbium:yttrium lithium fluoride) laser is commercially available with pulsed outputs near 1.5 μm and 0.85 μm (50 mJ at 10 Hz). In particular, a frequency doubled 0.85 μm output might be useful for pumping dyes,** but a detailed system analysis has to be made to compare it with a frequency-tripled Nd:YAG laser used for the same purpose.

A new and very promising tunable solid-state laser is Cr^{3+} doped alexandrite ($Cr:Al_2BeO_4$). This laser is being studied by a group at the Allied Chemical Company Laboratories in Morristown, New Jersey. Like the transition-metal tunable lasers described below, the Cr levels are strongly coupled to the host crystal lattice and therefore have strong phonon sidebands associated with the electronic transitions. The initial devices have been tunable in the 700 to 800 nm region and operated with pulsed flashlamp excitation at room temperature. Output energies were 70 mJ in 120 ns at 10 pps and 500 mJ in a 200 ns pulse. It appears quite possible to extend this output performance to 1J at 10 to 30 pps. Use of such a laser as a primary tunable source could be perhaps more effective than an Nd:YAG dye laser combination or the Nd:glass Raman shifting-doubling schemes. Figure B2 shows the threshold-tuning curve for this device. At present the overall efficiency for this laser is low (<0.1 percent).

CARBON DIOXIDE LASER

Carbon-dioxide-laser technology has been extensively developed for military applications, even more so than Nd:YAG lasers (except for target designators and rangefinders). A good deal of this technology has been transferred to industry where CO_2 lasers are used for machining, drilling, and welding applications. Industrial welding lasers on automotive production lines routinely operate with 20 kW of average output power. Some of these devices operate with electron-beam excitation followed by a sustainer voltage pulse while others operate only by direct electrical discharge pumping. Both methods of excitation have proven reliable for industrial welding type lasers. While e-beam pumping can be considered as a relatively well-developed and reliable technology, it does represent one more degree of complexity for Shuttle operation, especially since the very large e-beam injection voltages (>100 kV) are significantly larger than the voltages required for the direct electrical excitation lasers. A complete systems analysis is required for any meaningful comparison. Some experts feel that if an output of several joules is required in each pulse, increased uniformity

---

**This has already been demonstrated by Sanders Associates, Nashua, New Hampshire.

of e-beam excitation is an advantage over straight electrical discharge excitation. In a background-noise-limited lidar system, 15 joules per pulse at 10 pps is better than 1 joule per pulse at 150 pps. However, other systems requirements may make this comparison less critical.

The CO_2 laser can operate on dozens of lines in the 9 to 12 μm range for low-pressure (<1 atm) devices while a high-pressure (>15 atm) device can be continuously tuned over much of the same region. Overall power conversion efficiencies can be typically 10 percent for CO_2 lasers. There should be no major problem in space qualifying either a CW or pulsed CO_2 laser. The continuously tunable, high-pressure CO_2 laser has operated with line widths as low as 100 MHz, pulse energies of 100 mJ, and repetition rates of several hertz, and is a viable candidate for Shuttle lidar applications.

The Laser Development Corporation of Lexington, Massachusetts, has made some substantial progress in developing a single-frequency closed-cycle high-pressure tunable CO_2 TEA laser. A competitive but somewhat less sophisticated version of this tunable device is marketed by Lumonics of Canada, but without the closed-cycle capability. Both lasers use a UV preionization followed by a sustainer pulse. In principle, there should not be much more difficulty in space-qualifying (space-qualification here means unattended operation for 1 to 2 weeks in the Shuttle) a high-pressure CO_2 laser than a 1-atmosphere laser. In all likelihood, a maximum of 3 to 5 atmospheres of pressure using a few common isotopic combinations of carbon and oxygen in CO_2 would be all that is required in order to achieve the required spectral coverage.

DYE LASERS

Dye lasers are particularly useful for remote detection using resonant fluorescence or Raman scattering, as has been demonstrated in several laboratories throughout the world. One-joule devices using flashlamp excitation have been used in such experiments, while other devices with average output powers in excess of 100 W have been demonstrated. Perhaps the most useful configuration of a dye laser for the Space Shuttle would be one excited by a frequency-doubled (or tripled) Nd:YAG laser. Some of the advantages of such a scheme would be the use of a space-qualified Nd:YAG laser, avoidance of UV degradation problems of dyes in lamp pumped systems, and shorter output pulses for better range resolution.

The optical to optical conversion efficiency of a dye laser pumped by a frequency-doubled Nd:YAG laser can approach 50 percent in the best cases for the most favorable dyes. A number of laboratories (Sandia and Lawrence Livermore) have demonstrated a transform limited line width output from such a dye laser with line widths on the order of 100 MHz or less and high conversion efficiencies. A few other laboratories have also used a multitransverse mode doubled Nd:YAG laser to pump a dye laser with 30 to 50 percent conversion efficiency into a TEM_{00} output. These performance figures are quite impressive and represent a substantial improvement over what the lidar committee had previously considered.

APPENDIX B

RARE-GAS HALIDE LASERS

The rare-gas halide lasers such as KrF and ArF, which have recently become commercially available, operate in the UV/visible region with about 1-percent conversion efficiency and in a simple transverse electrical discharge similar to CO_2 TEA lasers. These lasers, which by themselves are somewhat tunable, could become excellent sources to pump dye lasers or for some tunable nonlinear mixing scheme to produce outputs in the UV/visible region. Frequency shifting of these rare-gas halide lasers with high efficiency using stimulated Raman scattering has already been demonstrated. Figure B3 shows a number of primary excimer laser frequencies along with the frequencies obtained for a single Stokes shift using several gases. Average output powers from such lasers of up to 40 W have been reported. The accelerated development of these lasers both by industry and the military makes them serious candidates for at least second-generation Shuttle lidar applications.

SEMICONDUCTOR DIODE LASERS

Semiconductor diode lasers are commercially available and have demonstrated an outstanding spectroscopic capability in several laboratories. Continuously operating devices have covered the range from 2.7 to over 30 μm by use of several alloy composition materials and temperature tuning. While lasers which operate continuously at liquid nitrogen temperature have been fabricated, the broad spectral coverage from a single device requires operating at temperatures down to 20 K. Closed cycle helium refrigerators which are presently used with semiconductor diode lasers require between 1 and 2 kW of electrical power to drive the compressors. The reliability of lead-salt diode lasers has not reached the level of other laser devices, with the major problems still being lifetime and variable spectral output characteristics. For a limited set of program objectives, a 77 K device used in a heterodyne radiometer mode could be useful.

NONLINEAR CONVERSION OF LASER FREQUENCY

Nonlinear conversion of primary laser frequencies could be an important adjunct to generating outputs in wavelength regions of interest for remote detection. While most of the physical mechanisms that can produce tunable output frequencies are still in the laboratory stage, there are some techniques which are and can be used in a practical system.

Second harmonic generation is probably the best such example of nonlinear frequency conversion where the primary source is an Nd:YAG laser or a dye laser. In addition, second harmonic generation of CO_2 laser radiation using chalcopyrite crystals such as $CdGeAs_2$ is a viable means of extending the output frequencies of CO_2 lasers. Such crystals are in use at Lincoln Laboratory for remote detection studies of molecular effluents using inhouse grown material and could be made available for some Shuttle experiments.

Sum and difference frequencies have also been generated using CW or pulsed CO and CO_2 laser frequencies in $CdGeAs_2$. By permuting the large number of available frequencies available from each of these lasers, a very large number of sum or difference frequencies can be obtained over a substantial portion of the infrared. By using low-pressure gas laser devices (i.e., space-qualified capillary lasers) there would be no problem of frequency calibration or maintaining the precise frequency for detection of a particular specie. Enough power (several milliwatts) can be generated using small lasers for use as a local oscillator in heterodyning applications.

Sideband generation on CO or CO_2 laser frequencies using an electro-optic modulator has produced enough power for lidar or heterodyning application. Tuning is performed by conventional microwave oscillators. The electro-optic crystal, CdTe, is presently the most efficient and has produced 80-percent pulsed conversion efficiencies for single-sideband generation using a CO_2 laser and modulation frequencies of several gigahertz.

The optical parametric oscillator has been extensively developed by Professor R. Byer at Stanford University to the point of having its output wavelength controlled by a computer. Tens of millijoules at 10 Hz can be obtained at wavelengths out to 2.5 μm with spectral resolutions near 0.1 cm^{-1}. Professor Byer has used his parametric oscillator system for remote detection studies in the troposphere. The parametric oscillator is still regarded, however, as a complicated device which has difficulty in maintaining single-frequency operation with wide spectral coverage.

Four-wave parametric frequency mixing could be quite useful in converting Nd:YAG, dye, or rare-gas halide laser radiation to wavelengths in the range 100 to 1000 nm. The conversion efficiencies in many wavelength ranges can be quite high while maintaining the spectral purity of the primary laser sources. In the UV/visible regions, gases such as barium or sodium are used as the nonlinear media. Some of the disadvantages of this scheme are the complicated heat pipe technology required to maintain high vapor pressures of these alkali metals and the saturation of electronic levels which limits the power scaling. Four-wave mixing using pulsed CO_2 laser radiation has been demonstrated using commercially available single crystals of germanium with optical power conversion efficiencies of several percent. Scaling of such a scheme to the modest energy levels required for Shuttle application is not out of the question.

The field of tunable lasers is moving ahead quite rapidly, and new devices will be developed which will be more advantageous than those presently available. One such development which bears watching is the solid-state lasers such as magnesium fluoride doped with the transition metal ions such as nickel, cobalt, or iron. These devices are presently being studied at Lincoln Laboratory using a CW or pulsed Nd:YAG laser as the excitation source. Nearly 2 W of continuous output at 40 percent optical-to-optical power conversion efficiency has been obtained. These lasers are tunable in the range 1.6 to 2.2 μm and can be operated either pulsed or CW using excitation from a Nd:YAG laser, a flashlamp, a tungsten lamp, or an array of GaAs diode lasers. The primary tuning range of this device makes it ideal for frequency shifting into other IR frequencies using nonlinear mixing in crystals or Raman down conversion in gases. The refractory nature of the host crystal means that high average powers can be expected from such a laser system (>100 W).

APPENDIX B

The list of candidate lasers and their characteristics in table BIII is intended to generally indicate not only what choices are available but to demonstrate the complexity and breadth of laser technology.

APPENDIX B

TABLE BI.- QUANTA-RAY DCR LASER SYSTEM[a]

Parameter	Oscillator	Amplifier	Etalon	Without etalon		
				SHG (c)	THG	FHG
Wavelength, nm	1064	1064	1064	532	355	266
Pulse energy, mJ	200	700	[b]150/500	[b]70/200	[b]25/80	[b]8/30
Average power, W at 10 pps	2	7	[b]1.5/5.0	[b]0.7/2.0	[b]0.25/0.8	[b]0.08/0.3

Pulse width	8 to 10 ns, nominal, at full drive
Pulse repetition rate	User selectable; single shot to 20 pps (average power constant above 15 pps)
Mode	Uniphase, unstable or diffraction coupled resonator (DCR)
Beam diameter	6.3 mm, nominal
Beam divergence	Less than 1.0 mrad
Pulse energy stability	Less than 5 percent peak to peak with amplifier and less than 7 percent peak to peak pulse to pulse, oscillator only
Pulse jitter	Less than 5 ns from Q-switch on pulse
Utility service required	Electric: 190 to 250 V, 30 A, 50 or 60 Hz, single phase Water: 2ℓ/min, tap water

[a] Unstable or diffraction coupled resonator (DCR).

[b] Dual values are given for oscillator only/with amplifier.

[c] Type II KD*P crystal; type I KD*P crystal values are about 30 percent less.

APPENDIX B

TABLE BII.- OUTPUT WAVELENGTHS OF Nd:YAG LASER

Wavelength, μm
0.946
1.052
1.061
1.064
1.074
1.112
1.116
1.123
1.318
1.338
1.358

APPENDIX B

TABLE BIII.- LASER SOURCES

Type	Wavelength	Single-mode (TEM_{00}) output	Device efficiency, percent	Comment
Nd:YAG	1.06 μm	<1J (app) at 10 Hz ≈10 ns pulse	1	Oscillator plus amplifier configuration
CO_2	9 to 11 μm multiline	1 to 10 J 1 to 50 Hz ≈150 ns pulse	5 to 10	Many more lines with isotopes or with N_2O
CO_2 at 20 atm	Tunable 9 to 11 μm	0.1 J 1 to 10 Hz	5	
CO	5 to 6.5 μm	Not a good pulsed source	10 to 30	Many lines with isotopes
HF	2.4 to 2.9 μm	≈1 J 1 to 10 Hz	10	Line separation ≈40 cm^{-1} Toxic exhaust
DF	3.5 to 4.2 μm	≈1 J 1 to 10 Hz	10	Line separation ≈20 cm^{-1} Toxic exhaust
KrF ArF XeF	250.0 nm 193.0 nm 350.0 nm	100 mJ with 100 ns pulse 50 mJ (pulsed) 50 mJ (pulsed)	<1 <1	Slightly tunable (0.4 nm) Commercially available Uses toxic gas system
Semiconductor diode	2.7 to 30 μm 0.75 to 0.9 μm	0.1 to 10 mW CW GaAlAs 20 mW CW	10 15	
Dye	300 to 1000 nm	0.1 to 3 J With 100 ns pulse With 10 ns pulse	 ≈1 10 to 30	Flashlamp pumped or Nd:YAG pumped using SH, TH of 1.06 μm
Copper Vapor	≈510.5 nm 578.2 nm	10^4 W peak 10 to 20 W (average) 10^4 Hz repetition rate	<1 (app)	Not scalable

APPENDIX B

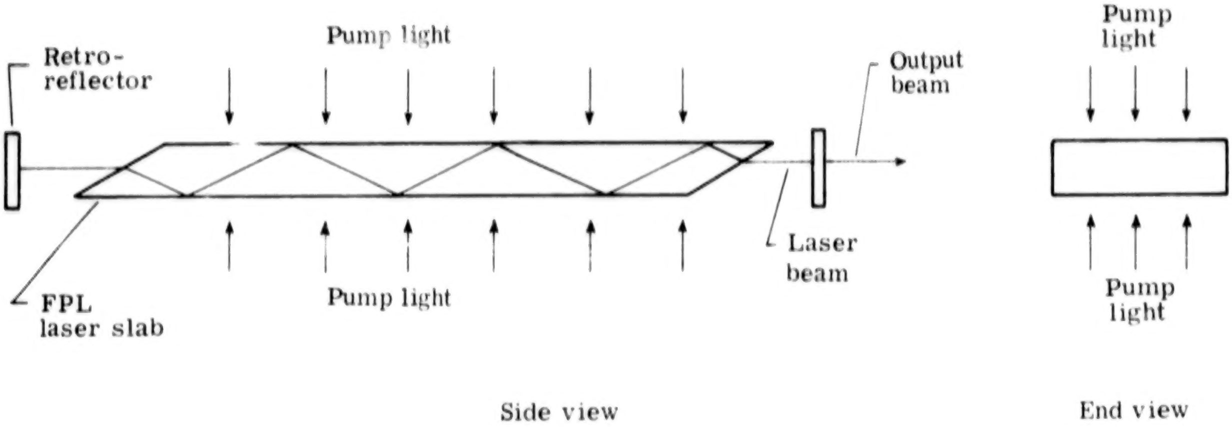
Retro-reflector
Pump light
Output beam
Pump light
FPL laser slab
Pump light
Laser beam
Pump light
Pump light
Side view
End view

Figure B1.- Concept of total internal reflection flashlamp-pumped laser.

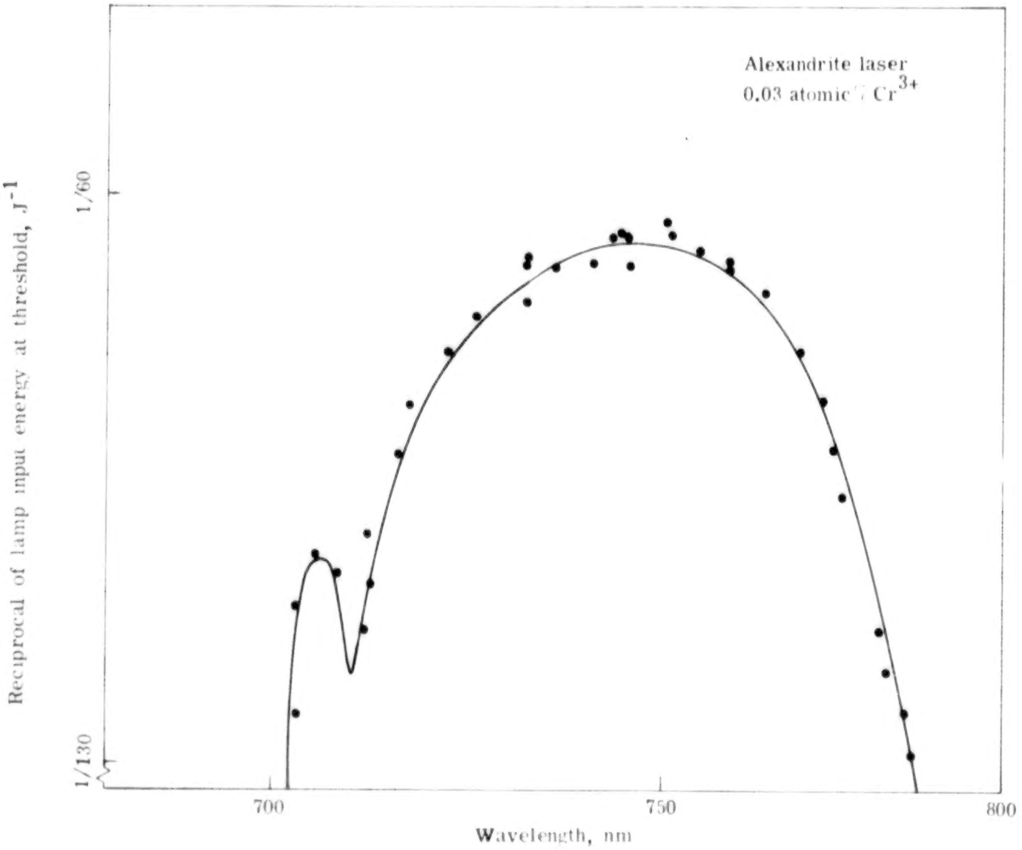

Figure B2.- Reciprocal laser threshold as function of wavelength.

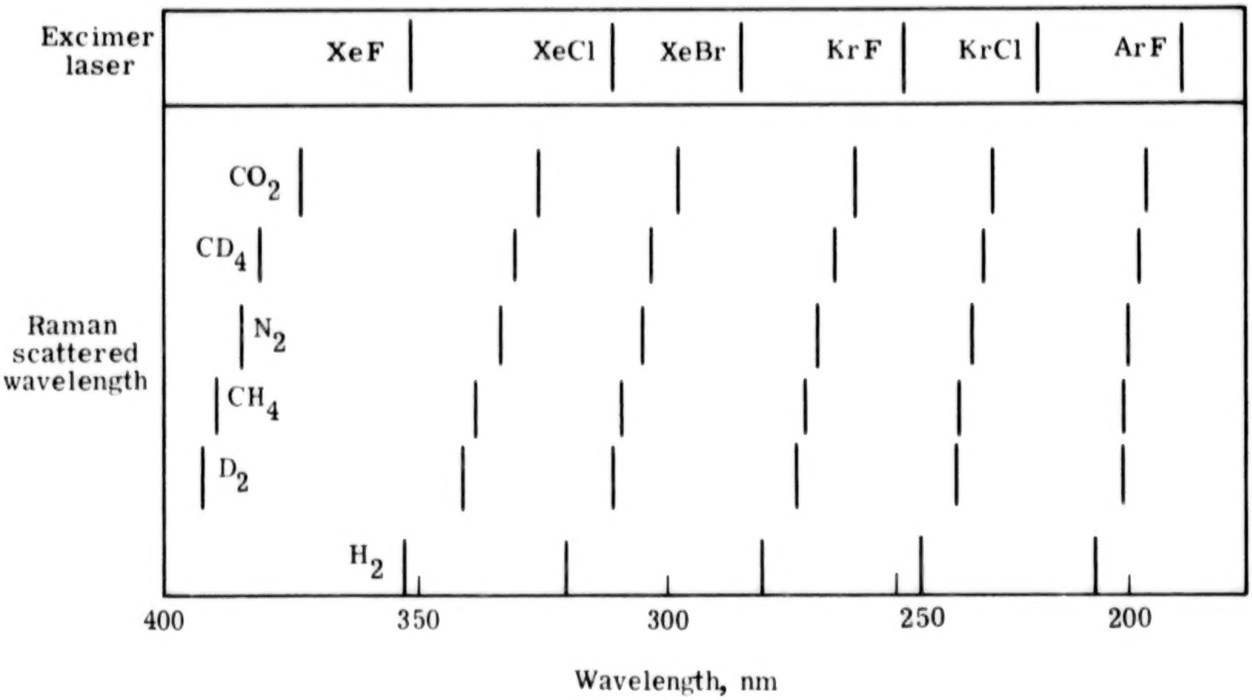

Figure B3.- Excimer laser frequencies and Stokes shifted frequencies.

APPENDIX C

TRANSMITTING AND RECEIVING OPTICS CONSIDERATIONS

INTRODUCTION

In order to define detailed requirements for a Shuttle lidar receiving optics system, one must consider the application or set of applications for which it is to be used. Fortunately, however, most atmospheric applications require a similar class of receiving optics which is well within the state of the art and, therefore, general requirements can be bounded. Limits for the various hardware parameters can be used to produce an initial design concept. Convolved with these hardware considerations, such as instantaneous field of view, area, baffling, wavelength range, size, weight, thermal and mechanical stability, surface quality, etc., are economic trade-offs, such as cost and Shuttle power versus weight, and considerations for eye safety. Exposure to laser energy, for example, can result from viewing a laser beam with the unaided eye or with the use of binoculars or telescopes. In addition, considerations for pointing and the accommodation of different detection systems must be examined.

LIDAR EQUATION AND SYSTEM CONSIDERATIONS

The fundamental lidar experimental geometry is shown in figure C1, where a laser pulse is shown propagating from a laser at point A with a divergence of δ_T. Located a distance X from the laser is a receiving optics system at point B having area A and an instantaneous field of view of δ_R. The general lidar equation for incident power $P(\lambda,R)$ on the receiving optics after crossover of the emitted laser pulse and receiver field of view is

$$P(\lambda,R) = \frac{cE(\lambda)Aq_T(\lambda,\Delta R)q_R(\lambda',\Delta R)f(\lambda,R)}{2R^2}$$

where R is the distance from the scattering volume to the receiver, $E(\lambda)$ is the laser output energy, c is the speed of light, $q_T(\lambda,\Delta R)$ is the transmission at λ from transmitter to scatterer, $q_R(\lambda',\Delta R)$ is the transmission at λ' from scatterer to the receiver, and $f(\lambda,R)$ is the backscattering function at R for λ. Wavelength λ' indicates that the scattered energy could be a shifted wavelength, e.g., Raman scattering from nitrogen. Transmission is defined as

$$q = \exp(-\tau) = \exp\left[-\int_0^R \beta(\lambda,R)\,dR\right]$$

where τ is the optical depth and β is the extinction coefficient. The equation for the current from a photodetector would include the receiving optical system transmission and photodetector spectral sensitivity. One sees, therefore, that the received signal is directly related to the area of the receiver, the transmission of the optical-filter system, and the photodetector sensitivity. Thus, the larger the mirror, the more photons collected; and the greater the quantum efficiency of the photodetector, the greater the signal received.

The background brightness noise, however, is dependent on the receiver field of view and the spectral bandpass of the optical-filter system. In general, the design should reduce the receiver field of view to as close to the transmitted laser pulse divergence as is possible and still maintain alignment. Obviously, the reduction of laser divergence is tied to the transmitting optics and laser safety considerations. (See fig. C2.) The safe radiation levels currently followed by civil and military laser safety officers are specified in the American National Standards Institute document ANSI-Z136.1-1973. There is a considerable margin for argument, however, depending on the amount of atmospheric scintillation (beam focusing by turbulence) and on how much protection should be provided for ground-based observers attempting to track a Shuttle borne lidar with light-gathering optics (binoculars or telescopes). While the letter of the specification provides eye safety for anyone viewing through objective diameters up to 80 mm (exceptionally large binoculars), the intent may be violated unless protection is also provided for the many owners of telescopes of appreciably larger aperture. Figure C2, therefore, shows the maximum permissible exposure for various collection optics up to 406 mm (16 in.) in diameter. In addition, the eye safety standard is somewhat laser wavelength dependent. The increased eye damage potential for the unaided eye, because of atmospheric focusing, however, presents a lesser hazard when averaged over larger apertures. The chosen design should also provide the minimum wavelength bandpass that is practical considering alignment of the filtering system and its transmission and considering the degree of collimation and beam size needed for the bandpass limiting device. For example, color filters need no collimation and can be fabricated in very large sizes, but the throughput of a Fabry-Perot etalon is very sensitive to collimation and beam size. Also, the photodetector's spectral responsivity depends in some cases on the angle of incidence of the collected light on the photocathode.

Another consideration affecting the optics design is the minimum range before the lidar return can be analyzed, i.e., after crossover of the transmitted laser pulse and the receiver field of view (FOV). (See fig. C1.) This minimum range R_{min} depends on X, δ_T, and δ_R. Also, the scatterers view the receiver area with a solid angle of A/R^2. For a one-meter receiver with an FOV of 10^{-3} rad, the scatterers will view the entire area when they are greater than 1 km distance. With an FOV of 10^{-5} rad, this distance becomes 100 km. For shorter distances the solid angle will be greater than the FOV allows, and a correction in the backscattering will have to be added that takes this into account.

Thus, these various design parameters are interrelated. For example: a reduction in receiver FOV to reduce background increases the minimum useful range and increases the difficulty of alignment and thermal/mechanical stability; a reduction in laser beam divergence with a collimating telescope to reduce the atmospheric footprint (to increase horizontal resolution) increases the energy density at the Earth's surface, which may be beyond the maximum permissible eye exposure, and increases the distance at which the full receiver area is used; a decrease in spectral bandpass to reduce background noise increases the difficulties associated with filter alignment and temperature control and usually results in a lower transmission.

OPTICAL RECEIVING SYSTEM

Candidate types of reflecting telescope designs for Shuttle lidar applications are shown in figure C3. It appears that it is safe to rule out a refracting system for Shuttle because of weight-cost-quality and transmission arguments for a combined applications payload. Shown in table CI are a number of studies which have been performed for large telescopes in space, and several of them have considered the lidar application. For example, SRI International considered three telescope configurations. Their pertinent characteristics are listed in table CII. The most exhaustive study is the ESA Spacelab report which presents a detailed design for a Shuttle lidar system. Table CIII lists design characteristics for Spacelab lidar telescope systems proposed by ESA, Perkin-Elmer, and SRI International. As can be seen, all three chose the Dall-Kirkham configuration of the Cassegrain telescope which uses an oblate spheroid primary mirror and a convex sphere secondary mirror. This configuration was chosen for a number of reasons, which include the relative ease and insensitivity of alignment, simplicity of fabrication, ease of baffling, good throughput, accessibility of focal plane for coupling to a number of photodetectors, tolerable aberrations, and close proximity of the heaviest elements of the lidar receiver (i.e., the primary mirror and detector package can be located such that a low center of gravity near the Shuttle pallet floor is achieved).

For a number of applications, a lidar telescope need not be of high optical quality (i.e., less than diffraction limited) since the signal is directly related to backscattered photons and mirror area. But for applications using heterodyning, the receiving optics should be diffraction limited. Heterodyning, however, is generally performed using IR lasers and a reasonable quality visible telescope would be of high quality in the IR. In any case, one-meter $\lambda/5$ quality visible telescopes are not very difficult to fabricate and should be used in order to accommodate all known applications. For example, the angular size of the Airy disc for a typical one-meter telescope of this type at $\lambda = 1\ \mu m$ is approximately 2.44 μrad (0.5 arc sec). Coma, which is the prime aberration for a Dall-Kirkham, is 0.2 arc sec as shown in figure C4. Neither consideration appears very critical for typical telescopes to be used for the lidar application.

Another requirement for the receiving telescope is the needed broad spectral range of operation from the UV to the thermal IR. Various mirror castings and their reflectance as a function of wavelength are shown in figure C5. As can be seen, aluminum offers good reflection over the entire range of most laser devices. Other advantages are its good adherence to glass and its ability to be overcoated easily with SiO_2 or MgF_2. Thus, one telescope should cover the entire spectral range of lidar applications.

APPENDIX C

DETECTOR COUPLING

Another general requirement briefly alluded to earlier is the necessity to couple a telescope to a particular filter-optical-detector system. Figure C6 shows a greatly magnified example of a ray trace for a telescope-lens combination. The lens is used to collimate the light exiting from the telescope. If the telescope has an FOV of δ then the decollimation of light emerging from an exit pupil, which is one-half the entrance pupil, is 2δ. Thus, to fully illuminate a 0.05 m diameter photomultiplier or an interference filter to achieve a 0.05 m collimated beam from a one-meter telescope, the FOV is magnified by a factor of 20. An FOV of 10^{-3} rad produces a beam of 0.02 rad decollimation. For narrow spectral band operation, this becomes very important. The relationship for a Fabry-Perot design can be described by the étendue, or light-gathering power, of the combined telescope-interferometer system. Matching the étendue of the Fabry-Perot with the étendue of the telescope yields

$$D_R \delta_R = D_{FP} \left(\frac{2F\delta\lambda}{\lambda_o} \right)^{1/2}$$

where D_R is the diameter of the telescope entrance aperture, D_{FP} is the Fabry-Perot plate diameter, F is the finesse of the Fabry-Perot, $\delta\lambda$ is the spectral resolution of the Fabry-Perot system, and λ_o is the center wavelength being received. Figure C7 shows an analysis of this for a series of plate diameters by plotting the telescope FOV as a function of diameter for a fixed $\lambda_o = 0.6$ µm and a free spectral range $F\delta\lambda = 2$ pm. The spectral resolution was 0.1 pm for these free spectral ranges. Figure C7 shows that for a one-meter telescope and Fabry-Perot diameters of 3 to 10 cm, the acceptance angle of the receiver should be approximately 10^{-4} rad. The efficiency for larger FOV's would be greatly reduced. Another way of plotting this relationship is shown in figure C8 (from Trauger and Roesler, 1972) where the ratio of the telescope diameter to etalon diameter is plotted as a function of FOV for various spectral resolutions. Again, it is seen that the bandpass limiting device might limit or dictate the field of view and, therefore, the laser divergence of the system.

TRANSMITTING OPTICS

In order to steer or change the divergence of a laser output, intervening optics must be addressed in a Shuttle lidar design. Typically, a telescope is used like the one shown in figure C6, but in the reverse sense. In order to decrease the divergence of a laser output, the diameter of the output beam is increased. The divergence is decreased in proportion to the ratio of the laser-beam diameter to the telescope-output-beam diameter. Steering can be accomplished by a two-axis beam steerer driven, for example, by sampling the reflected pulse from a distant target with a quadrant detector. For the Shuttle, this could be the ground reflection.

APPENDIX C

EXAMPLE CONCEPTS

As mentioned previously, a number of studies have produced conceptual designs for the Shuttle lidar atmospheric application. These designs, except for the environmental considerations of a Shuttle launch and orbital flight, are typical of a number of designs presently in use or in development for ground-based and aircraft-mounted lidars. A variety of these designs were presented at the Eighth International Laser Radar Conference held at Drexel University, Philadelphia, Pennsylvania, June 6-9, 1977. Copies of the conference proceedings can be obtained from the American Meteorological Society. An example design for an aircraft receiver system to measure stratospheric aerosols is shown in figure C9. It is being developed by the NASA Langley Research Center to support satellite measurements of stratospheric aerosols and shows an example of the design considerations mentioned in the previous sections.

The Perkin-Elmer design for the NASA Langley Spacelab-1 lidar proposal is shown in figures C10 and C11. Table CIV lists a weight summary for this design. The ESA proposed design is shown in figure C12.

REQUIREMENTS

Based on the foregoing considerations, an initial list of requirements for the Shuttle lidar is summarized in table CV. These requirements have been derived from the best information available concerning the various atmospheric measurements that might be performed with a Shuttle lidar.

An approach to the transmitting/receiving optics systems design might begin with, but not be limited to, the following initial studies: (1) Define spacecraft interface and environmental test requirements and volumetric limitations; (2) define optical design and tolerance analysis requirements; and (3) specify environmental and telescope performance test requirements. These requirements would be related to the results of further applications studies and system simulation calculations. After these iterations, detailed specifications will emerge that will become the design criteria for the transmitting/receiving optics system. Engineering analysis of the selected configuration will be performed to assure that the design meets the total lidar system requirements.

REFERENCE

Trauger, J. T.; and Roesler, F. L.: Fabry-Perot Spectrometer Adjustment for the Compensation of Doppler Shift From Rapidly Rotating and Rapidly Flowing Sources. Appl. Opt., vol. 11, no. 9, pp. 1964-1969, Sept. 1972.

APPENDIX C

TABLE CI.- TELESCOPE REFERENCE STUDIES

ESA SPACELAB BORNE LIDAR FOR ATMOSPHERIC RESEARCH	PHASE-A VOL. 1 & 2	CONTRACT-ESTEC nº 2437/75-pp	DOCUMENT nº DSES/SP/SC 76/L1/173
ESA LARGE INFRARED TELESCOPE	PHASE-A	DP/PS(76)18 NEUILLY, 5/19/76	
PERKIN-ELMER TELESCOPE DESIGN FOR TRACE/SPACELAB		REPORT NO. 13112	9/15/76
STARSAT-A SPACE ASTRONOMY FACILITY		NASA TM X-73326	JULY 76

TABLE CII.- PERTINENT CHARACTERISTICS OF THREE TELESCOPE CONFIGURATIONS

Feature	Newtonian	Cassegrain	Dall-Kirkham
Fabrication difficulty:			
Primary mirror	Moderately difficult (paraboloid)	Moderately difficult (paraboloid)	Moderately difficult (oblate spheroid)
Secondary mirror	Moderately simple (optical flat)	Extremely difficult (hyperboloid)	Extremely simple (convex sphere)
Center obscuration	Most	Intermediate	Least
Overall telescope weight	Most (added structure required to support detector at front of telescope tube)	Intermediate	Least (telescope can be slightly shorter than Cassegrain)
Ease of alignment	Extremely simple	Extremely difficult	Relatively simple
Sensitivity to alignment	Very insensitive	Very sensitive	Relatively insensitive
Ease of mounting on pallet	Most difficult (detector must be supported at front of telescope tube; raises center of gravity)	Fairly simple (center of gravity near pallet floor)	Fairly simple (center of gravity near pallet floor)
Ease of light shielding	Poorest	Very good	Best
Control of effective focal length	Minimal (governed solely by focal length of primary)	Good (provides moderately broad amplification range)	Excellent (provides extensive amplification range)

TABLE CIII.- SHUTTLE TELESCOPE DESIGNS

Design	Diameter of primary mirror, m	Configuration	F-number of primary mirror	Exit pupil, cm	FOV, mrad
Perkin-Elmer	0.5	Cassegrain Dall-Kirkham F/10	F/2	2.5	0.5 to 3
ESA	1.0	Cassegrain Dall-Kirkham F/7.6	F/2	---	0.1 to 1
SRI International	0.5	Cassegrain Dall-Kirkham	---	---	1

APPENDIX C

TABLE CIV.- WEIGHT SUMMARY OF PERKIN-ELMER DESIGN

Component	Weight, kg
Secondary mirror	0.34
Secondary support	0.34
Secondary support rods	2.9
Primary mirror	22.7
Primary support	79.4
Radiation shroud	22.7
Field stop assembly	2.3
Neutral density filter assembly	2.3
Etalon assembly	3.6
Filter assembly	2.7
Flip mirror assembly	3.4
Laser (including heat exchangers and electronics)	45.4
Laser tilt mirror	4.5
Insulation	9.1
Etalon support plate	4.8
Collimating optics	1.1
Focusing optics	1.1
PMT (two)	1.4
Power supply of PMT	0.91
Fold mirror	0.68
Temperature control/power supply	4.5
Miscellaneous hardware	22.7
Total	238.9

CONTENTS

Page

PREFACE . . . . iii 1/A5

INTRODUCTION 1 1/A8

SCIENTIFIC INVESTIGATIONS WITH SHUTTLE LIDAR 4 1/A11
  RATIONALE FOR LIDAR ON SPACE SHUTTLE 4 1/A11
  SCIENTIFIC OBJECTIVES 7 1/A14
    Introduction 7 1/A14
    Scientific Objective 1: Global Flow of Water Vapor and Pollutants 10 1/B3
    Scientific Objective 2: Stratospheric and Mesospheric Chemistry and Transport 24 1/C3
    Scientific Objective 3: Radiative Models 34 1/C13
    Scientific Objective 4: Meteorological Data 46 1/D12
    Scientific Objective 5: Upper Atmospheric Waves 58 1/E12
    Scientific Objective 6: Thermospheric Chemistry and Transport . . . 67 1/F7
    Scientific Objective 7: Magnetospheric Sun and Weather Relationships 74 1/F14
  CANDIDATE SHUTTLE LIDAR EXPERIMENTS 80 1/G6

SHUTTLE ATMOSPHERIC LIDAR PROGRAM EVOLUTION 89 2/A2

APPENDIX A - DESCRIPTIONS OF SHUTTLE BORNE LIDAR EXPERIMENTS 95 2/A8

APPENDIX B - LASERS OF POTENTIAL USE FOR SHUTTLE LIDAR 163 2/F7

APPENDIX C - TRANSMITTING AND RECEIVING OPTICS CONSIDERATIONS 175 2/G5

APPENDIX D - SPECTRAL DISCRIMINATORS AND DETECTORS FOR SHUTTLE LIDAR 193 3/A14

APPENDIX E - GLOSSARY 219 3/C13

APPENDIX C

TABLE CV.- PERFORMANCE REQUIREMENTS FOR SHUTTLE LIDAR

AREA	1 m
FOV	0.05 TO 5 mrad
λ	0.2 TO 12 μm
SIZE OF EXIT PUPIL	LESS THAN 10.16 cm
OPTICAL QUALITY	DIFFRACTION LIMITED AT 10.6 μm
STRAY LIGHT	TBD BY CONTRACTOR
ABERRATION	LESS THAN 5 μrad
MISALIGNMENT BETWEEN TELESCOPE AXIS AND LASER AXIS	LESS THAN 20 μrad
$T(\lambda)$	BETTER THAN 80 PERCENT BETWEEN 0.2 AND 12 μm
TELESCOPE ALIGNMENT AND STRUCTURAL STABILITY	SO THAT BLUR IS LESS THAN 5 μrad
PHYSICAL VOLUME	SEE SPACE TRANSPORTATION SYSTEM USER HANDBOOK
PHYSICAL WEIGHT	SEE SPACE TRANSPORTATION SYSTEM USER HANDBOOK
LAUNCH, OPERATION, STORAGE, ENVIRONMENT	SEE SPACE TRANSPORTATION SYSTEM USER HANDBOOK
POINTING SPACECRAFT	SEE SPACE TRANSPORTATION SYSTEM USER HANDBOOK

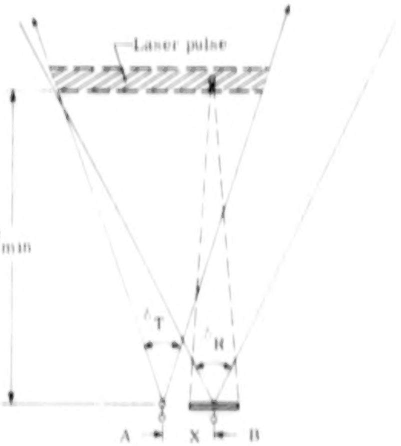
Laser pulse
R_{min}
θ_T
θ_R
A
X
B

Figure C1.- Transmitter/receiver beam geometry for typical lidar system.

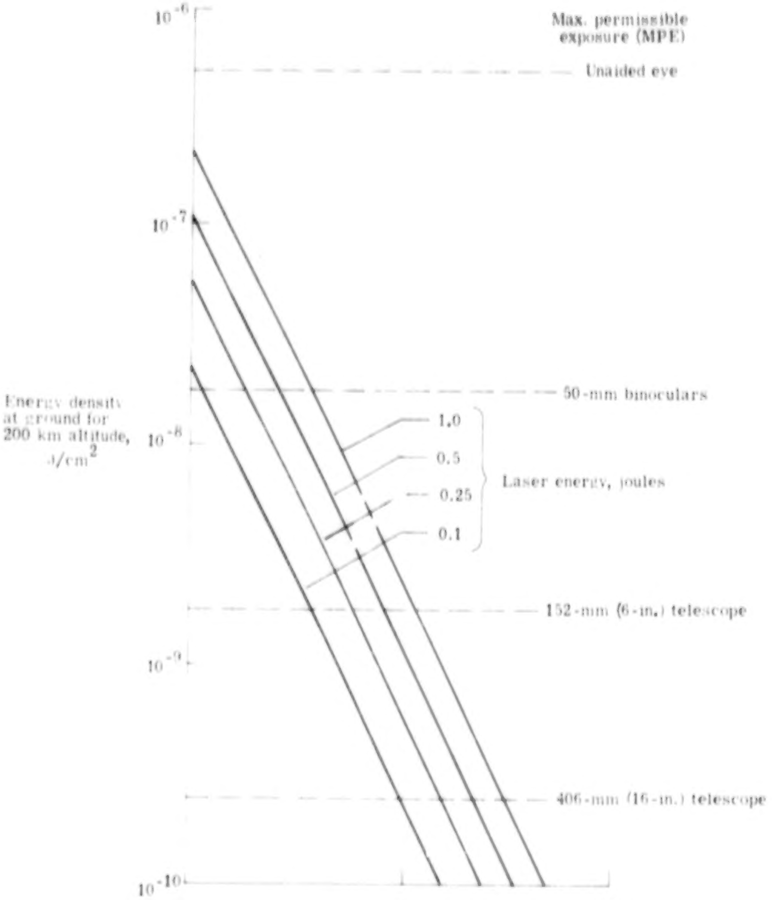

Figure C2.- Laser energy density on ground as function of beam divergence for different values of laser output energy. (Dashed lines indicate MPE for a particular receiving aperture and wavelengths from 0.4 to 0.7 µm.)

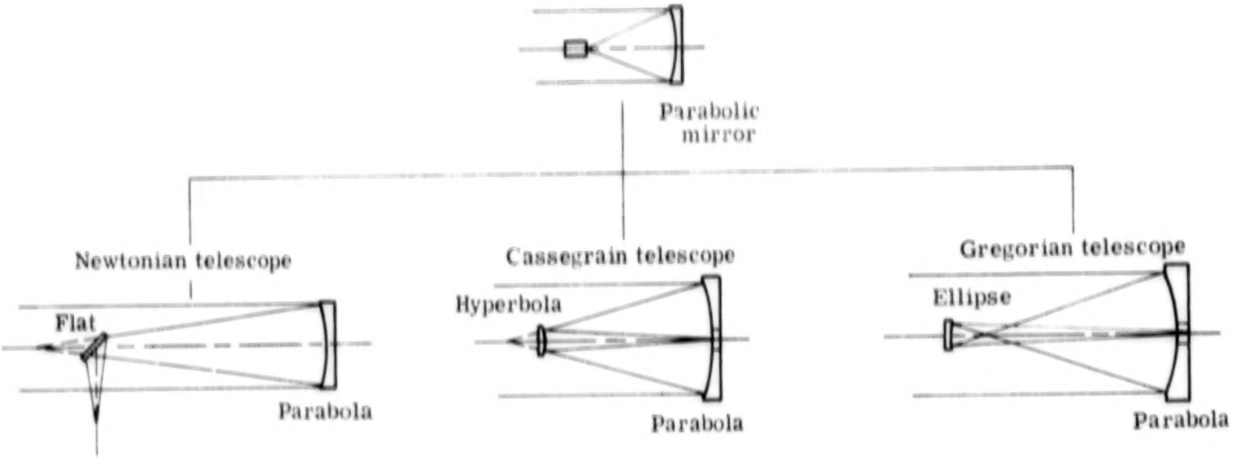
Parabolic mirror
Newtonian telescope
Flat
Parabola
Cassegrain telescope
Hyperbola
Parabola
Gregorian telescope
Ellipse
Parabola

Figure C3.- Reflective-telescope configurations considered for Shuttle lidar.

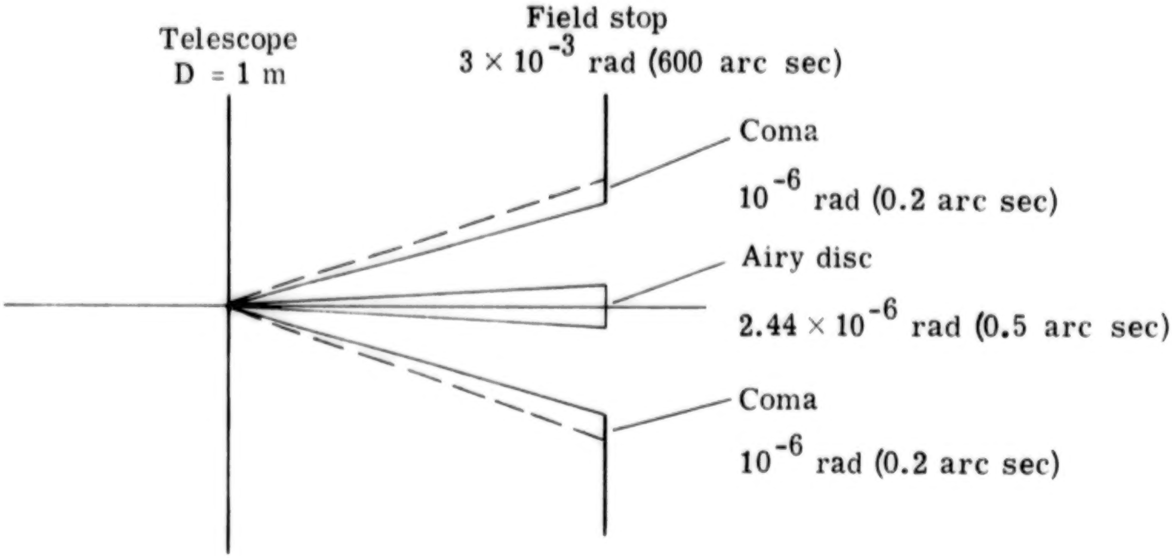
Telescope
D = 1 m
Field stop
3 × 10⁻³ rad (600 arc sec)
Coma
10⁻⁶ rad (0.2 arc sec)
Airy disc
2.44 × 10⁻⁶ rad (0.5 arc sec)
Coma
10⁻⁶ rad (0.2 arc sec)

Figure C4.- Relationship of Airy disc and coma for one-meter Dall-Kirkham telescope configuration.

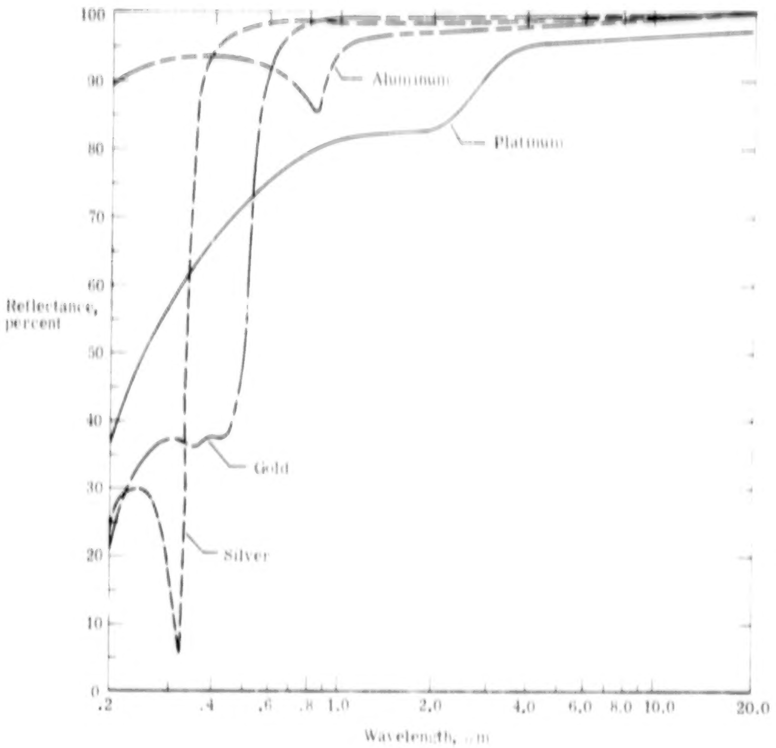

Figure C5.- Reflectance as function of wavelength for four different metal mirror coatings.

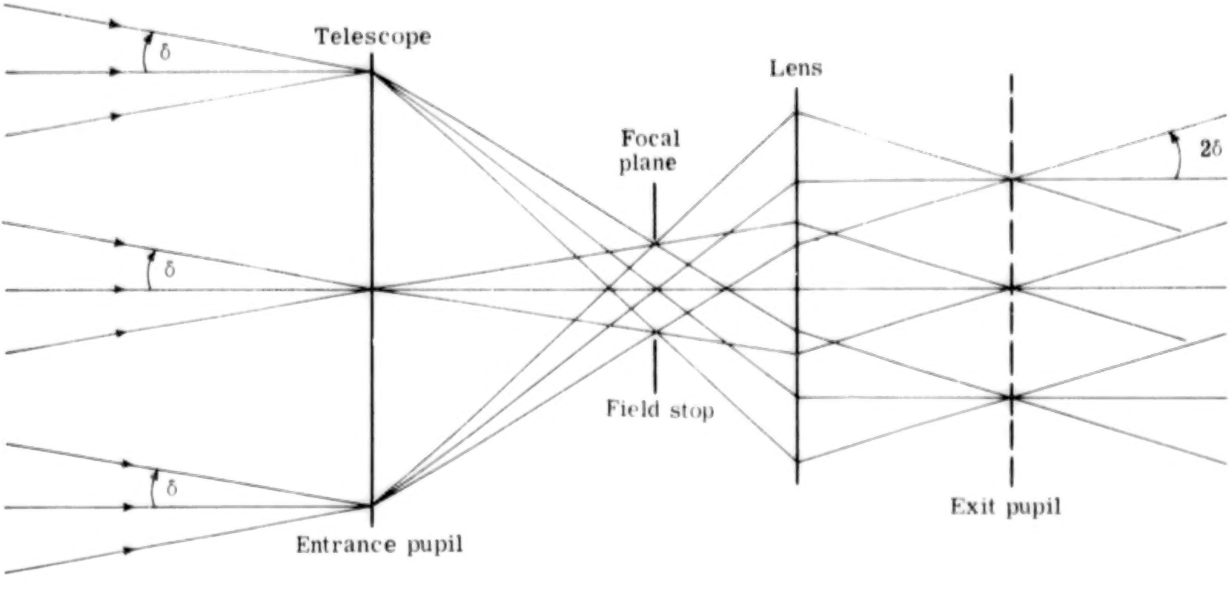
Telescope
δ
δ
δ
Lens
Focal plane
2δ
Field stop
Entrance pupil
Exit pupil

Figure C6.- Magnification of field angle δ with two-to-one coupling optics geometry.

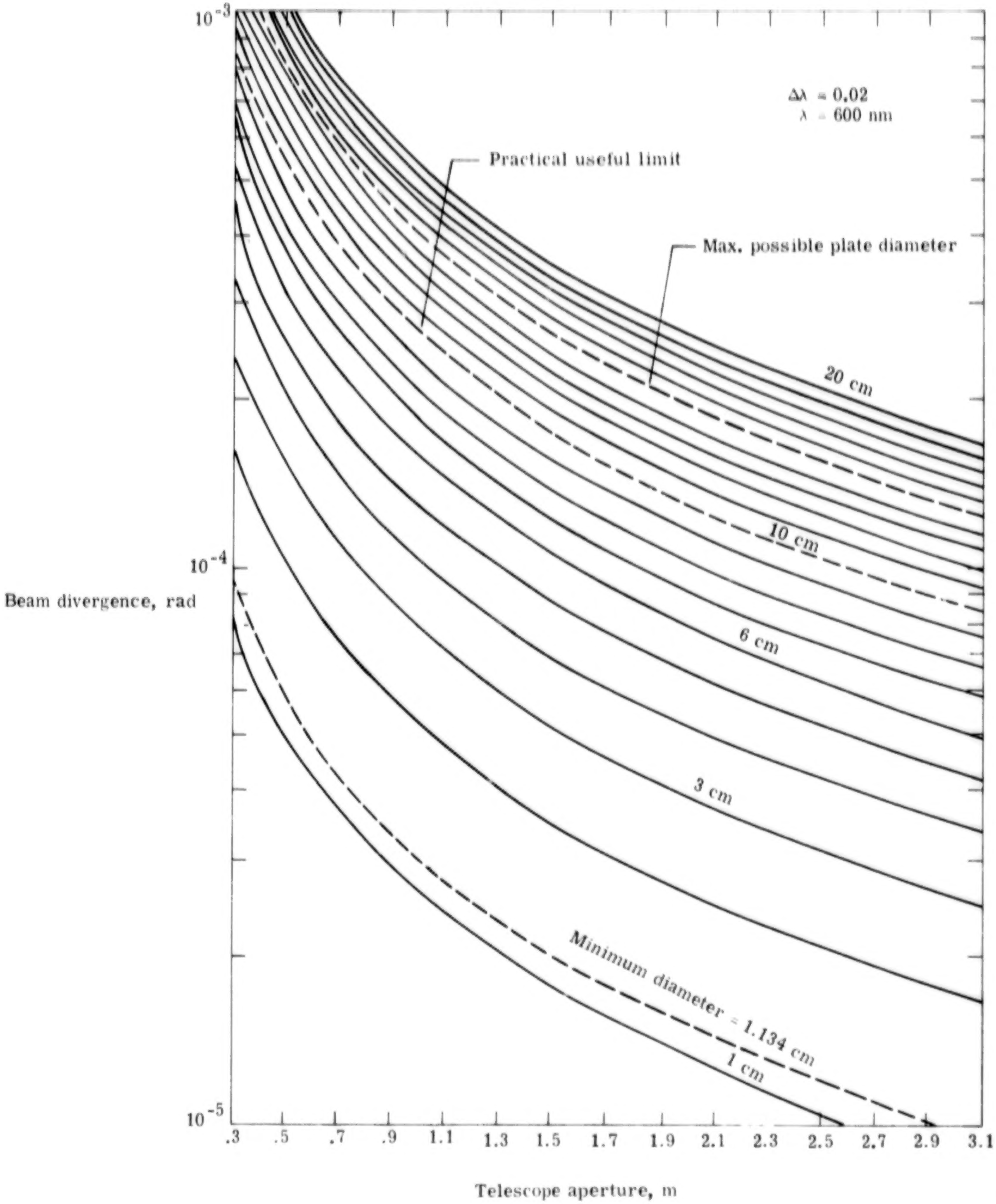

Figure C7.- Étendue constraint of telescope-etalon combination.

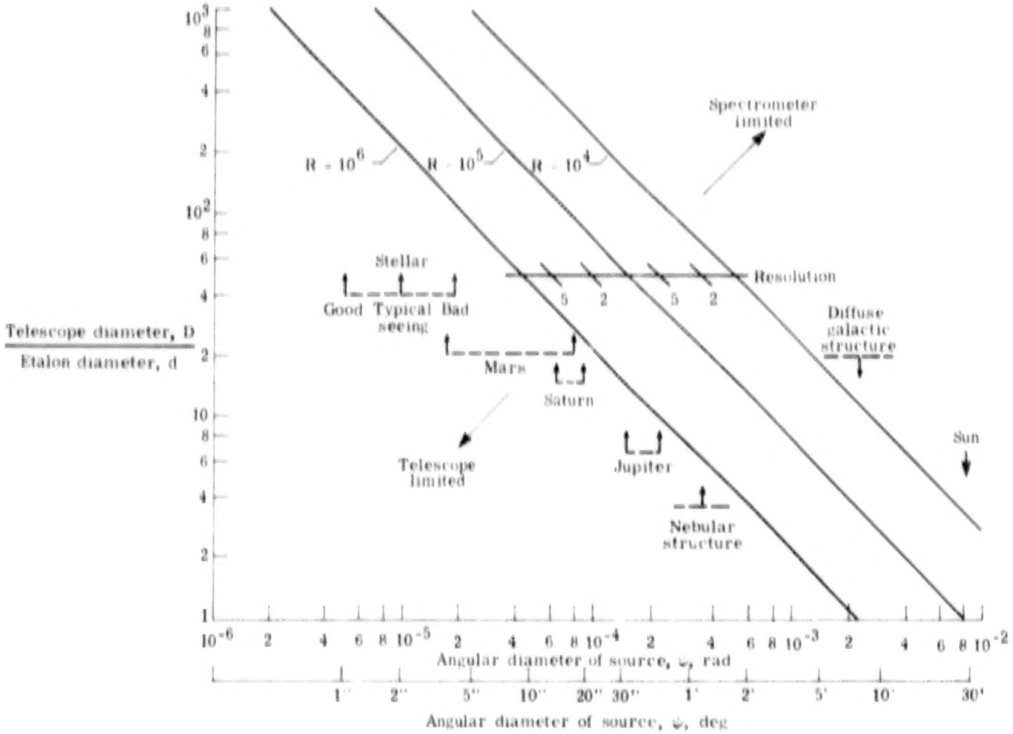

Figure C8.- Relative telescope to etalon aperture diameter ratio as function of FOV for given instrument resolution (from Trauger and Roesler, 1972).

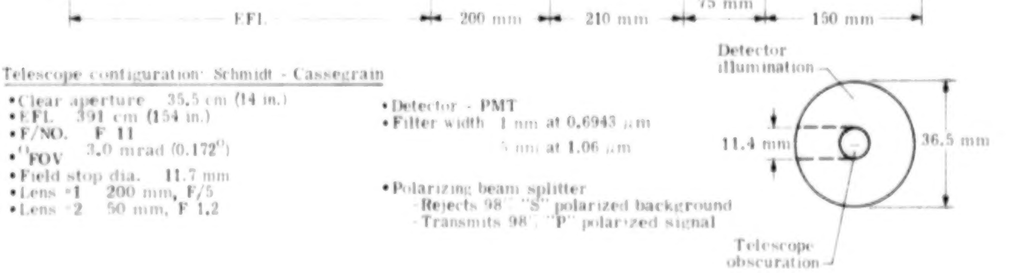
Telescope aperture (entrance pupil)
θFOV 0.172°
Field stop
Interference filter
Lens #1
3.36°
Rejected background ("S" polarized)
Lens #2
×2 mag. of exit pupil (detector)
36.5mm
Exit pupil
Field stop image
EFL
200 mm
210 mm
75 mm
150 mm
Telescope configuration: Schmidt - Cassegrain
•Clear aperture 35.5 cm (14 in.)
•EFL 391 cm (154 in.)
•F/NO. F 11
•θFOV 3.0 mrad (0.172°)
•Field stop dia. 11.7 mm
•Lens #1 200 mm, F/5
•Lens #2 50 mm, F 1.2
•Detector - PMT
•Filter width 1 nm at 0.6943 μm
5 nm at 1.06 μm
•Polarizing beam splitter
-Rejects 98% "S" polarized background
-Transmits 98% "P" polarized signal
Detector illumination
11.4 mm
36.5 mm
Telescope obscuration

Figure C9.- Telescope and coupling optics design for 35.5 cm diameter airborne-lidar receiver.

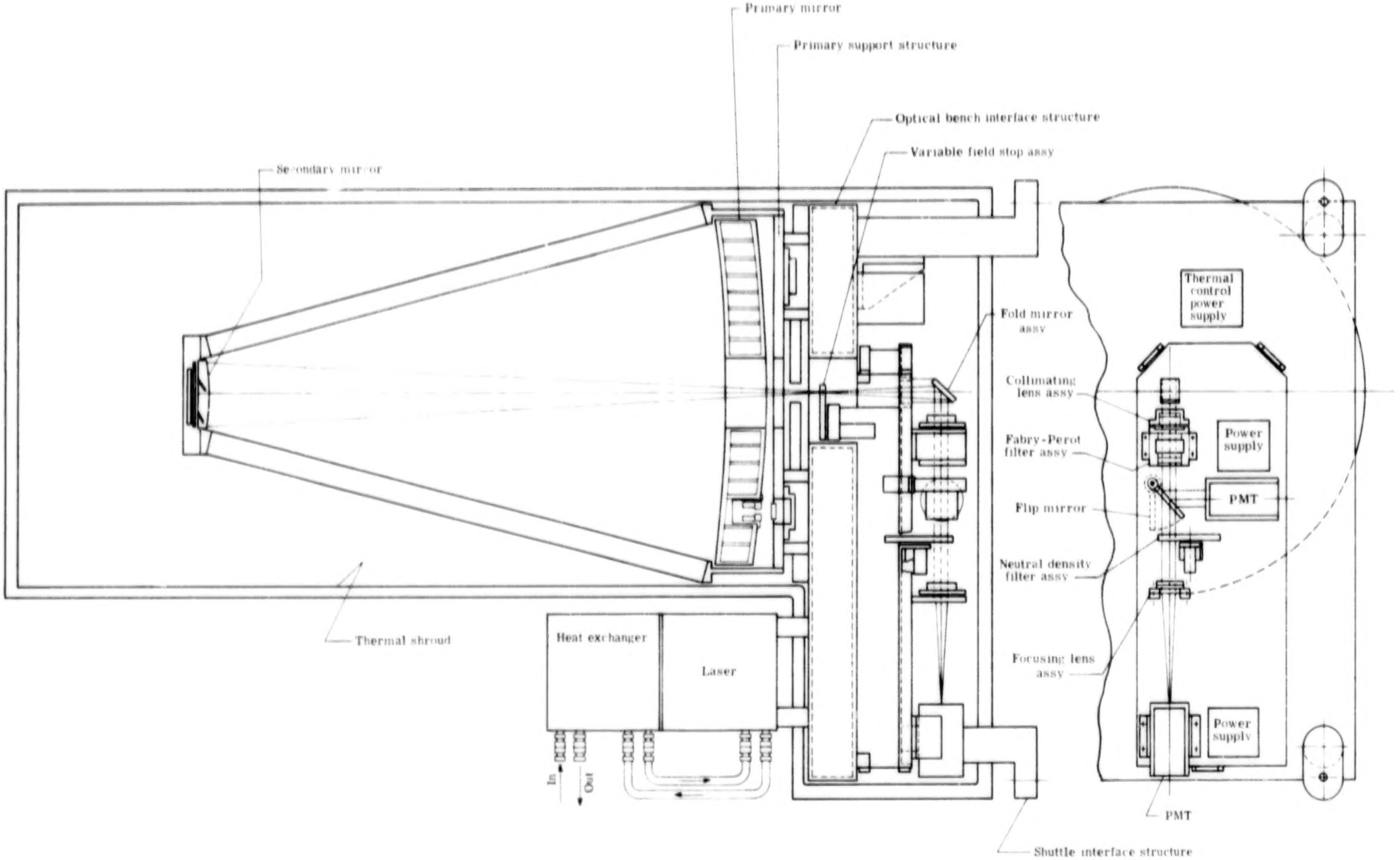
Primary mirror
Primary support structure
Optical bench interface structure
Variable field stop assy
Secondary mirror
Thermal control power supply
Fold mirror assy
Collimating lens assy
Fabry-Perot filter assy
Power supply
Flip mirror
PMT
Neutral density filter assy
Thermal shroud
Heat exchanger
Laser
Focusing lens assy
Power supply
In
Out
PMT
Shuttle interface structure

Figure C10.- Spacelab-lidar receiver proposed by Perkin-Elmer.

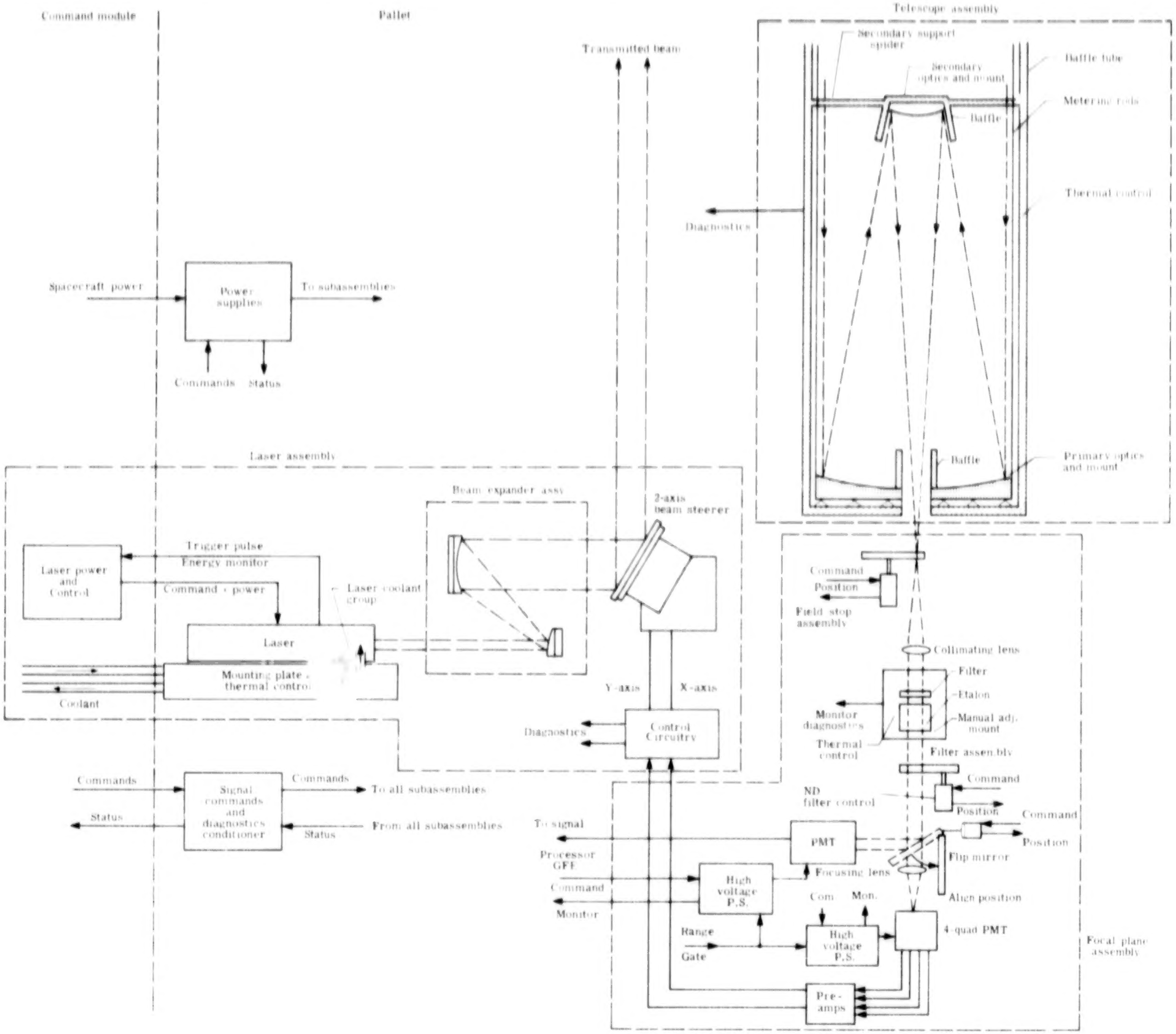
Command module
Pallet
Transmitted beam
Telescope assembly
Secondary support spider
Secondary optics and mount
Baffle tube
Metering rods
Baffle
Thermal control
Diagnostics
Baffle
Primary optics and mount
Spacecraft power
Power supplies
To subassemblies
Commands
Status
Laser assembly
Beam expander assy
2-axis beam steerer
Trigger pulse
Energy monitor
Laser power and Control
Command + power
Laser coolant group
Laser
Mounting plate + thermal control
Coolant
Y-axis
X-axis
Diagnostics
Control Circuitry
Command
Position
Field stop assembly
Collimating lens
Filter
Etalon
Monitor diagnostics
Manual adj. mount
Thermal control
Filter assembly
Commands
Signal commands and diagnostics conditioner
Commands
To all subassemblies
Status
Status
From all subassemblies
Command
ND filter control
Position
Command
To signal
PMT
Position
Processor GFE
Flip mirror
Focusing lens
Command
High voltage P.S.
Monitor
Com
Mon.
Align position
Range
Gate
High voltage P.S.
4-quad PMT
Focal plane assembly
Pre-amps

Figure C11.- Transmitter/receiver schematic of Perkin-Elmer Spacelab-lidar design.

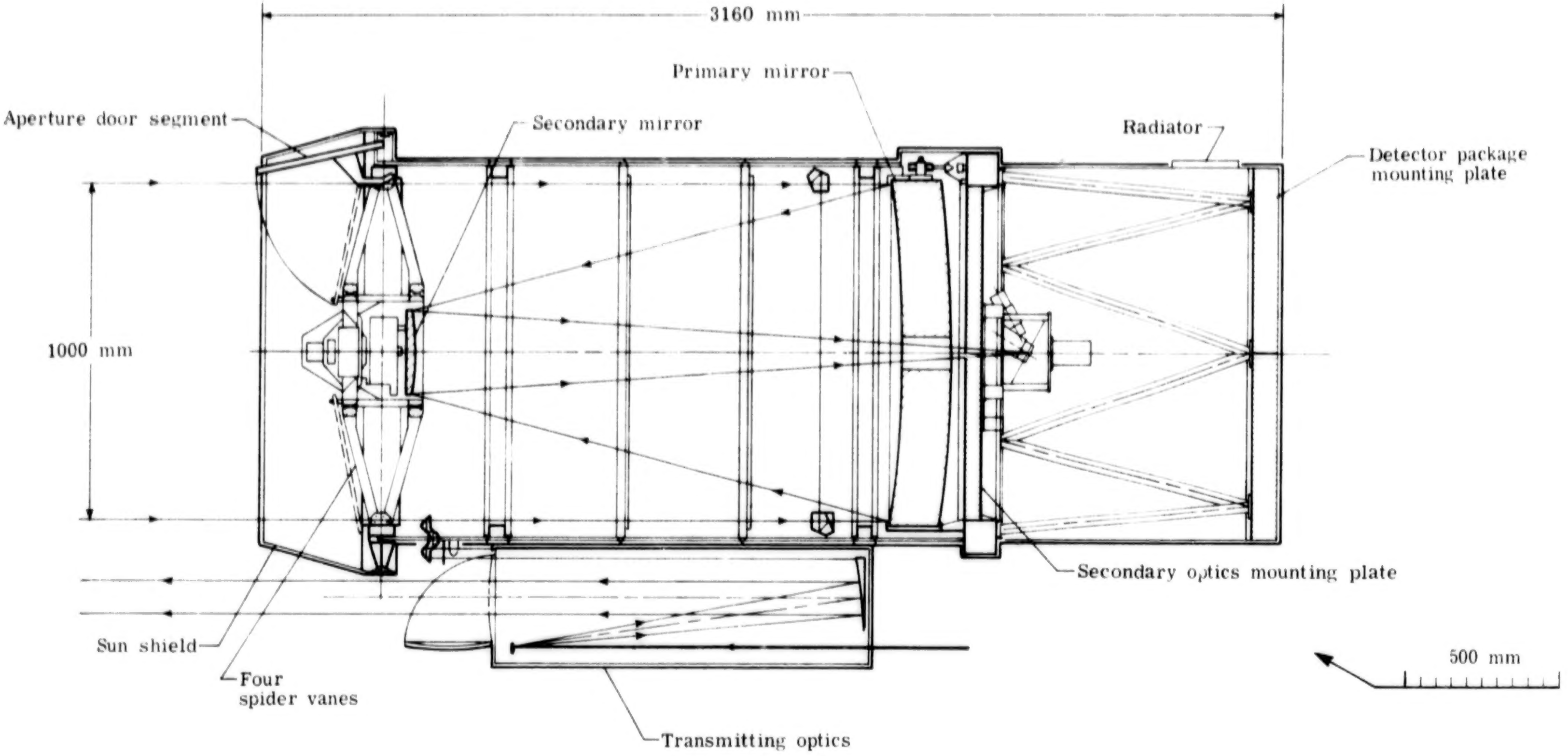
3160 mm
Primary mirror
Aperture door segment
Secondary mirror
Radiator
Detector package mounting plate
1000 mm
Secondary optics mounting plate
Sun shield
Four spider vanes
500 mm
Transmitting optics

Figure C12.- Schematic of ESA Spacelab-lidar receiver proposed by MATRA.

APPENDIX D

SPECTRAL DISCRIMINATORS AND DETECTORS FOR SHUTTLE LIDAR

Appendix D surveys possible methods and hardware available for spectrally isolating (or analyzing) and for detecting the received lidar signal. The most promising candidates are summarized, and other candidates and more detailed characteristics of all candidates are described.

SUMMARY OF MOST PROMISING CANDIDATES

Spectral Discriminators

Interference filters are excellent candidates for use on a first-generation Shuttle lidar. These filters are the simplest method for useful spectral discrimination, featuring light weight, small bulk, unpowered operation, and a history of lidar applications. Essentially, interference filters are fixed Fabry-Perot interferometers and are capable of bandwidths of 5 to 10 percent in the UV (0.2 to 0.3 μm) and 0.5 to 1 percent in the visible and infrared. Solid Fabry-Perot filters are similar in construction to common interference filters but use somewhat different techniques to achieve higher resolution. Typically, solid Fabry-Perot filters give a factor of 5 narrower bandpass than the interference filter devices but require a higher degree of thermal control, and so forth, to operate satisfactorily.

Still better spectral resolution and the ability to tune are offered by Fabry-Perot interferometers in the visible and in the UV. A typical plane Fabry-Perot consists of a set of quartz plates, up to 15 cm in diameter, with a CERVIT spacer. Instrumental resolution is typically of the order of 0.1 pm. The diameter of the etalon plates depends on the telescope aperture and on the laser beam divergence, because the étendue, or light-gathering power, of the etalon should match the étendue (area times beam divergence) of the lidar telescope. For a telescope aperture of 1 m and a beam divergence of 10^{-4} rad, an etalon with a plate diameter of 3 cm is appropriate, with a spectral resolution of 0.1 pm and a scannable bandpass (free spectral range) of 2 pm. The scannable bandpass can be increased or decreased by changing the etalon plate spacing.

Fabry-Perot interferometers have been used as receivers in ground-based atmospheric lidar systems, and a Fabry-Perot interferometer has been approved for flight in the Dynamic Explorer Satellite. As a class, they appear promising for space-borne lidar use in wind measurements and other applications that require high resolution or tunability.

Grating spectrometers are a less desirable alternative for the Shuttle lidar application, principally because of their greater size, weight, and complexity when compared to interference filters and etalons. It should also be remembered that the resolution of these devices is limited by the optical quality of the input beam, which could be considerably worse than diffraction-limited for down-looking lidar applications where the beam must be made eye-safe. The limiting formula (derived by R. C. Honey of SRI International) for the single-pass resolution R is

$$R = \frac{\lambda}{\Delta\lambda} < \frac{2.4W}{d\theta} \quad (1)$$

where

W width of ruled grating, independent of order or number of grooves

d diameter of lidar receiving aperture

θ half-angle of lidar field of view

An illustration of the importance of this limit is to calculate the size grating required to obtain a resolution of 0.5 nm for daytime background rejection at 589 nm, with a 1 mrad (full-angle) lidar beam and a 1 m receiver. The required grating is 30 cm wide, obviously a poor choice for a spectral discriminator when compared to an interference filter. Spectrometers may, however, find an eventual lidar application in multiwavelength studies of fluorescent returns in eye-safe portions of the UV or IR where the lidar can be operated with a small field of view.

Detectors

Table DI summarizes the characteristics of the most promising detector candidates for Shuttle lidar application. Photomultipliers are excellent candidates for use as Shuttle lidar detectors in the UV, visible, and near-infrared spectral regions. They have a history of use both in space and in lidar receivers; moreover, recent advances give high promise of yielding useful measurements out to the 1.06 μm line of the Nd:YAG laser. Avalanche photodetector modules are also making rapid advances and show good promise in this spectral region. At longer wavelengths, cooled semiconductor detectors (e.g., HgCdTe, InSb, PbSnTe), used either in the photoconductive or photovoltaic mode, offer excellent promise for use on an early Shuttle lidar mission. These detectors have been used both in space and in lidar receivers previously.

Heterodyne (i.e., coherent) detection in the IR has natural advantages over direct (incoherent) detection, both in sensitivity and in ability to measure small wavelength shifts. However, the advantages in sensitivity may not be so great as is often thought, because the sensitivity of incoherent detection benefits greatly from the reduced field of view and (filtered) optical bandwidth used in lidar receivers. The trade-offs between incoherent and coherent detection are described at some length in a later section. Coherent detectors have been used to make column-content gas measurements in a downward-looking airborne lidar system and may be expected to play a significant role in certain Shuttle lidar measurements.

Increasing numbers of array detectors are being flown in a variety of spaceflight applications. One possible lidar application is spatial scanning of the fringe pattern of a Fabry-Perot interferometer. Other possible applications include resolving individual clouds within the lidar field of view, spectral analysis for the Doppler shift of the ground echo, and monitoring the transmitted wavelength. To our knowledge, none of these applications has been demonstrated; these applications are mentioned here as possibilities for later missions in the evolutionary lidar program.

SPECTRAL DISCRIMINATORS

Interference Filters and Solid Etalons

Interference filters have been by far the most popular device for spectral discrimination in lidar systems to date. They are useful in the wavelength range 0.2 to 30 μm, can be readily accommodated to thermal environments, require no power, are small and lightweight, and are available from a number of manufacturers. Essentially, they are fixed Fabry-Perot interferometers and are capable of bandwidths of 5 to 10 percent in the UV (0.2 to 0.3 μm) and 0.5 to 1 percent in the visible and infrared. They are constructed using alternating quarter-wave dielectric coatings on a substrate to form a reflective surface, plus a half-wave layer spacer, and a repeat of the quarter-wave coatings which form the second reflective surface.

Of interest in the design of the telescope interface are the maximum acceptance angle and possible aperture size of interference filters. Since interference filters are Fabry-Perot devices, their resolution or bandpass is a function of acceptance angle, that is

$$\frac{\delta\lambda}{\lambda} = \alpha\theta^2 \tag{2}$$

where

θ cone half-angle, rad

$\delta\lambda$ bandpass for wavelength λ

α $= 1/2\ \mu^{*2}$

μ effective index of filter spacer

Most often used as the spacer dielectric are $ZnS(\alpha \approx 0.5)$ and $Cr(\alpha \approx 0.25)$. It is the limitation of the spacer characteristics and the ability to apply the dielectric layers uniformly in the manufacturing process which limit resultant bandwidth of the filter. Since the filter is used in an optical system that has some finite angle of acceptance, the angular effects on the bandpass must also be considered in the system design.

Solid Fabry-Perot filters are similar in construction to interference filters. Normally the reflective stacks for interference filters have reflectivity for a broad wavelength range, and the spacer is many wavelengths thicker than for a Fabry-Perot to achieve a higher resolution. Solid filters can be manufactured along Fabry-Perot principles using quartz (or similar conductors) as the spacer medium. Typically, these devices give a factor of 5 narrower bandpass than the interference filter devices but require a higher degree of thermal control, and so forth, to operate. Interference filters drift as $\delta\lambda \approx 0.25\delta T$, where temperature δT is given in Celsius. These devices are manufactured for a given wavelength by including dielectric stacks in series with the solid Fabry-Perot. These devices can be tuned slightly by simply tilting in the objective plane.

Fabry-Perot Interferometers

Fabry-Perot interferometers provide a means of achieving finer spectral resolution than is possible with conventional interference filters and permit tuning over a wide spectral range. Fabry-Perot interferometers can be used in a continuous range of wavelengths in the visible and in the ultraviolet, with the limitations imposed by reflective coatings of the plates. The resolution is a function of the etalon finesse and spacing. An instrumental resolution of 0.1 pm is easily attainable.

Fabry-Perot interferometers use both plane and spherical mirrors. For tuning, either pressure scanning or piezoelectric scanning systems are used. For space applications where high stability is required, permanently adjusted optically contacted plane etalons might be desirable. If this is the case, the scanning can be done spatially in the etalon fringe plane with an array detector.

Permanently adjusted etalons can be air-spaced or solid. Solid etalons covering a range of spacings from 0.3 mm to 30 mm are currently available commercially. For a solid etalon, compared with an air-spaced etalon, the dependence of resonant wavelength on angle is reduced by a factor of n^2, where n is the index of refraction. The n^2 advantage, however, is more than offset by the difficulty in manufacturing a large-diameter device of sufficient optical quality. The array of different Fabry-Perot types available is summarized in figure D1.

A parameter of importance in designing a Fabry-Perot interferometer system is the étendue V ($V = A\Omega$ where A is the beam area and Ω is the beam divergence) or light-gathering power of the system. In comparing the characteristics of a plane and a spherical Fabry-Perot, it is necessary to consider the étendue of the two devices for a given free spectral range and instrumental resolution. Although a spherical Fabry-Perot offers the advantages of smaller physical size and weight and more rapid scanning, the plane Fabry-Perot is advantageous as long as the plate diameter is greater than the spacing between the plates. Since it is routine practice to manufacture plane plates to an accuracy of $\lambda/200$ for any diameter up to 15 cm, the spherical Fabry-Perot is only advantageous if the required bandwidth or free spectral range is less than 1 GHz. It should also be noted that, in practice, the spherical Fabry-Perot cannot be spatially scanned. By spatially scanning a plane device with an array detector, approximately a factor of 10 is gained in sensitivity.

APPENDIX D

The area where present Fabry-Perot technology is likely to be pushed to its limits is probably in the design of high spectral resolution optical radar receivers. Systems in which the whole interference pattern of the Fabry-Perot is imaged by means of a television camera or photodiode array are most promising. Presently, this is an intensive area of investigation.

Commercially produced Fabry-Perot etalons.- Plane optically contacted air-spaced etalons of large aperture are now available commercially. For example, Imperial College Optical Systems (ICOS), London, is currently involved in the production of plates of diameters up to 15 cm and in the assembly of these into piezo-electrically driven etalons. Spherical Fabry-Perot etalons of free spectral range 7.5 GHz to 150 MHz and finesses in excess of 100 are available from ICOS and a number of firms in the United States.

Spatial scanning methods.- As previously mentioned, one technique for tuning a Fabry-Perot interferometer is to spatially scan the fringe pattern of a fixed etalon. This can be achieved in a number of ways, for example, by using electronic imaging devices or a Hadimard mask. In terms of stability and sensitivity, equal-area array detectors in the image plane seem to be the most promising of all the scanning techniques.

There are at least two technically feasible approaches to light detection from a Fabry-Perot interferometer used in a lidar system. Both employ a fiber optic bundle which converts the concentric ring bundle to a linear (or other) output wherein each linear element corresponds to a wavelength increment. One approach is to simply couple the linear array output of the fiber optical bundle to a bank of phototubes. Each tube represents a spectral element, and the output of the tube provides spatial information. High-speed photomultiplier tubes and data processing are required for this case. For example, in the pulse counting mode, 30 counts in 3 μs (≈1 km resolution) is an instantaneous count rate of 10 MHz, which is near the upper limit for pulse counting of moderate level signals. The photomultipliers and electronics are available from many sources, with a wide variety of photocathodes, packaging configurations, etc.

An alternative approach which eases the need to respond to very fast signals is shown in figure D2. This method employs a streak tube which spreads the time-spatial information across an image array detector which permits low data readout rates during laser off time. The output of the fiber optic bundle provides spectrally spaced input to the streak tube; the line image is electrically or magnetically scanned over the output phosphor, creating a two-dimensional wavelength versus time array. This information is further amplified by an image intensifier, the output of which is coupled in this case to a silicon diode array.

The elements of this system are available from many sources in the United States. Streak tubes have been used in several laboratory applications and are now provided commercially. There are other hardware combinations which accomplish the same result. The present example was chosen because it utilizes readily available parts. Weight for either detector system should be no more than a few kilograms.

APPENDIX D

Factors affecting performance of Fabry-Perot etalons on spacecraft.- The wavelength drift that can be tolerated in the operation of a Fabry-Perot etalon depends on its design and application. The stability requirements are most stringent in the measurements of atmospheric winds since a velocity of 5 m/s leads to a Doppler shift of only 0.01 pm at 0.6 μm. The control or measurement of such a change would represent a real challenge.

The factors affecting the stability of Fabry-Perot etalons have been outlined by Caplan (1975); his analysis related specifically to a pressure-scanned spectrophotometer, but many of the considerations are of general applicability. The location of the etalon, either within the pressurized module of Spacelab, or on a pallet as in the configurations considered in the ESA Phase A Study (Spacelab Borne Lidar for Atmospheric Research, 1976), is relevant. A pallet-mounted instrument should be free of effects associated with changes arising from the influence of pressure and temperature on the refractive index of the gas and of atmospheric pressure on the etalon spacers. However, the need to control the etalon temperature, chiefly to minimize the thermal expansion of etalon spacers, could be more troublesome for a pallet-mounted etalon. Presently available spacer materials, such as ultra-low-expansion titanium silicate, have temperature coefficients of about $10^{-8}/^{\circ}C$ and are capable of providing a stability of about 0.01 pm - rather better than the frequency stability of the most stable gas lasers in the visible part of the spectrum. For scanning of etalons by piezoelectric stacks, the temperature stability is rather poor since the piezoelectric materials have coefficients some two orders of magnitude larger. By suitable design of etalon and choice of materials, the effect of thermal expansion could be minimized so that the required temperature control could be within the range attainable in Spacelab usage.

Vertical mounting of the etalon plates would eliminate the effect of gravity also cited by Caplan (1975) - compression of etalon spacers by the upper plate, and plate sag - in testing of the system prior to launch; during operation no such effects would occur.

A Fabry-Perot interferometer has been approved for flight in the Dynamic Explorer satellite. This flight should provide some practical experience with the actual effects of the factors described above.

DIRECT, NONARRAY DETECTORS

Photomultipliers

Photomultipliers have been the most popular type of lidar detector for work in the visible and near-ultraviolet regions. The reasons for this popularity include fast rise time, appreciable quantum efficiency, and high internal gain; these factors eliminate the need for a low-noise preamplifier and permit detection of single photons. The quantum efficiency of a given tube is usually a rather strong function of wavelength and is determined by the particular photoemissive material used in its photocathode. Figures D3 to D5 show some examples of spectral response curves for various photocathodes. As can be seen, most materials have peak sensitivity for wavelengths between 200 and 800 nm, although some materials have useful sensitivities for wavelengths as long as 1.1 μm. Especially noteworthy is the InGaAsP photocathode (not shown in figs. D3 to D5), which has a quantum efficiency of 2 percent or more at the 1.06 μm wavelength of the Nd:YAG laser. (See for example Escher et al.,1976.) For the entire 200 to 1100 nm region and the complete set of photocathodes shown (figs. D3 to D5), quantum efficiencies range from less than 0.1 percent to as high as 30 percent.

Photomultipliers do require a high-voltage power supply, and in certain applications they require cooling to reduce dark current to acceptable levels. Nevertheless, many photomultipliers have already been used in space with very satisfactory performance.

The problem of detecting 1.06 μm return signals deserves special attention, both because of the selection of the Nd:YAG laser as a preferred source for space-borne lidar (appendix B) and because of the attractiveness of its 1.06 μm output for aerosol studies (appendix A). Over the last few years, very significant advances in PMT performance have been achieved at 1.06 μm, primarily as a result of work on classified military infrared systems. An example is the Varian PMT model VPM-164A, which appears to represent the current state of the art in devices available for unclassified projects. Its indium gallium arsenide phosphide (InGaAsP) photocathode has a quantum efficiency of 2 percent or better at 1.06 μm. This is about the same efficiency that has been employed in lidars for many years at the ruby wavelength using the S20 cathode. The InGaAsP photocathode is a very significant improvement over the 0.5 percent QE previously available in S1 photocathodes. In addition, the internally-generated noise level has been reduced to the point where, with moderate cooling, this noise component can be made negligible (less than 100 pulses per second) - again comparable to the best performance available at the ruby wavelength of only a few years ago. The noise performance of the Varian VPM-164A tube is discussed in more detail by Evans (1977). It should be noted that these tubes require special care, including continuous cooling to -20° C or below.

The Varian VPM-164A tube is in the process of being space-qualified and should have met all the space requirements (pressure, shock, humidity, etc.) by the time construction of a Shuttle lidar actually begins. In addition, its suitability for lidar applications (i.e., its rise time, uniformity of output, pulse shape, tendency for signal-induced noise, ruggedness, quantum efficiency, etc.) has been tested under a contract from NASA Langley Research Center to SRI International (Evans, 1978). If the PMT and other factors are found suitable, it will be used in a new airborne stratospheric aerosol lidar system being built by the NASA Langley Research Center. (See, e.g., Russell et al., 1978.) Expertise gained thereby should aid in evaluating the tube for space-borne lidar applications.

Photodiodes

Photodiodes, like photomultipliers, are based on the photoemissive effect, but they do not include an internal electron multiplier for amplification. Some vacuum and solid-state photodiodes offer rise times (0.1 to 100 ns) fast enough for lidar application. A YAG 444 photodiode was used to detect 1.06 μm returns on the ASSESS-II Spacelab lidar simulation mission conducted jointly by NASA and ESA in June 1976.

Avalanche Photodetector Modules

A device that falls into a middle ground between the photomultiplier tube (PMT) and the ordinary photodiode is the avalanche photodetector module. In the near infrared, avalanche photodetector modules have the advantages of higher quantum efficiencies than PMT's (15 to 30 percent as compared with about 3 percent for the 1060 nm PMT described above), while also having some internal electron gain. Because a low-noise preamplifier is required as part of the module, the gain is not as high as for PMT's. (See table DII for comparison.) Since there have been great advances in both types of detectors in recent years, their advantages should be carefully compared before hardware selection is made.

Photoconductive and Photovoltaic Detectors

In most of the infrared region of the spectrum, photoemissive elements are not available, and one must employ thermal or quantum detectors which exhibit internal photoeffects such as the generation of electron-hole pairs. This charge generation can either change the resistance of the device (yielding a photoconductor) or (for p-n junction detectors) produce a voltage (yielding a photovoltaic detector). The wavelength range of a detector is determined by the band gap of the material (for intrinsic detectors) or the ionization energy of impurity levels (for extrinsic detectors). Intrinsic detectors are available for wavelengths to about 14 μm, while radiation at longer wavelengths can be measured using extrinsic detectors. Table DII lists some presently available detectors.

HETERODYNE DETECTORS

With increasing wavelength in the infrared region, heterodyne (coherent) detection offers the promise of greatly increased sensitivity relative to that achievable with direct (incoherent) techniques. Coherent detection involves the mixing of two electromagnetic signals in a detector such that the magnitude of the beat frequency component is given by

$$i_{IF} = \frac{\sqrt{2\eta}Ge}{h\nu}(P_{LO}P_S)^{1/2} \tag{3}$$

where

i_{IF} detector current at beat (difference) frequency

η detector quantum efficiency

G	detector gain
e	electronic charge
$h\nu$	energy of one photon
P_{LO}	local oscillator power impinging on detector (larger of two electromagnetic signals)
P_s	power on detector from signal to be measured

It is clear that the heterodyne signal increases as the local oscillator power is increased, thus permitting the desired signal to override shot noise from the background and from succeeding amplifiers. Optical heterodyne detectors exploiting this basic principle have been built and used in many applications, including column-content gas measurements with continuous-wave CO_2 laser systems. (e.g., Menzies and Shumate, 1976, Shumate and Menzies, 1977). Some examples are shown in table DIII.

In addition to its potentially greater sensitivity, heterodyne detection also has natural advantages over incoherent detection in the measurement of small frequency increments (such as Doppler shifts and pressure broadening of spectral lines). These advantages, together with the greater sensitivity, could make coherent detection the method of choice in many space-borne lidar applications. Nevertheless, because of the increase in experimental complexity necessitated by a decision to use coherent detection, it is important in making this decision that coherent and incoherent methods be compared on an equal footing. As a guide to the experiment designer, therefore, some of the trade-offs between coherent and incoherent detection are considered in the following sections. Considered in turn are each of the four detection schemes: (1) incoherent detection of CW laser radiation, (2) coherent detection of CW laser radiation, (3) incoherent detection of pulsed laser radiation, and (4) coherent detection of pulsed laser radiation.

Incoherent Detection of CW Laser Radiation

For purposes of discussion, it is assumed that CW represents a chopping or modulation frequency of a few hundred hertz, or less. The background-limited noise-equivalent power P_n of a photoconductor is given by

$$P_n = 2\sqrt{\frac{P_b h\nu B}{\eta}} \tag{4}$$

where P_b is the background power received by the detector, B is the electrical bandwidth, and the other quantities are defined in equation (3).

The flux radiated by a black body at a temperature T in a wavelength interval λ to $\lambda + \Delta\lambda$ into the surrounding hemisphere is given by the Planck expression

$$H_b(\lambda, \Delta\lambda, T) = \frac{2\pi hc^2}{\lambda^5} \frac{1}{\exp\left(\frac{hc}{kT\lambda}\right) - 1} \Delta\lambda \tag{5}$$

The power received by the detector is

$$P_b = H_b(\lambda, \Delta\lambda, T) \frac{A\Omega}{2\pi} \alpha \tag{6}$$

where

A	area of telescope
Ω	$= \pi\theta^2$, solid angular field of view of telescope
θ	half-angle of FOV
α	transmission of cold filter

For the lidar, the emissivity of the telescope can be neglected in comparison with the emissivity of the Earth. The étendue being constant through an optical system without loss, $A\Omega$ can be calculated in front of the telescope or at the detector.

Combining equations (4), (5), and (6) and replacing $T = 290$ K, $\lambda = 10$ μm, $\Delta\lambda = 0.1$ μm, $A = 1$ m^2, $\alpha = 0.5$, $\eta = 0.5$, and $\theta = 10^{-4}$ rad or 10^{-5} rad results in

$$P_n \approx 2 \times 10^{-15} \text{ W/Hz}^{1/2} \qquad (\theta = 10^{-5} \text{ rad}) \tag{7}$$

$$P_n \approx 2 \times 10^{-14} \text{ W/Hz}^{1/2} \qquad (\theta = 10^{-4} \text{ rad}) \tag{8}$$

It should be noted that these values are two or three orders of magnitude smaller than those obtained from conventional calculations, which usually assume a rather wide detector FOV (e.g., 30°) and no spectral filtering of background radiation. The narrow FOV's and spectral filtering assumed are typical of a lidar receiver system. The aperture of 10^{-4} rad is the aperture proposed for the ESA lidar, and an aperture of 10^{-5} rad corresponds to the diffraction limit of a 1 m telescope at wavelength 10 μm. For various reasons (e.g., avoidance of beam splitter losses and backscattered transmitter radiation into the receiver) the FOV for a direct detection lidar would most likely be about 10 times the diffraction limit. (For example, the transmitted beam can be reflected off the backside of an obscuring secondary mirror in a Cassegrain telescope.) Hence, for concreteness, a 10^{-4} rad direct detection FOV is assumed in the following comparisons. The results should be appropriately adjusted for other FOV's.

APPENDIX D

Experimentally, Keyes and Quist (1970) have shown that the P_n of a Ge:Cu detector fully enclosed by liquid helium temperature was 10^{-15} W. More recently, Si:As detectors that operate in the 10 to 20 μm region have exhibited P_n of 2.5×10^{-17} W when similarly immersed. Consequently, liquid-helium-cooled detectors with a 10^{-4} rad FOV can be fabricated which have a background-limited P_n of 2×10^{-14} W, or smaller.

For a 1 m telescope on Spacelab with a 10^{-5} rad FOV, the average size of the speckle lobes will nearly equal that of the telescope; consequently, time-averaging of the speckle pattern returned from the Earth's surface, clouds, or aerosols will be needed. If, however, the transmitted laser beam is spread into a 10^{-4} rad cone, spatial averaging of speckle will occur since the lobes will be 10 times smaller and several will be detected simultaneously.

There is a question as to whether liquid helium temperatures can be achieved for the duration of a Shuttle flight; or would it be better to operate an infrared detector at liquid nitrogen temperature? In the latter case, the increased value of P_b results in higher P_n, according to equation (4). (For a photodiode, the factor of 2 in equation (4) is eliminated since there is no recombination-noise component, but this does not compensate for the full effect of raising the background temperature from 4.2 K to 77 K.) For a liquid-nitrogen-cooled photovoltaic detector, amplifier noise limits P_n to between 10^{-14} and 10^{-13} W.

Coherent Detection of CW Laser Radiation

Arams et al. (1967) have derived equations for P_n for coherent detection using the photoconductor Ge:Cu at liquid helium temperature. With a post-detection time constant τ, the equation becomes

$$P_n = 2\,\frac{h\nu_s B}{\eta\sqrt{B\tau}} + \frac{k(T_M + T_{IF})B}{G\sqrt{B\tau}} \tag{9}$$

where

η	detector quantum efficiency
B	IF bandwidth
k	Boltzmann constant
T_M	temperature of mixer (infrared detector)
T_{IF}	effective noise temperature of preamplifier
G	infrared detector gain

For a typical high-frequency Ge:Cu detector and commercially available preamplifier, the noise-equivalent power (calculated) for $B = 1$ MHz, $\tau = 1$ s, and $T = 4.2$ K is found to be 8×10^{-17} W.

Further, Peyton et al. (1970) have derived equations for P_n for coherent detection using a photovoltaic detector which can operate at 77 K rather than the 4.2 K needed for Ge:Cu. In this case, P_n becomes

$$P_n = \frac{h\nu_s B}{\eta\sqrt{B\tau}} + \frac{k(T_M + T_{IF})B}{G\sqrt{B\tau}} \tag{10}$$

The factor of 2 improvement in fundamental detection limit (first term on the right-hand side) stems from the absence of recombination noise in the photodiode.

In a comparison of theory with experiment, Arams found the measured P_n to be only 6 percent higher than the theoretical value. If the local oscillator power is sufficient to overcome the mixer and amplifier noise contributions, then for a 1 MHz bandwidth and 1 s post-detection integration time a photovoltaic detector with quantum efficiency of 0.4 will yield $P_n = 5 \times 10^{-17}$ W.

It is reasonable to assume that the laser frequency stability will permit a bandwidth of as small as 1 MHz to be employed during coherent detection. (The frequency stability of continuous-wave CO_2 lasers is usually much better than 1 MHz.) Consequently, a wide-bandwidth (100 MHz) preamplifier can be used in conjunction with a second mixer and a narrow-bandwidth (1 MHz) Doppler tracking receiver. (This technology is currently being used, for example, in a laser terrain avoidance system developed by United Technologies Research Center and at the M.I.T. Lincoln Laboratory laser radar facility.) In fact, bandwidths less than 1 MHz may be useful in reducing P_n still further.

To summarize the case of CW operation, an incoherent detection system with 10^{-4} rad FOV, 1 Hz electrical bandwidth, and 0.1 μm optical bandwidth and a coherent detection system with 1 MHz electrical (optical) bandwidth and 1 s integration time yield the following sensitivities:

LHe cooled Si:As photoconductor (incoherent)	2×10^{-14} W
LHe cooled Ge:Cu photoconductor (incoherent)	2×10^{-14} W
LN cooled HgCdTe photodiode (incoherent)	2×10^{-13} W
LN cooled HgCdTe photodiode (coherent)	5×10^{-17} W

Incoherent Detection of Pulsed Laser Radiation

If a range resolution of 1 km is required, the detector frequency response should be at least 166 kHz. For an extrinsic photoconductor, such as doped germanium or silicon, this wide bandwidth requires smaller time constants, which will result in an increase in Johnson noise due to the load resistor and amplifier. This raises P_n for the fully enclosed case from 5×10^{-17} W for $B = 1$ Hz to about 2×10^{-14} W (by the square root of the bandwidth ratios).

However, since P_n in a Shuttle application is governed by background radiation fluctuations, assuming the same conditions stated previously, the resulting P_n using equation (4) is 8×10^{-12} W when a 166 kHz bandwidth is used. Thus background radiation fluctuations are still the limiting source of noise. For an intrinsic photovoltaic device, such as HgCdTe, operating at 77 K, $P_n = 8 \times 10^{-11}$ W for pulsed operation. The HgCdTe photodiodes can be fabricated with flat frequency response to 1 GHz, whereas the extrinsic photoconductors must be doped with compensating donors in order to approach this high-speed capability; but this results in an accompanying reduction in responsivity. Thus for very high-speed applications, the intrinsic photodiodes become comparatively better.

Coherent Detection of Pulsed Laser Radiation

In a heterodyne detection mode, P_n for a single pulse of laser radiation is given by

$$P_n = \frac{h\nu_s B}{\eta} \tag{11}$$

For a 1 MHz bandwidth, and $\eta = 0.5$, $P_n = 4 \times 10^{-14}$ W. The biggest effect of pulsed operation on coherent detection is expected to be degradation due to the fact that speckle effects cannot be suitably averaged, as was the case for CW operation. It does appear that spatial averaging can be employed successfully if a heterodyne detector array is used. (The frequency stability of continuous-wave CO_2 lasers is adequate for use with 1 MHz bandwidth receivers.) If the transmitter has a reasonably high pulse repetition rate (e.g., 100 Hz), time averaging can be employed to increase the signal-to-noise ratio. For this case, a 1 s integration time (average of 100 pulses) results in $P_n = 4 \times 10^{-15}$ W. However, for direct detection, pulse-to-pulse averaging can also be used to reduce the effect of background fluctuations. Hence, a 100-shot direct-detection (10^{-4} rad) P_n of 8×10^{-13} W is the appropriate value for comparison with the coherent 100-shot (10^{-5} rad) P_n. This yields

$$\frac{(P_n)_{\text{coherent}}}{(P_n)_{\text{direct}}} = 5 \times 10^{-3}$$

where the coherent P_n is for 10^{-5} rad and 1 MHz and the direct P_n is for 10^{-4} rad and 166 kHz. Note that this ratio increases by an order of magnitude if an FOV of 10^{-5} rad can be used for the direct detection system.

Other Considerations

The foregoing sections of appendix D have concentrated mainly on the difference in ultimate detection sensitivity between coherent and incoherent detection. There are other factors which enter into considerations for application on the Shuttle, and these are presented in the following section.

Transmitter/receiver size.- For incoherent detection, the transmitting telescope is usually smaller than the receiving telescope, so that the receiver field of view ($\theta = d/f$, where d is the detector size and f is the receiver focal length) is filled by the area projected by the laser beam onto the scattering surface. If P_o is the transmitted power, A_R is the receiver area, and L is the pathlength to the irradiated (Lambertian) reflector of reflectivity ξ, the received power is

$$P_R = \frac{\xi P_o}{\pi L^2} A_R \tag{12}$$

If the detector size is increased to the point where the projected transmitter and receiver areas are equal, the area of each speckle lobe returned to the receiver is $A_{sp} = A_T < A_R$. Thus several speckle lobes are simultaneously collected and averaged by the receiver.

For coherent detection, when the receiver area is equal to the transmitter area, the received power is also given by equation (12), but the field of view (limited by the étendue of the system) is $\lambda/\sqrt{A_R}$. Since the size of the speckle lobe at the receiver is equal to the transmitter aperture, there is no destructive interference caused by speckle. If, on the other hand, the receiver diameter is larger than the transmitter diameter, several speckle lobes are collected by the detector simultaneously and destructive interference occurs since the phases of each lobe are uncorrelated. Consequently, for coherent detection, the receiver aperture should not be larger than the transmitter aperture.

Doppler shift due to hills and valleys.- The question has been raised as to the influence of hills and valleys on the beat frequency of the return signal during heterodyne detection. The beat frequency is not affected by changes in terrain because the detected signal is produced by laser radiation reflected from many "glints" on the rough surface, each of which is fixed in distance from a spacecraft moving parallel to the Earth's surface. A related theoretical analysis has been verified experimentally by several groups. Most notably, the Laser Absorption Spectrometer (LAS) measurements described by Shumate and Menzies (1977) were made with a fixed beat frequency of 3 MHz which was achieved by pointing the telescope at the ground slightly ahead of the aircraft. If hills and valleys with slopes to 45^o were to have influenced the return signal, variations in beat frequency of up to 10 MHz would have been observed. No such variations were seen, in agreement with theory. Also, depolarization of the 10 μm radiation by scattering is not expected to be significant. (See, e.g., Brandewie and Davis, 1972.)

Wavelength considerations.- This comparison between coherent and incoherent detection has been restricted to 10 μm since that is the wavelength where most of the relevant theoretical and experimental work has been done. It is also an important wavelength region for some early Shuttle missions. At longer wavelengths, coherent detection becomes increasingly more favorable; at shorter wavelengths, incoherent detection becomes better, being decidedly superior at the 1.06 μm wavelength of the Nd:YAG laser. It should be recognized, however, that the narrow-bandwidth optical filter required to shield the incoherent detector from external background radiation will limit its usefulness to the narrow passband region; whereas for coherent detection the sensitive region of the infrared is governed by the local oscillator wavelength. This can be an important consideration for continuously or discretely tunable laser measurements which might involve tuning over more than 1.0 μm.

System design.- Any optical elements in the receiver that attenuate either the transmitted or received power must be considered in any final evaluation of which detection scheme to use. For coherent detection, in order to have both the local oscillator power and the received power impinge on the mixer element colinearly, a beam splitter is used; this will cause some of the available laser power to be lost. There are techniques (e.g., feeding in the local oscillator power through the backside of the detector) which can reduce this loss. Other optical losses, such as those due to diplexing the transmit/receiver channels when using the same telescope, are common to both incoherent and coherent detection. The penalty for increasing the receiver FOV in the incoherent detection system is increased noise.

Conclusions

On the basis of ultimate detector sensitivity considered in isolation, a coherent detector is two to three orders of magnitude better than a liquid-helium-cooled incoherent detector. However, the signal-to-noise ratio of the overall lidar system is the important performance indicator, and this factor may not improve in direct proportion to detection sensitivity for the reasons mentioned. Hence, an overall signal-to-noise calculation and design considerations specific to the particular Spacelab lidar experiment should be the deciding factors in selection of the detection scheme to be employed.

ARRAY AND IMAGING DETECTORS

One possible application of an array detector - resolving the interference pattern of a Fabry-Perot etalon - has already been described in this appendix. Another possible application would be to provide spatial resolution within a wide lidar field of view, for example, in cloud studies. This would permit sampling a wide swath along the suborbital path or matching the field of view of co-aligned passive radiometers, thus permitting more precise comparisons. Still another possible application would be in measuring the ground echo amplitude without detector saturation by using (for example) a streak tube to sweep the return signal across an array as a function of time. To date none of these applications of imaging detectors are known to have been implemented in any lidar. Hence, they are suggested here as possible later-generation features of the evolutionary Spacelab lidar.

The range of types of array detectors is broad, including photodiode arrays, optical fiber arrays coupled to photomultipliers, multichannel plates, vidicons, charge-coupled devices, and charge-injection devices. (For a recent review, see Carruthers, 1977.) Development is proceeding very rapidly, with units usually custom built for specific applications. It is therefore difficult to characterize the range of possibilities by examples as in tables DI to DIII. Nevertheless, table DIV attempts a general overview. It can be seen that several types of array detectors have already been flown on spacecraft; many others are now being developed for future space flights.

APPENDIX D

REFERENCES

Arams, F. R.; Sard, E. W.; Peyton, B. J.; and Pace, F. P.: Infrared 10.6-Micron Heterodyne Detection With Gigahertz IF Capability. IEEE J. Quantum Electron., vol. QE-3, no. 11, pp. 484-492, Nov. 1967.

Brandewie, Richard A.; and Davis, Walter C.: Parametric Study of a 10.6-μ Laser Radar. Appl. Opt., vol. 11, no. 7, pp. 1526-1533, July 1972.

Caplan, James: Temperature and Pressure Effects on Pressure-Scanned Etalons and Gratings. Appl. Opt., vol. 14, no. 7, pp. 1585-1591, July 1975.

Carruthers, George R.: Electronic Imaging for Space Science and Applications. Astronaut. & Aeronaut., vol. 15, no. 10, pp. 56-68, Oct. 1977.

Escher, J. S.; Antypas, G. A.; and Edgecumbe, J.: High-Quantum-Efficiency Photoemission From an InGaAsP Photocathode. Appl. Phys. Lett., vol. 29, no. 3, pp. 153-155, Aug. 1976.

Evans, W. E.: Design of an Airborne Lidar for Stratospheric Aerosol Measurements. Final Report. NASA CR-145179, 1977.

Evans, Wm. E.: Evaluation of a Near-Infrared Photomultiplier for Airborne Lidar Applications. Final Report. NASA CR-145380, 1978.

Keyes, R. J.; and Quist, T. M.: Low-Level Coherent and Incoherent Detection in the Infrared. Semiconductors and Semimetals, Volume 5, R. K. Willardson and Albert C. Beer, eds., Academic Press, pp. 321-355, 1970.

Menzies, Robert T.; and Shumate, Michael S.: Remote Measurements of Ambient Air Pollutants With a Bistatic Laser System. Appl. Opt., vol. 15, no. 9, pp. 2080-2084, Sept. 1976.

Peyton, B.; Sard, E.; Lange, R.; and Arams, F. R.: Infrared 10.6-μm Photodiode Heterodyne Detection. Proc. IEEE, vol. 58, no. 10, pp. 1769-1770, Oct. 1970.

Russell, P. B.; McCormick, M. P.; McMaster, L. R.; Pepin, T. J.; Chu, W. P.; and Swissler, T. J.: SAM II Ground-Truth Plan - Correlative Measurements for the Stratospheric Aerosol Measurement-II (SAM II) Sensor on the NIMBUS G Satellite. NASA TM-78747, 1978.

Shumate, M. S.; and Menzies, R. T.: The Airborne Laser Absorption Spectrometer - A New Instrument for Remote Measurement of Atmospheric Trace Gases. Proc. of Fourth Joint Conference on Sensing of Environmental Pollutants, American Chemical Soc., pp. 420-422, 1977.

Spacelab Borne Lidar for Atmospheric Research - Phase A Study, Volume 1. Doc. No. DSES/SP/SC 76/LI/173, Centre National d'Etudes Spatiales, Engins MATRA, Service D'aéronomie du CNRS (Toulouse), 1976.

APPENDIX D

BIBLIOGRAPHY

Bates, B.; Bradley, D. J.; Kohno, T.; and Yates, H. W.: An Optically Contacted Permanently Adjusted High Finesse Fabry-Pérot Interferometer. J. Sci. Instrum., vol. 43, no. 7, pp. 476-477, July 1966.

Bates, B.; Conway, J. K.; McKeith, C. D.; and Yates, H. W.: Optically Contacted, Fabry-Perot Interferometer Filter for the Middle Ultraviolet. Appl. Opt., vol. 12, no. 1, pp. 140-142, Jan. 1973.

Bradley, D. J.: Applications of High Resolution Spectroscopic Techniques to Space Research and Laser Physics. Optica Acta, vol. 15, no. 5, pp. 431-450, Sept.-Oct. 1968.

Chabbal, R.: Investigation Into the Best Conditions for Using a Fabry-Perot Photoelectric Spectrometer. J. Rech. Cent. Nat. Rech. Sci., vol. 5, pp. 138-186, Sept. 1953.

Fried, David L.: Optical Heterodyne Detection of an Atmospherically Distorted Signal Wave Front. Proc. IEEE, vol. 55, no. 1, pp. 57-67, Jan. 1967.

Lau, E.: Interference Fringes of High Path-Difference Obtained by the Combination of Two Interference Systems With Different Dispersions. Ann. Phys., vol. 10, no. 1, pp. 71-80, June 24, 1931.

Okada, Masakutsu; and Ieiri, Shogo: Electronic Tuning of Dye Lasers by an Electrooptic Birefringent Fabry-Perot Etalon. Opt. Comm., vol. 14, no. 1, pp. 4-7, May 1975.

Peyton, Bernard J.; DiNardo, Anthony J.; Kanischak, Gerald M.; Arams, Frank R.; Lange, Ronald A.; and Sard, Eugene W.: High-Sensitivity Receiver for Infrared Laser Communications. IEEE J. Quantum Electron., vol. QE-8, no. 2, pp. 252-263, Feb. 1972.

Photomultiplier Tubes, Electron Multipliers, and Photodiodes. PIT-700B, Electronic Components, RCA Corp., Dec. 1971.

Siegman, A. E.: The Antenna Properties of Optical Heterodyne Receivers. Appl. Opt., vol. 5, no. 10, pp. 1588-1590, Oct. 1966.

Tolansky, S.: High Resolution Spectroscopy. Metheun (London), 1947.

APPENDIX D

TABLE DI.- CHARACTERISTICS OF MOST PROMISING DETECTORS FOR SHUTTLE LIDAR

(a) Direct, nonarray detectors

Type	Useful wavelength range, µm	Operating temperature (a)		Cut-off frequency, Hz	Quantum efficiency (b)	Noise-equivalent power, W/Hz$^{1/2}$ (c)
		Optimum	Maximum			
Photomultiplier	≲1.1	−30° C	150° C	5×10^7 to 5×10^8	≲0.005	
Examples:						
Amperex 56 TVVP	0.2 to 0.75	−100° C		10^8	0.2	≈10^{-14}
VPM-164A[d]	0.15 to 1.1	−20° C		10^8	≈0.02 at 1.06 µm	10^{-18}
VPM-154M					≈0.2 at 0.53 µm	
RCA 7265	0.3 to 0.75	−100° C	85° C	10^8	≈0.20	10^{-12}
EMI 9684QB	0.15 to 1.1	−180° C	60° C	10^8	0.5 at 0.85 µm	10^{-15}
Avalanche photodiode						
Examples:						
Ge	≲2			10^8	0.5	≈10^{-13}
Si	0.4 to 1.1	−40° C	70° C	5×10^7	0.5	≈10^{-13}
GaAs	≲0.9			~10^8	0.5	≈10^{-13}
Photoconductive						
Examples:						
GeCu	≲30	10 K		10^9		10^{-13}
HgCdTe	≲22	77 K	140 K	5×10^6		7×10^{-12}
Photovoltaic						
Examples:						
InSb	≲5.5	≲77 K	≲150 K	10^7	0.60	≈10^{-13}
PbSnTe	≲12	≲77 K	≲100 K	3×10^5	0.60	≈10^{-12}
	≲14	≲77 K	≲195 K	2×10^9	0.50	≈10^{-12}

[a] Performance shown is achievable at optimum temperature; performance degraded but operation possible at maximum temperature.

[b] At optimum wavelength unless otherwise noted.

[c] Optimum is not for device operating at maximum cut-off frequency.

[d] Tested for lidar suitability by SRI International under contract from NASA Langley Research Center (Evans, 1978).

(b) Heterodyne detectors[a]

Local oscillator (b)	Photomixer	Useful temperature range, K	Cut-off frequency, MHz	Noise-equivalent power, W/Hz (c)
CO_2	PV:HgCdTe	[d]70 to 120	50 to 1000	1 to 2×10^{-19}
	PC:GeCu	4 to 20	50 to 750	1 to 2×10^{-19}
	PC:GeHg	4 to 28	50 to 500	1 to 2×10^{-19}
	PV:PbSnTe	≈77	5 to 50	1 to 2×10^{-19}
Two $^{12}C^{16}O_2$ waveguide lasers; grating tunable	Mercury-cadmium telluride; PV; LN_2 cooled; quantum efficiency of 20 percent	Photomixer can operate between 60 and 140	40 MHz; postdetection integration time between 0.1 and 10 s depending on application	1.5×10^{-16}

[a] Most heterodyne work has been carried out near λ = 10.6 µm.

[b] Laser local oscillator and associated power supplies are key factors in determining weight and power requirements (cooler type is also important).

[c] P_n will, in general, be inversely proportional to bandwidth.

[d] Mixer temperature.

TABLE DII.- PHOTOCONDUCTIVE AND PHOTOVOLTAIC DETECTORS

Material	Peak wavelength, μm	Nominal operating temperature, K	Available response times, μs
InSb	5	77	<1
HgCdTe	[a]3 to 15	70 to 100	0.005 to 0.3
PbSnTe	[a]6 to 14	77	0.02 to 0.1
InAs	3	77	<1
GeAu	7	<60	<2
GeHg	11	<30	<1
GeCu	25	<20	<1

[a] Depends upon specific alloy composition.

APPENDIX D

TABLE DIII.- HETERODYNE DETECTORS[a]

[3 to 12 μm region]

Local oscillator (b)	Photomixer	Useful wavelength range, μm	Useful temperature range, K	Cut-off frequency, MHz	Noise-equivalent power, W/Hz (c)
CO_2	PV:HgCdTe	9 to 11	[d]70 to 120	50 to 1000	1 to 2 × 10^{-19}
	PC:GeCu	9 to 11	4 to 20	50 to 750	1 to 2 × 10^{-19}
	PC:GeHg	9 to 11	4 to 28	50 to 500	1 to 2 × 10^{-19}
	PV:PbSnTe	9 to 11	≈77	5 to 50	1 to 2 × 10^{-19}
CO	PV:InSb	4.5 to 4.9	≈77	15 to 100	≈2 to 4 × 10^{-19}
	PC:GeAu		≈77	5 to 50	5 × 10^{-19}
	PV:HgCdTe		≈77	5 to 100	≈2 to 4 × 10^{-19}
HF	PV:InSb	2.7 to 3.3	≈77	15 to 100	≈2 to 4 × 10^{-19}
DF	PV:InSb	3.5 to 3.9	≈77	15 to 100	≈2 to 4 × 10^{-19}
HeNe	PV:InSb	3.39	≈77	15 to 100	≈2 to 4 × 10^{-19}
Tunable diode (TDL)[e]	PV:HgCdTe	8.5	77	150	≈2 to 4 × 10^{-19}
	PV:HgCdTe	9.6	30		
Heterodyne receivers in JPL laser absorption spectrometer (active)					
Two $^{12}C^{16}O_2$ waveguide lasers; grating tunable	Mercury-cadmium telluride; PV; LN_2 cooled; quantum efficiency of 20 percent	9 to 11	Photomixer can operate between 60 and 140 K	40 MHz; postdetection integration time between 0.1 and 10 s depending on application	1.5 × 10^{-16}
Heterodyne receiver in JPL laser heterodyne radiometer (passive)					
$^{14}C^{16}O_2$ waveguide laser; grating tunable	Mercury-cadmium telluride; PV; LN_2 cooled; quantum efficiency of 20 percent	9 to 12	Photomixer can operate between 60 and 140 K	3 db roll-off at 800 MHz; postdetection integration time normally 10 s	1.5 × 10^{-15}

[a] Most heterodyne work has been carried out near λ = 10.6 μm.

[b] Laser local oscillator and associated power supplies are key factors in determining weight and power requirements (cooler type is also important).

[c] P_n will, in general, be inversely proportional to bandwidth.

[d] Mixer temperature.

[e] Under development in 4 to 12 μm region.

TABLE DIV.- ARRAY AND IMAGING DETECTORS

Type	Useful wavelength range, μm	Useful temperature range, °C	Cut-off frequency, MHz	Quantum efficiency	Noise-equivalent power, $W/Hz^{1/2}$
Photodiode array	<1.2	-70 to -100	>400, electronics limited	≤1.0	10^{-16}
Silicon-target vidicon[a]	<0.9	-30 to 30		0.5, wavelength dependent	
Fiber optic array plus PMT's	<0.9	-30 to 30	>400	0.5, wavelength dependent	10^{-12} or [b]10^{-18}
Multichannel plate[c,d]	<0.9	-30 to 50	[e]<0.1	0.5, wavelength dependent	10^{-16}
Charge-coupled devices[d,f]	<1.2	To -100	10	1.0	10^{-12}
Charge-injection devices[d,f]	<1.2	To -100	10	1.0	10^{-12}

[a] Low dynamic range (10^2) and poor linear response.

[b] P_n photocathode dependent, photocathodes with IR response have larger P_n.

[c] Require active memory for effective use.

[d] Rapid technology advances.

[e] Limited by pixel charge.

[f] More support logic to run charge injected device than charge coupled device.

APPENDIX D

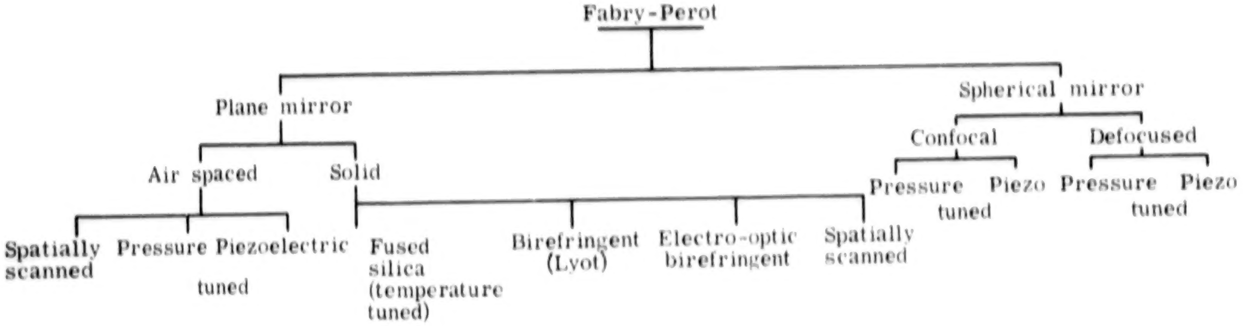
Fabry-Perot
Plane mirror
Spherical mirror
Air spaced
Solid
Confocal
Defocused
Pressure
Piezo
tuned
Pressure
Piezo
tuned
Spatially scanned
Pressure
Piezoelectric
tuned
Fused silica (temperature tuned)
Birefringent (Lyot)
Electro-optic birefringent
Spatially scanned

Figure D1.- Different Fabry-Perot types and applications.

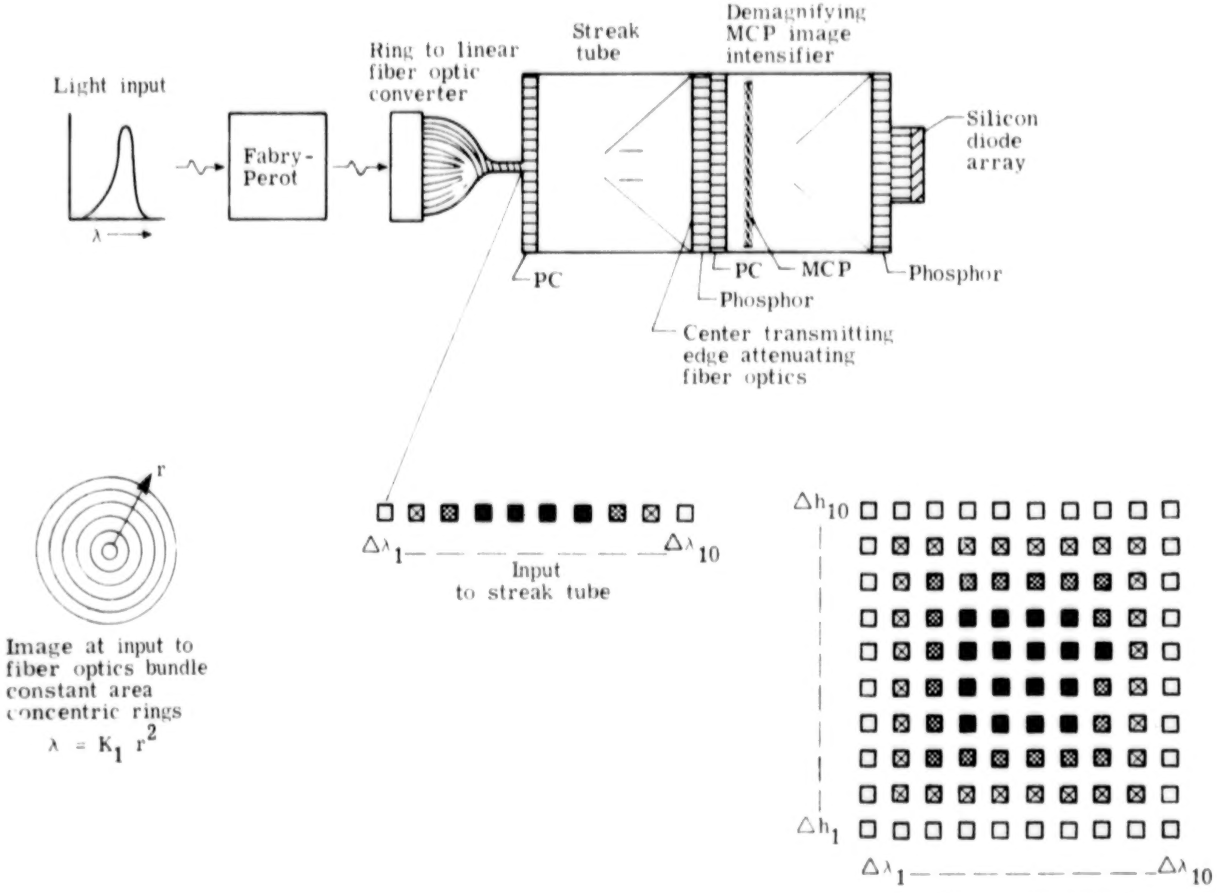
Light input
λ
Fabry-Perot
Ring to linear fiber optic converter
Streak tube
Demagnifying MCP image intensifier
Silicon diode array
PC
PC
MCP
Phosphor
Phosphor
Center transmitting edge attenuating fiber optics
r
Image at input to fiber optics bundle constant area concentric rings
λ = K1 r2
Δλ1
Δλ10
Input to streak tube
Δh10
Δh1
Δλ1
Δλ10
Streak tube output

Figure D2.- Possible arrangement for spatially scanning fringe pattern of a Fabry-Perot detector.

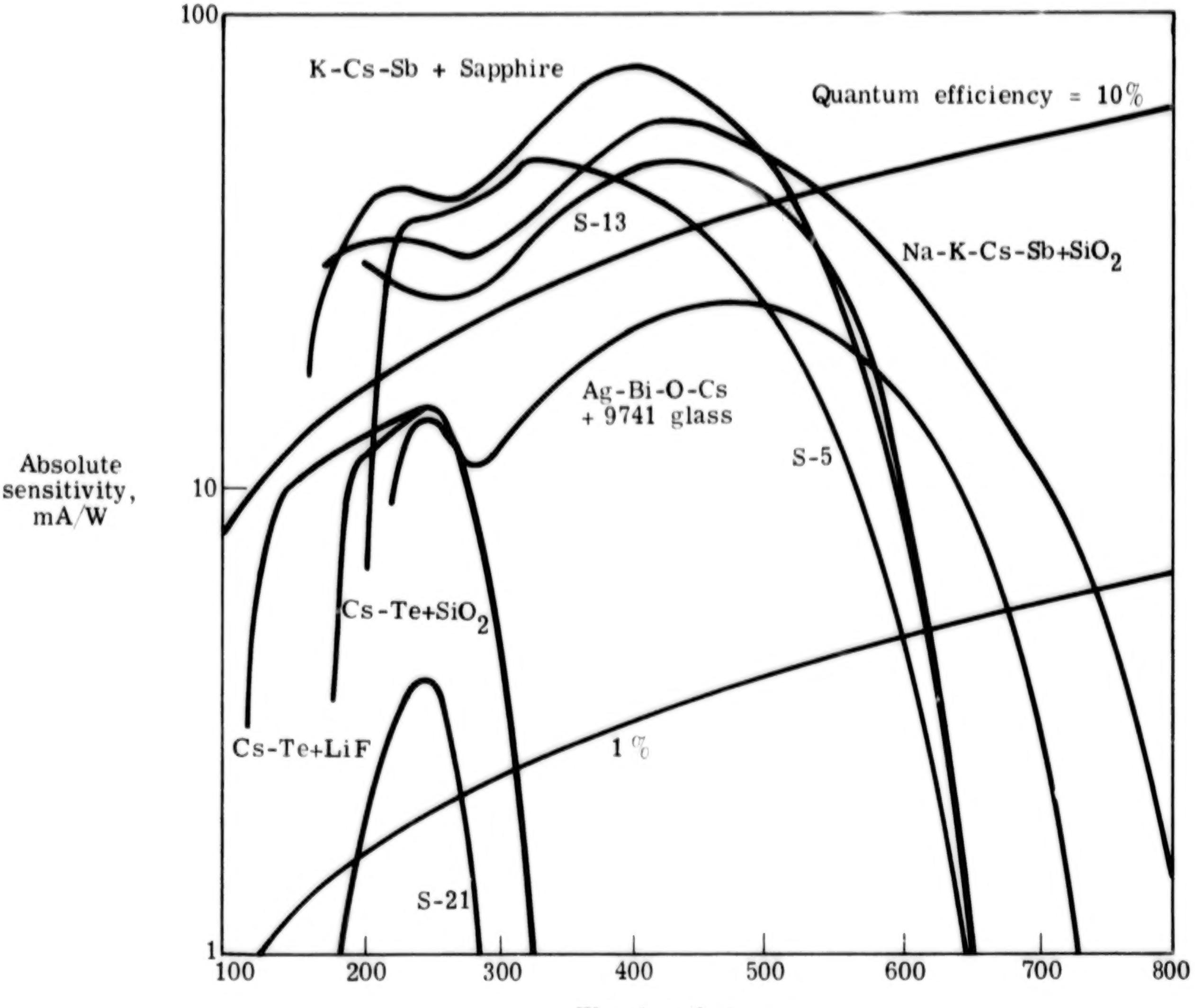

Figure D3.- Spectral response of photocathode surfaces sensitive in near-ultraviolet and visible regions, including effects of window transmission. (From Photomultiplier Tubes, RCA Corp., 1971)

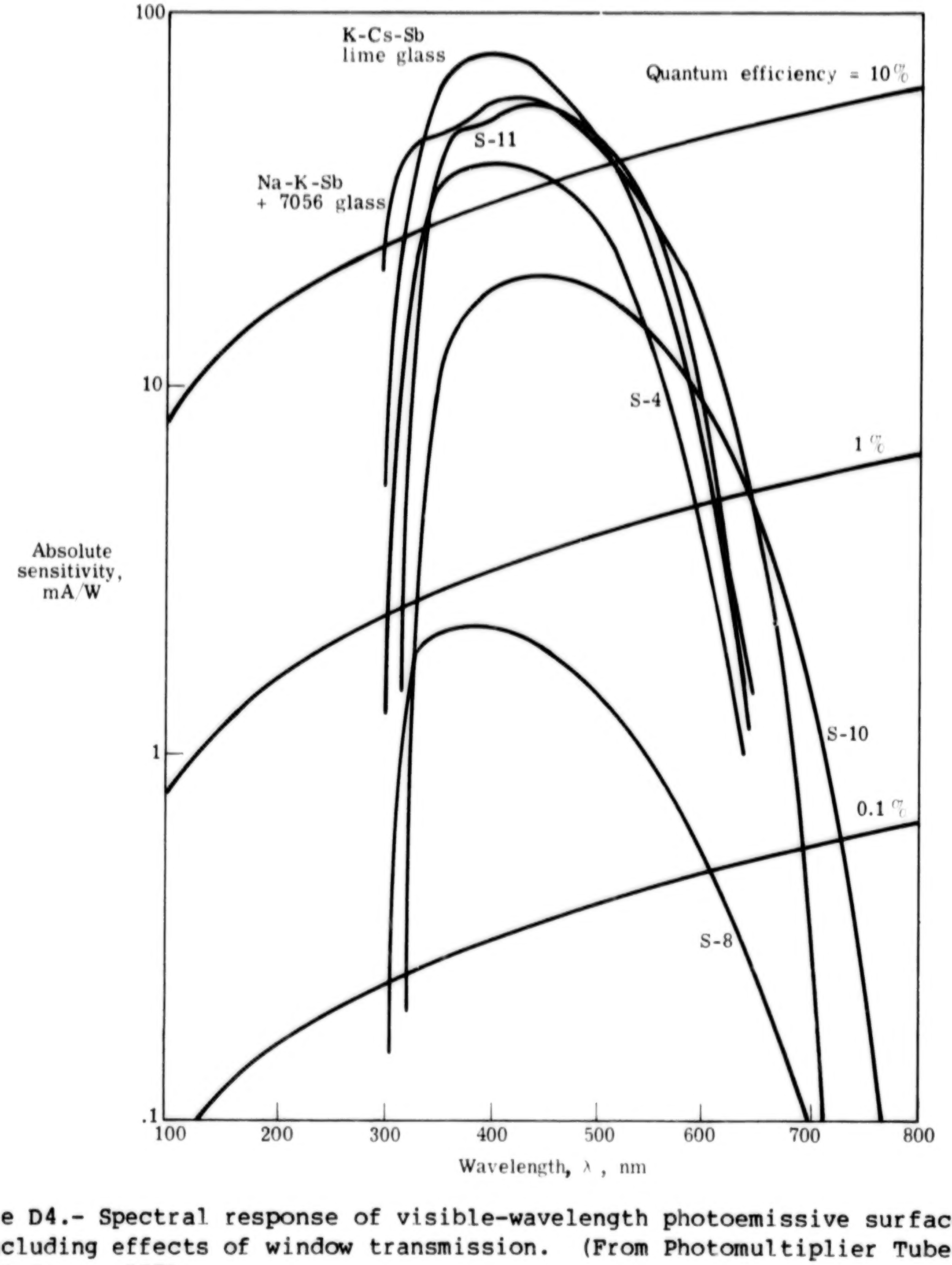

Figure D4.- Spectral response of visible-wavelength photoemissive surfaces, including effects of window transmission. (From Photomultiplier Tubes, RCA Corp., 1971)

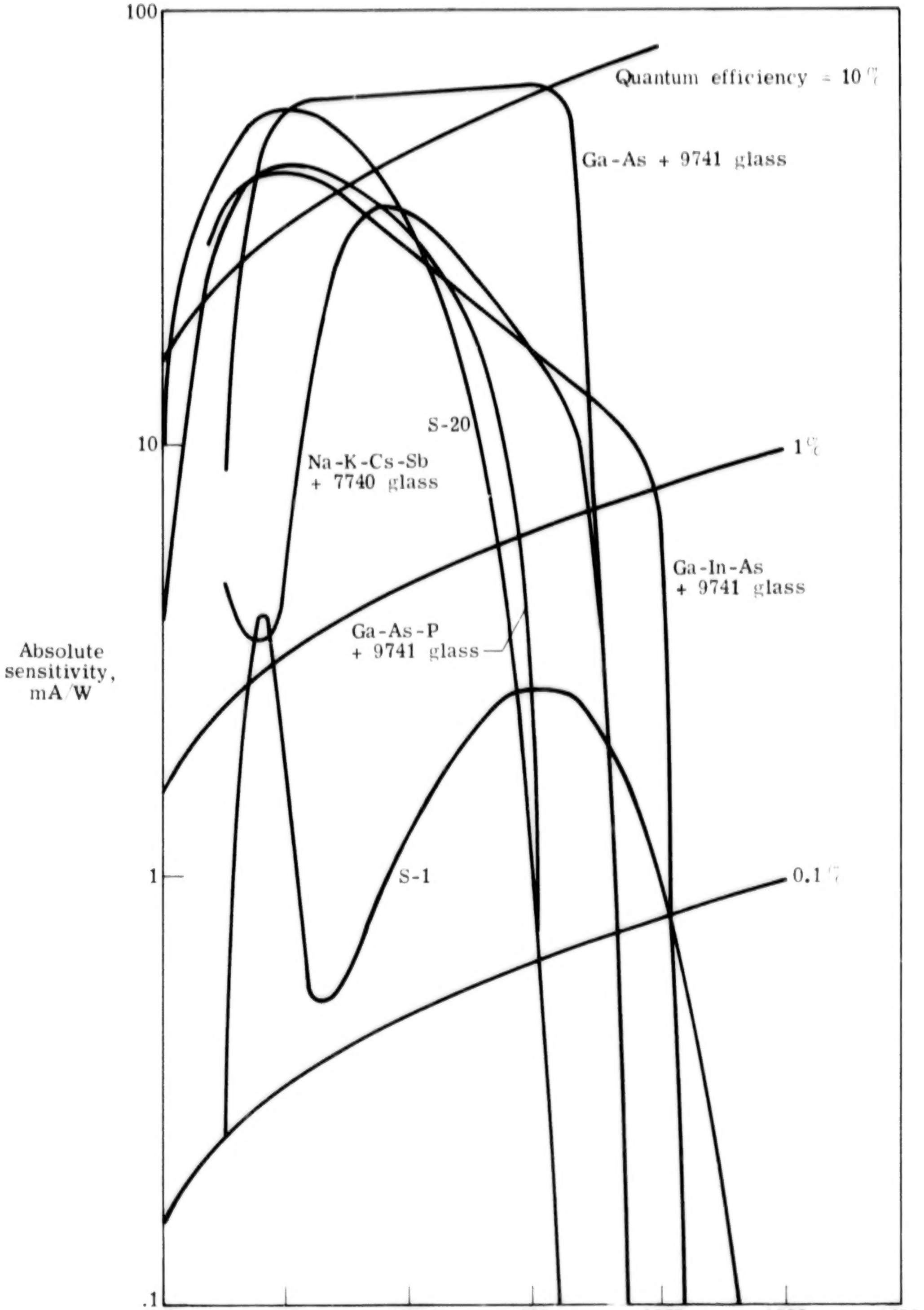

Figure D5.- Absolute spectral response of photocathodes sensitive to near-infrared and visible wavelengths, including window effects. Separate curves indicate QE in percent. (From Photomultiplier Tubes, RCA Corp., 1971)

APPENDIX E

MICROFILMED FROM
BEST AVAILABLE COPY

GLOSSARY

AEM	Applications Explorer Mission
ATMOS	Atmospheric Trace Molecules Observed by Spectroscopy
BUV	backscatter ultraviolet
CFM's	chlorofluoromethanes
CLIR	Cryogenic Limb-Scanning Interferometer and Radiometer
CW	continuous wave
DCR	Diffraction Coupled Resonator
DIAL	Differential Absorption Lidar
EFL	effective focal length
ERB	Earth Radiation Budget
ERBSS	Earth Radiation Budget Satellite System
ESA	European Space Agency
ESMR	Electrically Scanning Microwave Radiometer
FHG	fourth harmonic generation
FOV	field of view
FPL	flashlamp-pumped laser
FWHM	full width at half maximum
GARP	Global Atmospheric Research Program
GATE	Global Atmospheric and Transport Experiment
GISS	Goddard Institute of Space Sciences
HALOE	Halogen Occultation Experiment
HCN	Hurricane Model
HIRS	High Resolution Infrared Sounder
IR	infrared
JPL	Jet Propulsion Laboratory
LHS	Laser Heterodyne Spectrometer
LIMS	Limb Infrared Monitor of the Stratosphere
LLLTV	Low-light level television
LRIR	Limb Radiance Inversion Radiometer
MAP	Measurement of Atmospheric Pollution Instrument
METROMEX	Meteorological Measurement Experiment
MF	medium frequency
MST	mesosphere/stratosphere/troposphere
NASA	National Aeronautics and Space Administration
NLC	noctilucent cloud
NMC	National Meteorological Center
NOAA	National Oceanic and Atmospheric Administration
OGO	Orbiting Geophysical Observatory
PMT	photomultiplier tube
pps	pulses per second
PRF	pulse repetition frequency
QE	quantum efficiency
SAGE	Stratospheric Aerosol and Gas Experiment
SAM	Stratospheric Aerosol Measurement
SAMS	Stratosphere and Mesosphere Sounder
SBUV/TOMS	Solar Backscatter Ultraviolet/Total Ozone Mapping System
SCAMS	Scanning Microwave Spectrometer

APPENDIX E

SEED	Science Objectives, Experiment Descriptions, and Evolutionary Flow Document
SHG	second harmonic generation
SME	Solar Mesosphere Explorer
SNR	signal-to-noise ratio
SOAP	$Ca_2La_8(SiO_4)_6O_2$
TEA	Transverse Excited Atmosphere
THG	third harmonic generation
UARS	Upper Atmosphere Research Satellite
UV	ultraviolet
VFM	Very Fine-Mesh Model
VHF	very high frequency
VTPR	Vertical Temperature Profile Radiometer
YAG	yttrium aluminum garnet
YALO	$Y_3Al_5O_{12}$
c	speed of light
h	Planck's constant
K	eddy diffusion coefficient
k	Boltzmann constant
P_n	noise-equivalent power
R_{max}	maximum backscattering ratio
T	temperature
X or x	h[illegible]zontal distance
Z or z	[illegible]cal distance
×2,×3,×4	[illegible]ency doubled, tripled, and quadrupled
λ	[illegible]ngth
ρ	[illegible]ensity

MICROFI[illegible] FROM
BEST AVAILA[illegible] COPY

NASA-Langley, 1979

90 %

50 %

END

6-25-81